2011

Statistical image reconstruction for quantitative computed tomography

Joshua Evans
Virginia Commonwealth University

Statistical image reconstruction for quantitative computed tomography

by

Joshua D. Evans

Director: Jeffrey F. Williamson, Ph.D.

Professor & Chair, Division of Medical Physics, Department of Radiation Oncology

A dissertation presented to the School of Medicine of Virginia Commonwealth University in partial fulfillment of the requirements for the degree of

DOCTOR OF PHILOSOPHY

July 2011

Richmond, Virginia

Acknowledgements

I would like to express deep appreciation to:

My family and friends for their never ending love and support for all of my endeavors up to this point and into the future.

My research advisor, Dr. Jeffrey Williamson, for his support and guidance throughout the course of this research. His curious nature has led to many interesting findings through the years, and I feel privileged to have had the chance to work so closely with him on these projects.

My Washington University collaborators; Dr. Joseph O'Sullivan, Dr. Bruce Whiting and Dr. David Politte; for the many insightful conversations concerning the Alternating Minimization algorithm.

My dissertation committee members; Dr. Jeffrey Williamson, Dr. Joseph O'Sullivan, Dr. Martin Murphy and Dr. Douglas Arthur; for taking the time to guide the research described here.

Paul Klahr and Charles Cassudakis from Philips Healthcare for their sharing of time and expertise in support of this research.

The National Institutes of Health (R01 CA 75371, P01 CA 116602 and 5P30 CA 016059, J. Williamson, Principal Investigator) and Varian Medical Systems for partial funding of this research.

Table of Contents

Preface

This dissertation is based on the following papers referred to in the text by their roman numerals:

I. J. D. Evans, D. G. Politte, B. R. Whiting *et al.*, “Noise-resolution tradeoffs in x-ray CT imaging: a comparison of Penalized Alternating Minimization and Filtered Backprojection algorithms,” Med. Phys., 38(3), 1444-1458 (2011).

II. J. D. Evans, D. G. Politte, B. R. Whiting *et al.*, “Effect of contrast magnitude and resolution metric on noise-resolution tradeoffs in x-ray CT imaging: a comparison of non-quadratic penalized alternating minimization and filtered backprojection algorithms,” Proc. of SPIE - Physics of Medical Imaging, conf 7961-83 (2011).

III. J. D. Evans, B. R. Whiting, D. G. Politte *et al.*, “Prospects for quantitative imaging on commercial fan-beam CT scanners: Experimental assessment of analytic and polyenergetic statistical reconstruction algorithms,” Under Review at Phys. Med. Biol., (2011).

IV. J. D. Evans, B. R. Whiting, J. A. O'Sullivan *et al.*, “Prospects for in vivo estimation of photon cross-sections using post-processing dual-energy CT imaging on a commercial scanner: comparison of analytic and polyenergetic statistical reconstruction algorithms,” Manuscript in preparation, (2011).

Abstract

Statistical iterative reconstruction (SIR) algorithms for x-ray computed tomography (CT) have the potential to reconstruct images with less noise and systematic error than the conventional filtered backprojection (FBP) algorithm. More accurate reconstruction algorithms are important for reducing imaging dose and for a wide range of quantitative CT applications. The work presented herein investigates some potential advantages of one such statistically motivated algorithm called Alternating Minimization (AM). A simulation study is used to compare the tradeoff between noise and resolution in images reconstructed with the AM and FBP algorithms. The AM algorithm is employed with an edge-preserving penalty function, which is shown to result in images with contrast-dependent resolution. The AM algorithm always reconstructed images with less image noise than the FBP algorithm. Compared to previous studies in the literature, this is the first work to clearly illustrate that the reported noise advantage when using edge-preserving penalty functions can be highly dependent on the contrast of the object used for quantifying resolution. A polyenergetic version of the AM algorithm, which incorporates knowledge of the scanner's x-ray spectrum, is then commissioned from data acquired on a commercially available CT scanner. Homogeneous cylinders are used to assess the absolute accuracy of the polyenergetic AM algorithm and to compare systematic errors to conventional FBP reconstruction. Methods to estimate the x-ray spectrum, model the bowtie filter and measure scattered radiation are outlined which support AM reconstruction to within 0.5% of the expected ground truth. The polyenergetic AM algorithm reconstructs the cylinders with less systematic error than FBP, in terms of better image uniformity and less object-size dependence. Finally, the accuracy of a post-processing dual-energy CT (pDECT) method to non-invasively measure a material's photon cross-section information is investigated. Data is acquired on a commercial scanner for materials of known composition. Since the pDECT method has been shown to be highly sensitive to reconstructed image errors, both FBP and polyenergetic AM reconstruction are employed. Linear attenuation coefficients are estimated with residual errors of around 1% for energies of 30 keV to 1 MeV with errors rising to 3%-6% at lower energies down to 10 keV. In the ideal phantom geometry used

here, the main advantage of AM reconstruction is less random cross-section uncertainty due to the improved noise performance.

1. Introduction

X-ray computed tomography (CT), first introduced in the early 1970's, has grown to become one of the most important imaging modalities in modern medicine for both diagnostic and therapeutic applications. In x-ray transmission tomography, photons produced in an x-ray tube are transmitted through the patient to form projections that represent the attenuation along the ray connecting the source and detector. Projections acquired at many angles around an object allow tomographic reconstruction of the object's interior based on Radon's theory from 1917. The intensity of each reconstructed image pixel is related to the total attenuation coefficient of the material occupying that location. Advances in hardware technology, such as slip-ring gantry designs, helical scanning trajectories and increasing the number of axial slices acquired per rotation allow modern day acquisition of an entire volume of CT data in a few seconds.

X-ray CT has found use in a broad range of diagnostic and therapeutic applications owing to its ability to visualize three-dimensional (3D) anatomical structure, excellent contrast and fast data acquisition. Many applications utilize the information in CT images qualitatively, e.g., comparing the relative intensity to identify tissue changes in support of a diagnosis or using the geometric information for localizing certain anatomical structures. In radiation therapy (RT), CT simulators are used to visualize target volumes in 3D allowing highly conformal doses of radiation to be delivered. The advent of flat panel detectors has led to the development of in-room cone-beam CT imaging systems used for image-guided RT to reduce daily targeting errors. Other applications endeavor to use the quantitative information of reconstructed CT image intensities. For example, to calculate the delivered RT dose in heterogeneous 3D patient geometries or to assess bone mineral density changes indicative of osteoporosis. In these quantitative applications, small systematic and random errors in reconstructed image intensity may undermine the clinical efficacy of the intended task.

The focus of this dissertation research is in the application and characterization of an advanced CT image reconstruction algorithm that has the potential to improve the accuracy of reconstructed image intensities in support of quantitative CT applications.

The following introduction sections present the major concepts, background and rationale for this research. First, the general properties and assumptions of the conventional reconstruction method that can lead to systematic and random image uncertainties are outlined. An introduction to a class of statistically motivated reconstruction algorithms is then provided. These algorithms have the potential to reduce systematic and random uncertainties. The potential clinical impact of more accurate image reconstruction for quantitative CT is then presented. Special focus is on the topic of reducing CT patient dose and the specific quantitative CT problem of estimating low-energy photon cross-section information. The aim and novelty of the remaining chapters is then summarized.

1.1. Filtered back-projection (FBP) for x-ray CT image reconstruction

Despite the major advances in CT scanner hardware and data acquisition techniques, commercially utilized reconstruction algorithms have changed relatively little since the introduction of the first clinical scanner in 1972. Filtered backprojection (FBP)[1] has been the reconstruction algorithm of choice because it is fast and supports image quality sufficient for most qualitative applications of CT. The backprojection technique essentially "smears" the measured attenuation line-integral equally amongst pixels along each source-detector ray passing through the patient. A basic filter, a ramp function, is applied to the data to remove the effect of a 1/r blurring artifact inherent in the backprojection process. Other filter modifications are often employed, such as a window function to limit reconstruction to frequencies within the Nyquist sampling limit. The use of a weighting function in the backprojection operation extends the basic FBP algorithm from parallel beam to modern fan-beam acquisition geometries. Further algorithm modifications have been developed in recent years to reconstruct data acquired from cone-beam geometries allowing acquisition of an entire volume of data in a single rotation.

The use of FBP for image reconstruction in x-ray CT is based on some limiting assumptions. First, it is assumed that the projection measurements are noiseless. Noise in the projection data propagates through the image reconstruction process resulting in image intensity variations in otherwise homogeneous regions (i.e. random error). Excessive noise can limit the clinical utility of the reconstructed images by hiding low-

contrast objects. Projection noise can be reduced by increasing the photon flux through the patient, but at the cost of increased radiation dose imparted to the patient. To reduce image noise, conventional FBP techniques alter the filter to further reduce the amplitude of high-frequency signals in the data, since noise tends to be high frequency in nature. However, as edges are also high frequency structures, increased image smoothing results in a blurring of physical edges, i.e., reduced resolution. The relationship between reducing image noise at the cost of reduced edge resolution is referred to as the *noise-resolution tradeoff* and is characteristic of all image smoothing strategies.

The second assumption of the analytic Radon transform inversion performed by FBP is that the measured data are linear functions of the attenuation line integral along each source-detector ray. Actual measured CT data can suffer from a number of physical processes that give rise to a nonlinear relationship between the attenuation line integral and the logged data. One such process arises from the fact that the Bremsstrahlung photons emitted from modern day x-ray tubes consist of a spectrum of energies up to the accelerating tube potential, which deviates significantly from the monoenergetic assumption of FBP. Since low energy photons are absorbed more readily than high energy photons, the average energy of the x-ray spectrum becomes greater as the beam traverses an object. The beam is then said to be "harder" than it was when incident on the object. The polyenergetic x-ray spectrum leads to a non-linear relationship between attenuation and the thickness of an absorber that invalidates the linear assumption of FBP. The beam-hardening (BH) phenomenon leads to the characteristic cupping artifact (i.e. systematic error)[2]. Modern day scanners pre-condition the data in an attempt to linearize it prior to the FBP reconstruction[3]. Most data correction schemes are based on the assumption that the object is water-equivalent. As patients contain heterogeneous distributions of bone and soft tissue, residual artifacts often remain.

Radiation that is scattered within an object and reaches a detector other than that of the original ray path is another cause of nonlinear CT detector response. The severity of the effect from scattered radiation is directly related to the relative fractions of detected signal due to scattered and primary radiation, i.e. the scatter-to-primary ratio (SPR). In a uniform object, scattered radiation causes cupping artifacts similar to the BH effect as the

SPR is greatest for rays traversing thicker portions of the object[4]. The systematic underestimation arises since the scattered radiation leads to an increase in detected signal (i.e. an underestimate of attenuation), causing the image intensity to be decreased. Scatter, as it adds a nearly uniform background to the measured data is also known to decrease image contrast. When highly attenuating objects such as bone or metal are present, beam-hardening and scattered radiation non-linearities are enhanced, causing systematic streaking artifacts[5] which severely limit the clinical utility of the images. If an estimate of the distribution of scattered radiation is available, it can be subtracted from the measured data prior to FBP reconstruction. However, even with an ideal scatter subtraction, reconstructed image noise increases because the scattered intensity contains high frequency noise not accounted for in the smoothly varying scatter estimates[6,7].

1.2. Statistical iterative reconstruction (SIR) for x-ray CT

In contrast to deterministic FBP reconstruction, statistical reconstruction algorithms pose image reconstruction as an optimization problem[8]. The goal of the optimization is to find the image that maximizes the likelihood of observing the measured CT projection data. The likelihood term in the objective function is derived from an assumed statistical distribution of the measured data, hence "statistical" in the name. A forward model simulates the CT data formation process and is used in estimating the data means from the current image estimate. The chosen algorithm then iteratively refines the image estimate to maximize the fit between the measured data and the simulated data means according to the likelihood term of the objective function.

The simple Poisson distribution of photon counting statistics is most often assumed to describe the measured data. Due to the fact that physical CT detectors are energy-integrating, the measured data are more accurately represented by the compound Poisson distribution[9], although it has been shown that the simple Poisson distribution is an acceptable approximation for x-ray CT[10]. Reconstruction founded on a statistical description of the data does not in itself lead to images with less noise. In fact, the image most likely to match the measured data is often unacceptably noisy[11] termed as an "over-fitting" of the data. One strategy is to impose constraints on the image to satisfy *a priori* assumptions about the object being imaged, for example smoothness. The assumption of

image smoothness is enforced by including a function that penalizes neighboring pixel-to-pixel intensity variations, assumed to be noise, in the objective function. Roughness penalties effectively reduce image noise, at the expense of blurring physical edges. For these *penalized likelihood* methods, the tradeoff between noise and resolution is controlled by weighting the relative importance of the penalty function in the penalized objective function.

An algorithm that provides a noise-resolution tradeoff advantage means that it can reconstruct an image from the same dataset with less image noise for comparable edge resolution, or conversely better edge resolution for the same amount of image noise. Quadratic penalties are commonly employed to regularize statistical reconstructions, but they grow rapidly for large pixel variations and tend to over-blur high-contrast edges. Edge-preserving penalty functions are designed to reduce the magnitude of the penalty for large intensity differences with the goal of preserving high-contrast resolution. However, detailed study of the resulting contrast-dependent nature of these edge-preserving penalty functions and their effect on the noise-resolution tradeoff is lacking. Studies quantifying the noise-resolution tradeoff advantage of statistical algorithms in x-ray CT are limited to matching the resolution of high-contrast objects[12-14] and often utilize simple quadratic penalty functions. The aim of chapter 2 is to assess the noise-resolution tradeoff properties of one such edge-reserving penalty function. In this work, a novel statistical iterative reconstruction algorithm, Alternating Minimization (AM) is used. The AM algorithm is discussed in more detail in the following chapters, Appendix 1 and the appended papers this dissertation is based on.

The SIR forward model allows the flexibility to incorporate many of the non-linear processes of CT data acquisition physics that invalidate the underlying assumptions of FBP. Both the polyenergetic nature of the x-ray spectrum and an estimate of scatter can be directly incorporated into the forward model. Furthermore, arbitrarily complex acquisition geometries and effects such as detector blurring can be incorporated, whereas FBP is derived for parallel beam geometry and requires weighting corrections or interpolation for other geometries. This research focuses on the ability of SIR to reduce systematic artifacts from data non-linearities such as beam-hardening and scatter.

Literature has shown that the implicit beam-hardening correction of a polyenergetic statistical model reconstructs images with improved freedom from systematic cupping artifacts than FBP reconstruction of linearized data[15,16]. However, these comparisons are limited to simulation studies or real data studies using experimental bench-top systems. Chapter 3 investigates the CT system characterizations necessary to implement a polyenergetic SIR algorithm on a commercially available CT scanner and the quantitative accuracy achievable.

1.3. Impact for quantitative CT applications and the reduction of CT imaging dose

Quantitative CT applications rely on one-to-one relationships relating reconstructed image intensities to the quantity of interest, which break down in the presence of systematic (scatter, BH, etc.) and random errors (noise). For many quantitative applications, the absolute accuracy of the reconstructed intensity may be relatively unimportant if the method is calibrated against relevant control samples. However, the reconstructed image intensity for a given material needs to be *consistent*; that is, intensity for a given material should be independent of location within the scan subject, size of the scan subject, and location of the scan subject within the field-of-view (FOV)[17,18]. Residual errors will remain when the test object varies in size, composition or location relative to the calibration sample. Quantitative CT applications such as bone mineral density measurement[19,20], brain perfusion imaging[21], and cardiac perfusion imaging[22] have all been shown to suffer a loss of accuracy from residual systematic errors. The development and characterization of reconstruction algorithms that reduce systematic and random errors is thus important for a broad range of clinical quantitative CT applications.

As described in the following sections, the specific quantitative CT problem of estimating photon cross-sections from CT images has the potential for clinical impact in radiation therapy. This quantitative CT problem has been shown to be highly sensitive to uncertainties in image intensity and motivates the investigation of more accurate image reconstruction algorithms.

Dose calculation inaccuracies in low energy photon brachytherapy

Variations in the atomic composition of tissues impact megavoltage (MV) and kilovoltage (kV) radiation therapy dose absorption differently. In the MV energy range the dominant mechanism of photon interaction is Compton scattering, which depends mainly on a material's electron density. Quantitative methods for inferring electron density from CT image intensity have been shown capable of supporting dose calculations in the heterogeneous patient-specific geometry with an accuracy of 5% or better[23,24].

The current practice for calculating dose from low energy brachytherapy modalities is based on the TG-43 protocol[25] which assumes the patient is a homogeneous sphere of water. The compositional differences between tissue and water can lead to large dose calculation errors for low energy brachytherapy sources. In fact, dose-volume histogram (DVH) metrics commonly used for dose prescription and plan assessment such as D90 (the dose that covers 90% of the target volume) have been shown to deviate as much as 30% when incorporating tissue composition and heterogeneities[26-29]. Even higher energy brachytherapy sources like Ir-192 and Yb-169, can suffer dose calculation errors on the order of 5% to 30% when neglecting tissue composition and geometry[30,31]. The greater effect of tissue composition for kV photon modalities is due to the increased likelihood of photoelectric absorption, which is strongly dependent on a material's atomic number.

Permanent implantation of low energy Pd-103 and I-125 seeds has become a major modality in the treatment of prostate cancer[32]. For prostate cancer, the rate of both local tumor control and normal tissue toxicity have been correlated with delivered dose[33-35]. For breast cancer, accelerated partial breast irradiation (APBI) utilizing Ir-192 brachytherapy sources shortens the treatment delivery time to 1 week in comparison to 6-7 weeks for conventional whole-breast treatment[36]. Recently, there has been interest in permanent seed implantation[37] and intracavitary delivery using electronic x-ray sources[38,39] for partial breast irradiation, which has the potential to further reduce costs and shorten treatment delivery time. Preliminary studies on outcomes of Pd-103 seed implantation in the breast have shown a dose-relationship for skin toxicity[40]. The APBI literature using higher energy Ir-192 sources is more extensive and also show correlation

between dose metrics and treatment toxicity[41,42]. The inaccurate calculation of dose has the effect of flattening the dose-response curve making it more difficult to detect statistically significant changes in dose-outcome relationships[43]. Dose calculation inaccuracies also make it difficult to compare the efficacy of different treatment modalities, for example comparing outcomes for partial breast irradiation using intracavitary Ir-192 delivery and Pd-103 permanent seed implantation. Thus, methods to improve patient-specific dose calculations stand to make a clinical impact on outcomes for patients treated with these low energy brachytherapy modalities.

Methods of accurately calculating dose for low energy brachytherapy sources in patient-specific heterogeneous geometries exist, for example Monte Carlo simulation[27,28] or discrete ordinates methods[44,45]. However, they must be provided with accurate information about the material occupying each voxel location. Recommended bulk tissue compositions are derived from a handful of measurements that exhibit large sample-to-sample variability[46,47]. In addition, large patient-specific variations exist in the relative amount of tissue types present in an anatomic region, for example the relative amount of adipose and glandular tissues in the breast[48,49]. Uncertainty in bulk tissue composition and large patient-to-patient variability highlight the need for a method to measure patient-specific material information. Single-energy (SE) CT methods used to calculate patient-specific heterogeneity corrections for MV photon dose calculation are unsuitable in the kV range due to the dependence on both electron density and atomic number.

Dual-energy CT (DECT) for non-invasive measurement of photon cross-sections

Dual-energy CT measurements can be used to decouple the dependence of attenuation on two independent material parameters. At the core of DECT are two-parameter models that relate CT image intensity to an underlying parameter set. Models that parameterize a material's attenuation based on effective atomic number (Z_{eff}) and electron density (ρ_e)[50] are physically intuitive, as they are directly related to the physical processes of attenuation. Much effort in the literature has been focused on this type of parameterization in DECT for material characterization[50-53]. For example, Bazalova et al.[51] used a DECT material characterization method to estimate Z_{eff} and ρ_e from real data with mean accuracies of 2.8% and 1.8% respectively for a range of materials. They

further reported dose calculated using the DECT estimated Z_{eff} and ρ_e values to be within 1% of dose calculated with exactly assigned material parameters for 18 MV, 6MV and 250 kVp photon beams. However, the effect of the uncertainty in Z_{eff} and ρ_e is unclear for low energy brachytherapy (20 – 30 keV) dose calculation where the PE mechanism dominates. What is ultimately desired for accurate dose calculation is an accurate representation of a material's radiological properties including the total attenuation coefficient, mass-energy absorption coefficient, and partial and differential cross-sections for individual interaction processes. Williamson et al. showed that the widely used models that parameterize attenuation as functions of Z_{eff} and ρ_e do not accurately represent low energy cross-sections, especially PE partial cross-sections or mass-energy absorption coefficients[54].

To date, very few experiences have been reported in the literature that systematically assess the accuracy achievable of photon cross-section estimation using multi-energy CT data. Midgley has shown the ability to represent low energy photon cross-sections with 1.5% accuracy. However the model is impractical for clinical use as it requires scans at 4 energies and also utilizes near monochromatic characteristic x-ray beam scanning that cannot be easily extrapolated to clinical practice[55,56]. Another 2-parameter model, the basis-vector model (BVM), represents the attenuation of an unknown substance as a linear combination of the attenuation functions of two known and well-chosen basis materials. Williamson et al. have demonstrated the ability of the computationally simple BVM to represent low energy cross-sections from ideal simulated DECT images with around 1% accuracy[54], making it a viable candidate for cross-section estimation. The method described by Williamson et al. utilizes reconstructed image information, and is thus termed a 'post-processing' technique. Goodsitt et al. reported recently on their experience using the commercial GE dual-energy system for estimating linear attenuation coefficients in the energy range of 40 keV to 120 keV[57]. Though the details of the proprietary GE system are unknown, they do report that low energy cross-sections estimates can quickly deviate greater than 20% from reference and are extremely sensitive to imaging errors.

Similarly, Williamson et al. used an error propagation analysis to demonstrate that the post-processing DECT cross-section estimation is exquisitely sensitive to reconstructed CT image intensity uncertainties[54]. DECT cross-section estimation pushes CT image reconstruction to a limit of precision and accuracy not likely achievable using conventional preprocessing corrections and FBP reconstruction. Given the apparent advantages of statistical reconstruction algorithms in reconstructing images with both less noise (random error) and artifacts (systematic error) it is hypothesized that SIR can further improve the performance of the otherwise poorly conditioned DECT photon cross-section problem. Chapter 4 compares the accuracy of a post-processing DECT cross-section estimation method operating on images reconstructed with FBP and SIR algorithms using data acquired on a commercial scanner.

Reduction of CT imaging dose

X-ray CT, in using ionizing radiation for image formation, delivers a quantifiable amount of radiation dose to the scan subject. Epidemiological studies of atomic bomb survivors and radiation workers have shown a statistically significant increase of cancer incidence for effective doses in the range of 10-100 mSv[58,59]. While there is no direct evidence of increased cancer risk from CT procedures, the currently accepted linear no-threshold model can be used to extrapolate risk to the low doses on the order of 10 mSv or less, common to CT[60]. Recent publications have highlighted the increased utilization of CT as a potential public health issue[61] which raises the question of the clinical benefit from performing a CT exam relative to the associated risk of carcinogenesis. In the diagnostic realm, the increased use of CT for pediatric patients and screening of high-risk, but asymptomatic, patients for lung cancer, colon cancer and heart disease is highly relevant to this risk-benefit discussion. In radiation oncology, image-guided therapy approaches may include cone-beam CT studies for nearly all fractions over a 5 week treatment course. The growing public consciousness of the increasing utilization of CT in the medical field and the associated carcinogenic potential makes dose reduction an important topic to address.

Reducing the dose imparted from each individual CT examination plays an important role in reducing the collective risk to the general public. The most direct way to reduce

dose from a CT is to reduce the x-ray flux. However, image noise will subsequently increase and could limit the clinical utility of the images by reducing the visibility of low-contrast objects[62]. Increasing the aggressiveness of image smoothing techniques to reduce noise in low dose images comes with the well known tradeoff of reduced edge resolution, which can also limit clinical utility by obscuring small objects. Dose reduction by reducing flux or increasing image smoothing is thus limited by the noise-resolution tradeoff for a particular reconstruction algorithm. An algorithm with a noise-resolution tradeoff advantage will be able to reconstruct an image with comparable image resolution and less noise. Equivalently, such an algorithm could reconstruct images with similar image noise and resolution from noisier data, i.e., data acquired with less patient dose. The noise-resolution tradeoff advantages of SIR algorithms over FBP thus represent the potential for dose reduction by utilizing the acquired data more efficiently.

Noise-resolution tradeoff studies often quote factors of 2 to 10 by which the SIR algorithm can reduce dose relative to FBP[12-14]. However, these comparisons match resolution only for high-contrast objects and typically only use quadratic penalty functions. Edge-preserving penalty functions are designed to penalize high- and low-contrast structures differently. Making dose reduction potential assessments at matched high-contrast resolution for algorithms utilizing edge-preserving penalties may not be appropriate for clinical tasks concerned with visualizing low-contrast structures. Chapter 2 explores considerations necessary to assess the noise-resolution tradeoff advantage, and subsequent potential for dose reduction, of SIR algorithms that utilize edge-preserving penalty functions.

Another important dose-reduction issue is the calculation of patient dose from a CT exam. Current CT dose assessment is based on measurements made in reference phantoms[63] and therefore do not account for even gross patient changes such as body size[64,65]. A non-invasive method to measure patient-specific cross-section information would significantly improve the accuracy of patient-specific dose calculations from kV imaging procedures.

1.4. Research aims and organization

With the potential benefits of more accurate and dose-efficient statistical reconstruction in mind, the work described in this dissertation aims to further the assessment of potential SIR advantages. The noise performance advantages of SIR algorithms have been explored in the literature, however detailed studies are limited to quadratic penalty functions and only when matching resolution for high-contrast structures such as bones or steel bb's. Chapter 2 explores the noise-resolution tradeoff, and implicit dose reduction potential, of edge-preserving penalized likelihood reconstruction. A range of contrast magnitudes are investigated, including low-contrast interfaces characteristic of organ boundaries relevant to the radiation therapy soft-tissue segmentation task.

More accurate modeling of CT physics is expected to provide images with less systematic error from data non-linearities than FBP. In particular, there are examples in the literature that demonstrate modeling the polychromatic x-ray spectrum leads to images with less systematic error from the BH artifact. However, these studies only compare the relative variation of image intensities within a uniform object and assess absolute accuracy in only a few small samples. Furthermore, these comparisons are made in either simulation studies or with real data acquired on experimental bench-top systems. Chapter 3 addresses practical issues for implementing the polyenergetic AM algorithm on a commercial CT scanner with absolute accuracy on the order of 0.5%. Consistency of image intensities is also compared between the AM and FBP algorithms. The accuracy and consistency of reconstruction are investigated using uniform cylinders of varying material, size, and location within the FOV.

From simulation studies in the literature, post-processing DECT methods seem capable of representing photon cross-sections in support of more accurate dose calculation for kV photon modalities. Furthermore, the problem has been shown to be highly sensitive to image intensity errors. Few experiences of estimating photon cross-sections from multi-energy data acquired on a commercial CT system appear in the literature. Chapter 4 assesses the experimental accuracy achievable of a post-processing photon cross-section estimation method for data acquired on a commercially available

CT scanner. Polyenergetic statistical image reconstruction, with advantages of less image noise and less systematic artifacts, is compared to FBP reconstruction for potential improvements to the highly sensitive problem of cross-section estimation from DECT images.

2. Noise-resolution tradeoffs in x-ray CT image reconstruction using edge-preserving penalty functions

2.1. Background

It is known that an image which maximizes the likelihood of observing the measured data often has an undesirable amount of noise[11,66]. Noise can be reduced by terminating iterations prior to convergence[67], however it is difficult to control the noise and resolution properties. In addition, the resolution will be dependent on the particular optimization algorithm that is used[68]. A popular alternative for controlling noise in statistical reconstruction algorithms is by incorporating *a priori* assumptions about the image, e.g. smoothness, in the objective function typically in the form of penalty functions. This process, termed *regularization*, has several attractive properties. Regularization constrains the optimization, which better conditions the ill-posed reconstruction problem ultimately leading to an accelerated rate of image convergence. It should be noted that the penalized estimate may sacrifice accuracy since the maximum of likelihood will not be reached. Penalized likelihood methods allow control over the noise-resolution tradeoff by changing the relative importance of the penalty in the optimization. As noise properties are controlled by the choice of penalty function shape and relative penalty weighting in the objective function, the particular choice of optimization algorithm can be reduced as long as the maximum of the penalized likelihood objective function is reached[8,68]. Herein, we refer to the relative weight of the penalty function in the objective function as the *smoothing strength*.

Previous investigators have studied the noise-resolution tradeoffs in x-ray CT using statistical reconstruction methods. La Riviere et al.[12] employed a Poisson-based penalized likelihood algorithm for smoothing sinogram data prior to FBP reconstruction. A quadratic penalty function was used for regularization and the resolution of the resultant images was quantified by a Gaussian model fit to image-intensity profiles through high-contrast bone edges. Multiple reconstructions were performed with varying smoothing strengths allowing noise-resolution tradeoff curves to be plotted. The tradeoff

curves demonstrate improved noise performance over a range of resolutions for their penalized likelihood sinogram smoothing process in comparison to an adaptive trimmed mean filter approach[69].

Ziegler et al.[14] evaluated the noise performance of a statistical reconstruction algorithm that uses convex surrogates to the Poisson log-likelihood and ordered subsets to increase convergence rate (OSC)[70]. Rather than using regularization, OSC iterations were stopped after the modulation transfer function (MTF) measured using steel bb's was slightly better than achievable with FBP. The FBP kernel was then modified to match the OSC MTF. Ziegler et al. demonstrated that the OSC iterative reconstruction improves signal-to-noise ratio (SNR) by a factor of 2.1 to 3.0 over FBP. Their study used no penalty function and compared SIR and FBP image noise only for equivalent resolution as measured by high-contrast steel bb's.

Thibault et al.[13] presented an interesting study of statistical reconstruction using edge-preserving penalty functions, demonstrating improved cross-plane resolution and reduced cone-beam windmill artifacts in a 3eD multi-slice helical scanning geometry. The effect of several edge-preserving penalty shapes was compared to one another. The smoothing strength for each shape was tuned to match noise in the resultant penalized likelihood images. Resolution was reported as the 50% MTF value measured from a tungsten wire in a GE performance phantom. The results illustrate how the different penalty function shapes lead to varying resolution. For one of the edge-preserving penalty shapes, noise and resolution was compared to FBP reconstruction with "standard" and "bone" filters available on the GE scanner. The edge-preserving penalized reconstruction returned 50% and 10% MTF values similar to the FBP high-resolution bone filter, with less noise than the standard filter. However, a single smoothing strength was used for comparing penalized likelihood and FBP reconstruction without attempting to match noise or resolution. Still the edge-preserving penalized likelihood method showed impressive improvement over conventional FBP stimulating further investigation.

2.2. Methodology and results

First, the terms to describe the CT geometry are defined. All image reconstructions in this dissertation work were carried out in a 2-dimensional axial geometry shown in figure 1. The image space, **x**, refers to the grid of 512x512 rectangular image pixels. The CT sinogram data space, **y**, is defined by the angle of each source-detector ray, γ, and each gantry angle, ϕ.

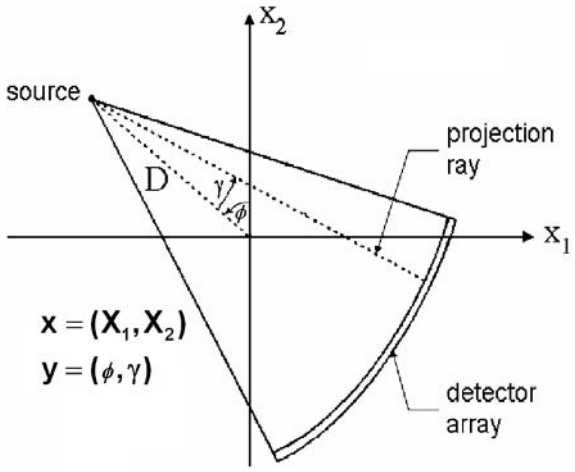

Figure 1. The axial CT geometry used for all reconstructed images in this work.

The Alternating Minimization (AM) algorithm reformulates the classic maximization of the Poisson log-likelihood as a minimization of Csiszar's I-divergence[71], $I(d \,\|\, g)$, an information-theoretic metric that quantifies the discrepancy between the measured data d and the expected data means g that are calculated from the current image estimate μ. The I-divergence equals the negative of the log-likelihood minus an entropy term, meaning that minimizing the I-divergence is equivalent to maximizing the log-likelihood. The AM algorithm is briefly outlined in the appended papers (papers I – IV) and an overview of the algorithm is included in Appendix 1. The full derivation of the algorithm can be found in O'Sullivan 2007[72].

The penalized objective function consists of the I-divergence and a roughness penalty to enforce the assumption of image smoothness:

$$\Phi(\boldsymbol{\mu}) = I(d \,\|\, g) + \lambda \cdot R(\boldsymbol{\mu}). \qquad (1.1)$$

The strength of the image smoothing is controlled by λ, which specifies the relative importance of the penalty function in the optimization.

The log-cosh edge-preserving penalty function

Quadratic penalty functions are effective at suppressing noise, but can over-blur high-contrast structures as the penalty magnitude rapidly increases for large neighboring pixel differences. The continuously defined log-cosh function[73,74] used in this work is similar to the piecewise Huber penalty[75]. The common theme for these edge-preserving penalty functions is to reduce the magnitude of the penalty function for large pixel differences that are likely to be physical edges. The log-cosh penalty function is defined as:

$$R(\boldsymbol{\mu}) = \sum_{x} \sum_{x' \in N(x)} w(x') \cdot \left(\frac{1}{\delta}\right) \log\left[\cosh\left(\delta\left(\mu(x) - \mu(x')\right)\right)\right]. \quad (1.2)$$

The weighting function *w(x)* (equation (4.15) in Appendix 1) controls the neighborhood, *N(x)*, for penalty calculation and includes the four directly adjacent pixels. The parameter δ controls the pixel intensity difference for which the penalty transitions from quadratic to linear growth. Increasing δ causes the transition to linear growth to occur at smaller intensity differences. Figure 2 plots the log-cosh penalty function for two values of δ used in this work. δ=100 transitions for pixel differences of approximately 50% and is closer in shape to a quadratic penalty function. δ=700 transitions for pixel differences of approximately 10% and is closer in shape to a linear function making it strongly edge-preserving.

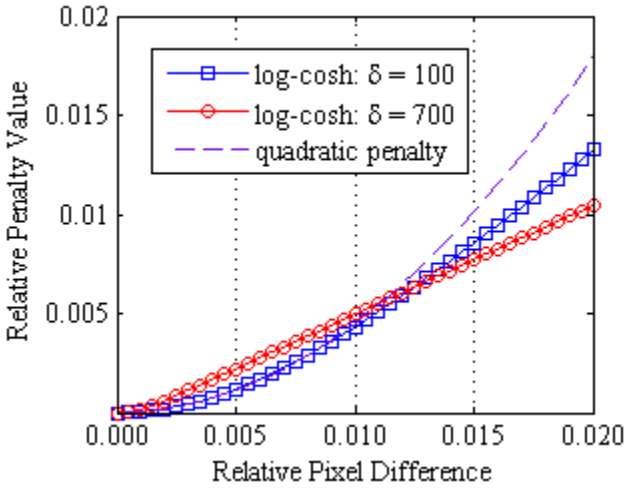

Figure 2. Comparison of quadratic and edge-preserving log-cosh roughness penalties. The parameter δ controls the transition from quadratic to linear growth for the log-cosh penalty function. Note that the functions are scaled here for plotting purposes.

Simulation summary

With the goal of isolating the smoothing properties of the reconstruction algorithms, an ideal monoenergetic simulation environment (E = 61 keV) was used to avoid systematic artifacts from non-linearities such as BH and scatter. Two simulation phantoms are utilized, each consisting of a 20 cm diameter water cylinder with various 2 cm diameter cylindrical contrast inserts. The c*lock phantom*, shown in figure 3, contains 8 inserts of varying contrast [±7% : +238%], each a constant distance from the center (5.5 cm) allowing contrast dependence of the noise-resolution tradeoff to be assessed. Paper I also utilized a *radial phantom* containing 4 inserts of the same contrast (+30%) at varying radial distances from the FOV center (2 cm to 6.5 cm) to assess the spatial dependence of the noise-resolution tradeoff.

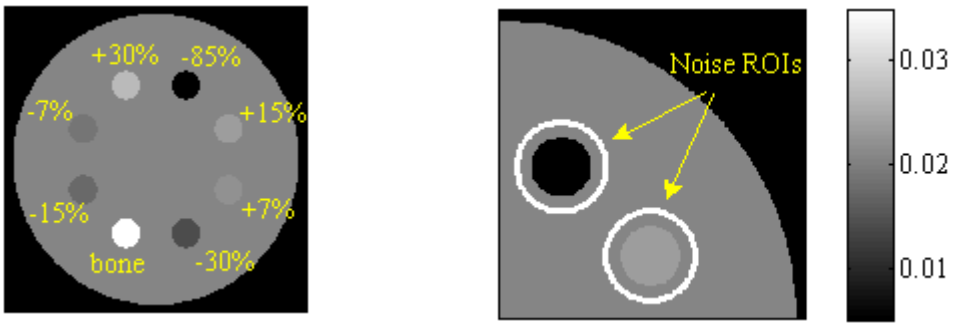

(a) (b)

Figure 3. (a) The *Clock phantom* consists of a 20 cm diameter water cylinder with 2 cm inserts of varying contrast used for assessing the contrast-dependence of the noise-resolution (NR) tradeoff. (b) Regions-of-interest for measuring noise around each contrast insert.

Noiseless monoenergetic data was simulated for the two phantoms in an axial CT geometry composed of 1056 gantry positions (ϕ) equally spaced around a full 360º rotation. There were 384 detectors (γ), each subtending an arc angle of 4.0625 minutes. Source-to-isocenter distance was 570 mm and source-to-detector distance was 1005 mm, giving a detector width of 1.2 mm and projected width at isocenter of 0.67 mm. The image space consisted of 512 x 512 square pixels each 0.5 mm on a side. Simple Poisson noise was added to the data with variance approximating that observed in data acquired on the Philips Brilliance big bore scanner.

To assess the tradeoff of noise and resolution, the synthetic noisy sinogram datasets were reconstructed with a range of smoothing strengths for each algorithm. The FBP algorithm used throughout this dissertation research includes a Gaussian kernel in the filter for image smoothing. For FBP, the logged sinogram data were reconstructed using Gaussian smoothing filters of varying FWHM. Refer to paper I for more detail regarding the FBP algorithm. The penalized AM algorithm is investigated with the two log-cosh penalty shapes displayed in figure 2. *AM-700* uses δ=700 and is strongly edge-preserving. *AM-100* uses δ=100 and is more conservative as it is similar in shape to a quadratic penalty function. Both AM-100 and AM-700 images were reconstructed with a range of smoothing strengths, λ in the penalized objective function (1.1). For each case, the AM algorithm was run for 250 iterations using 22 ordered subsets (refer to Appendix 1). Due to the large number of iterations employed, the AM images are very near

complete convergence, thus the conclusions presented here could reasonably be extrapolated to other algorithms that seek to maximize the same penalized likelihood objective function.

Image noise was evaluated in the water background around each contrast insert within all reconstructions. The standard deviation, as a percent of the mean, was calculated for pixels in a circular annulus surrounding each contrast insert as shown in figure 3.

The resolution metric used in this work is based on the Modulation Transfer Function (MTF). While x-ray transmission CT is not a shift-invariant linear system, the MTF is considered to be a valid measure of local impulse response, providing insight into the effect of reconstruction on edge blurring. As described in more detail in paper I, the MTF was calculated from a model fit to the edge-spread function (ESF) for each contrast insert.

The pre-sampled ESF was constructed for each contrast insert by plotting each pixel's intensity as a function of distance to the analytically defined insert edge. In this way, the transition between the water background and the contrast insert can be visualized. Sampling pixels around a circular insert to form an ESF represents an average of the edge response function within the sampled region of interest, thus reducing effects of resolution anisotropy and non-uniformity.

Edge response shape of the strongly edge-preserving penalty function

Figure 4 shows the ESF of the bone insert for noise-matched FBP and AM-700. It is interesting to note the effect that the strongly edge-preserving AM-700 penalty function significantly alters the shapes of the high-contrast bone insert ESF and MTF. The steep central transition and softer shoulder roll-off necessitated use of a Gaussian-exponential model for fitting, in contrast to the pure Gaussian blurring model which accurately models the FBP image frequency response.

To plot tradeoff curves that illustrate how the image noise and resolution vary as a function of smoothing strength for a particular algorithm, it is useful to extract a single value as a surrogate of edge sharpness. La Riviere[12], reports the FWHM of a Gaussian

blurring model fit to a bone edge. This is an intuitive surrogate as a wider Gaussian represents a blurrier edge. However, our 6-parameter Gaussian-exponential model did not lead to such a straight-forward metric. Figure 4 shows the bone insert's MTF for the noise-matched FBP and AM-700 images. Given the long MTF tails for AM-700 high-contrast structures, conventional MTF metrics like the 10% MTF and 50% MTF were found to provide a poor characterization of the curves. Taking the noise-matched bone MTFs in figure 4 as an example, the 10% MTF for AM-700 is 2.79 lp / mm and for FBP is 0.53 lp / mm. As a surrogate of edge sharpness, the MTF curve is integrated to a chosen spatial frequency *x*:

$$A_x = \frac{1}{x}\int_0^x MTF(f)df \qquad (1.3).$$

Intuitively, the MTF area (A_x) represents the fraction of ideal input signal that is recovered for spatial frequencies less than or equal to *x*. The choice of cutoff frequency *x* is relatively arbitrary. The results presented here integrate the MTF up to 0.5 lp / mm as it is near the frequency where MTF shape is seen to differ the most for FBP and AM-700 and is also close to the American College of Radiology's (ACR) accreditation requirement of 0.6 lp / mm. Paper II compares results when integrating the MTF up to the Nyquist frequency of 1.0 lp / mm.

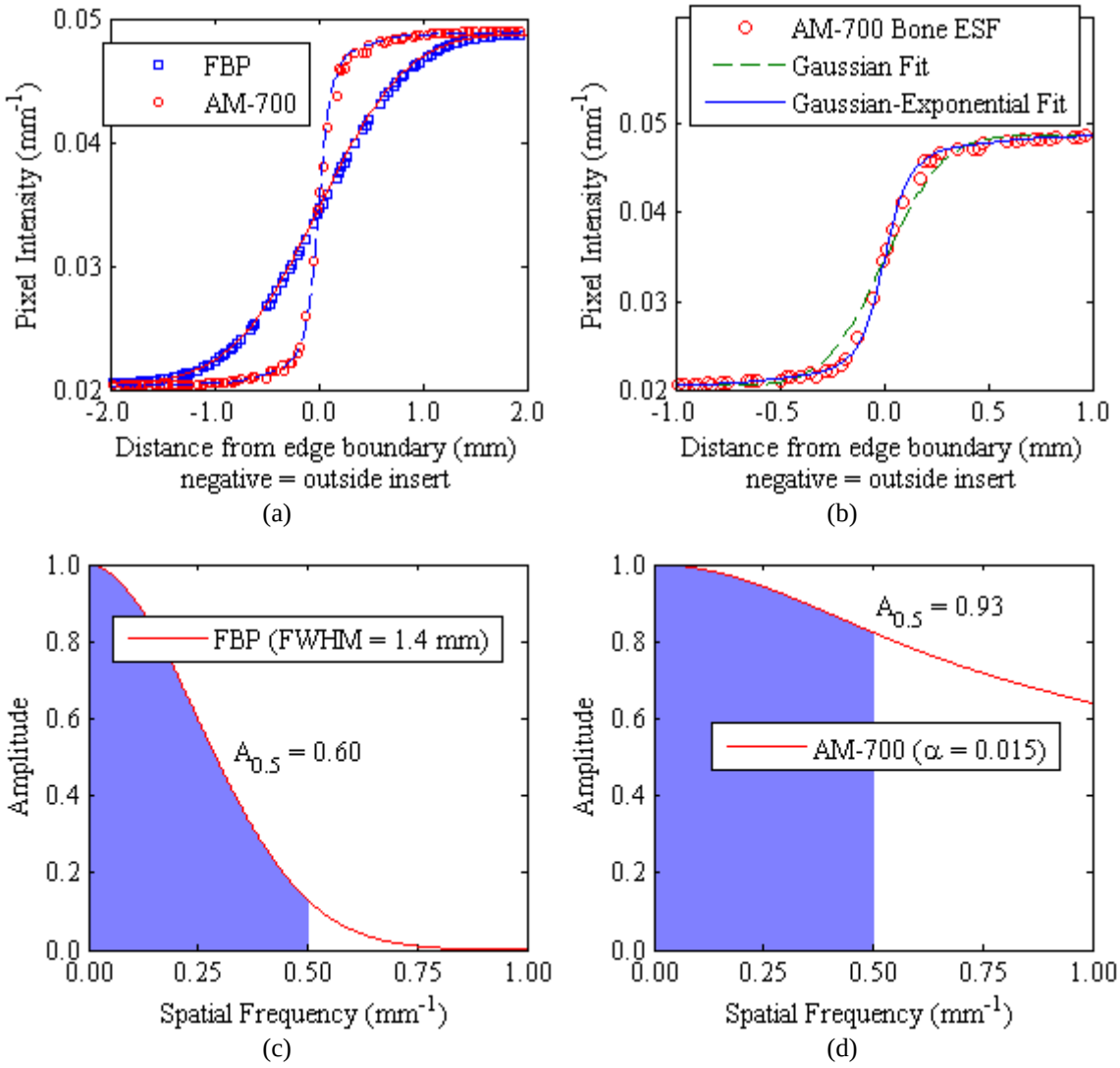

Figure 4. (a) Comparison of the bone ESF reconstructed with FBP and strongly edge-preserving AM-700 at nearly matched image noise (~ 1.09% ± 0.01%). Corresponding lines represent the Gaussian-Exponential model fit used to estimate the MTF. (**b**) The AM-700 high-contrast edges were poorly fit by the Gaussian blurring model, motivating the Gaussian-Exponential ESF model. (**c**) and (**d**) display the MTF for the noise-matched FBP and AM-700 bone inserts respectively.

Contrast-dependent tradeoff of noise and resolution

With a noise measurement and single value surrogate of edge sharpness for each contrast insert in hand, a curve characterizing the tradeoff between noise and resolution can be plotted for each algorithm. Figure 5 displays the noise-resolution tradeoff curves for 4 of the contrast inserts within the clock phantom. The qualitative trends for the other contrast inserts follow those presented here.

The AM tradeoff curves always lie below the corresponding FBP tradeoff curves, implying that the penalized AM algorithm reconstructs images with either less image noise for the same resolution metric or sharper edges for matched image noise. The more strongly edge-preserving AM-700 results in clearly contrast dependent noise-resolution tradeoffs with increasing advantage of statistical reconstruction for increasing insert contrast.

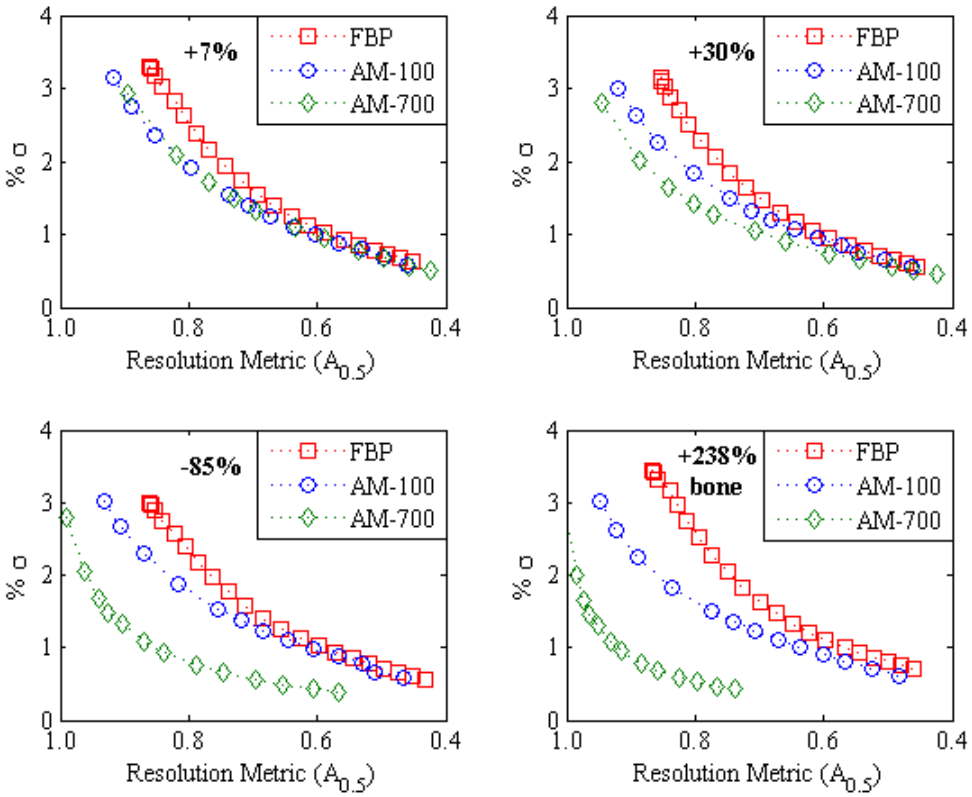

Figure 5. Noise-resolution tradeoff curves for 4 contrast inserts as labeled. The strongly edge-preserving AM-700 reconstructions show clear dependence on the contrast for which resolution is quantified.

It is interesting to note that the noise in the water background around each contrast insert is essentially constant. This means that the contrast-dependent nature of the AM tradeoff curves are due to differences in resolution. Figure 6 illustrates the result that the edge-preserving log-cosh penalty function causes resolution to vary within a single image depending on contrast.

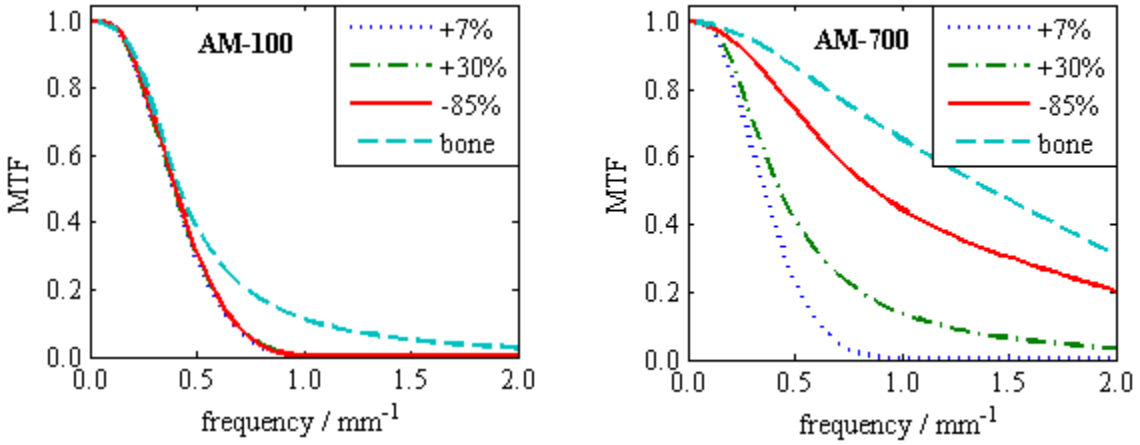

Figure 6. MTF curves for selected inserts of varying contrast within a single image for (a) AM-100 and (b) AM-700 show the contrast dependent resolution of the edge-preserving log-cosh penalty function.

Paper I discusses in detail the results of investigating the spatial dependence of the noise and resolution within the *radial phantom* images. It is shown that the noise and resolution vary as a function of location differently for the AM and FBP algorithms. Interestingly, the ratio of FBP to AM image noise calculated at a matched MTF area value is seen to be relatively invariant over the FOV.

Implications for dose reduction potential

An algorithm that can reconstruct an image of comparable resolution with less noise from the same projection data offers a potential for dose reduction. From the assumptions that image noise is proportional to projection noise[1,76,77] and that projection variance is inversely proportional to patient dose, the dose fraction is calculated as the ratio of AM variance to FBP variance at a given value of the resolution surrogate,

$$\text{dose fraction} = \frac{\sigma^2_{AM}(A_x)}{\sigma^2_{FBP}(A_x)}. \qquad (1.4)$$

Intuitively, the dose fraction represents the fraction of dose necessary for the AM algorithm to achieve the same image noise and resolution as the FBP algorithm. Figure 7 plots the dose fraction as a function of contrast for a matched resolution surrogate value of $A_{0.5}$ = 0.75. Here again, AM-700 shows strong contrast-dependence with the dose fraction varying from 70% at low-contrast to 5% for the high-contrast bone insert.

The resolution value for calculating dose reduction potential is an arbitrary choice. The MTF area value displayed in figure 7 was chosen as it lies near the middle of the noise-resolution curves. Paper II compares the dose reduction potential for different resolution points along the noise-resolution curves. Paper II also investigates the dependence of the dose reduction potential on the choice of MTF integration limit used for calculating the resolution surrogate metric. While the value of reported dose reduction is shown to depend on these choices, the general trend of contrast-dependent dose reduction potential for edge-preserving penalty functions remains.

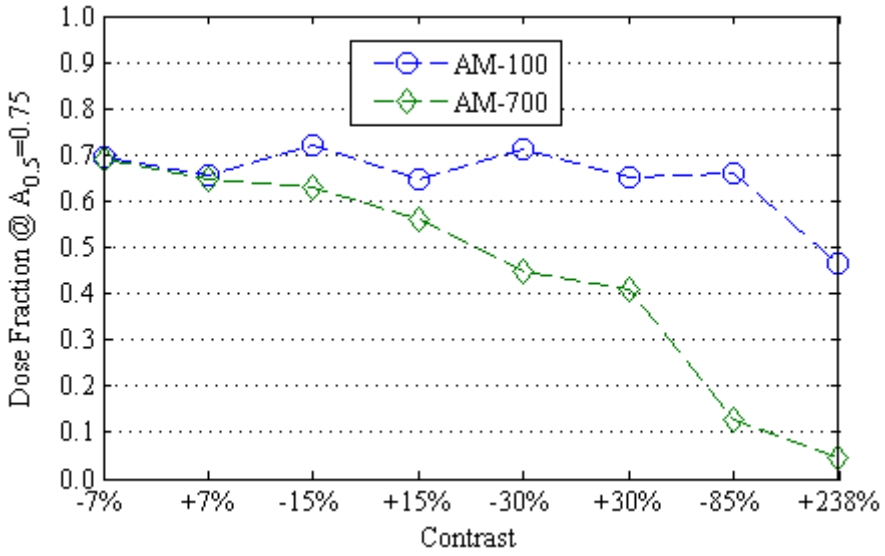

Figure 7. Dose fraction curves for AM-100 and AM-700. The contrast-dependent nature of the strongly edge-preserving AM-700 penalty function is clearly seen.

2.3. Discussion

For both log-cosh penalty shapes, the AM noise-resolution curves lie below the FBP curves. Thus, AM will reconstruct images with less image noise than FBP for matched resolution. As discussed in the introduction, an algorithm that reconstructs images with less image noise (random error) is advantageous for quantitative CT applications and for reducing patient dose without sacrificing image quality.

Edge-preserving penalty functions are designed to generate contrast-dependent resolution. This work is the first to clearly illustrate how the reported advantage of edge-preserving penalized likelihood methods can be highly dependent on the contrast of the object for which resolution is quantified. All previous noise-resolution studies to

illustrate statistical reconstruction advantage in x-ray CT[12-14] do so for high-contrast objects such as bone or steel bb's. As shown in figure 6, the resolution for low-contrast structures can be much lower than high-contrast structures for edge-preserving penalties. The results here imply that when comparing the noise-resolution tradeoff of an edge-preserving penalized likelihood method, the resolution should be quantified using objects with contrast relevant to the intended clinical task. For the soft-tissue segmentation task in radiation oncology, balancing noise and low-contrast resolution is particularly important.

A difficulty in penalized reconstruction methods is choosing optimal parameters to control the penalty function shape. The log-cosh penalty function used here controls the amount of edge preservation by the parameter δ, which defines the transition point to linear growth. Thibault et al.[13] present a novel penalty function formulation with three parameters. The three parameters define the transition point as well as the penalty growth in both low- and high-contrast regions allowing more control over the penalty shape. Future work could extend the methods of comparing noise-resolution tradeoff developed here to investigate other local neighborhood penalty shapes, non-local penalties[75], or anisotropic penalty weighting[78].

The very different shape of the edges reconstructed with the strongly edge-preserving penalty function (figure 4) made it difficult to use conventional measures of edge sharpness as surrogates for resolution. Edge-preserving penalty functions have been noted to reconstruct images with a noise texture that can be objectionable to observers who are accustomed to viewing FBP reconstructions[13]. An interesting question for future work would be what effect the different edge shape has on the diagnostic utility of the image. Ideal observer models that use the MTF and noise-power spectrum (NPS) to calculate a detectability index have been shown to correlate well with human observer performance in CT lung nodule detection[79]. These ideal models may provide a mechanism to link physical performance metrics, e.g. MTF and NPS, to observer performance potentially allowing task-based optimization of reconstruction parameters.

3. Implementation and validation of a polyenergetic SIR algorithm on a commercial CT scanner

3.1 Background

The beam-hardening (BH) artifact was recognized soon after the introduction of the first clinical CT scanners[2]. Correction schemes encounter difficulty due to the fact that the BH artifact is dependent on the size and composition of the object. Pre-processing methods attempts to linearize the data prior to FBP[3], but are limited by the common assumption that the object is water equivalent. Post-processing approaches use an initial reconstruction to segment the image into soft-tissue and bone. The data can then be corrected based upon the estimated amount of bone along each projection ray[80]. Dual-energy imaging can also be used to eliminate the beam-hardening artifact by modeling the energy-dependent information of each image voxel[81]. However, DE methods require an additional scan and are highly sensitive to noise and errors as shown in the following chapter. Stonestrom et al. presents a good overview of BH correction methods[82]. Statistical reconstruction algorithms seem well-suited to reducing systematic errors from beam-hardening as they can incorporate the root cause of BH, the polyenergetic spectrum, in the forward model.

De Man et al.[15] presented a maximum-likelihood method that incorporates an estimate of the polyenergetic x-ray spectrum in the forward model. An ideal x-ray spectrum provided by the vendor was used. Noiseless, scatter-free simulations were used to assess the effectiveness of the polyenergetic SIR algorithm in alleviating cupping and streaking artifacts from BH relative to a known truth. Real transmission data from scanning a plastic cylinder containing high-Z inserts and a human skull phantom was also acquired on a commercial Siemens scanner. The real data results show polyenergetic SIR effectively reduced cupping and streaking artifacts, though only qualitatively.

Another polyenergetic statistical method is presented by Elbakri et al.[16,83]. Simulation studies were employed to quantify the systematic error in reconstructed intensities due to BH. The polyenergetic SIR method results in less root mean square

error than conventional FBP and a post-processing method that segments the image into bone and tissue. The simulation experiment was also used to illustrate the sensitivity of reconstruction to spectral mismatches, which is further addressed in the following sections. Finally, real data of a 15 cm diameter water phantom was acquired on a table-top x-ray CT system. The polyenergetic SIR algorithm was shown to estimate the density of potassium phosphate solutions of varying concentration to within 1.2%, whereas FBP error was around 20%.

While encouraging, the literature to date on polyenergetic statistical reconstruction seems to only assess the criterion that image intensities for a given material be consistent within an object. As discussed in the introduction, quantitative applications also require image intensity for a given material to be independent of object size and location within the FOV. Furthermore, the absolute quantitative accuracy of the polyenergetic SIR methods is investigated only in simulation studies or limited data cases acquired on experimental CT systems.

3.2. Methodology and results

The aim of this project is to assess the accuracy with which the polyenergetic AM algorithm can reconstruct data acquired on a commercially available CT scanner. The polyenergetic x-ray spectrum of the scanner must be estimated to "commission" the algorithm for polyenergetic AM reconstruction of real data. As a first step, homogeneous cylindrical phantoms are used to quantify the polyenergetic AM algorithm's accuracy. Systematic errors are also compared between the polyenergetic AM and FBP algorithms for a range of quantitative CT consistency criteria. Details regarding methodology and results can be found in paper III.

The polyenergetic forward model

The log-cosh penalized AM algorithm as described in chapter 2 and Appendix 1 is utilized here. This chapter incorporates the polyenergetic x-ray spectrum $I_0(\mathbf{y}, E)$ and scatter $\sigma(\mathbf{y})$ into the forward model:

$$g(\mathbf{y}:\mathbf{c}) = \sigma(\mathbf{y}) + \sum_E I_0(\mathbf{y}, E) \cdot \exp\left(-\sum_{x \in X} \sum_{i=1}^{N} h(\mathbf{y} \mid x) \cdot \mu_i(E) \cdot c_i(x) \right). \qquad (1.5)$$

An accurate estimate of the x-ray spectrum is necessary to obtain quantitatively accurate image intensities[16]. If the mean energy of the spectrum is too high, the reconstructed image intensity will be overestimated to compensate for the additional penetrating power of the over-hardened spectrum estimate. The same logic follows for a spectrum estimate that is softer than the actual spectrum. The methods for estimating the x-ray spectrum and scatter are discussed below, and some considerations necessary to achieve accurate polyenergetic AM reconstruction of real data are highlighted.

To test the absolute accuracy of the AM algorithm reconstructing real data, the forward model uses a single-basis image model that is matched to the material composition of the test phantom:

$$\mu(\mathbf{x}, E) = \mu_{phantom}(E) \cdot c(\mathbf{x}). \qquad (1.6)$$

In this case, the pixels occupied by the phantom material will ideally have reconstructed image intensity of $c(x)$=1.0. This gives us a ground truth to assess how well the polyenergetic AM algorithm has been "commissioned" for reconstruction of real data.

Experimental setup summary

Homogeneous cylindrical phantoms of water, PMMA and Teflon are used to assess the accuracy of the polyenergetic AM algorithm as shown in figure 8. The water cylinder consists of 20.3 cm (diameter) of water enclosed by 6 mm of acrylic. PMMA cylinders of four diameters [5.1 cm : 30.5 cm] and Teflon cylinder of three diameters [5.1 cm : 17.8 cm] are used to evaluate the consistency criterion that intensity be independent of object

size. The consistency criterion that intensity be independent of location within an object is evaluated by comparing intensities in the center and periphery of the homogeneous cylinders. The cylinders are scanned both centered in the FOV and shifted 9 cm to assess the criterion that intensity be independent of location within the FOV.

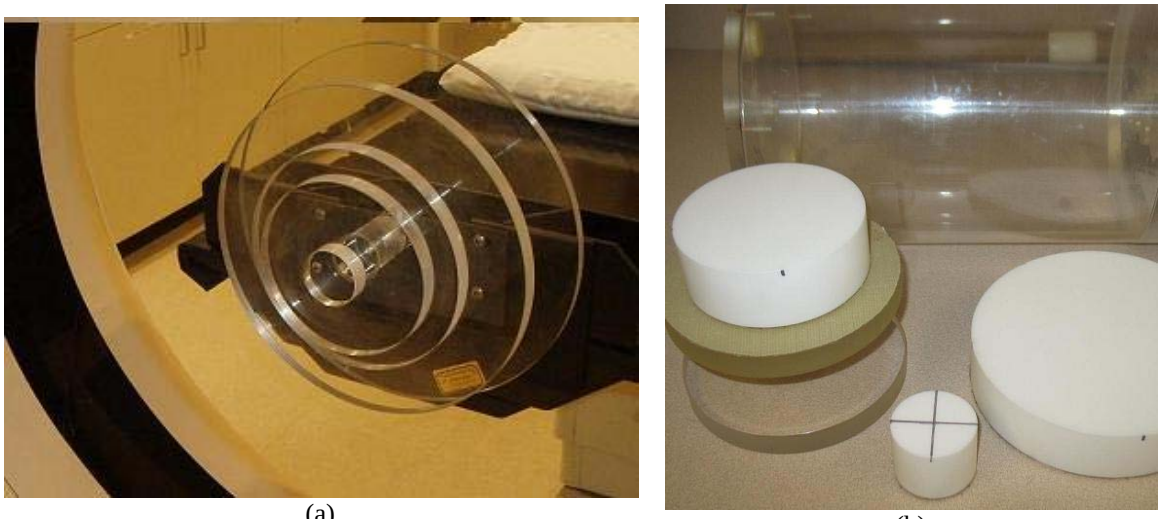

(a) (b)

Figure 8. Homogeneous phantoms used for validating polyenergetic AM reconstruction on the Philips Brilliance scanner. (a) The PMMA cylinders set up for scanning. (b) The Teflon cylinders in the foreground with the water cylinder's acrylic shell in the background.

In this project, all data was acquired on the Philips Brilliance Big Bore CT scanner in VCU's radiation oncology department with an axial protocol, (identified as "axial pelvis protocol" by the vendor's software) with detector slice thickness of 0.75 mm and beam collimation of 3.0 mm, allowing 4 slices per rotation to be acquired. Three clinically available tube potentials were investigated; 90 kVp, 120 kVp and 140 kVp. Proprietary software provided by Philips Healthcare allowed any of the standard data preprocessing corrections to be applied or omitted. Two sets of processed data were generated from each raw dataset; one with the Philips water-equivalent BH correction turned on for conventional FBP reconstruction, and one with the BH correction omitted for reconstruction with the polyenergetic AM algorithm. Four reconstructions of each CT dataset were performed:

- **$AM_{Sc\text{-}OFF}$**: polyenergetic AM with no scatter estimate
- **$AM_{Sc\text{-}ON}$**: polyenergetic AM with a constant scatter estimate
- **$FBP_{BH\text{-}ON}$**: FBP from BH-corrected data
- **$FBP_{BH\text{-}OFF}$**: FBP of BH-uncorrected data

The most direct comparison of AM and FBP reconstruction is between the **$AM_{Sc\text{-}OFF}$** and the **$FBP_{BH\text{-}ON}$** reconstructions as both attempt to correct for beam-hardening, but not for scatter. No scatter correction is used for FBP reconstruction as the Brilliance scanner utilizes a 1-D anti-scatter grid (ASG) for physical scatter rejection and does not employ any scatter correction to the data.

X-ray spectrum measurement

The x-ray spectrum, $I_0(\mathbf{y}, E)$, required by the polyenergetic AM forward model was obtained by fitting the semi-empirical Birch-Marshall spectrum model[84], including tungsten characteristic x-rays, to narrow-beam attenuation curves measured through high purity aluminum and copper filters. The "equivalent x-ray spectrum"[85,86] is thus an idealized spectrum that matches the attenuation properties of the actual spectrum. The BM spectrum model is parameterized by the known anode angle and two unknown free parameters, tube potential (*kVp*) and millimeters of inherent aluminum filtration (*mmAl*). A model was used to calculate the expected transmission of a particular BM spectrum passing through each metal filter, which included first-order corrections for energy-integrating detectors and detector sensitivity. An exhaustive search over the spectrum parameters *mmAl* and *kVp* was performed to minimize the difference between modelled transmission and measured transmission. As discussed in more detail in paper III, the fitting of an equivalent x-ray spectrum to measured attenuation data is found to give results with comparable accuracy to Monte Carlo simulation or direct spectrum measurement.

Transmission of the Brilliance scanner's x-ray beam was measured through fifteen aluminum filters and fifteen copper filters. The maximum thickness for each material, 4.3 cm for Al and 1.5 cm for Cu, were chosen to attenuate the beam to roughly 10^{-3} of its primary intensity. Narrow beam geometry was achieved by use of a collimator assembly

(figure 9a) that was hung off the front of the CT table to avoid table attenuation and scatter. Transmission ratios were obtained by taking the ratio of the measured signal with and without the filter in place. The CT detector array is used for transmission measurements versus an independent ionization chamber to form a closed measurement-model loop. This allows the equivalent spectrum fitting to compensate for errors between the simple transmission model and the actual detector sensitivity.

Transmission measurement and equivalent spectrum fitting was only performed for the CAX detector location. The resultant equivalent spectra (shown in figure 9b) fit the measured data to within 1.35% RMS error for all three tube potentials. For detectors away from central-axis, both the mean energy and the fluence will be significantly modulated by the bowtie filter. The central axis spectrum was computationally hardened for off-axis detectors using the known material and geometry of the bowtie filter and a $1/\cos\gamma$ correction for oblique filtration through the slab of equivalent aluminum filtration. The modelled and measured air profiles were found to be in good agreement (paper III).

In his dissertation regarding the polyenergetic AM algorithm, Liangjun Xie[87] shows that the mean energy of the estimated spectrum needs to be within 2 keV of truth to maintain reconstructed image accuracy of 2%. Thus, to achieve the 0.5% accuracy demonstrated later, the equivalent spectrum fitting required careful consideration. For example, the aluminum filters were found to contain approximately 0.5% Fe by mass. Neglecting to account for the Fe contamination in the transmission model was found to lower the mean energy of the best-fit spectrum by 1.9 keV.

The presence of the bowtie filter compounds this effect as the mean energy of the spectrum will vary widely over the source-detector array. Inadequate modeling of the spectrum across the detector array will cause systematic artifacts relative to the imaging axis for AM reconstruction. The excellent agreement of measured and modeled air profiles shown in paper III, give us confidence that we are modeling the geometry of the BT filter correctly. However, the ultimate test of the accuracy of the CAX spectrum

estimate and off-axis hardening model is in the accuracy of the reconstructed image intensities.

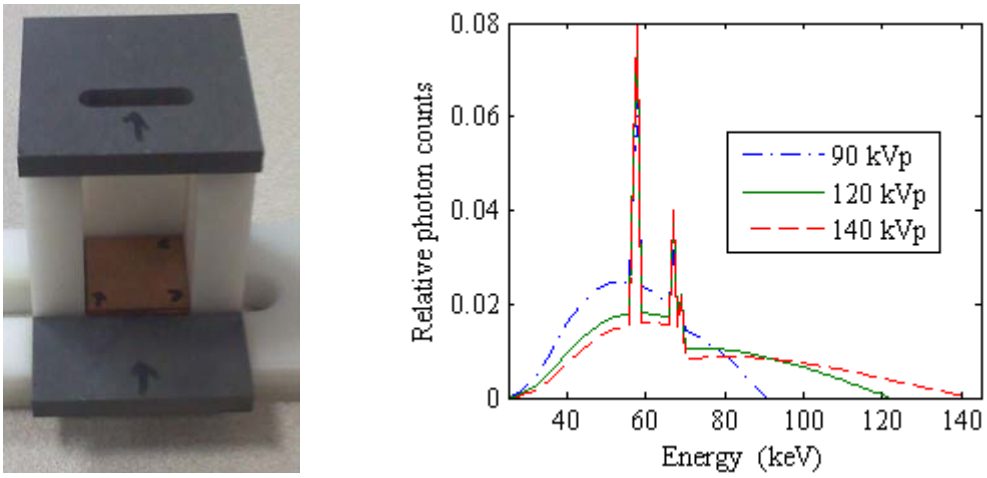

(a) (b)

Figure 9. (a) The collimator assembly for transmission measurements used in fitting the equivalent spectrum model. The lead collimators are ¼" thick to block scattered radiation. The collimator opening is ¼" wide allowing approximately 5 to 6 detectors to be irradiated per view, and ¾" long in the z-direction. (b) The Equivalent Birch-Marshall x-ray spectra for the three nominal tube potentials investigated in this work. All three spectra were normalized to have unit area for this plot.

Scatter measurement

The Philips Brilliance scanner uses a 1-D anti-scatter grid for physical scatter rejection. While efficient at rejecting large angle scatter, a non-negligible component of scatter is from small-angle coherent scattering[88] which will bypass the ASG foils. The residual scatter signal is experimentally measured with a beam-stop technique[89,90]. A ¼" thick block of lead absorbs the primary radiation, *P*, incident on the phantom. Measuring the signal with and without the lead beam-stopper allows the source of the detected signal to be separated into primary, *P*, and scattered, *S*, radiation components. Refer to paper III for the detailed methodology and results.

Two important considerations must be made when using a beam-stop technique to measure scatter. The first is due to the presence of off-focal radiation *P'*, for example from scattering within the bowtie filter. As shown in figure 10, off-focal radiation has the potential to bypass the lead beam-stopper and contribute to the detected signal. Note that the scatter angles in the figure are exaggerated. Off-focal radiation, is present in the absence of a scan subject, and is thus considered as effective primary radiation. The off-

focal signal can be measured by scanning the lead beam-stopper in air and was estimated to comprise 1.7% to 2.2% of the effective primary signal for the varying tube potentials, which is in agreement with the literature[90]. If not accounted for, the off-focal radiation will be counted as object scatter, representing an additive error, leading scatter to be overestimated by 1.7% to 2.2% for all object sizes.

The physical presence of the lead beam-stopper can also systematically bias the scatter estimate if not accounted for. Due to shadowing of the lead beam-stopper, the amount of off-focal radiation and scatter produced in the object are both reduced. To account for this effect, the beam-stop measurement is made with lead blocks of varying width. A linear fit is then used to extrapolate to a beam-stopper of zero width. If neglected, blocker shadowing leads to systematically under-estimated scatter measurements. The effects of blocker shadowing and off-focal radiation, while opposite in direction, are not compensatory. The blocker shadowing effect is object-dependent, while the off-focal effect is not. Both corrections must be made to accurately estimate scatter.

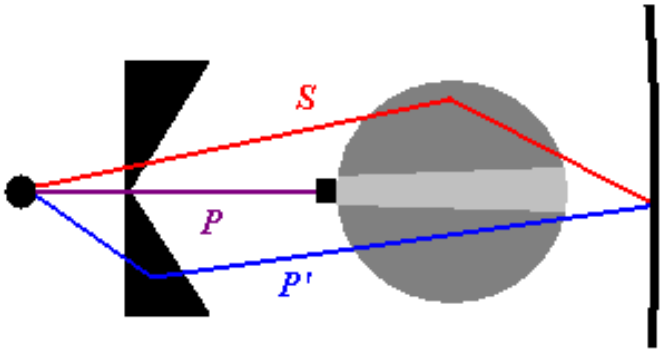

Figure 10. Diagram of the scatter beam-stopper method for scatter measurement. The primary radiation *P* is absorbed by ¼" of lead allowing the scattered radiation, *S*, to be estimated. Off-focal radiation *P'* bypasses the beam-stopper and will mimic scatter if not accounted for. The shadowing of the beam-stopper, shown as the light gray area, is accounted for by performing beam-stopper measurements for varying stopper widths and extrapolating to a zero width blocker.

In this work, scatter was measured for all phantom cylinders at all three tube potentials on the central axis (CAX) detector location. Only the largest PMMA and Teflon cylinders, with diameters of 30.5 cm and 17.8 cm respectively, were estimated to have a scatter-to-primary ratio (SPR) greater than 1% ranging up to 3.6%. Scatter

estimates provided to the AM forward model were assumed to be constant for all gantry angles and detector locations.

Radial averaging method

The radial symmetry of the cylindrical phantoms is exploited to assess the systematic deviation of image intensities within each object. Pixels within the reconstructed cylinder are binned according to their distance *D* to the cylinder centroid, and the mean intensity for all pixels within each bin. Plotting each *radial bin mean* as a function of distance to center gives the *mean profile*. As shown in figure 11, the mean profile effectively reduces the effect of image noise, allowing the systematic cupping artifact to be visualized.

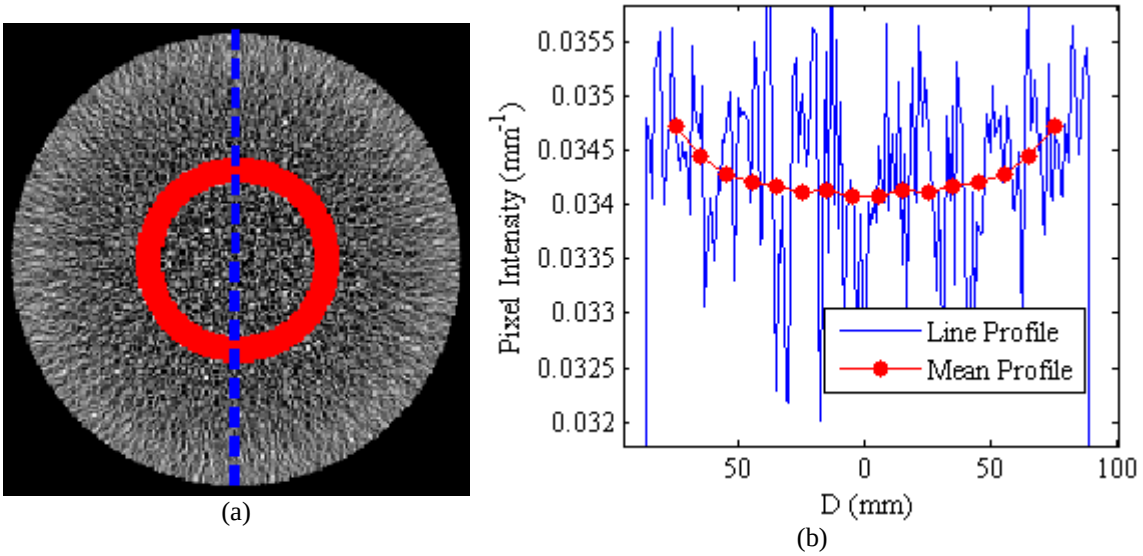

(a) (b)

Figure 11. Illustration of the radial averaging method for reducing image noise to assess systematic intensity deviations. (a) $FBP_{BH\text{-}ON}$ image of the 17.8 cm Teflon disk at 120 kVp which shows appreciable cupping. The red annulus shows the pixels within one of the radial bins used for averaging. The blue dotted line shows the location of a traditional line profile. (b) Shows how the mean profile reveals the structure of the cupping that is difficult to detect from a line profile due to image noise.

Polyenergetic AM accuracy

Recall that the polyenergetic AM algorithm here uses a single-basis object model matched to the material of the cylinder being scanned, in which case the reconstructed image intensity within the phantom is expected to be $c(x)$=1.0. Figure 12 plots the mean AM profiles for two cylinder cases. It is seen for the 15.9 cm PMMA cylinder at 90 kVp (SPR = 0.4%), the mean reconstructed image intensities are well within 0.5% of expected

with and without the scatter estimate. However, for the largest Teflon disk (17.8 cm) at 140 kVp, which has a SPR of 2.7%, a scatter estimate is needed to remove residual cupping and bring mean intensity throughout the cylinder to within 0.5% of expected. The examples shown in figure 12 illustrate the general finding that a scatter estimate is needed to bring accuracy to within 0.5% when SPR is greater than 1%. Paper III presents the mean profiles of AM and FBP for all cylinder materials and diameters at 120 kVp.

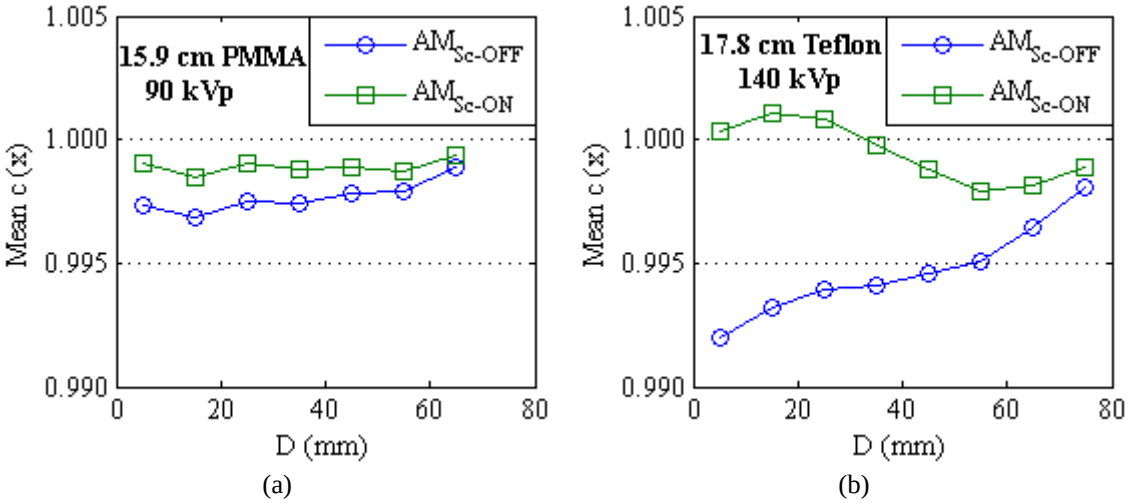

(a) (b)

Figure 12. Mean profiles of the polyenergetic AM algorithm for (a) the 15.9 cm PMMA cylinder at 90 kVp and (b) the 17.8 cm Teflon cylinder at 140 kVp. Including the scatter estimate improves the accuracy of the AM image intensities, especially for the largest Teflon cylinder shown here that has a SPR of 2.7%.

The percent error of each AM radial bin mean is calculated in relation to the expected truth intensity of 1.0. The overall accuracy of polyenergetic AM reconstruction is summarized by plotting the cumulative distribution of all radial bin errors in figure 13. The radial bins for all materials, object sizes, and tube potentials are grouped together. AM reconstruction using a constant scatter estimate from the beam-stop measurements is shown to bring most (90%) of the radial bins to within 0.45% of truth compared to AM_{Sc-OFF} with 90% of radial bins within 0.84% of truth. The reduction in bias from scatter correction is greatest for larger disks where SPR was greater than 1%.

The largest residual errors in the tails of the CDFs in figure 13 are due to two error trends observed in both AM and FBP reconstructions. One trend is that image intensity is systematically underestimated for peripheral pixels of the 5.1 cm PMMA and Teflon

cylinders in air. The roll-off of the smallest cylinders in air is observed in both PMMA and Teflon, at all tube potentials, and in all FBP and AM reconstructions. When reconstructing 2.5 cm cylinders in the 20.3 cm water background, the peripheral roll-off is not observed. The error trends are illustrated and discussed in more detail in Paper III. As both reconstruction algorithms exhibit the same error trends, it is not thought to be an inherent limitation of the AM algorithm.

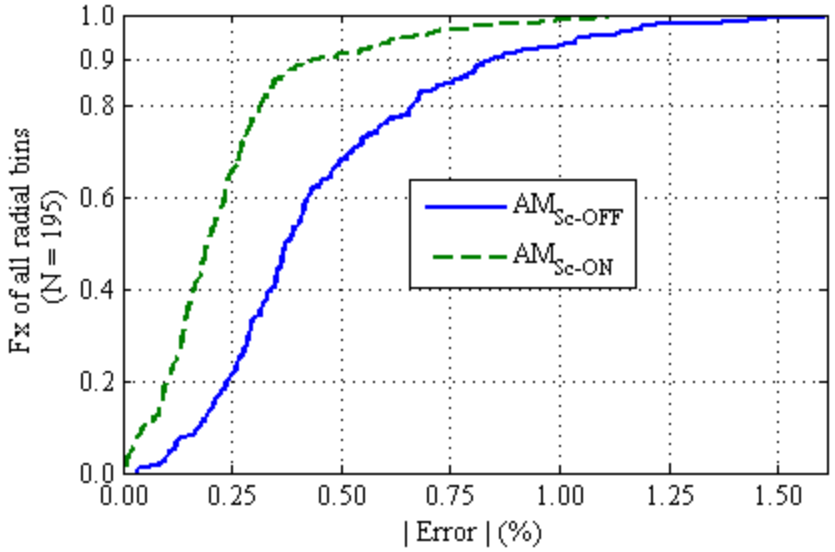

Figure 13. Cumulative distribution functions of the mean error. Radial bins from all materials, all cylinder diameters and all kVp's are grouped together (N=195). The constant scatter correction is seen to bring most of the radial bin means to within 0.5% accuracy.

Comparison of AM and FBP consistency

Figure 14 displays the mean profiles for the 20.3 water and 11.4 cm Teflon cylinders at 120 kVp. The profiles are normalized to the centermost radial bin mean to illustrate the variation of mean image intensity across the homogeneous uniform cylinders. The effect of the vendor's BH correction is seen by comparing $FBP_{BH\text{-}ON}$ and $FBP_{BH\text{-}OFF}$. The BH correction is seen to bring mean intensity variation across the water cylinder to 0.5% for the water cylinder, but for the higher atomic number Teflon cylinder the mean intensity varies more than 1.25%. The implicit beam-hardening correction of the polyenergetic AM algorithm reconstructs these cylinder cases with mean intensity variation well below 0.5%.

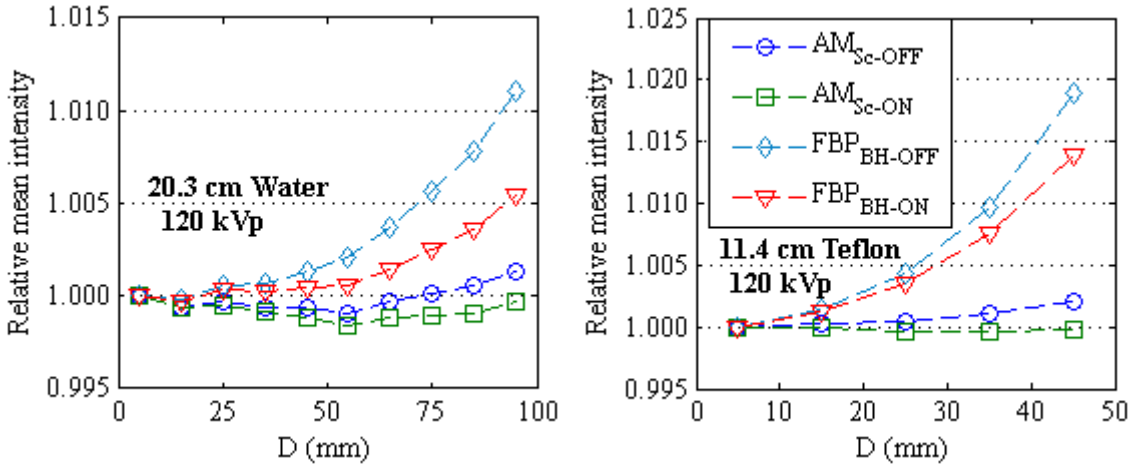

Figure 14. Relative mean profiles (normalized to centermost bin mean) illustrate the systematic cupping artifact. All four reconstruction algorithms are compared for (a) the 20.3 cm water cylinder at 120 kVp and (b) the 11.4 cm Teflon cylinder at 120 kVp.

The Uniformity Index (UI) is calculated as the percent difference between the most central and peripheral bin means. Figure 15 summarizes the results for each algorithm by plotting the CDF of uniformity for all cylinder cases. The most direct comparison between FBP and AM is for $FBP_{BH\text{-}ON}$ and $AM_{Sc\text{-}OFF}$ as both attempt to correct for beam-hardening, but not scatter. The polyenergetic AM algorithm is shown to reconstruct the uniform cylinders with less mean variation than FBP. Note that the largest UI values for the AM algorithm are due to the two error trends discussed in paper III, not cupping. For FBP, the largest UI values are from cupping in the Teflon cylinders.

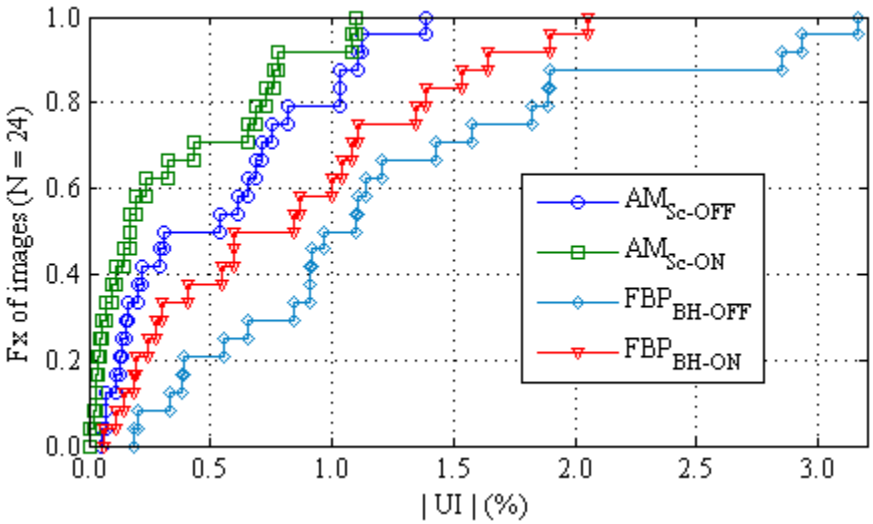

Figure 15. Cumulative distribution functions of the Uniformity Index (UI) for all reconstructed cylinders (8 cylinders at 3 tube potentials) sorted by reconstruction algorithm.

The presented results are with the cylinders centered in the FOV. The accuracy and uniformity were also investigated for reconstructions when the cylinders were shifted 9 cm away from the FOV center. As illustrated in paper III, the shifted cylinder intensities on the edge proximal to the FOV center are seen to be systematically underestimated by 0.5% to 1.5%. This error trend was observed in the shifted cylinders for all materials, sizes, tube potentials, and reconstruction algorithms. When shifted from the FOV center, the scatter can no longer be assumed to be symmetric across the detector array or constant for each gantry angle, thus the proximal edge depression may be alleviated by incorporating detector and gantry angle dependent scatter estimates in image reconstruction. Excluding the proximal edge AM accuracy and uniformity results for the shifted cylinders were nearly identical to the case of the centered cylinders.

The effect of object size is also well illustrated in paper III. It is shown that $FBP_{BH\text{-}ON}$ reconstructs the range of PMMA cylinders [5.1 cm to 30.5 cm] to have overall mean intensity within 0.75% of each other. However, for the Teflon cylinders [5.1 cm to 17.8 cm] mean intensity using $FBP_{BH\text{-}ON}$ varies up to 2.5%. In comparison, polyenergetic $AM_{Sc\text{-}OFF}$ reconstructs the range of both PMMA and Teflon cylinders with overall mean intensities that vary less than 0.5% across all cylinder diameters.

3.3. Discussion

In support of quantitative CT applications, the results of this project show that polyenergetic AM reconstruction of energy-uncompensated data better meets a range of consistency criteria than FBP reconstruction using a commercially available BH correction. AM intensity showed less dependence on location within an object as evidenced by the comparison of uniformity within the homogeneous cylinders. AM also demonstrated consistently less object-size dependence (< 0.5%), especially for the high-Z Teflon cylinder where FBP was found to deviate up to 3%. The shifted cylinders showed similar accuracy and consistency results as the center cases, illustrating independence on location within the FOV. However, the shifted cylinders were observed to suffer systematic underestimations of ~ 0.5% to 1.5% on the proximal edge that is thought to be due to asymmetric scatter. Quantitative applications in which the target tissue is near the periphery of the patient will need to consider this effect, for example DE cross-section estimation for breast brachytherapy.

Assessing reconstructed AM intensities relative to a ground truth is necessary to ensure that the x-ray spectrum, which varies significantly across the detector array due to the bowtie filter, is estimated as accurately as possible. The results showing that polyenergetic AM reconstructed cylinders over a range of materials and sizes within 0.5% of expected are exciting considering the sensitivity to spectral mismatch[87]. This gives us confidence in the central-axis spectral estimates and the model employed for off-axis spectral hardening due to the bowtie filter, supporting future polyenergetic AM research with data acquired on our Brilliance CT scanner.

However, as discussed in paper III, AM reconstructed intensities will have a different interpretation when using a single-basis object model, equation (1.6), that is not matched to the scan subject material and will thus have different energy-dependence. From the forward model, equation (1.5), the AM image intensity using mismatched object-basis materials can be expected to represent the spectrum-weighted ratio of subject and object-model linear attenuation coefficients. This is similar to the interpretation of FBP intensities as attenuation coefficients at the spectrally-averaged effective energy. Preliminary investigations have found support for this interpretation of mismatched

single-basis AM intensities. For future work, an interesting question to investigate would be the effect on polyenergetic AM image quality. Also, more complex object models could be investigated, for example, representing the object as a weighted sum of N=2 basis materials, using mass constraints to condition the single-energy CT reconstruction[16].

Scattered radiation was demonstrated to cause residual systematic underestimations. Even with a highly collimated beam (3.0 mm width in the z-direction) and a 1-D ASG, SPR greater than 1% was observed for the largest PMMA and Teflon cylinders and was sufficient to compromise quantitative accuracy. Methods to estimate and correct for scatter will be even more important for quantitative applications involving large scan subjects or utilizing cone-beam geometries that inherently accept more scatter.

4. Assessment of a post-processing DECT method for photon cross-section estimation on a commercial CT scanner

4.1. Background

The core of any quantitative dual-energy CT measurement technique is a parameterized representation of the linear attenuation coefficients which describe the radiological properties of the scanned object. The parameters and associated basis functions can be related to physical material properties, such as electron density and effective atomic number[50]; interaction processes, such as photoelectric absorption and Compton scattering[91]; or as a weighted mixture of two known basis materials[92]. CT measurements at two energies, which represent linear attenuation, can then be used to solve for the unknown model parameters.

Parameterization by effective atomic number and electron density is physically intuitive as they are directly related to the interaction processes of x-ray attenuation. In this work, we are concerned mainly with the ability of the models to accurately fit tissue attenuation coefficient data as the accuracy of attenuation coefficients can be directly related to the accuracy of our intended application of dose calculation[93]. Williamson et al.'s study showed that parameterization by Z_{eff} and ρ_e can lead to attenuation coefficient errors on the order of 5% to 10% in the range of interest for low energy brachytherapy sources[54]. An alternative model of representing a substance as a mixture of two well-chosen basis materials, the basis vector model (BVM), was found to fit energy absorption coefficients to within 1% for low-Z materials and isolated errors of 1% to 5% for high-Z materials when using ideal dual-energy image sets[54].

Recently, Goodsitt et al. reported on their experience using a commercially available GE dual-energy CT scanner to estimate low-energy cross-sections (in the form of synthesized monochromatic images) for known tissue-equivalent phantom materials[57]. Photon cross-section estimates were assessed at a number of energies between 40 keV and 120 keV, with reported accuracies between 1% and 20%, mainly depending on the

test material of interest. The GE dual-energy system employs a pre-reconstruction method, i.e., the model operates on the sinogram data, not reconstructed images. The GE system is proprietary, meaning we don't have knowledge of the basis materials or the calibration procedure used.

The aim of this project is to assess the experimental accuracy achievable of the post-processing photon cross-section estimation method described in Williamson et al.[54] for data acquired on a commercially available CT scanner. Specifically, the accuracy with which the post-processing method can estimate the linear attenuation coefficient of known test substances is investigated. The polyenergetic AM algorithm, with expected performance advantages in terms of less random error from image noise and less systematic error from artifacts, is compared to FBP for the highly sensitive post-processing DECT method. As discussed in the introduction, an accurate method to non-invasively measure photon cross-section information would be of considerable value for a range of medical applications including the calculation of dose from kV imaging procedures and low energy photon brachytherapy cancer treatment modalities. To the best of the author's knowledge, this work represents the first systematic analysis of a post-processing method operating on dual-energy data acquired using a commercially available CT scanner for *in vivo* estimation of the linear attenuation coefficient.

4.2. Methodology and results

Details regarding the methodology and results presented in this chapter can be found in the appended paper IV.

Post-processing DECT cross-section estimation

The basis vector model (BVM)[54,92] utilized here assumes that the linear attenuation coefficient of an unknown material x can be accurately represented as a linear combination of two basis materials denoted by α and β:

$$\mu_x(E) = w_\alpha \cdot \mu_\alpha(E) + w_\beta \cdot \mu_\beta(E), \qquad (2.1)$$

where w_α and w_β are the weighting coefficients for each basis substance. Assuming CT image intensity is proportional to the linear attenuation coefficient, CT images from data acquired at two different energies provide a set of two BVM equations:

$$\begin{aligned}\mu(\mathbf{x},E_1) &= w_\alpha(\mathbf{x})\mu_\alpha(E_1) + w_\beta(\mathbf{x})\mu_\beta(E_1)\\ \mu(\mathbf{x},E_2) &= w_\alpha(\mathbf{x})\mu_\alpha(E_2) + w_\beta(\mathbf{x})\mu_\beta(E_2)\end{aligned}. \quad (2.2)$$

Using basis material intensities obtained from calibration scans, $\left(\mu_\alpha(E_1),\mu_\alpha(E_2),\mu_\beta(E_1),\mu_\beta(E_2)\right)$, equation (2.2) can be solved on a pixel-by-pixel basis, resulting in a pair of basis coefficient images $\left(w_\alpha(\mathbf{x}),w_\beta(\mathbf{x})\right)$. This is a post-processing dual-energy CT (pDECT) method as the reconstructed images are used to estimate basis coefficients, not the sinogram data. From the DE basis coefficient images and known composition and density of the calibrated basis materials, equation (2.1) can be used to estimate the linear attenuation coefficient at voxel **x** at any energy:

$$\mu(\mathbf{x},E) = w_\alpha(\mathbf{x})\cdot\mu_\alpha(E) + w_\beta(\mathbf{x})\cdot\mu_\beta(E). \quad (2.3)$$

Experimental setup summary

Solutions and solid industrial plastics of known composition and density were used to assess the accuracy of the pDECT estimated linear attenuation coefficients (μ_{DE}) in comparison to reference values obtained from NIST (μ_{NIST}). The three basis materials and eight test substances (refer to table 1 in paper IV) investigated here represent a range of densities and atomic compositions representative of biological tissues. These are physical realizations of the substances used in Williamson et al.'s study[54] on the BVM's cross-section fitting accuracy using ideal DECT measurements. A calibrated analytical balance with estimated uncertainty of 0.1 mg was used to mix solutions of precise percent-by-mass composition and to calculate density from known sample volumes. For the industrial plastic materials, an elemental analysis was obtained to account for impurities such as iron, which if neglected, lead NIST reference mass-attenuation coefficients to deviate by as much as 1.5% in the low energy range.

Each testing substance was scanned separately, and was immobilized in the center of a cylindrical water phantom using an out-of-field acrylic plate. This is the most ideal geometry as basis materials are calibrated in identical geometry as the test substances. The *head phantom* geometry refers to 20.3 cm diameter of water in a 6 mm thick acrylic shell (total diameter of 21.5 cm). A 26 cm x 35 cm elliptical acrylic shell was placed around the 21.5 cm water cylinder to test pDECT with dimensions more representative of a pelvic patient. This setup is referred to as the *body phantom* geometry. Figure 16 shows the physical phantom materials and two FBP images of ethanol centered in the head and body phantom geometries.

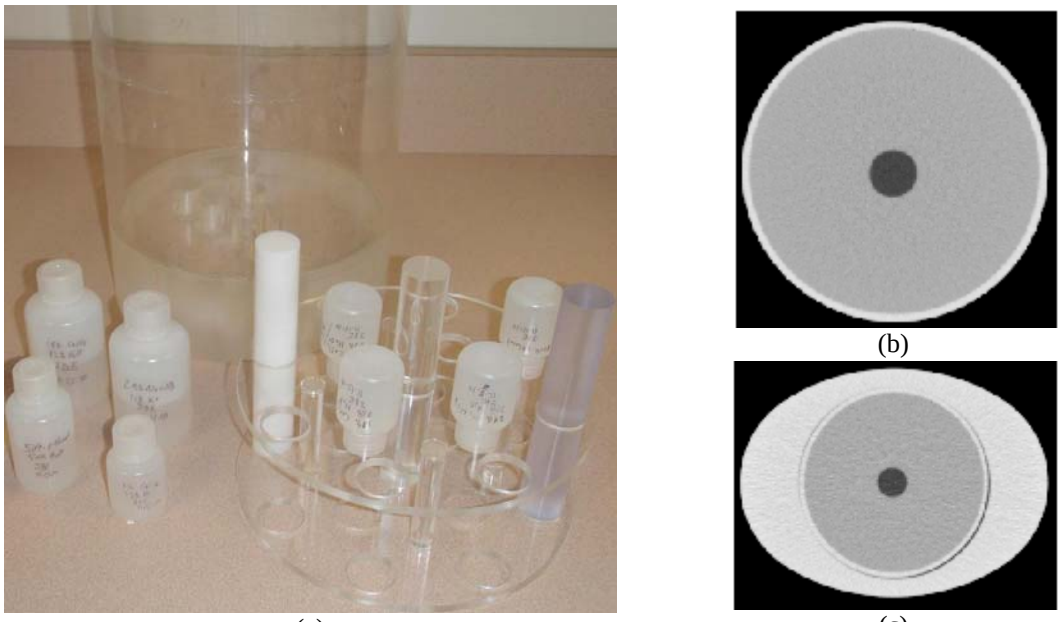

(a) (b) (c)

Figure 16. (a) The phantom setup used for pDECT analysis of solution and solid plastic rods with known composition. FBP images at 90 kVp of the ethanol sample centered in (b) the 21.6 cm water cylinder referred to as the *head phantom* and (c) the 26 cm x 35 cm elliptical *body phantom*.

All dual-energy CT data were acquired on the Philips Brilliance Big Bore CT scanner utilizing clinically available protocols and scan parameters. The same *Axial Pelvis* scan protocol described in Chapter 3 to commission the polyenergetic AM algorithm is employed here using a slice thickness of 3 mm. Dual-energy scans are obtained at 90 kVp and 140 kVp using maximum allowable tube currents of 220 mAs and 175 mAs, respectively. These acquisition parameters lead to $CTDI_{vol}$ dose values, as reported on the scanner from commissioning measurements in a pelvis phantom, of 8.7 mGy and 22.7

mGy at 90 kVp and 140 kVp, respectively. To reduce the uncertainty of the basis material calibration measurements in the body phantom geometry, data from repeat scans were averaged to simulate a higher dose acquisition. All of the test substances, unless otherwise noted in the following sections, were acquired with the standard acquisition parameters described above.

The robustness of dual-energy methods depends on the ability to discern small differences in material composition, which in turn is affected by the energy separation between the low- and high-energy scanning spectra[94]. Increasing the spectral separation by lowering the tube potential of the low-energy scan is limited by signal statistics, since a softer beam will have less penetrating power. In this work, the low-energy scan is acquired at 90 kVp as it was the lowest calibrated tube potential available on the scanner. Based on Primak et al.'s analysis[95] of additional filtration of the high-energy beam to improve DECT discrimination of iodine and bone, a 0.5 mm thick tin filter was designed to be retrofitted to the Brilliance scanner's collimation system. The equivalent spectrum method of fitting a spectrum model to measured transmission data described in Chapter 3 and paper III was used to estimate the spectrum of the Brilliance scanner's 140 kVp beam with the 0.5 mm tin filter in place. The equivalent spectrum model was found to fit the measured transmission data with 1.45% RMS error. Figure 17 shows the tin filter and the three equivalent x-ray spectra used in this dual-energy project. Note that in figure 17 all three x-ray spectra are normalized to have unit area. In actuality, the 0.5 mm tin filter reduces the total particle fluence of the 140 kVp beam to 25% of its unfiltered intensity. This means that DECT estimates derived using the tin filtered 140 kVp beam are not dose-matched to the unfiltered case, making direct comparison more difficult.

(a)

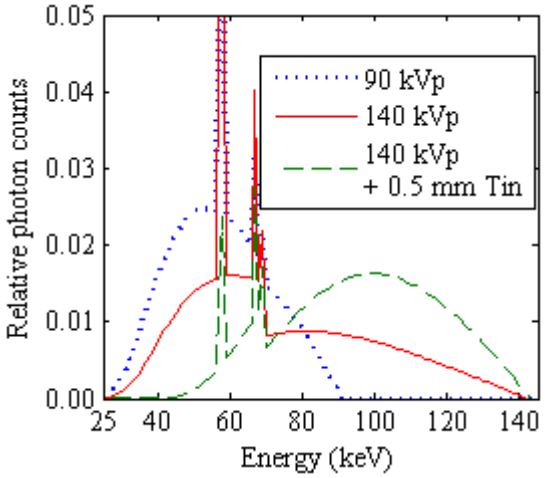

(b)

Figure 17. (a) A tin filter 0.5 mm thick was designed to be retrofitted to the scanner's x-ray collimator assembly. (b) The equivalent x-ray spectra used for dual-energy scanning. Note that all x-ray spectra are normalized to unit area for plotting purposes.

The raw dual-energy scan data, corrected only for dark current, were exported from the scanner for processing and reconstruction. As described in chapter 3, proprietary software was used to generate two sets of processed data (both will all standard system corrections applied) from each raw dataset; one with the vendor's BH correction turned on for conventional FBP reconstruction, and one with the BH correction turned off for reconstruction with the polyenergetic AM algorithm.

As there is no vendor-supported BH correction for the 140 kVp beam with the additional tin filtration, FBP reconstruction is performed only for datasets acquired with the standard 90 and 140 kVp tube potentials. The log-cosh penalized polyenergetic AM algorithm was used to reconstruct data at all three tube potentials, including the tin filtered 140 kVp beam. Penalty parameters of δ=15 and λ=5x10^{-4} were used for all AM reconstructions and were chosen empirically to reconstruct images with acceptable noise and resolution. As a first-order method to match resolution between AM and FBP images, the FBP algorithm's filter was tuned to reconstruct images of the PMMA rod with similar edge sharpness as the polyenergetic AM algorithm.

Dual-energy image pairs scanned with the 90 kVp and the un-filtered 140 kVp beams are referred to as the *standard energy pair*. Image pairs using the 90 kVp and the tin

filtered 140 kVp beam is referred to as the *tin energy pair*. The term *DE scenario* is used to refer to the particular choices of DE energy pair, reconstruction algorithm and phantom geometry for which one of the test substances is investigated.

The basis material image intensities for each scanning energy j $\left(\mu_\alpha(E_j), \mu_\beta(E_j)\right)$ required for pDECT analysis were averaged within circular regions-of-interest (ROIs) centered on the material of interest, as illustrated in figure 18d. Given a pair of reconstructed DE images $\left(\boldsymbol{\mu}(E_1), \boldsymbol{\mu}(E_2)\right)$, the pair of BVM equations in (2.2) are used to calculate the basis material coefficient images $\left(\mathbf{w}_\alpha, \mathbf{w}_\beta\right)$. Williamson et al.[54] showed that the substances investigated here were more accurately represented using two pairs of basis materials. Test substances with Z_{eff} lower than water were better modeled by a basis pair of (α,β)=(water, polystyrene) while higher Z materials were represented by a basis pair of (α,β)=(water, 23% $CaCl_2$ solution). Pixels are assigned one of the two basis pairs by comparing high- and low-kVp image intensity (paper IV). To avoid potential bias in comparing one reconstruction algorithm to another due to varying magnitudes of image noise, pixels that are known to lie within the test substance were assigned the ideal basis pair.

Equation (2.3) can then be used to estimate the linear attenuation coefficient of the material occupying each pixel at any energy. Figure 18 shows the coefficient images calculated for the 50/50 ETOH (ethanol) and water solution centered in the head phantom geometry. The coefficients were calculated from AM reconstruction of the standard energy pair.

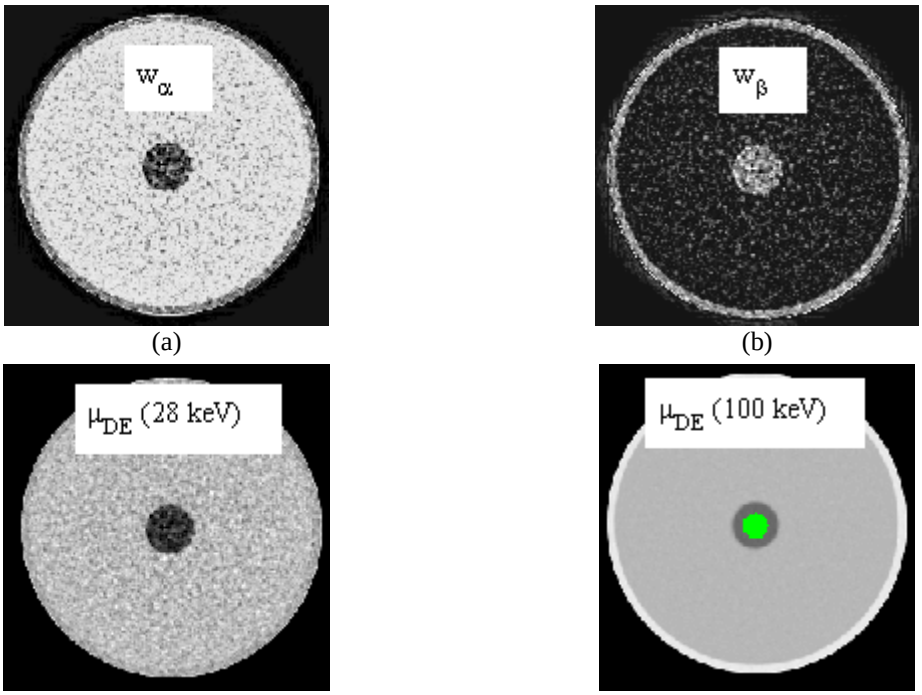

Figure 18. (a) and (b) Basis material coefficient images for the 50% ethanol (ETOH) and water solution centered in the head phantom calculated from AM images using the standard energies. Coefficient images are windowed to [-0.1 : +1.1]. Simulated monoenergetic images can then be calculated at any energy. Shown here are monoenergetic images computed at (c) 28 keV and (d) 100 keV windowed to [-50% : +20%] of the mean water intensity. The voxels (1x1x3 mm^3) used for region-of-interest (ROI) averaging are highlighted in green in (d).

Distribution of pDECT estimated linear attenuation coefficients

For pixels known to contain one of the test substances, the bias of the linear attenuation coefficient estimated for a particular pDECT scenario is assessed as the ratio to the reference value from NIST: $\left(\mu_{DE}(\mathbf{x},E)/\mu_{NIST}(E)\right)$. Figure 19 compares the distribution of pDECT linear attenuation coefficient ratios at 28 keV using AM and FBP reconstruction for pixels within the PMMA rod (head phantom, standard energy pair). The standard deviation of the bias for pixels within the test substance gives a measure of random cross-section estimation uncertainty due to image noise. The mean of the bias distribution is a measure of the systematic cross-section uncertainty. Figure 19 shows that for this DE scenario, both AM and FBP reconstruction estimate the PMMA linear attenuation coefficient at 28 keV with mean bias of less than 1.4%. However, the improved noise performance of the AM algorithm leads to cross-section estimates with less pixel-to-pixel variation than FBP (σ_{FBP} = 12.2%, σ_{AM}=7.5%).

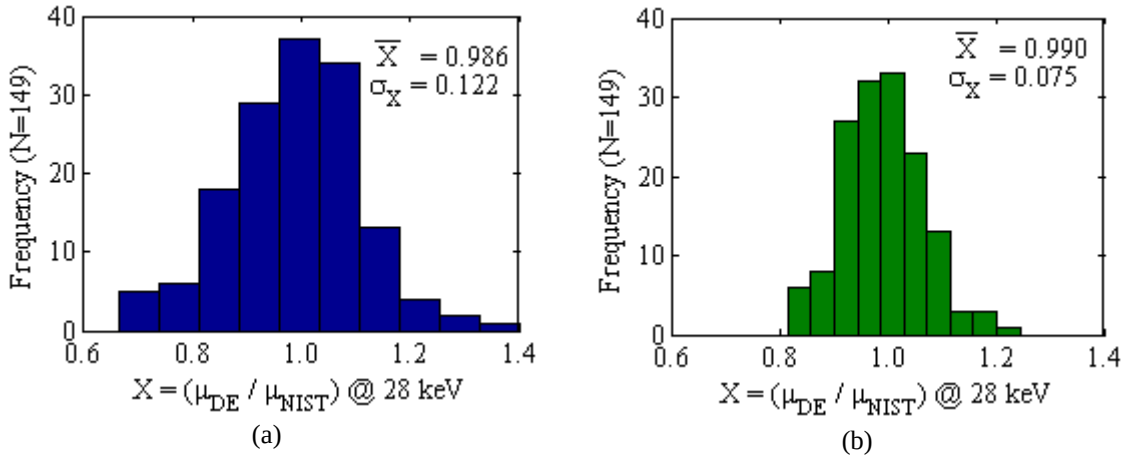

Figure 19. Distribution of the linear attenuation coefficient ratio at 28 keV for pixels within the PMMA ROI. Here the PMMA rod was scanned in the head phantom with the standard energy pair and reconstructed with 1x1x3 mm^3 voxel dimensions. The bias distribution for this DE scenario is compared when images are reconstructed with (a) FBP and (b) polyenergetic AM.

Table 2 in paper IV reports the mean and standard deviation of the bias distributions for each test substance at both 28 keV and 200 keV from all pDECT scenarios. It is seen that the random cross-section uncertainty is larger in the body phantom, which is not surprising as the same scanning dose is used for both phantom geometries. Also, low-Z materials tend to have a higher level of random cross-section uncertainty than the high-Z materials; a result that is illustrated later in this chapter. Table 2 in paper IV further supports the general result of less random cross-section estimation uncertainty when using AM reconstruction.

Mean accuracy of pDECT estimated linear attenuation coefficients

The mean linear attenuation coefficient bias averaged over all pixels within the test substance ROI, $\left(\overline{\mu_{DE}}(E)_{\mathbf{x}\in ROI} \Big/ \mu_{NIST}(E) \right)$, is plotted as a function of energy in figure 20. Mean estimation bias for all eight test substances is compared here when using FBP and AM reconstruction (standard energy pair, head phantom geometry). The mean bias is well within 1.0% for energies above 30 keV to 40 keV. For energies below 30 keV, mean bias exceeds 1% rising to 2% to 3% at 10 keV for most materials and up to 6% for Teflon.

The mean bias results for all other DE scenarios are shown in paper IV, figure 4. It is shown that additional filtration of the 140 kVp beam confers similar pDECT accuracy as using the standard, unfiltered beam. As noted above, the scanning dose when using the standard and tin energy pairs is not matched due to the reduction in fluence from the additional 0.5 mm of tin. However, as shown in the following paragraphs, scanning dose can have a marked effect on the mean pDECT accuracy and thus it may be the case that the benefit of increased spectral separation becomes more evident with matched dose.

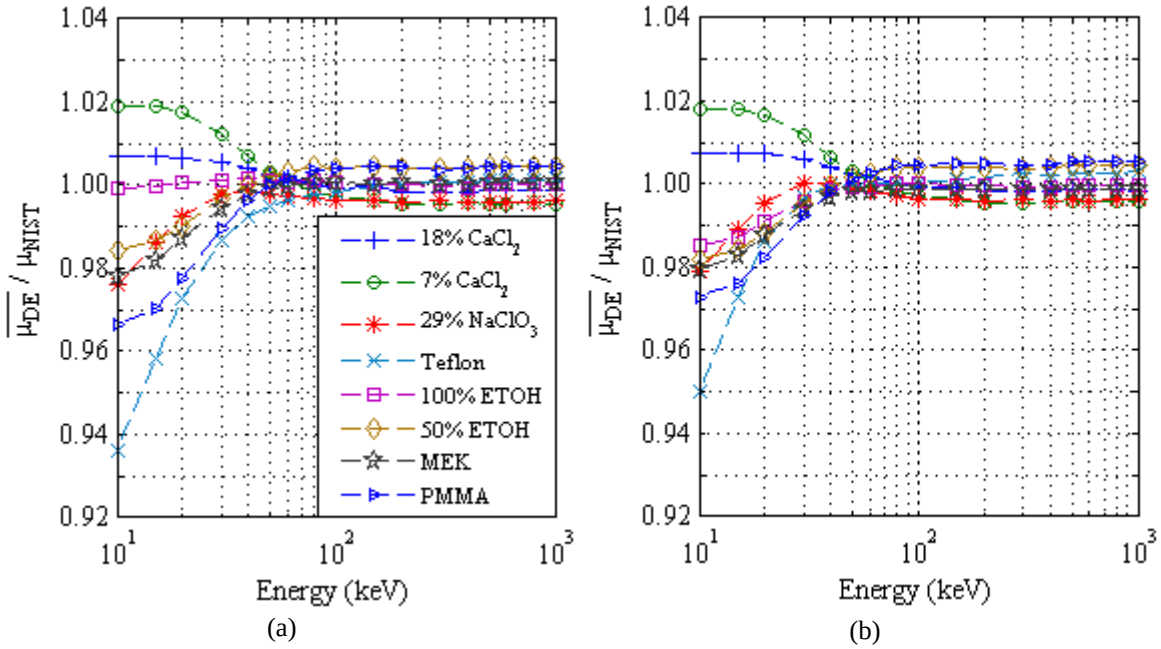

Figure 20. Mean pDECT bias as a function of energy for all test substances scanned within the head phantom using the standard energy pair. Mean pDECT bias is estimated by averaging a large number of the 1x1x3 mm^3 voxels within each test substance. Here the accuracy of the pDECT estimation of the linear attenuation coefficient is compared when using (a) FBP and (b) AM reconstruction.

The original results for pDECT accuracy in the body phantom geometry when using the same scanning dose as in the head phantom geometry exhibited large errors at low energies. Errors of 20% to 60% at 10 keV are seen for some low-Z materials in Figure 21a, which displays the mean pDECT bias in the body phantom when using FBP reconstruction of the standard energy pair. Large low-energy errors in the body phantom were also found when using AM reconstruction of both the standard and tin energy pairs.

Data acquired with insufficient photon counts not only leads to unacceptably noisy images, but can also result in systematic streaking artifacts[69]. Careful investigation into the reconstructed images revealed that the mean intensity within the low-Z materials was indeed being systematically increased due to a streaking artifact. Current scanning protocols utilize the maximum tube current per rotation available, so data averaging was employed to simulate higher dose acquisitions. The mean reconstructed intensity within the basis material ROI was found to decrease as more data was averaged prior to reconstruction. Figure 21b displays the mean pDECT bias for the same scanning scenario as 21a (body phantom, standard energy pair, FBP reconstruction), but when the three basis materials and the MEK test substance were acquired with a higher effective scanning dose. For figure 21b, seven scans of the same volume and four adjacent slices (increasing the effective slice width from 3 mm to 12 mm) were averaged together to simulate a higher effective scanning dose. It is clear that adequate signal statistics is required to avoid systematic artifacts that can quickly sacrifice mean pDECT accuracy.

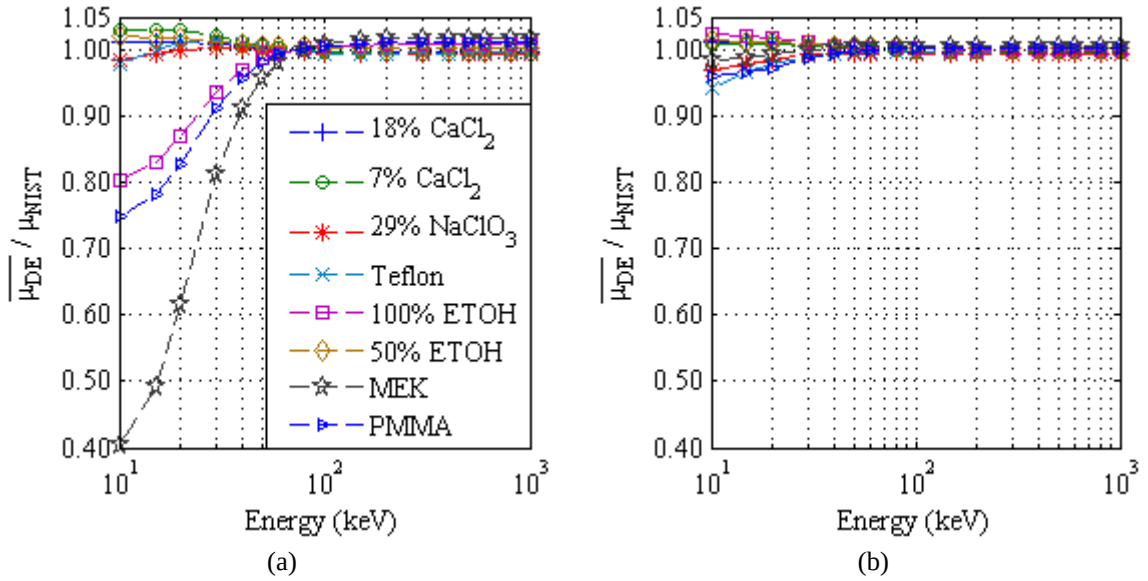

Figure 21. Mean pDECT bias as a function of energy for all test substances scanned within the body phantom using the standard energy pair and FBP image reconstruction. (a) When scanned using the standard dose mean pDECT bias is unacceptably large. The slice width for this data is the standard 3 mm in *z*. (b) When a higher effective dose is used for scanning the basis materials and the MEK test substance, mean pDECT bias is substantially reduced to levels seen in the head phantom. Here, a higher effective dose is achieved by averaging seven repeat acquisitions for a slice of data 12 mm wide in *z*.

Scattered radiation was also investigated as a potential source of systematic error in the body phantom geometry. To test the magnitude of a scatter correction on the pDECT cross-section accuracy, a uniform scatter estimate of approximately SPR = 3% on the central axis was included in the forward model (equation (1.5)) for AM reconstruction of the body phantom scanned with the standard energy pair. The scatter magnitude for the body phantom used here is from the measurements of the 30.5 cm PMMA cylinder used in chapter 3 as the two phantoms were seen to have similar attenuation as the body phantom geometry. The pDECT cross-section accuracy from images using a scatter estimate showed negligible improvement over the accuracy from images with no scatter correction seen here. This supports the argument that matching basis calibration and test substance geometries reduces the effect of non-linearities such as scatter in the post-processing DE method.

Sensitivity of pDECT estimation to reconstructed image uncertainty

The law of propagation of uncertainty[96] was used as outlined in Williamson et al. [54] to further investigate the sensitivity of the pDECT linear attenuation coefficient estimates to uncertainty in input reconstructed images. Note that the term 'uncertainty' refers to the total uncertainty from both systematic, e.g. streaking and cupping artifacts, and random components, e.g. image noise. Figure 22a plots the percent unexpanded uncertainty of the linear attenuation coefficient estimate (coverage factor of k=1) as a function of energy for all eight test substances given the same reconstructed image uncertainty. In figure 22a, all test substances were chosen to have the same total image uncertainty of 0.50% (90 kVp) and 0.25% (140 kVp). Uncertainty for the basis materials was chosen to be 0.07% (90 kVp) and 0.03% (140 kVp). These levels of input image-intensity uncertainty were chosen as they well approximate the image noises reconstructed with 1x1x3 mm^3 voxel dimension using the standard scanning protocol. Figure 22a illustrates that for the same reconstructed image uncertainty, pDECT attenuation coefficient estimation is more sensitive for low-Z test substances that use the (water, polystyrene) basis pair than the high-Z test substances that use the (water, 23% $CaCl_2$) basis pair.

Figure 22b plots the estimated pDECT uncertainty as a function of energy, using the image noise measured in 90 kVp and 140 kVp images reconstructed with both AM and

FBP. The MEK and 7% $CaCl_2$ test substances are chosen as examples of low-Z and high-Z materials, respectively. AM and FBP images for both materials shown here were reconstructed using 1x1x3 mm^3 voxels acquired with the standard scanning dose. Figure 22b shows that the uncertainty of the linear attenuation coefficient for the high-Z 7% $CaCl_2$ solution at 20 keV is 5% and 10% when using AM and FBP reconstruction, respectively. For the low-Z MEK test substance, pDECT uncertainty at 20 keV is 21% and 35% for AM and FBP reconstruction, respectively. Again, it is the noise advantage of the statistically motivated AM algorithm that results in less uncertainty of the estimated linear attenuation coefficient than when using FBP.

Paper IV further utilizes the propagated error analysis to estimate image uncertainties necessary to achieve a target level of pDECT estimated cross-section uncertainty for each test material (table 3). For example, to achieve a target cross-section uncertainty of 3% at 20 keV for the high-Z test substances using the same standard scanning dose used here, image uncertainty for individual image voxels on the order of 0.30% and 0.15%, for 90 kVp and 140 kVp respectively, would be required. For the low-Z materials, 90 kVp and 140 kVp image uncertainty on the order of 0.10% and 0.05% would be required. Paper IV also uses the reconstructed image noises to estimate the pixel size required (assuming the same scanning dose is used) to reduce the image uncertainty to achieve the target attenuation coefficient uncertainty of 3% at 20 keV for all eight test substances. For the high-Z test substances, pixels roughly on the order of 3x3x3 mm^3 for FBP and 2x2x3 mm^3 for AM would be required if using the same scanning dose. To achieve the target uncertainty for low-Z materials, pixels on the order of 14x14x3 mm^3 for FBP and 9x9x3 mm^3 for AM would be required.

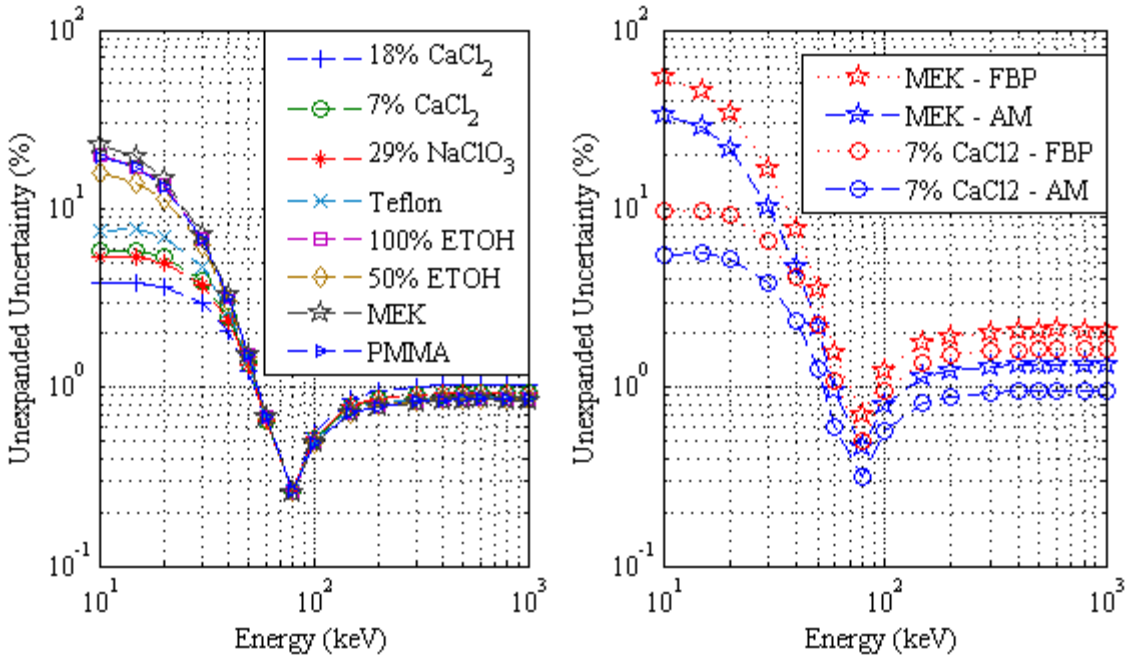

(a) (b)

Figure 22. Unexpanded uncertainty (coverage factor k=1) of the pDECT linear attenuation coefficient estimate from input image uncertainties. (a) Given the same input reconstructed image uncertainty for each material, it is seen that some test materials are more sensitive to input errors than others. (b) Using the image noise measured from the reconstructed images as the input image uncertainty, it is seen that the AM algorithm's noise advantage leads to less pDECT uncertainty than FBP. For (b) images are reconstructed using 1x1x3 mm^3 voxel dimensions with data acquired using the standard scanning dose protocol.

4.3. Discussion

The post-processing DECT method is shown to estimate linear attenuation coefficients with bias of less than 1% for energies in the range of 30 keV to 1 MeV with errors rising to between 3% and 6% at 10 keV. Given that the 2-parameter models themselves often have a model-fitting accuracy of around 1%[54,55], the experimental results here are quite encouraging. The mean attenuation coefficient errors here are slightly better than those reported recently by Goodsitt et al[57]. Goodsitt reported synthesized monochromatic images of tissue-equivalent phantom materials to have errors between 1% and 20% for energies between 40 keV and 120 keV. It is difficult to directly compare results as the methods differ in a variety of ways. The test materials used, energy pairs and scanning doses are all different. In addition, the GE dual-energy system uses a proprietary pre-processing method for which we do not have knowledge of the basis materials or the calibration procedure. However, their results do support the

common theme that DECT attenuation coefficient estimation is highly susceptible to errors that can arise from varying scan subject size or even the assumed material density.

The mean pDECT bias in this work is found to be comparable when test substances are scanned in smaller head-like phantoms and larger body-like phantoms, however adequate scanning dose must be used to maintain acceptable signal statistics. Both the propagated error analysis and the experimental results in the larger phantom highlight the extreme sensitivity of the pDECT estimation of linear attenuation coefficients to reconstructed image errors. Increasing the energy separation of the scanning spectra via additional filtration of the high kVp beam is shown to confer similar pDECT estimation performance as when using the standard energy pair, even though the total photon fluence of the tin filtered beam is approximately 25% of its original intensity. Future work is ongoing to quantify and match the dose of the varying dual-energy scanning procedures.

The calibration procedure used in this study, in which the basis materials are scanned in the exact geometry as the test substances, is the most ideal case. Quantitative CT applications are known to suffer a loss of accuracy when calibration and test geometries are mismatched[19,97] due to non-linearities, such as beam-hardening and scatter, which induce deviations from image uniformity. An essential question to address in future pDECT studies is the effect of more complex phantoms including multiple substances in a given slice and varying the calibration and test geometries. Chapter 3 showed the polyenergetic AM algorithm to reconstruct images with better consistency than FBP, and thus polyenergetic AM may reasonably be hypothesized to outperform FBP for more complex phantom setups.

The noise-resolution advantage of the AM algorithm illustrated in chapter 2 directly leads to less random uncertainty of the cross-section estimates for a given dose and resolution. FBP images can be more aggressively smoothed, however the edges will become blurrier. Neighboring pixels can be averaged to reduce random uncertainty, but at the cost of larger grid sizes. Thus, AM reconstruction for pDECT cross-section estimation can achieve a target level of random uncertainty with less image smoothing, smaller pixel dimensions or lower imaging dose than for conventional FBP

reconstruction. The noise advantage of using statistical reconstruction algorithms is a crucial advantage for the pDECT cross-section estimation problem, which has been shown to be highly sensitive to reconstructed image uncertainty.

Statistical reconstruction algorithms offer other possibilities for estimating cross-section information from CT data. While the post-processing method presented here operates on the reconstructed images, the AM algorithm can be modified to directly estimate the basis material coefficients by operating jointly on the dual-energy sinograms[98]. The AM algorithm's object model, equation (4.1), using N=2 materials is a restatement of the BVM representation of an unknown material as a linear combination of two basis materials ((2.3)). The integrated dual-energy AM (iDE-AM) algorithm then finds the basis material coefficients that minimize the sum of the I-divergence at each scanning energy. Initial simulation studies have shown that direct estimation of the basis components from the DE data using the iDE-AM algorithm leads to more accurate cross-section estimation than the post-processing DECT method using either FBP or AM reconstruction[99]. However, the current unregularized implementation of the iDE-AM algorithm was found to converge very slowly. This indicates the importance of incorporating penalty functions and other forms of *a priori* information to improve the numerical conditioning of the problem. The preliminary results are promising and certainly warrant future investigation beyond the research presented here. Prior to applying the iDE-AM algorithm to real data, methods to increase the convergence rate of the iDE-AM algorithm will need to be explored such as regularization and ordered subsets.

5. Conclusion

The dissertation research presented herein has focused on assessing the advantages of statistical reconstruction in comparison to conventional FBP for x-ray CT. Chapter 2 presented a simulation study of the noise-resolution tradeoff advantage of the edge-preserving log-cosh penalized AM algorithm. The results show that the log-cosh penalized AM algorithm always reconstructs images with less image noise than FBP for comparable resolution. It was also shown that edge-preserving penalties can lead to edge shapes that are very different than FBP or quadratic penalty functions. For the more conservative quadratic-like penalty shape, the AM-100 dose fraction was about 70%, indicating AM would require 70% of the imaging dose to reconstruct an image with comparable quality to FBP. The complex dependence of MTF shape on the regularization penalty function form leads to significant variation of dose-enhancement ratios attributable to SIR on contrast level, penalty function shape, and metric used to quantify resolution. Using the strongly edge-preserving penalty function, the AM-700 dose fraction ranged from 70% to 10% when matching resolution for low- and high-contrast structures, respectively. The results indicate that when investigating noise-resolution advantages of edge-preserving penalty functions, resolution should be matched for an object with contrast relevant to the intended clinical task.

Chapter 3 presented results of commissioning the polyenergetic AM algorithm for reconstruction of data acquired on a commercial CT scanner. Methods for accurately estimating the x-ray spectrum and modeling the off-axis effect of the bowtie filter were outlined, highlighting the care necessary to achieve accurate reconstruction. Using a series of homogeneous cylindrical phantoms, the accuracy and consistency of the polyenergetic AM algorithm was tested for three clinically available tube potentials. Absolute image intensity was found to be within 0.5% of expected when using a constant scatter estimate. Of interest to quantitative CT applications, the polyenergetic AM algorithm is shown to reconstruct images with better uniformity and less object-size dependence than FBP reconstruction using the vendor's BH correction. Though some errors greater than 0.5% warrant future investigation, the results give us confidence in the

methods for characterizing the x-ray spectrum and estimating scatter in support of future research using the polyenergetic AM algorithm for reconstruction of commercially acquired data.

In chapter 4 the experimental accuracy of a post-processing DECT method for estimating photon cross-sections was investigated for data acquired on a commercial scanner. The noise advantage of the AM algorithm was seen to support pDECT cross-section estimation with less random uncertainty than FBP. Linear attenuation coefficients were estimated to within 1% of reference for energies from 30 keV to 1 MeV, with errors rising to 2% to 3% for lower energies down to 10 keV and isolated errors of up to 6%. The results were similar when test substances were scanned in both smaller head-size phantoms and larger body-like phantoms, though the importance of scanning with adequate dose to maintain acceptable signal statistics was evident in the larger phantom. The mean pDECT bias, quantified by averaging over a large number of pixels to reduce statistical uncertainty, was found to be similar when using FBP and AM reconstruction, likely due to the ideal procedure of matching calibration and test geometries. The polyenergetic AM algorithm may show improved mean bias in future investigations that include more complex geometries. The main advantage of the statistical AM algorithm shown here lies in the improved noise performance, meaning the AM algorithm can achieve a target level of uncertainty using less scanning dose, or smaller pixels than FBP. Additional filtration of the high energy beam is shown to result in similar mean accuracy, even though the scanning dose is much lower. Future work is already underway to quantify and match the scanning dose for different dual-energy acquisition protocols. Still, these first experimental results of pDECT cross-section estimation showing mean accuracy of 1% to 6% in the 10 keV to 1 MeV energy range from data acquired on commercially available hardware are encouraging for future research.

The research, described here as a whole, highlights the potential of statistically-motivated algorithms to further improve the accuracy of CT reconstruction in support of quantitative applications. The demonstrated noise- and systematic artifact-reduction advantages of the penalized AM algorithm have the potential to reduce patient dose for

CT imaging procedures while maintaining a high level of diagnostic utility. A wide range of quantitative CT applications stand to benefit from more quantitatively accurate images due to statistical image reconstruction's considerable potential for reducing random and systematic image uncertainties. While much work remains to be done to fully realize this potential, the work presented here significantly advances SIR research.

References

[1]A. C. Kak and M. Slaney, *Principles of Computerized Tomographic Imaging* (IEEE Press, New York, 1988).

[2]R. A. Brooks and G. Di Chiro, "Beam hardening in x-ray reconstructive tomography," Phys Med Biol **21** (3), 390-8 (1976).

[3]W. D. McDavid, R. G. Waggener, W. H. Payne, and M. J. Dennis, "Correction for spectral artifacts in cross-sectional reconstruction from x rays," Med Phys **4** (1), 54-7 (1977).

[4]P. M. Joseph and R. D. Spital, "The effects of scatter in x-ray computed tomography," Med Phys **9** (4), 464-72 (1982).

[5]B. De Man, J. Nuyts, P. Dupont, G. Marchal, and P. Suetens, "Metal streak artifacts in x-ray computed tomography: A simulation study," IEEE Trans Nucl Sci **46** (3), 691-696 (1999).

[6]K. J. Engel, C. Herrmann, and G. Zeitler, "X-ray scattering in single- and dual-source CT," Med Phys **35** (1), 318-32 (2008).

[7]L. Zhu, J. Wang, and L. Xing, "Noise suppression in scatter correction for cone-beam CT," Med Phys **36** (3), 741-52 (2009).

[8]J. A. Fessler, "Statistical Image Reconstruction Methods for Transmission Tomography," in *Handbook of Medical Imaging, Volume 2. Medical Image Processing and Analysis*, edited by M. Sonka and J. M. Fitzpatrick (SPIE, Bellingham, 2000), pp. 1-70.

[9]B. R. Whiting, P. Massoumzadeh, O. A. Earl, J. A. O'Sullivan, D. L. Snyder, and J. F. Williamson, "Properties of preprocessed sinogram data in x-ray computed tomography," Med Phys **33** (9), 3290-303 (2006).

[10]G. M. Lasio, B. R. Whiting, and J. F. Williamson, "Statistical reconstruction for x-ray computed tomography using energy-integrating detectors," Phys Med Biol **52** (8), 2247-66 (2007).

[11]C. L. Byrne, "Iterative image reconstruction algorithms based on cross-entropy minimization," IEEE Trans Image Process **2** (1), 96-103 (1993).

[12]P. J. La Riviere, "Penalized-likelihood sinogram smoothing for low-dose CT," Med Phys **32** (6), 1676-83 (2005).

[13]J. B. Thibault, K. D. Sauer, C. A. Bouman, and J. Hsieh, "A three-dimensional statistical approach to improved image quality for multislice helical CT," Med Phys **34** (11), 4526-44 (2007).

[14]A. Ziegler, T. Kohler, and R. Proksa, "Noise and resolution in images reconstructed with FBP and OSC algorithms for CT," Med Phys **34** (2), 585-98 (2007).

[15]B. De Man, J. Nuyts, P. Dupont, G. Marchal, and P. Suetens, "An iterative maximum-likelihood polychromatic algorithm for CT," IEEE Trans Med Imaging **20** (10), 999-1008 (2001).

[16]I. A. Elbakri and J. A. Fessler, "Segmentation-free statistical image reconstruction for polyenergetic x-ray computed tomography with experimental validation," Phys. Med. Bio. **48**, 2453-2477 (2003).

[17]E. C. McCullough, "Factors affecting the use of quantitative information from a CT scanner," Radiology **124** (1), 99-107 (1977).

[18]J. D. Evans, B. R. Whiting, D. G. Politte, J. A. O'Sullivan, P. Klahr, and J. F. Williamson, "Prospects for quantitative imaging on commercial fan-beam CT scanners: Experimental assessment of analytic and polyenergetic statistical reconstruction algorithms," Under Review at Phys. Med. Biol. (2011).

[19]S. D. Boden, D. J. Goodenough, C. D. Stockham, E. Jacobs, T. Dina, and R. M. Allman, "Precise measurement of vertebral bone density using computed tomography without the use of an external reference phantom," J Digit Imaging **2** (1), 31-8 (1989).
[20]C. E. Cann, "Quantitative CT for Determination of Bone Mineral Density: A Review," Radiology **166**, 509-522 (1988).
[21]M. Konig, "Brain perfusion CT in acute stroke: current status," Eur J Radiol **45 Suppl 1**, S11-22 (2003).
[22]C. Valdiviezo, M. Ambrose, V. Mehra, A. C. Lardo, J. A. Lima, and R. T. George, "Quantitative and qualitative analysis and interpretation of CT perfusion imaging," J Nucl Cardiol **17** (6), 1091-100 (2010).
[23]F. C. P. du Plessis, C. A. Willemse, and M. G. Lotter, "The indirect use of CT numbers to establish material properties needed for Monte Carlo calculation of dose distributions in patients," Medical Physics **25** (7), 1195-1201 (1998).
[24]W. Schneider, T. Bortfeld, and W. Schlegel, "Correlation between CT numbers and tissue parameters needed for Monte Carlo simulations of clinical dose distributions," Phys Med Biol **45** (2), 459-78 (2000).
[25]M. J. Rivard, B. M. Coursey, L. A. DeWerd, W. F. Hanson, M. S. Huq, G. S. Ibbott *et al.*, "Update of AAPM Task Group No. 43 Report: A revised AAPM protocol for brachytherapy dose calculations," Med Phys **31** (3), 633-74 (2004).
[26]H. Afsharpour, J. P. Pignol, B. Keller, J. F. Carrier, B. Reniers, F. Verhaegen *et al.*, "Influence of breast composition and interseed attenuation in dose calculations for post-implant assessment of permanent breast 103Pd seed implant," Phys Med Biol **55** (16), 4547-61 (2010).
[27]J. F. Carrier, M. D'Amours, F. Verhaegen, B. Reniers, A. G. Martin, E. Vigneault *et al.*, "Postimplant dosimetry using a Monte Carlo dose calculation engine: a new clinical standard," Int J Radiat Oncol Biol Phys **68** (4), 1190-8 (2007).
[28]O. Chibani and J. F. Williamson, "MCPI©: A sub-minute Monte Carlo dose calculation engine for prostate implants," Med. Phys. **32**, 3688-3698 (2005).
[29]G. Landry, B. Reniers, L. Murrer, L. Lutgens, E. B. Gurp, J. P. Pignol *et al.*, "Sensitivity of low energy brachytherapy Monte Carlo dose calculations to uncertainties in human tissue composition," Med Phys **37** (10), 5188-98 (2010).
[30]G. Lymperopoulou, P. Papagiannis, A. Angelopoulos, P. Karaiskos, E. Georgiou, and D. Baltas, "A dosimetric comparison of 169Yb and 192Ir for HDR brachytherapy of the breast, accounting for the effect of finite patient dimensions and tissue inhomogeneities," Med Phys **33** (12), 4583-9 (2006).
[31]E. Pantelis, P. Papagiannis, P. Karaiskos, A. Angelopoulos, G. Anagnostopoulos, D. Baltas *et al.*, "The effect of finite patient dimensions and tissue inhomogeneities on dosimetry planning of 192Ir HDR breast brachytherapy: a Monte Carlo dose verification study," Int J Radiat Oncol Biol Phys **61** (5), 1596-602 (2005).
[32]P. Grimm and J. Sylvester, "Advances in brachytherapy," Rev Urol **6 Suppl 4**, S37-48 (2004).
[33]J. Kao, N. N. Stone, A. Lavaf, V. Dumane, J. A. Cesaretti, and R. G. Stock, "(125)I monotherapy using D90 implant doses of 180 Gy or greater," Int J Radiat Oncol Biol Phys **70** (1), 96-101 (2008).
[34]W. R. Lee, "Permanent prostate brachytherapy: the significance of postimplant dosimetry," Rev Urol **6 Suppl 4**, S49-56 (2004).
[35]N. N. Stone, L. Potters, B. J. Davis, J. P. Ciezki, M. J. Zelefsky, M. Roach *et al.*, "Customized dose prescription for permanent prostate brachytherapy: insights from a multicenter analysis of dosimetry outcomes," Int J Radiat Oncol Biol Phys **69** (5), 1472-7 (2007).
[36]D. W. Arthur, F. A. Vicini, R. R. Kuske, D. E. Wazer, and S. Nag, "Accelerated partial breast irradiation: an updated report from the American Brachytherapy Society," Brachytherapy **2** (2), 124-30 (2003).

[37]J. P. Pignol, B. Keller, E. Rakovitch, R. Sankreacha, H. Easton, and W. Que, "First report of a permanent breast 103Pd seed implant as adjuvant radiation treatment for early-stage breast cancer," Int J Radiat Oncol Biol Phys **64** (1), 176-81 (2006).
[38]A. Dickler, M. C. Kirk, N. Seif, K. Griem, K. Dowlatshahi, D. Francescatti *et al.*, "A dosimetric comparison of MammoSite high-dose-rate brachytherapy and Xoft Axxent electronic brachytherapy," Brachytherapy **6** (2), 164-8 (2007).
[39]V. K. Mehta, O. Algan, K. L. Griem, A. Dickler, K. Haile, D. E. Wazer *et al.*, "Experience with an electronic brachytherapy technique for intracavitary accelerated partial breast irradiation," Am J Clin Oncol **33** (4), 327-35 (2010).
[40]J. P. Pignol, E. Rakovitch, B. M. Keller, R. Sankreacha, and C. Chartier, "Tolerance and acceptance results of a palladium-103 permanent breast seed implant Phase I/II study," Int J Radiat Oncol Biol Phys **73** (5), 1482-8 (2009).
[41]M. Haley, S. Beriwal, D. E. Heron, H. Kim, J. Falk, R. Johnson *et al.*, "MammoSite((R)) accelerated partial breast irradiation: a single-institution outcomes analysis with 2 years of followup," Brachytherapy **8** (1), 9-13 (2009).
[42]D. E. Wazer, S. Kaufman, L. Cuttino, T. DiPetrillo, and D. W. Arthur, "Accelerated partial breast irradiation: an analysis of variables associated with late toxicity and long-term cosmetic outcome after high-dose-rate interstitial brachytherapy," Int J Radiat Oncol Biol Phys **64** (2), 489-95 (2006).
[43]A. Brahme, "Dosimetric precision requirements in radiation therapy," Acta Radiol Oncol **23** (5), 379-91 (1984).
[44]K. A. Gifford, J. L. Horton, T. A. Wareing, G. Failla, and F. Mourtada, "Comparison of a finite-element multigroup discrete-ordinates code with Monte Carlo for radiotherapy calculations," Phys Med Biol **51** (9), 2253-65 (2006).
[45]K. Zourari, E. Pantelis, A. Moutsatsos, L. Petrokokkinos, P. Karaiskos, L. Sakelliou *et al.*, "Dosimetric accuracy of a deterministic radiation transport based 192Ir brachytherapy treatment planning system. Part I: single sources and bounded homogeneous geometries," Med Phys **37** (2), 649-61 (2010).
[46]D. R. White, E. M. Widdowson, H. Q. Woodard, and J. W. Dickerson, "The composition of body tissues (II). Fetus to young adult," Br J Radiol **64** (758), 149-59 (1991).
[47]H. Q. Woodard and D. R. White, "The composition of body tissues," Br J Radiol **59** (708), 1209-18 (1986).
[48]R. A. Geise and A. Palchevsky, "Composition of mammographic phantom materials," Radiology **198** (2), 347-50 (1996).
[49]M. J. Yaffe, J. M. Boone, N. Packard, O. Alonzo-Proulx, S. Y. Huang, C. L. Peressotti *et al.*, "The myth of the 50-50 breast," Med Phys **36** (12), 5437-43 (2009).
[50]R. A. Rutherford, B. R. Pullan, and I. Isherwood, "Measurement of effective atomic number and electron density using an EMI scanner," Neuroradiology **11** (1), 15-21 (1976).
[51]M. Bazalova, J. F. Carrier, L. Beaulieu, and F. Verhaegen, "Dual-energy CT-based material extraction for tissue segmentation in Monte Carlo dose calculations," Phys Med Biol **53** (9), 2439-56 (2008).
[52]B. J. Heismann, J. Leppert, and K. Stierstorfer, "Density and atomic number measurements with spectral x-ray attenuation method," J. Appl. Phys. **94** (3), 2073-2079 (2003).
[53]M. Torikoshi, T. Tsunoo, M. Sasaki, M. Endo, Y. Noda, Y. Ohno *et al.*, "Electron density measurement with dual-energy x-ray CT using synchrotron radiation," Phys Med Biol **48** (5), 673-85 (2003).
[54]J. F. Williamson, S. Li, S. Devic, B. R. Whiting, and F. A. Lerma, "On two-parameter models of photon cross sections: application to dual-energy CT imaging," Med Phys **33** (11), 4115-29 (2006).
[55]S. M. Midgley, "A parameterization scheme for the x-ray linear attenuation coefficient and energy absorption coefficient," Phys Med Biol **49** (2), 307-25 (2004).

[56]S. M. Midgley, “Materials analysis using x-ray linear attenuation coefficient measurements at four photon energies,” Phys Med Biol **50** (17), 4139-57 (2005).
[57]M. M. Goodsitt, E. G. Christodoulou, and S. C. Larson, “Accuracies of the synthesized monochromatic CT numbers and effective atomic numbers obtained with a rapid kVp switching dual energy CT scanner,” Med Phys **38** (4), 2222-32 (2011).
[58]E. Cardis, M. Vrijheid, M. Blettner, E. Gilbert, M. Hakama, C. Hill *et al.*, “Risk of cancer after low doses of ionising radiation: retrospective cohort study in 15 countries,” Bmj **331** (7508), 77 (2005).
[59]D. A. Pierce and D. L. Preston, “Radiation-related cancer risks at low doses among atomic bomb survivors,” Radiat Res **154** (2), 178-86 (2000).
[60]D. J. Brenner, R. Doll, D. T. Goodhead, E. J. Hall, C. E. Land, J. B. Little *et al.*, “Cancer risks attributable to low doses of ionizing radiation: assessing what we really know,” Proc Natl Acad Sci U S A **100** (24), 13761-6 (2003).
[61]D. J. Brenner and E. J. Hall, “Computed tomography--an increasing source of radiation exposure,” N Engl J Med **357** (22), 2277-84 (2007).
[62]C. J. Martin, D. G. Sutton, and P. F. Sharp, “Balancing patient dose and image quality,” Appl Radiat Isot **50** (1), 1-19 (1999).
[63]AAPM, “AAPM Report No. 96: The Measurement, Reporting, and Management of Radiation Dose in CT - Report of AAPM Task Group 23 of the Diagnostic Imaging Council CT Committee of the American Association of Physicists in Medicine,” **Medical Physics Publishing** (2008).
[64]X. Li, E. Samei, W. P. Segars, G. M. Sturgeon, J. G. Colsher, G. Toncheva *et al.*, “Patient-specific radiation dose and cancer risk estimation in CT: part II. Application to patients,” Med Phys **38** (1), 408-19 (2011).
[65]X. Li, E. Samei, W. P. Segars, G. M. Sturgeon, J. G. Colsher, G. Toncheva *et al.*, “Patient-specific radiation dose and cancer risk estimation in CT: part I. development and validation of a Monte Carlo program,” Med Phys **38** (1), 397-407 (2011).
[66]D. L. Snyder, M. I. Miller, L. J. Thomas, and D. G. Politte, “Noise and edge artifacts in maximum-likelihood reconstructions for emission tomography,” IEEE Trans Med Imaging **6** (3), 228-38 (1987).
[67]E. Veklerov and J. Llacer, “Stopping Rule for the MLE Algorithm Based on Statistical Hypothesis Testing,” IEEE Trans Med Imaging **6** (4), 313-9 (1987).
[68]J. A. Fessler and W. L. Rogers, “Spatial resolution properties of penalized-likelihood image reconstruction: space-invariant tomographs,” IEEE Trans Image Process **5** (9), 1346-58 (1996).
[69]J. Hsieh, “Adaptive streak artifact reduction in computed tomography resulting from excessive x-ray photon noise,” Med Phys **25** (11), 2139-47 (1998).
[70]C. Kamphuis and F. J. Beekman, “Accelerated iterative transmission CT reconstruction using an ordered subsets convex algorithm,” IEEE Trans Med Imaging **17** (6), 1101-5 (1998).
[71]I. Csiszar, “Why least squares and maximum entropy? An axiomatic approach to inference for linear inverse problems,” Annals of Statistics **19**, 2032-2066 (1991).
[72]J. A. O'Sullivan and J. Benac, “Alternating minimization algorithms for transmission tomography,” IEEE Trans Med Imaging **26** (3), 283-97 (2007).
[73]P. J. Green, “Bayesian reconstructions from emission tomography data using a modified EM algorithm,” IEEE Trans Med Imaging **9**, 84-93 (1990).
[74]J. D. Evans, D. G. Politte, B. R. Whiting, J. A. O'Sullivan, and J. F. Williamson, “Noise-resolution tradeoffs in x-ray CT imaging: a comparison of Penalized Alternating Minimization and Filtered Backprojection algorithms,” Med Phys **38** (3), 1444-1458 (2011).
[75]D. F. Yu and J. A. Fessler, “Edge-preserving tomographic reconstruction with nonlocal regularization,” IEEE Trans Med Imaging **21** (2), 159-73 (2002).

[76]D. Chesler, S. Riederer, and N. Pelc, "Noise Due to Photon Counting Statistics in Computed X-Ray Tomography," Journal of Computer Assisted Tomography **1** (1), 64-74 (1977).
[77]W. H. Press, S. A. Teukolsky, W. T. Vetterling, and B. P. Flannery, *Numerical Recipes in C*, 2 ed. (Cambridge University Press, 1992).
[78]J. Wang, T. Li, and L. Xing, "Iterative image reconstruction for CBCT using edge-preserving prior," Med Phys **36** (1), 252-60 (2009).
[79]S. Richard, X. Li, G. Yadava, and E. Samei, "Predictive models for observer performance in CT: Applications in protocol optimization," Proc. of SPIE - Physics of Medical Imaging **7961**, 79610H (2011).
[80]P. M. Joseph and R. D. Spital, "A method for correcting bone induced artifacts in computed tomography scanners," J Comput Assist Tomogr **2** (1), 100-8 (1978).
[81]R. E. Alvarez and A. Macovski, "Energy-selective reconstructions in X-ray computerized tomography," Phys Med Biol **21** (5), 733-44 (1976).
[82]J. P. Stonestrom, R. E. Alvarez, and A. Macovski, "A framework for spectral artifact corrections in x-ray CT," IEEE Trans Biomed Eng **28** (2), 128-41 (1981).
[83]I. A. Elbakri and J. A. Fessler, "Statistical image reconstruction for polyenergetic X-ray computed tomography," IEEE Trans Med Imaging **21** (2), 89-99 (2002).
[84]R. Birch and M. Marshall, "Computation of bremsstrahlung X-ray spectra and comparison with spectra measured with a Ge(Li) detector," Phys Med Biol **24** (3), 505-17 (1979).
[85]J. M. Boone, "Equivalent spectra as a measure of beam quality," Med Phys **13** (6), 861-8 (1986).
[86]J. M. Boone, "The three parameter equivalent spectra as an index of beam quality," Med Phys **15** (3), 304-10 (1988).
[87]L. Xie, "X-ray computed tomography image reconstruction: Energy-integrating detector and performance analysis," Dissertation, Washington University in St. Louis, 2008.
[88]K. Engel, C. Baumer, J. Weigert, and G. Zeitler, "Spectral analysis of scattered radiation in CT," Proceedings of SPIE - Physics of Medical Imaging **6913** (2008).
[89]M. Endo, S. Mori, T. Tsunoo, and H. Miyazaki, "Magnitude and effects of x-ray scatter in a 256-slice CT scanner," Med Phys **33** (9), 3359-68 (2006).
[90]P. C. Johns and M. Yaffe, "Scattered radiation in fan beam imaging systems," Med Phys **9** (2), 231-9 (1982).
[91]R. A. Brooks, "A quantitative theory of the Hounsfield unit and its application to dual energy scanning," J Comput Assist Tomogr **1** (4), 487-93 (1977).
[92]L. A. Lehmann, R. E. Alvarez, A. Macovski, W. R. Brody, N. J. Pelc, S. J. Riederer *et al.*, "Generalized image combinations in dual KVP digital radiography," Med Phys **8** (5), 659-67 (1981).
[93]I. Lux and L. Koblinger, *Monte Carlo particle transport methods: neutron and photon calculations* (CRC Press, Boca Raton, 1991).
[94]F. Kelcz, P. M. Joseph, and S. K. Hilal, "Noise considerations in dual energy CT scanning," Med Phys **6** (5), 418-25 (1979).
[95]A. N. Primak, J. C. Ramirez Giraldo, X. Liu, L. Yu, and C. H. McCollough, "Improved dual-energy material discrimination for dual-source CT by means of additional spectral filtration," Med Phys **36** (4), 1359-69 (2009).
[96]B. N. Taylor and C. E. Kuyatt, "Guidelines for evaluating and expressing the uncertainty of NIST measurement results," Report No. NIST Technical Note 1297, National Institute of Standards and Technology, Washington, D.C., 1994.
[97]E. A. Zerhouni, M. Boukadoum, M. A. Siddiky, J. M. Newbold, D. C. Stone, M. P. Shirey *et al.*, "A standard phantom for quantitative CT analysis of pulmonary nodules," Radiology **149** (3), 767-73 (1983).

[98]J. A. O'Sullivan, J. Benac, and J. F. Williamson, “Alternating Minimization Algorithm for Dual Energy X-ray CT,” Proc. IEEE International Symposium on Biomedical Imaging, 579 - 582 (2004).
[99]J. Benac, “Alternating minimization algorithms for X-ray computed tomography: multigrid acceleration and dual energy application,” Thesis, May 2005,” Doctor of Science, Washington University, 2005.
[100]H. M. Hudson and R. S. Larkin, “Accelerated image reconstruction using ordered subsets of projection data,” IEEE Trans Med Imaging **13** (4), 601-9 (1994).

Appendix 1

The Alternating Minimization algorithm

A description of the Alternating Minimization (AM) algorithm is presented here. This is based on O'Sullivan's 2007 paper[72] to which the reader is referred for a full treatment of its derivation.

The CT sinogram data space, **y**, is defined by the angle of each source-detector ray, γ, and each gantry angle, ϕ. An object is represented in image space, **x**, as a map of linear attenuation coefficients, $\mu(\mathbf{x}, E)$, that depend on spatial location, *x*, and energy, *E*. The material at location *x* is represented as a weighted sum of *N* basis materials:

$$\mu(\mathbf{x}, E) = \sum_{i=1}^{N} \mu_i(E) c_i(\mathbf{x}) = \boldsymbol{\mu}(E) \cdot \mathbf{c}(\mathbf{x}), \quad (4.1)$$

where $\mu_i(E)$ denotes the linear attenuation spectrum of the i-th basis material. The reconstruction algorithm will estimate *N* images that represent the partial density of each basis material in each voxel; $c_i(\mathbf{x})$. Statistical iterative reconstruction (SIR) algorithms pose image reconstruction as an optimization problem. Assuming photon-counting statistics, the Poisson likelihood given by

$$p(d \mid \mathbf{c}) = \prod_{y} e^{-g(\mathbf{y}:\mathbf{c})} \frac{g(\mathbf{y}:\mathbf{c})^{d(\mathbf{y})}}{d(\mathbf{y})!}, \quad (4.2)$$

which describes the probability of observing the measured data $d(\mathbf{y})$, given the expected mean values $g(\mathbf{y}:\mathbf{c})$ from the image estimate $\mathbf{c}$. Most SIR algorithms seek to find the image $\hat{\mathbf{c}}$ that maximizes the log-likelihood:

$$\hat{\mathbf{c}} = \arg\max_{\mathbf{c}} \left[\ln\left(p(d \mid g(\mathbf{y}:\mathbf{c})) \right) \right] = \arg\max_{\mathbf{c}} \left[\sum_{y \in Y} \left[d(\mathbf{y}) \ln g(\mathbf{y}:\mathbf{c}) - g(\mathbf{y}:\mathbf{c}) \right] \right]. \quad (4.3)$$

In contrast, the Alternating Minimization algorithm seeks to identify the image that minimizes Csiszar's I-divergence:

$$\hat{\mathbf{c}} = \arg\min_{\mathbf{c}} \left[I\left(d \parallel g(\mathbf{y}:\mathbf{c}) \right) \right] = \arg\min_{\mathbf{c}} \left[\sum_{y \in Y} \left\{ d(\mathbf{y}) \ln \left[\frac{d(\mathbf{y})}{g(\mathbf{y}:\mathbf{c})} \right] - d(\mathbf{y}) + g(\mathbf{y}:\mathbf{c}) \right\} \right]. \quad (4.4)$$

I-divergence is an information-theoretic measure of the discrepancy between two functions, in this case the measured data $d(\mathbf{y})$ and the expected data means $g(\mathbf{y})$. Csiszar showed that the I-divergence is the only consistent metric to measure discrepancy between two functions subject to non-negativity constraints[71]. Comparing equations (4.3) and (4.4) it is seen that the I-divergence is proportional to the negative of the Poisson log-likelihood, meaning that minimization of the I-divergence is functionally equivalent to maximizing the Poisson log-likelihood.

The forward model simulates the CT data acquisition process and is used to calculate the expected data means from the current image estimate. The forward model used in this work is defined as

$$g(\mathbf{y}:\mathbf{c}) = \sigma(\mathbf{y}) + \sum_{E} I_0(\mathbf{y}, E) \cdot \exp\left(-\sum_{x \in X} \sum_{i=1}^{N} h(\mathbf{y} \mid x) \cdot \mu_i(E) \cdot c_i(x) \right). \quad (4.5)$$

The system matrix, $h(\mathbf{y} \mid \mathbf{x})$, is the average distance traveled by photons crossing pixel x that are incident on the face of detector element γ for gantry angle ϕ and is pre-computed

to increase the speed of the iterative algorithm. An estimate of background events, i.e. scattered radiation, is represented by $\sigma(\mathbf{y})$, which can also vary for each source-detector ray and gantry angle. $I_0(\mathbf{y},E)$ represents the x-ray spectrum and it also can vary as a function of detector location and gantry angle, for example due to the presence of a bowtie filter or tube current modulation. Incorporating the x-ray energy spectrum directly in the AM algorithm's forward model represents an implicit beam-hardening correction.

AM is so named because the minimization (M-step) alternates between minimizing over an exponential family of functions, ε, and a linear family of functions, ℓ. The exponential family of functions to describe the data model of equation (4.5) is defined as:

$$\varepsilon = \left\{ \mathbf{q} \left| \begin{array}{l} q(\mathbf{y},E) = I_0(\mathbf{y},E)\cdot\exp\left(-\sum_{x\in X}\sum_{i=1}^{N} h(\mathbf{y}\mid x)\mu_i(E)c_i(x) \right);\ \text{for } E\neq 0 \\ q(\mathbf{y},0) = \beta(y) \end{array} \right. \right\}. \quad (4.6)$$

Thus, ε is the set of mean monoenergetic photon counting sinograms, $q(\mathbf{y},E)$, corresponding to the population of non-negative image solutions, $\{\mathbf{c}(\mathbf{x})\}$. Scattered counts are accounted for by the dummy energy $E=0$. The linear family of functions to describe the measured data is defined by:

$$\ell(\mathbf{d}) = \left\{ p(\mathbf{y},E) \mid \sum_E p(\mathbf{y},E) = d(\mathbf{y}) \right\}. \quad (4.7)$$

$\ell(\mathbf{d})$ is the total set of non-negative noisy monoenergetic sinograms consistent with the measured sinogram. As a direct measure of the number of photons with energy *E* in the measured data is not available, the AM algorithm estimates $p(\mathbf{y},E)$ at each iteration. It can be shown [72] that $p(\mathbf{y},E)$ can be inferred from the measured data $d(\mathbf{y})$ and the current mean sinogram estimate $q(\mathbf{y},E)$:

$$p(\mathbf{y},E) = d(\mathbf{y})\frac{q(\mathbf{y},E)}{\sum_{E'} q(\mathbf{y},E')}. \quad (4.8)$$

The linear family constrains the energy sum of the estimate to equal the total counts of the measured data. Using the exponential family of functions to describe the data means corresponding to the population of solution images and the linear family to describe the measured data, the minimization in (4.4) can be cast as a double minimization of the I-divergence between $\mathbf{p}$ and $\mathbf{q}$:

$$\hat{\mathbf{c}}(\mathbf{x}) = \arg\min_{q \in \varepsilon} \left[\arg\min_{p \in \ell} I(\mathbf{p} \,\|\, \mathbf{q}) \right]. \qquad (4.9)$$

Here $\hat{\mathbf{c}}(\mathbf{x})$ is the image estimate that minimizes the I-divergence between $p(\mathbf{y}, E)$ and $q(\mathbf{y}, E)$.

Using the measured data $d(\mathbf{y})$ along with the image estimate $\hat{\mathbf{c}}^{(k)}(\mathbf{x})$ from the previous iteration, k, equations (4.6) and (4.8) are used to estimate the monoenergetic projections $\hat{p}^{(k)}(\mathbf{y}, E)$ and $\hat{q}^{(k)}(\mathbf{y}, E)$. Backprojections of these quantities are then computed according to

$$\tilde{b}_i^{(k)}(\mathbf{x}) = \sum_{y \in \mathbf{y}} \sum_{E} \mu_i(E) h(y \mid \mathbf{x}) \hat{p}^{(k)}(y, E), \qquad (4.10)$$

$$\hat{b}_i^{(k)}(\mathbf{x}) = \sum_{y \in \mathbf{y}} \sum_{E} \mu_i(E) h(y \mid \mathbf{x}) \hat{q}^{(k)}(y, E). \qquad (4.11)$$

Finally, the next iterate of the image, $\hat{\mathbf{c}}^{(k+1)}(\mathbf{x})$, is then calculated for each basis substance using a pre-computed scaling factor $Z_i(\mathbf{x})$:

$$\hat{c}_i^{(k+1)}(\mathbf{x}) = \hat{c}_i^{(k)}(\mathbf{x}) - \frac{1}{Z_i(\mathbf{x})} \ln\left(\frac{\tilde{b}_i^{(k)}(\mathbf{x})}{\hat{b}_i^{(k)}(\mathbf{x})} \right). \qquad (4.12)$$

For each basis substance, *i*, two backprojections and a forward projection are performed for every image update step making the AM algorithm a computationally intensive algorithm in comparison to FBP. To help increase the speed of convergence, the AM algorithm also has the ability to perform iterations using ordered subset techniques[100]. The general method is to break the data into *M* mutually exclusive subsets

of the projection data and perform iterations and generate image updates using these subsets of data. The algorithm's speed of convergence using the ordered subsets (OS) technique increases nearly as the number of subsets *M*.

The penalized objective function to be optimized is defined as the sum of the I-divergence and the roughness penalty, $R(\mathbf{c}')$:

$$\hat{\mathbf{c}}(\mathbf{x}) = \arg_c \min_{q\in\varepsilon} \min_{p\in\ell} \left[I(\mathbf{p} \,\|\, \mathbf{q}) + \lambda \cdot R(\mathbf{c}') \right], \qquad (4.13)$$

where λ controls the relative importance of the penalty function. The log-cosh function used in this work computes a penalty for a pixel *x* as a function of the pixel intensities in the local neighborhood *N(x)* according to

$$R\left(c_i(\mathbf{x})\right) = \sum_x \sum_{x'\in N(x)} w(x') \cdot \left(\frac{1}{\delta}\right) \log\left[\cosh\left(\delta\left(c_i(x) - c_i(x')\right)\right)\right]. \quad (4.14)$$

The neighboring pixels are weighted as 1.0 for directly adjacent pixels and 0 for all other pixels:

$$w(x') = \begin{cases} 1 & ; \text{directly adjacent} \\ 0 & ; \text{all others} \end{cases}. \qquad (4.15)$$

Incorporating the roughness penalty does not greatly increase the complexity of the image update step in equation(4.12). The penalty function is minimized by setting the derivative of the function to zero and is numerically solved using a Newton-Raphson method[77].

Appendix 2

Noise-resolution tradeoffs in x-ray CT imaging: A comparison of penalized alternating minimization and filtered backprojection algorithms

Noise-resolution tradeoffs in x-ray CT imaging: A comparison of penalized alternating minimization and filtered backprojection algorithms

Joshua D. Evans[a),b)]
Department of Radiation Oncology, Virginia Commonwealth University, Richmond, Virginia 23298

David G. Politte and Bruce R. Whiting
Mallinckrodt Institute of Radiology, , Washington University, St. Louis, Missouri 63110

Joseph A. O'Sullivan
Department of Electrical and Systems Engineering, Washington University, St. Louis, Missouri 63130

Jeffrey F. Williamson[a),c)]
Department of Radiation Oncology, Virginia Commonwealth University, Richmond, Virginia 23298

(Received 12 July 2010; revised 30 December 2010; accepted for publication 6 January 2011; published 22 February 2011)

Purpose: In comparison with conventional filtered backprojection (FBP) algorithms for x-ray computed tomography (CT) image reconstruction, statistical algorithms directly incorporate the random nature of the data and do not assume CT data are linear, noiseless functions of the attenuation line integral. Thus, it has been hypothesized that statistical image reconstruction may support a more favorable tradeoff than FBP between image noise and spatial resolution in dose-limited applications. The purpose of this study is to evaluate the noise-resolution tradeoff for the alternating minimization (AM) algorithm regularized using a nonquadratic penalty function.

Methods: Idealized monoenergetic CT projection data with Poisson noise were simulated for two phantoms with inserts of varying contrast (7%–238%) and distance from the field-of-view (FOV) center (2–6.5 cm). Images were reconstructed for the simulated projection data by the FBP algorithm and two penalty function parameter values of the penalized AM algorithm. Each algorithm was run with a range of smoothing strengths to allow quantification of the noise-resolution tradeoff curve. Image noise is quantified as the standard deviation in the water background around each contrast insert. Modulation transfer functions (MTFs) were calculated from six-parameter model fits to oversampled edge-spread functions defined by the circular contrast-insert edges as a metric of local resolution. The integral of the MTF up to 0.5 lp/mm was adopted as a single-parameter measure of local spatial resolution.

Results: The penalized AM algorithm noise-resolution tradeoff curve was always more favorable than that of the FBP algorithm. While resolution and noise are found to vary as a function of distance from the FOV center differently for the two algorithms, the ratio of noises when matching the resolution metric is relatively uniform over the image. The ratio of AM-to-FBP image variances, a predictor of dose-reduction potential, was strongly dependent on the shape of the AM's nonquadratic penalty function and was also strongly influenced by the contrast of the insert for which resolution is quantified. Dose-reduction potential, reported here as the fraction (%) of FBP dose necessary for AM to reconstruct an image with comparable noise and resolution, for one penalty parameter value of the AM algorithm was found to vary from 70% to 50% for low-contrast and high-contrast structures, respectively, and from 70% to 10% for the second AM penalty parameter value. However, the second penalty, AM-700, was found to suffer from poor low-contrast resolution when matching the high-contrast resolution metric with FBP.

Conclusions: The results of this simulation study imply that penalized AM has the potential to reconstruct images with similar noise and resolution using a fraction (10%–70%) of the FBP dose. However, this dose-reduction potential depends strongly on the AM penalty parameter and the contrast magnitude of the structures of interest. In addition, the authors' results imply that the advantage of AM can be maximized by optimizing the nonquadratic penalty function to the specific imaging task of interest. Future work will extend the methods used here to quantify noise and resolution in images reconstructed from real CT data. [DOI: 10.1118/1.3549757]

Key words: computed tomography, alternating minimization, nonquadratic regularization, noise, resolution

I. INTRODUCTION

Conventional filtered backprojection (FBP) algorithms[1] provide an exact solution to the inverse problem of computed tomography (CT) under the assumption that a complete set of noiseless transmission measurements are available, which are linear functions of the attenuation line integral through the patient. However, phenomena such as measurement noise,[2] scatter,[3,4] beam-hardening,[5] and high-contrast edge effects[6] lead to data nonlinearity and artifacts such as streaking and cupping in the reconstructed image. The classic expectation-maximization algorithm of Lange and Carson[7] was formed around the statistical nature of x-ray CT data and provided the foundation for a class of statistically motivated algorithms that can directly incorporate many of these nonlinear signal-formation processes into their data models. The reader is referred to Fessler's[8] overview of statistical image reconstruction (SIR) algorithm methodology. The promise of better image quality via a more realistic modeling of the underlying CT physics has motivated many investigations of statistical algorithms, despite the extensive computational resources they demand.

It seems intuitive that SIR algorithms that explicitly model CT-signal statistics would be able to reconstruct images with less noise than FBP from the same noisy projection data set. However, it is known that the image most likely to match the measured data suffers from excessive image noise.[9,10] A widely used approach to suppress image noise in statistically based reconstruction algorithms is to modify the objective function to incorporate some *a priori* assumptions about the scan subject, e.g., the local neighborhood penalty function investigated by this study that enforces the assumption of image smoothness. As with any noise-reduction method, there is an associated cost. In CT image reconstruction, one of the most tangible costs of noise reduction is loss of spatial resolution. The degradation of spatial resolution associated with noise reduction constitutes what we will refer to as the *noise-resolution tradeoff*.

An algorithm with a better noise-resolution tradeoff would have an advantage in a number of clinical situations. Better noise-resolution tradeoff means that an algorithm can reconstruct images from the same data with either less image noise for similar resolution or better image resolution for similar image noise. By extension, an algorithm that provides a noise-resolution tradeoff advantage could provide images of comparable image quality, in terms of both noise and resolution, from data with more noise, i.e., data acquired with lower imaging dose, an important area of concern in diagnostic radiology.[11] Pediatric imaging and lung cancer screening are relevant clinical scenarios where improved reconstruction techniques for low dose CT would be clinically valuable.

SIR algorithms could also find use in quantitative CT applications. The very specific application of estimating the photon cross-sections from dual-energy measurements has been shown to be extremely sensitive to the accuracy of the measured CT values.[12] Cupping and streaking artifacts from data nonlinearities such as beam-hardening and scatter represent systematic shifts in CT image intensity. The focus of this work is to assess the suppression of random errors, i.e., image noise. Measurement noise can be reduced by averaging over a large number of pixels within a homogeneous region but at the expense of reduced spatial resolution. This may, in turn, introduce large systematic dose-calculation errors in low energy photon-emitting treatment modalities that exhibit large dose gradients, such as brachytherapy. An algorithm that can provide superior noise-resolution tradeoff may prove useful in such quantitative CT applications where both low noise and high resolution are important.

In this work, we assess the noise-resolution tradeoff, in comparison with FBP, for the alternating minimization (AM) algorithm,[13] which provides for an exact update solution to the objective function. A nonquadratic penalty function is used to regularize the AM algorithm and to tradeoff noise and resolution. Previous investigators have assessed the noise-resolution tradeoff to evaluate SIR algorithms using parabolic surrogates to model the Poisson log-likelihood,[14,15] adaptive statistical sinogram smoothing techniques,[14] and iterative reconstruction algorithms for cone-beam CT imaging geometries.[16,17] In contrast with these previous studies that have quantified resolution only for high-contrast structures, our study investigates the impact of structure contrast on the reported noise-resolution tradeoff. An ideal monoenergetic simulation environment is used to avoid artifacts arising from data nonlinearity, such as scattered radiation and beam-hardening, the goal being to isolate the smoothing effects of the two algorithms. In this way, we form a baseline of noise-resolution tradeoff performance for the FBP and alternating minimization algorithms for ideal Poisson-counting projection data. Future work will extend the methods for the quantification of noise and resolution in this paper to images reconstructed from real CT data.

II. MATERIALS AND METHODS

II.A. CT image reconstruction

II.A.1. Penalized AM reconstruction

The penalized monoenergetic version of the alternating minimization algorithm is used to reconstruct the synthetic projection data. The AM algorithm reformulates the classic maximization of the Poisson log-likelihood as an alternating minimization of Csiszar's[18] *I*-divergence between the measured data d and the expected data means g

$$I(d \| g) = \sum_{y \in Y} \left(d(y) \ln \frac{d(y)}{g(y;\mu')} - d(y) + g(y;\mu') \right), \qquad (1)$$

where μ' is the current image estimate. The *I*-divergence is the negative of the log-likelihood, meaning that minimization of the *I*-divergence is identical to the maximization of the log-likelihood. For full details of the alternating minimization algorithm, the reader is referred to O'Sullivan's 2007 paper.[13] A log-cosh penalty term is included in the AM algorithm's objective function to enforce our *a priori* assumption of image smoothness

$$\Phi(\mu') = I(d \| g) + \alpha \cdot R(\mu'), \tag{2}$$

where α controls the relative weight of the penalty function. The roughness penalty computes a penalty for a pixel x as a function of the pixel intensities in the local neighborhood $N(x)$. The penalty chosen for this study is defined as

$$R(\mu') = \sum_x \sum_{x' \in N(x)} w(x') \cdot \left(\frac{1}{\delta}\right) \log[\cosh(\delta(\mu'(x) - \mu'(x')))]. \tag{3}$$

The neighboring pixels are weighted as 1.0 for directly adjacent pixels and 0 for all other pixels

$$w(x') = \begin{cases} 1; & \text{directly adjacent} \\ 0; & \text{all others} \end{cases}. \tag{4}$$

Purely quadratic penalty functions effectively suppress noise, but tend to blur high-contrast edges as the penalty grows quickly for large pixel intensity differences. The continuously defined edge-preserving log-cosh function[19] is similar to a Huber penalty,[20] which is quadratic for small pixel-to-pixel variations, so as to suppress noise, and linear for larger variations, so as to preserve edge boundaries. The parameter δ controls the pixel intensity difference for which the penalty transitions from quadratic to linear growth. Increasing δ causes the transition to linear growth to occur at smaller intensity differences. Two different values of δ are investigated to study the effect on image noise and resolution. We let *AM-100* denote images reconstructed with the penalized AM algorithm with δ=100, which transitions to linear penalty growth for pixel differences approximately 50% of the water background. *AM-700* denotes the AM algorithm using a log-cosh penalty with δ=700, which has a growth transition for pixel differences around 10% of background. Figure 1 plots both of the log-cosh penalties investigated in this work and a quadratic penalty function for comparison. Note that the Lagrange multipliers used in Fig. 1 were chosen purely for plotting purposes to showcase the different penalty growth. Values of α for AM-700 nearly an order of magnitude smaller than for AM-100 were necessary to reconstruct images with acceptable quality. AM-100 and AM-700 represent two bounds of potential clinically relevant penalty parameter value choices: AM-100 is closer in shape to a quadratic penalty and AM-700 is closer in shape to a linear penalty. Results for δ values between 100 and 700 would reasonably be expected to lie between the two presented parameter values.

To evaluate the tradeoff between image noise and resolution, a set of images was reconstructed with varying log-cosh penalty Lagrange multipliers [α in Eq. (2)]. Here we use the term *smoothing strength* to refer to both the Lagrange multiplier α for the AM algorithm and the full-width at half maximum (FWHM) of the Gaussian-modified ramp filter in the FBP algorithm described in Sec. II A 2. For each data case, an unpenalized AM image is reconstructed as a performance baseline. Both penalty function parameter values of the alternating minimization algorithm were run for 250 iterations with 22 ordered subsets, used to increase the convergence rate.[21] The number of iterations was chosen from preliminary simulations that showed the images were well converged.

II.A.2. Filtered backprojection reconstruction

Weighted filtered backprojection as described in Kak and Slaney[1] is used to backproject the filtered fan beam projection data. The filter $H(f)$ is a modified ramp filter defined in frequency space as

$$H(f) = s \cdot |f| \cdot W(f) \cdot G(f). \tag{5}$$

Here s is a constant scale factor that ensures the image intensities represent the correct units of linear attenuation (mm^{-1}) and $|f|$ is the ramp function. The window function that causes the ramp filter to roll off at $f \geq 0.9 \cdot f_N$ (f_N =Nyquist frequency) with a raised cosine function to suppress high-frequency noise is given by

$$W(f) = \begin{cases} 1, & 0 \leq f < 0.9 \cdot f_N \\ 0.5 \cdot \left(1 + \cos\left(\frac{\pi \cdot (f - 0.9 \cdot f_N)}{0.1 \cdot f_N}\right)\right), & 0.9 \cdot f_N \leq f < f_N \\ 0, & f \geq f_N \end{cases}. \tag{6}$$

Figure 2 displays the windowed ramp filter. The cosine roll-off in the window function was incorporated to suppress high-frequency ringing artifacts observed in prior simulations at Washington University when a rectangular window function was employed. The frequency at which the cosine roll-off kicks in (90% of Nyquist) was chosen as the highest frequency that suppressed the ringing artifacts in order to retain as much high-frequency content as possible. When compared side-by-side to reconstructions from the proprietary Siemens FBP, trained observers were unable to distinguish which FBP implementation was used for each image. $G(f)$ is the Fourier transform of a Gaussian smoothing kernel that further reduces the amplitude of high spatial frequencies. A series of images with varying levels of noise and resolution is achieved by varying the FWHM of the Gaussian smoothing kernel. For consistency, the system matrix used

for the filtered backprojection algorithm is the same as that used for the penalized AM algorithm.

II.B. Simulated projection data

II.B.1. Virtual CT system

The virtual third generation CT system (Fig. 3) is composed of 1056 gantry positions (β) equally spaced around a full 360° rotation. There are 384 detectors (γ), each subtending an arc angle of 4.0625 min. The source-to-isocenter distance is 570 mm and the source-to-detector distance is 1005 mm. This gives a virtual detector width of 1.2 mm and a projected width at isocenter of 0.67 mm. The image space x is composed of 512×512 square pixels with a length of 0.5 mm on a side, providing a field-of-view (FOV) of 256 mm.

We simulate monoenergetic projection data with no scattering to avoid beam-hardening and scatter artifacts in the image reconstruction. Simulated projection data are generated by integrating the ray-traces through the analytically defined phantoms over the detector area

$$d(y:\mu) = I_0 \cdot \int_{\gamma'=\gamma-\Delta\gamma/2}^{\gamma'=\gamma+\Delta\gamma/2} \exp\left(-\sum_i \mu_i \cdot l_i(\gamma')\right) d\gamma' . \qquad (7)$$

The phantom image μ_i is defined as a superposition of i analytically defined ellipses. I_0 is the number of incident photons on the scan subject and $l_i(\gamma')$ is the analytical path length through the ith ellipse of uniform composition along the ray γ'. A data-model mismatch is present as the data are generated using an analytical forward projector and the reconstruction algorithms use discrete projection. The artifacts from this mismatch are minimal and methods to avoid contamination in the image noise and resolution metrics are discussed in Sec. II C.

Simple Poisson noise is included in the analytically ray-traced, noiseless sinogram data by randomly varying the incident photon fluence I_0. Though CT-signal statistics have been shown to follow the compound Poisson distribution,[22] previous literature has shown that approximating this more complex distribution by the simple Poisson distribution, assumed by AM, does not significantly affect image quality.[23] An incident fluence of 100 000 photons per detector leads to a percent standard deviation of ~0.3% for unattenuated source-detector rays, which approximates experimentally observed noise levels in projection data exported from our Philips Brilliance Big Bore CT simulator using a typical clinical scanning protocol (120 kVp, 325 mA s, and 0.75 mm slice thickness). To investigate the impact of projection noise on the noise-resolution tradeoff, noisy sinograms are generated for $I_0=25\,000$ photons per detector (25k projection noise case) and $I_0=200\,000$ photons per detector (200k projection noise case), which represent low dose and low noise imaging protocols, respectively. Noiseless projection data are also reconstructed with all algorithms and smoothing strengths for use in the quantification of noise and resolution.

II.B.2. Phantoms

Two simulation phantoms were used in this work to investigate the tradeoff between noise and resolution (Fig. 4). Both phantoms consist of a background 20 cm diameter water cylinder and various 2 cm diameter cylindrical inserts. The water background is set to $\mu=0.0205$ mm^{-1} corresponding to the 61 keV energy of our monoenergetic simulation. The main noise-resolution tradeoff comparison is made using the c*lock phantom*, which contains eight inserts of varying contrast. Each insert center is located 5.5 cm from the image FOV center. The clock phantom allows us to investigate the effect of varying contrast magnitudes on the noise-resolution tradeoff.

The *radial phantom* contains four contrast inserts at varying radial distances from the FOV center. Inserts with the same contrast (+30%) and varying distance from the FOV center (2–6.5 cm) allow us to investigate the spatial dependence of the noise-resolution tradeoff.

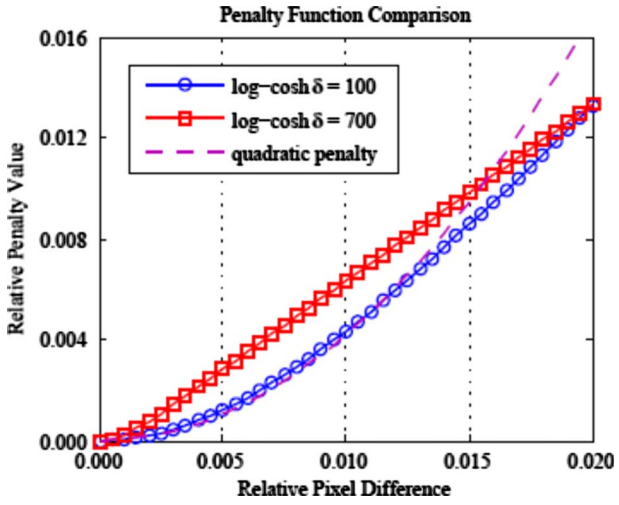

FIG. 1. Comparison of penalty function shape for the two log-cosh penalties investigated in this work and a quadratic penalty. Quadratic penalty functions grow too quickly for large pixel differences and consequently overblur high-contrast edges. Note that the log-cosh penalties are scaled (α) for plotting purposes and do not correspond to the values used in simulation.

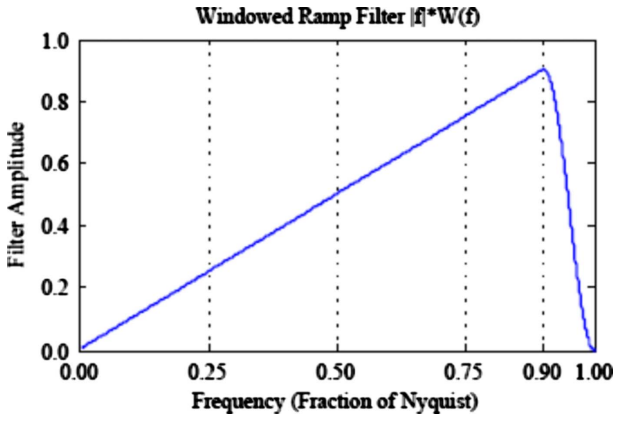

FIG. 2. Windowed ramp filter (no Gaussian smoothing kernel included). Ramp filter is rolled off for frequencies $\geq 90\%$ of f_N with a cosine function to suppress high-frequency noise. This filter was chosen in preliminary simulations to reconstruct images that are qualitatively indistinguishable from Siemens clinical images.

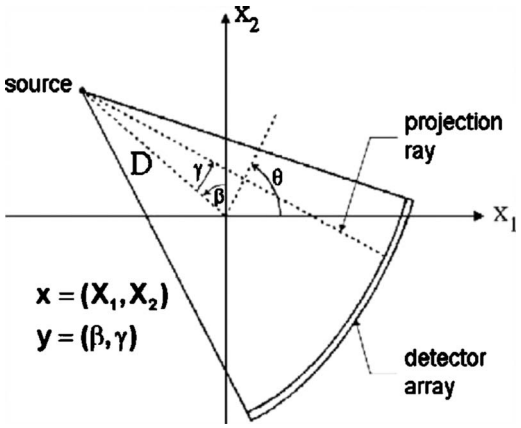

FIG. 3. Third generation virtual CT geometry. Square pixels, 0.5 mm on a side, compose the image space denoted by x. The rays connecting source angle β and detector index γ form the sinogram space y.

II.C. Noise and resolution measurement

II.C.1. Noise measurement

Image noise is assessed in the water region surrounding each contrast insert. For an image reconstructed from a noisy projection data set, the image noise is the standard deviation, as a percent of the water background value, for the pixels inside the noise region of interest (ROI):

$$\%\ \text{noise} = 100 \cdot \frac{\sigma_{\text{ROI}}}{\mu_{\text{water}}}. \tag{8}$$

The noise ROI for each insert is an annulus that includes image pixels in the water background lying within 4–6 mm (inclusive) of the insert boundary, shown in Fig. 5, containing 756 pixels. A subtraction image between the noiseless and noisy data reconstructions is used for the variance measurement to remove systematic bias, such as sampling artifacts, from the calculation.

To reduce computational burden, spatial statistics are used to quantify image noise in lieu of ensemble statistics. To test this, 30 monoenergetic data sets of the clock phantom, each with a different Poisson noise realization, were created and reconstructed with a single smoothing strength for each of the three algorithms. The ensemble noise in each image pixel for each algorithm was calculated from the resultant sequence of 30 images. The results of this comparison showed the use of spatial statistics within an annular ROI for noise quantification to be an adequate approximation of the average ensemble noise around each insert. The ensemble noise was seen to be slowly varying with radial distance from the FOV center, which is also shown in the radial phantom results of Sec. III D. The dependence of noise on distance from the insert edge was found to be negligible due to the circular symmetry of the ROI and slowly varying radial dependence of the noise.

An algorithm that can reconstruct an image of comparable resolution with less noise from the same projection data offers the clinical advantage of patient dose reduction. We assume that the image noise is proportional to relative projection noise[1,24] and that projection variance is inversely proportional to the patient dose. From these assumptions, we can formulate an answer to the question "For the same image noise and resolution, how much can the AM algorithms reduce patient dose in comparison to FBP?" We calculate the dose fraction as the ratio of AM variance to FBP variance at a constant resolution metric value

$$\text{dose fraction} = \frac{\sigma^2_{\text{AM}}}{\sigma^2_{\text{FBP}}}. \tag{9}$$

Intuitively, the ratio of variances, or dose fraction, represents the fraction of dose necessary for the AM algorithm to achieve the same image noise as the FBP algorithm with the same resolution metric for the chosen contrast insert.

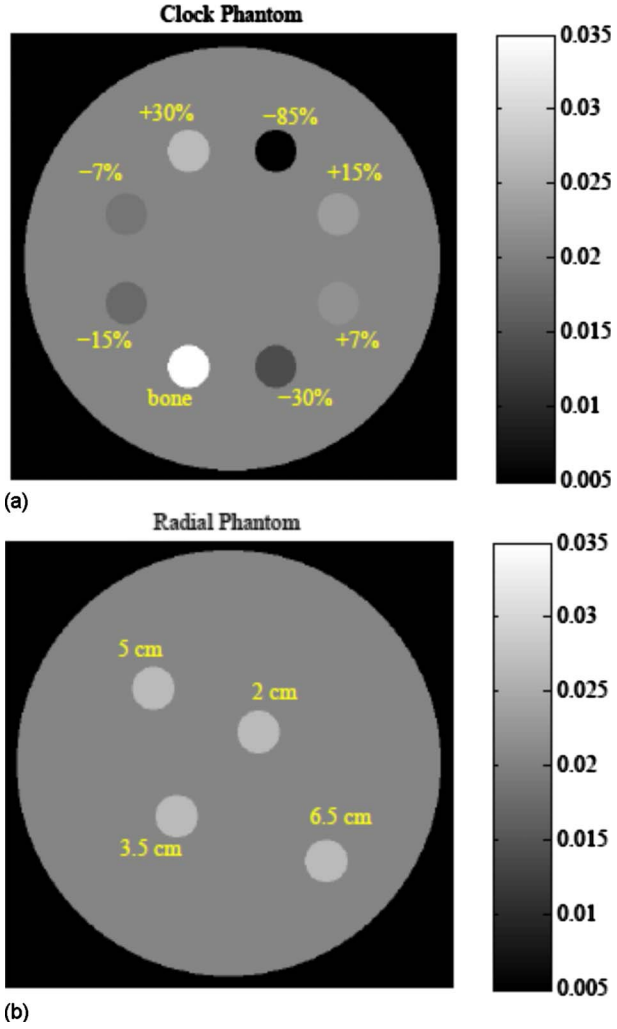

FIG. 4. Simulation phantoms consist of a 20 cm water cylinder with various 2 cm diameter contrast inserts. (a) The *clock phantom* with eight inserts of varying contrast allows comparison of the noise-resolution tradeoff for varying magnitude of contrast. (b) The *radial phantom* with four inserts of the same contrast (+30%) and varying distance from the FOV center allows the spatial dependence of the noise-resolution tradeoff to be investigated.

II.C.2. Resolution measurement

The resolution metric used in this work is based on the modulation transfer function (MTF). While x-ray transmission CT is not a shift-invariant linear system, we believe that

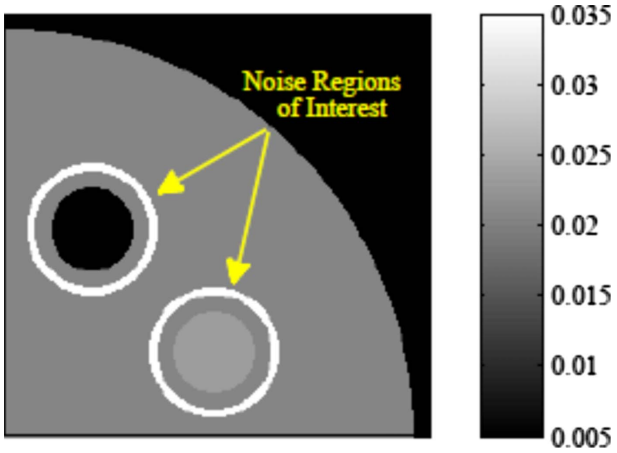

FIG. 5. Each insert's annular noise region of interest consists of the 756 image pixels whose centers lie between 4 and 6 mm from the insert boundary.

MTF analysis as a measure of local impulse response can still provide insight into the effect of reconstruction on edge blurring. The radial phantom study was designed to investigate the spatial variation of noise and resolution for each reconstruction algorithm.

The edge-spread function (ESF) was differentiated to obtain the line-spread function (LSF) and the Fourier transform of the LSF was calculated to obtain the MTF

$$\mathrm{LSF}(r) = \frac{d}{dr}(\mathrm{ESF}(r)), \tag{10}$$

$$\mathrm{MTF}(f) = |\mathrm{FT}(\mathrm{LSF}(r))|. \tag{11}$$

Here r is the distance between the pixel center and the known edge location. The circular symmetry of the contrast inserts can be used to construct a supersampled edge-spread function from the reconstructed image. Since our simulation phantom is comprised of a set of circular structures, we can plot each reconstructed image pixel's intensity as a function of the distance (r) between its center and the analytically defined insert edge. As multiple pixels will have the same distance to the edge, the mean intensity at each unique distance is calculated and used for subsequent estimation of the MTF. Sampling pixels around a circularly symmetric insert to form a supersampled edge-spread function represents an average of the edge response function within the region of interest. In this way, we can view the transition between the water background and the contrast insert. This idea of using circular symmetry to oversample an edge-spread function is similar to Thornton's use of a sphere[25] to measure the in-plane MTF and slice-sensitivity profile for a multislice CT scanner. Figure 6 displays a flowchart illustrating the resolution measurement technique for the −30% contrast insert reconstructed with FBP (FWHM=2.0 mm). The location of the analytically defined insert edge is superimposed on the reconstructed image to aid visualization.

An edge-spread function model was then fit to the supersampled ESF [$\mathrm{ESF}_{\mathrm{insert}}(r)$]. While the image noise is measured on images reconstructed from the noisy projection data sets, the edge-spread function is derived from images reconstructed from the noiseless projection data set to avoid bias from the image noise and to improve the model fitting. The model fitting is used to further reduce noise from the supersampled ESF prior to differentiation and Fourier transformation. Although ESFs are extracted from images reconstructed from noiseless projection data, the individual data points exhibit fluctuations due to effects such as partial volume averaging of finite voxels and the mismatch between data and reconstruction forward projectors. To avoid instability in the MTF arising from numerical differentiation of noisy data, we

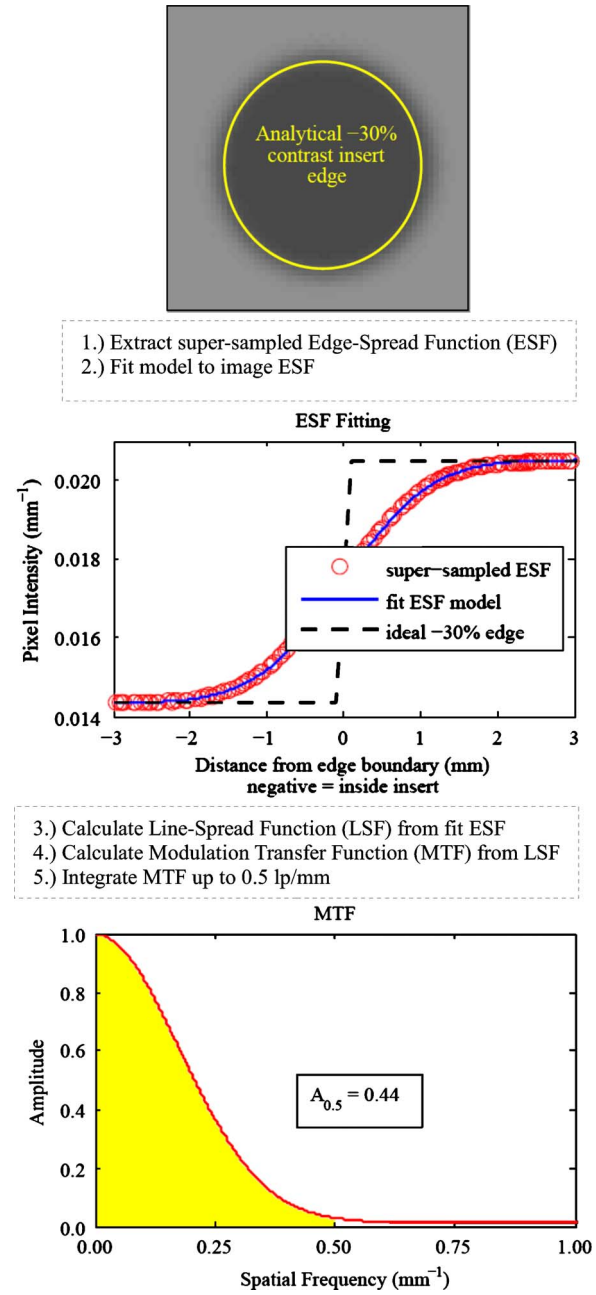

FIG. 6. Illustration of the resolution measurement for the −30% insert reconstructed using FBP with FWHM=2.0 mm.

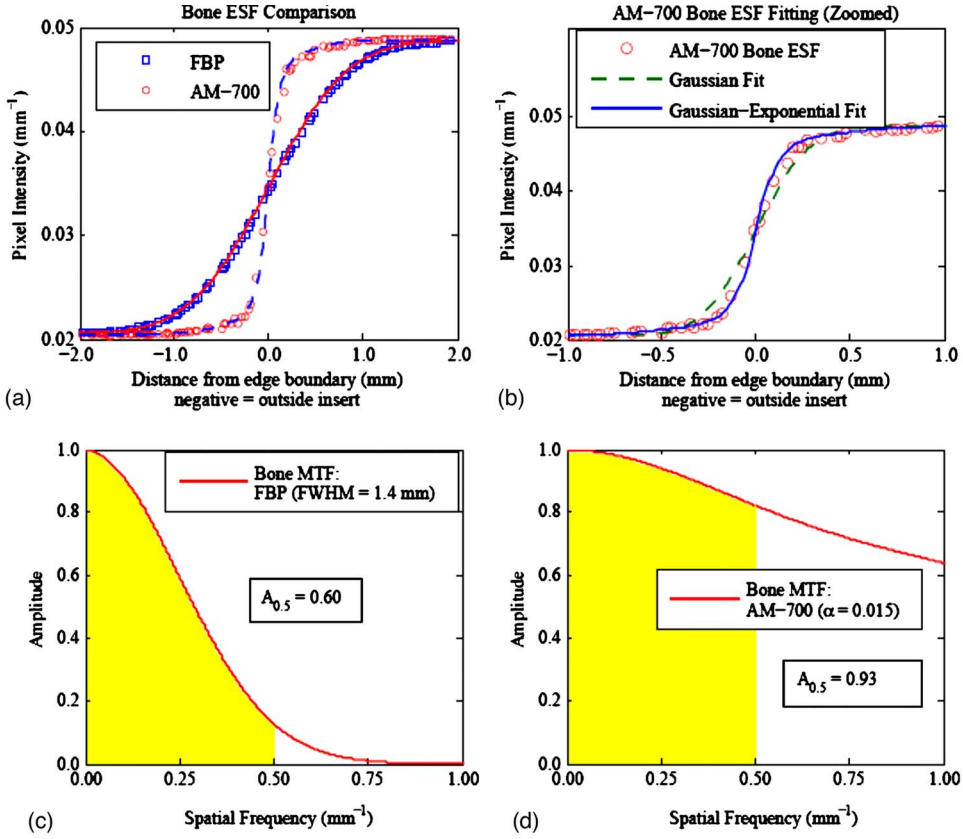

FIG. 7. (a) Comparison of the bone insert ESF shape for the FBP algorithm with FWHM=1.4 mm and the AM-700 algorithm with α=0.015. The corresponding lines represent the Gaussian-exponential model fit used for the estimation of the MTF. Smoothing strengths were chosen for comparison as they reconstructed nearly matched image noise ($\sim$1.09% $\pm$ 0.01%). Note the difference in ESF shape between the two algorithms in (a) at nearly matched image noise. The FBP edge-spread functions were found to be well fit by both Gaussian and Gaussian-exponential blurring models. (b) zooms in on the AM-700 ESF fitting to show that the Gaussian blurring model had trouble fitting the steep central transition and shoulder roll-off seen in the AM-700 high-contrast edges. This finding motivated the use of the Gaussian-exponential blurring model to fit all of the edge-spread functions in this work. (c) and (d) display the MTF calculation for the FBP and AM-700 bone inserts, respectively.

use an ESF model that assumes the line-spread function is well-described by a linear combination of Gaussian and exponential components[26]

$$\mathrm{ESF}^{\dagger}(r) = a \cdot \{1 - \exp(-b \cdot |r|)\} + c \cdot \{erf(d^{1/2} \cdot |r|)\}, \quad (12)$$

$$\mathrm{ESF}(r) = \begin{cases} \mathrm{ESF}^{\dagger}(r); & \text{if } r \geq 0 \\ -\mathrm{ESF}^{\dagger}(r); & \text{if } r < 0 \end{cases}, \quad (13)$$

$$\mathrm{ESF}_{\mathrm{fit}}(r) = e + f \cdot \mathrm{ESF}(r). \quad (14)$$

The MATLAB function *fminsearch* is used to find the six parameters $a-f$ that minimize the relative least-squares difference between the reconstructed image ESF and the ESF model. The second image in Fig. 6 shows the supersampled $\mathrm{ESF}_{\mathrm{insert}}(r)$ and the fitted model. All contrast inserts within an image are fitted separately. Each fitted ESF model is then differentiated to obtain the LSF, which is then Fourier transformed to calculate the MTF for the reconstructed contrast insert of interest.

To analyze the noise-resolution tradeoff for a particular reconstruction algorithm, i.e., how the image noise and resolution vary with increasing smoothing strength, it is useful to extract a single parameter to characterize resolution for each contrast insert in each image. This will allow us to plot a curve of how the edge resolution is degraded as the image noise is reduced. La Rivière[14] reported the FWHM of a Gaussian blurring model fitted to line profiles of high-contrast bone inserts. This is an intuitive metric as a wider Gaussian represents a blurrier edge. However, our six-parameter Gaussian-exponential model does not lead to such a straightforward metric.

We choose to report the area under the MTF curve up to 0.5 lp/mm as a single-value surrogate of edge resolution. The 0.5 lp/mm integration limit was chosen as it is near the frequency where MTF shapes differ the most between FBP and AM-700, as shown later in Fig. 7. It is also close to the ACR's accreditation requirement of 0.6 lp/mm for high-contrast resolution. The MTF area for a particular reconstructed insert edge is calculated as the area under the MTF up to 0.5 lp/mm or

$$A_{0.5} = \frac{\int_0^{0.5\ \mathrm{lp/mm}} \mathrm{MTF}(f)df}{0.5}. \quad (15)$$

The MTF area is normalized to 0.5, as this is the area under an ideal MTF curve that has amplitude 1.0 for all spatial

frequencies. Refer again to Fig. 6 for the calculated MTF and subsequent MTF area metric of an example contrast insert. Intuitively, the MTF area represents the fraction of ideal input signal that is recovered for spatial frequencies less than or equal to 0.5 lp/mm.

III. RESULTS

III.A. Necessity of Gaussian-exponential edge-spread function model

Previous investigators have characterized CT image resolution under the assumption of Gaussian blurring, e.g., the FWHM of a Gaussian ESF model[14] as a surrogate for resolution. Our preliminary work revealed that purely Gaussian blurring models did not fit the AM-700 high-contrast edges well. Figure 7 illustrates the different shapes of the high-contrast bone insert ESF and subsequent calculated MTFs as reconstructed with the FBP and AM-700 algorithms. The smoothing strengths of the noiseless FBP and AM-700 edge-spread functions in Fig. 7 were chosen for comparison as they led to nearly the same image noise ($\sim 1.09\% \pm 0.01\%$) when reconstructing the 100k noisy data set.

The steep central transition and shoulder roll-off of the AM-700 high-contrast edges was found to be poorly fit by a purely Gaussian blurring model [Fig. 7(b)] and motivated us to use the edge-spread function model [Eq. (12)], which assumes the blurring kernel has both Gaussian and exponential components. The Gaussian-exponential model was used to fit all reconstructed image edge-spread functions in this work to provide a consistent methodology. No loss of ESF fitting quality with the Gaussian-exponential model was seen for the edges that were well fit by the purely Gaussian model, such as all FBP edges, all AM-100 edges, and AM-700 low-contrast ($\leq 30\%$) edges.

In contrast with the FBP bone MTF [Fig. 7(c)], in which the amplitude quickly drops, the AM-700 bone MTF [Fig. 7(d)] shows an initial drop for low frequencies due to the rounded shoulder of the AM-700 ESF and retention of higher spatial frequencies due to the sharp central transition of the ESF. For high-contrast structures reconstructed by the AM-700 algorithm, the ESF and MTF shape were found to be markedly different than those seen in the literature.[15,16,25,27] Conventional MTF metrics, such as the spatial frequency corresponding to 10% MTF and 50% MTF, were found to provide poor characterization of the curves, given the long MTF tails of the high-contrast AM-700 structures. For example, the 10% MTF for AM-700 bone insert shown in Fig. 7(d) occurs at a frequency of 2.79 lp/mm, while the corresponding FBP MTF is essentially zero at this frequency. The desire for a single-valued metric that describes a clinically relevant feature common to all the MTF shapes characteristic of our study motivated our use of the MTF area as a surrogate for resolution.

III.B. Noise-resolution tradeoff for varying contrast

For each reconstructed clock phantom image, the relative noise in the water background and the MTF area were determined independently for each of the eight contrast inserts. Plotting the image noise as a function of resolution (MTF area) for a set of images reconstructed by a particular algorithm with varying levels of smoothing strength describes the noise-resolution tradeoff characteristic of the algorithm.

Figure 8 compares the noise-resolution tradeoff between the FBP algorithm and the AM algorithm, with $\delta = 100$ and $\delta = 700$ for images reconstructed from the 100k noisy projection data. The tradeoff curves for the clock phantom's eight contrast inserts are plotted separately to show how the tradeoff varies with the magnitude of contrast. Each point along a curve represents an image with a unique smoothing strength. For display purposes, the unpenalized AM images are not included on the AM tradeoff curves as the image noise is greater than 6% and reduces the scale of the noise axis. The noise in the water background around each contrast insert within a single reconstructed image is essentially the same. Thus, the differences seen in the AM tradeoff curves for varying magnitudes of insert contrast are due to differences in the resolution. This is a direct result of the nonquadratic local neighborhood penalty function. Also, note that the FBP algorithm appears to have a lower achievable resolution than AM; this is a result of the raised cosine roll-off windowed ramp function used for FBP in this work.

For all magnitudes of contrast, the AM tradeoff curves lie below the FBP algorithm curve. Both AM-100 and AM-700 reconstruct images with either less image noise for the same resolution metric, sharper edges for matched image noise or, by extension, images with similar resolution and image noise for less patient dose. The AM-700 algorithm shows an increasing benefit as the contrast magnitude used for resolution comparison is increased. The clock phantom study shows us that the noise-resolution tradeoff advantage of the penalized AM algorithm in comparison with conventional FBP is dependent on the contrast magnitude used for resolution calculation and the choice of parameter value for AM's edge-preserving penalty function.

III.C. Effect of projection noise magnitude

As outlined in Sec. II C 1, the potential for dose reduction that the AM algorithm offers is calculated as the ratio of AM-insert variance to FBP-insert variance when matching the resolution metric for a chosen contrast insert. By applying spline interpolation to the tradeoff curves of Fig. 8, FBP and AM noise levels for a matched resolution metric of $A_{0.5} = 0.75$ were estimated. The resulting AM-to-FBP variance ratio (for all three projection noise realizations) is plotted as a function of contrast in Fig. 9. The magnitude of projection noise investigated in the three noise realizations does not appear to have a marked effect on the advantage of the AM algorithm. The maximum impact of low dose (25k) and low noise (200k) imaging techniques relative to 100k is seen for the AM-700 low-contrast structures ranging from 0.66 to 0.81 [Fig. 9(b)]. This variation was overshadowed by the variation due to contrast magnitude for the AM-700 algorithm, for which the variance ratio ranges from 0.69 to 0.05 (100k projection noise realization). Figure 9 shows that

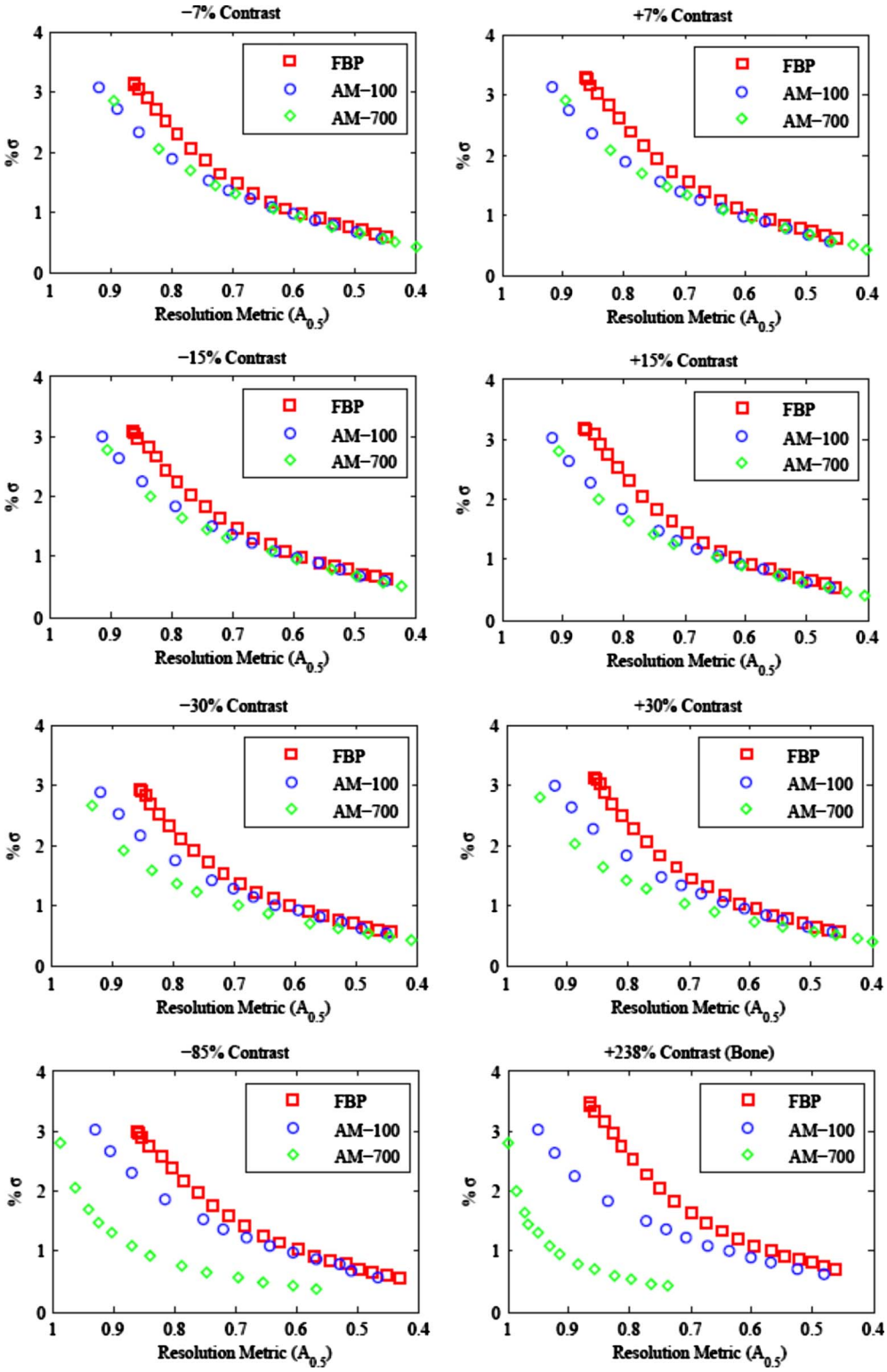

FIG. 8. Noise-resolution tradeoff curves for the clock phantom reconstructed with 100k projection noise. Note the reverse x-axis. As the smoothing strength is increased, noise is reduced at the cost of reduced resolution. The tradeoff curve for AM with δ=700 for the penalty function is markedly different for structures of varying contrast.

the potential for dose reduction is largely driven by the contrast magnitude chosen for matching image resolution.

III.D. Spatial dependence of noise-resolution tradeoff

The dependence of resolution, noise, and variance ratio on spatial location is illustrated in Figs. 10 and 11. Within a single reconstructed image, FBP noise varies more with FOV location than the AM image noise [Fig. 10(a)]. In contrast, Fig. 10(b) shows that AM resolution increases with distance from the FOV center, while FBP resolution is nearly spatially constant. Figure 11 shows the spatial variation of noise and variance ratios for AM and FBP images with a matched spa-

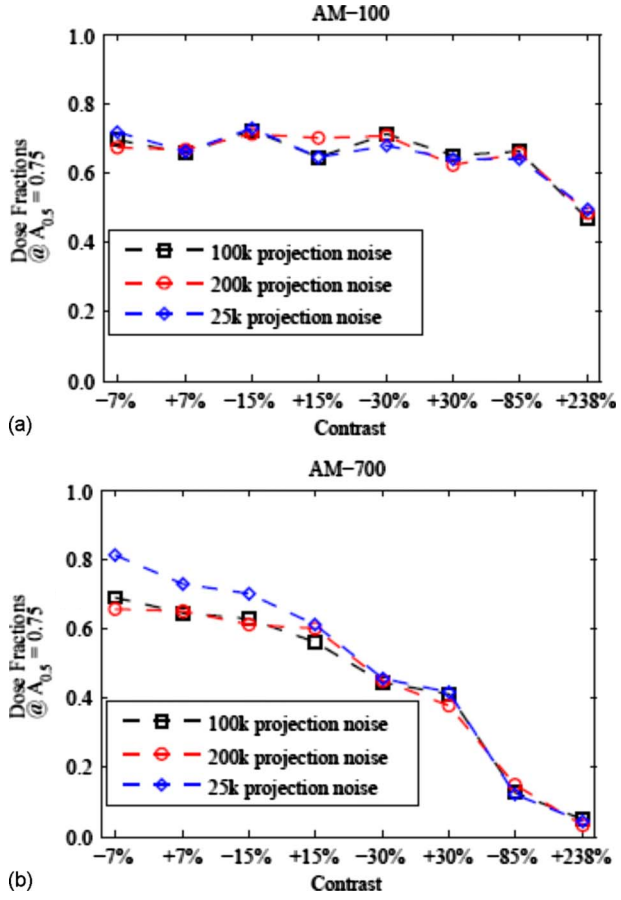

FIG. 9. AM/FBP variance ratio at a matched resolution value of $A_{\mathrm{MTF0.5}}=0.75$ for each of the eight inserts of the clock phantom. (a) and (b) display the results for AM-100 and AM-700, respectively. The 100k projection noise case is plotted as the baseline with the low noise (200k) and low dose (25k) cases plotted for comparison. As can be seen, the three noise realizations cause some variability in the dose fractions, but this is overshadowed by the choice of penalty function parameter values and contrast magnitude effects.

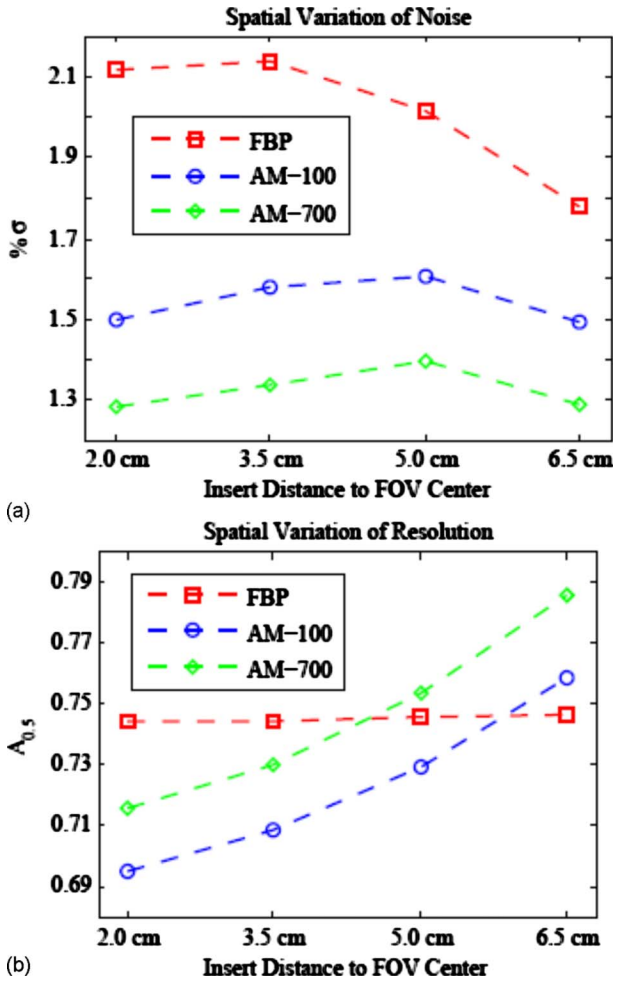

FIG. 10. Results of the radial phantom study showing the spatial dependence of (a) noise and (b) resolution within a single reconstructed image from each algorithm. The smoothing strengths were chosen such that the resolution metric for the reconstruction algorithms were similar for purposes of comparison. The AM resolution increases with distance from the FOV center, while the FBP algorithm's resolution does not. FBP image noise varies more spatially than for the AM algorithm.

tial resolution metric of $A_{0.5}=0.75$. For all algorithms, resolution-matched image noise decreases with increasing distance from the FOV center. This is not surprising, as the projection noise for the peripheral insert locations is smaller due to a shorter average path length through the phantom for the source-detector rays that traverse the peripheral image pixels. The dose fraction of the AM algorithm is nearly the same for all four insert locations [Fig. 11(b)] with dose fractions ranging from 0.65 to 0.70 for AM-100 and from 0.41 to 0.45 for AM-700.

III.E. Reconstructed image comparison

Figure 12 shows images of the simulated clock phantom reconstructed from the 100k noisy data set with similar resolutions ($A_{0.5}\sim 0.75$) around the high-contrast bone insert. The AM-700 image noise level is only 25% of that of the FBP image. While the AM-700 high-contrast resolution metric value nearly matches that of the FBP images, the low-contrast inserts exhibit subjectively poorer resolution than that of the FBP algorithm. In comparison, the AM-100 algorithm was found to offer comparable resolution to the FBP for all contrast inserts, with about 70% of the noise relative to FBP.

Note the presence of an artifact around the phantom edge in the AM images [Figs. 12(b) and 12(c)]. The literature[9,28] has shown these artifacts are in fact inherent to maximum likelihood reconstruction methods and arise from mismatches between the SIR algorithm's forward model and the true physical detection process. Zbijewski[28] shows that reconstructing on a finer voxel grid alleviates much of the edge artifact, but this will lead to much longer computing times. While the smallest penalty strength (α_{min}) was found to eliminate the edge artifact around the internal contrast inserts for both AM-100 and AM-700, further work will be needed to address the ringing artifact around the phantom edge if it is determined to be of clinical concern.

III.F. Qualitative real data comparison

Real CT data includes effects from physical phenomena such as beam-hardening and scatter, which are known to de-

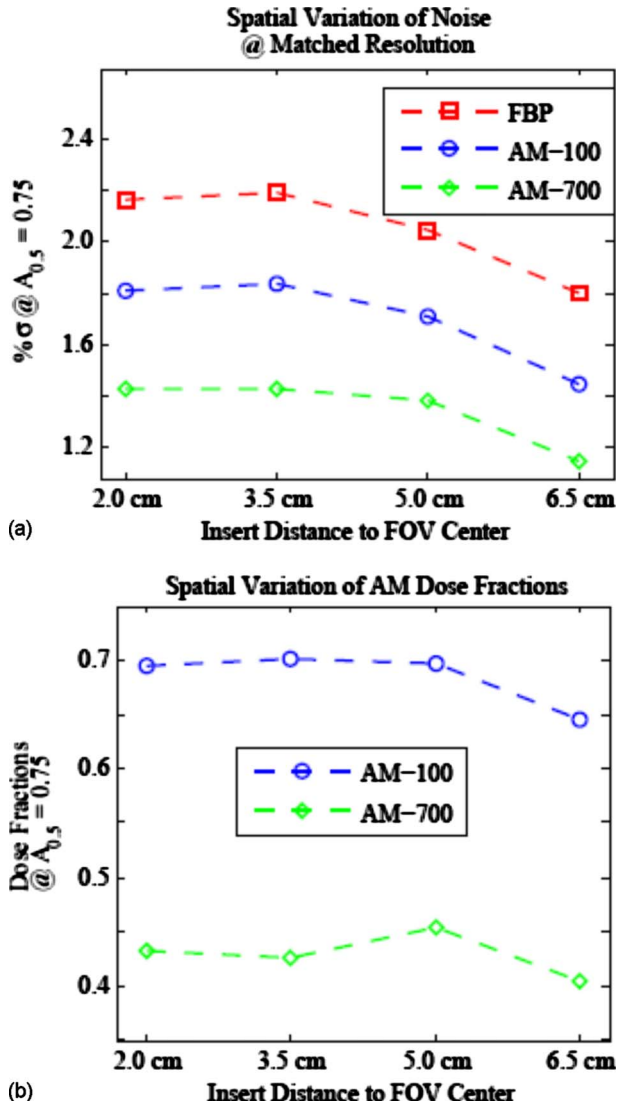

FIG. 11. Comparison of the noise-resolution tradeoff for varying distance from FOV center. When compared at matched resolution (noise interpolated to matched $A_{0.5}=0.75$), (a) the FBP and AM algorithms show similar variation of noise across the FOV and (b) the dose fraction stays nearly constant for all inserts.

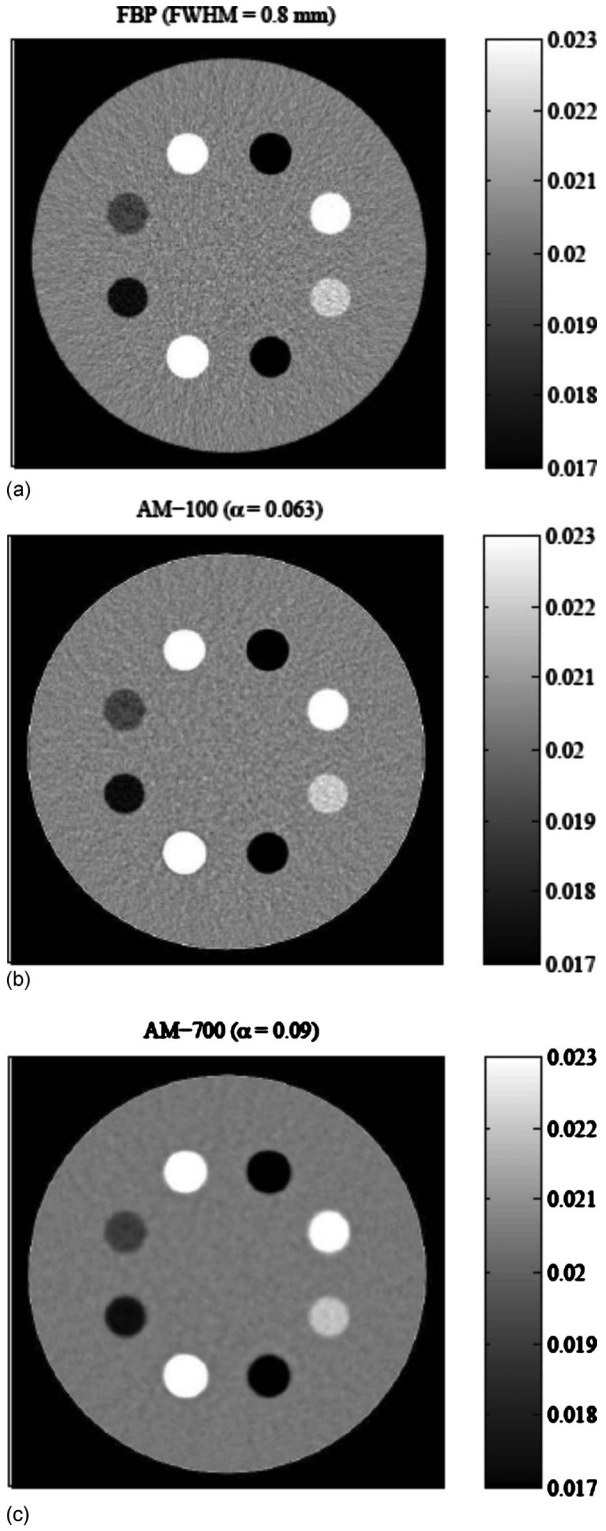

FIG. 12. Reconstructed images of the simulated clock phantom data with nearly matched bone insert (7 o'clock position) resolution metric of $A_{0.5} \sim 0.75$. All images set to identical ±15% window [0.017:0.023] mm^{-1} for display of image noise. Noise around the bone insert is (a) 2.04% for FBP, (b) 1.36% for AM-100, and (c) 0.47% for AM-700.

grade image quality. Figure 13 illustrates the ability of the penalized AM algorithm to reconstruct images from axial sinograms acquired on the Philips Brilliance Big Bore scanner. Smoothing strengths for the three reconstructions were tuned to give nearly the same noise in a 2×2 cm^2 square ROI (1600 total pixels) in the center of the water region. For the low-contrast detectability insert (6 o'clock) differences among the three reconstructions could not be visually discerned. However, profiles through the high-contrast insert, located at 4 o'clock, reveal sharper edge discrimination for the AM-700 algorithm [Fig. 13(b)], which motivates future work to investigate the noise-resolution tradeoff using real CT data.

IV. DISCUSSION

This work compares the noise-resolution tradeoff of the conventional filtered backprojection algorithm to that of the alternating minimization algorithm with two different parameter values for a local edge-preserving penalty function. This is not the first work comparing the noise-resolution tradeoff between filtered backprojection and statistical iterative algo-

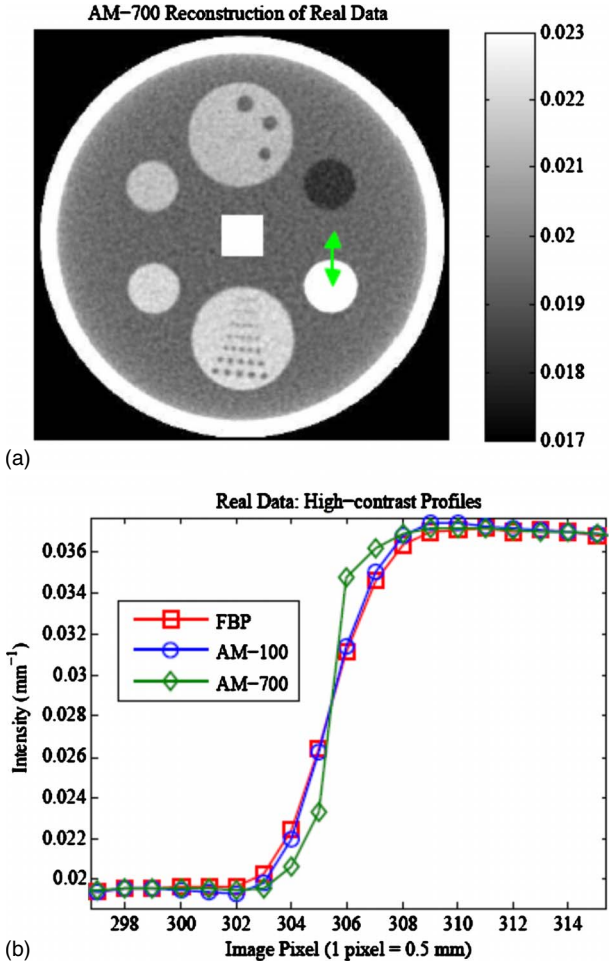

FIG. 13. (a) AM-700 reconstructed image of the multipin layer of a daily QA phantom from real data acquired on a Philips Brilliance Big Bore CT scanner. Smoothing strengths were adjusted to match noise (~0.94% in the central square ROI) within 0.005% among the AM-700, AM-100, and FBP images. (b) Visible differences in the high-contrast insert (4 o'clock) are illustrated in the profiles.

rithms. However, it is the first to do so for the alternating minimization algorithm for x-ray transmission tomography, which supports an exact solution to the maximization of the Poisson log-likelihood (M-step). The conclusions from the simulation study presented here could reasonably be extrapolated to other SIR algorithms that seek to maximize the same penalized-likelihood objective function, since the AM solution images are very near complete convergence due to the large number of iterations employed. It is also the first, to the best of the authors' knowledge, to characterize the noise-resolution tradeoff curves and subsequent dose-reduction factors for a range of contrast magnitudes.

In this paper, we selected the normalized MTF integral up to a cutoff frequency of 0.5 lp/mm as a convenient, but somewhat arbitrary, single-parameter metric for quantifying spatial resolution. Other integration limits up to the Nyquist frequency were considered but were found to increase the reported AM-700 advantage due to AM-700's longer MTF tails for high-contrast structures. For comparing FBP and AM resolution, the 0.5 lp/mm limit was chosen to ensure significant overlap of the nonzero frequency content of the corresponding MTFs, which potentially have very different shapes and high-frequency tails. This limit was considered to be a conservative choice for reporting dose-reduction potential. While in theory the MTF is a linear-systems metric and CT resolution is known to be spatially variant over the FOV,[29] we believe that a MTF derived from a supersampled edge-spread function objectively describes the spatial frequency content in the local region. The concept of measuring the MTF for structures within a CT image dates back three decades[27] and is still a topic of debate to this day. To the author's knowledge, no gold standard metric for quantifying CT image resolution has been embraced by the community, making direct comparison of our results and other works difficult.

Not surprisingly, the log-cosh penalized alternating minimization algorithm, which models detector counting statistics, reconstructs images with less noise than conventional filtered backprojection images of comparable resolution. In contrast with other investigations that matched high-contrast structure resolution, e.g., bone and steel beads, our study shows that the noise-resolution tradeoff for nonquadratic neighborhood penalty functions markedly varies with contrast magnitude of the edge used for quantifying resolution. The apparent advantage of using the log-cosh penalized AM algorithm when comparing high-contrast resolution was found to be moderately to substantially diminished when the resolutions of low-contrast edges were compared. Moreover, this variation was found to strongly depend on the chosen penalty function parameters.

Despite some loss of benefit for low-contrast objects, the ratio of variances for high-contrast objects in this work implies that the penalized AM algorithm is capable of reconstructing images with comparable quality to FBP using 10%–70% of the dose required by FBP, depending on the penalty function parameters (Fig. 9). This is compatible with the growing clinical literature; Stayman[30] reported SIR-to-FBP image SNR ratios of about 1.6 for a PET system. For x-ray transmission CT, Ziegler[15] reported SIR-to-FBP noise ratios of 2.1 to 3.0, implying dose-reduction factors of 4.4 to 9.0. La Rivière[14] described an expectation-maximization sinogram smoothing technique which achieved a noise-resolution tradeoff similar to the adaptive trimmed mean filter approach[2] that uses 50% less dose. These studies exhibit a range of dose-reduction factors for a number of reasons. Since the dose-reduction factor is a ratio of variances at an arbitrary value of the resolution metric, choosing a different value of the resolution metric along the noise-resolution tradeoff curve for matching will change the reported variance ratios. In addition, there are differences between the SIR and the FBP reconstruction algorithms used in the literature and the metrics used to quantify resolution. In spite of these differences, our reported dose-reduction potentials for high-contrast structures are in reasonable agreement with the published literature.

Varying the magnitude of noise in the projection data was found to only minimally affect the variance ratio at a matched spatial resolution in our simulations (Fig. 9). In con-

trast, Ziegler *et al.*[15] showed that projection noise level does affect the SIR-to-FBP noise ratio. His work further showed that this effect was stronger for points farther from the FOV center than those near the center. Our range of distances from the FOV center (2–6.5 cm) was much smaller than those in Ziegler's work (1.5–20 cm). We found the contrast magnitude and penalty parameter choice to have a greater effect on the variance ratio than projection noise.

As our work utilized a spatially invariant penalty function, it would be expected that AM images exhibit spatially variant and anisotropic resolution.[29] Our study of the radial phantom shows that the resolution and noise vary differently with distance from the FOV center of AM and FBP images (Fig. 10). In contrast with studies that report FBP resolution to degrade with increasing distance,[15] the FBP algorithm in this work showed little spatial variation of resolution. This difference could stem from slight differences in the FBP algorithm or the larger range of distances to FOV center that Ziegler investigated. The variation of AM resolution with distance from the FOV center [Fig. 10(b)] illustrates the nonuniform nature of the AM resolution. Interestingly, we found the AM-to-FBP variance ratio for a fixed resolution to be approximately constant over the FOV (Fig. 11).

Resolution anisotropy was studied by separating the total annular ROIs around the insert edges in the radial phantom into four Cartesian quadrants and calculating the associated MTFs using the same procedure described above. The quadrant MTFs in the FBP image were found to vary little from the MTF of the total ROI. The penalized AM quadrant MTFs were found to vary from one another, especially in the tangential and radial directions, indicative of anisotropic resolution. The AM anisotropies were found to be small compared to the differences between the AM and FBP algorithms, perhaps in part due to the highly symmetric nature of the phantoms investigated here. The resolution metric calculated from the total annular ROI represents an average of the local resolution in the region surrounding each contrast insert.

Methods for designing spatially variant quadratic penalty functions that achieve a target response have been described in the literature and shown to support nearly uniform and isotropic resolution for PET and transmission x-ray CT problems.[30–32] Ahn and Leahy[33] reported on the design of nonquadratic regularization penalties with similar goals in PET.[33] Design of penalty functions, both quadratic and nonquadratic, that include the ideas of spatially variant[29] and nonlocal penalty functions[20] to achieve desirable properties such as uniform, isotropic resolution are important areas of ongoing work for x-ray transmission CT.

The quantitative results presented in this work have been performed exclusively in an idealized 2D x-ray CT simulation environment, with projection noise assumed to follow the simple Poisson distribution. While this data model allows detection of very subtle effects of reconstruction algorithm on noise-resolution tradeoffs, obviously clinical translation requires handling complex detector nonlinearities and nonideal behaviors. Both the AM (Ref. 13) and parabolic surrogates[34] SIR algorithms generalize to more complex data models which include polyenergetic spectra, scatter, and correlated noise, all of which are necessary to extract statistically optimal smoothed images from measured sinogram data. SIR algorithms including the known polyenergetic x-ray spectrum in their forward model have been shown to outperform FBP reconstruction preceded by sinogram linearization corrections in terms of nonuniformity from beam-hardening artifacts.[35] Our example clinical case (Fig. 13) suggests (but by no means proves) that our main conclusions are preserved, at least qualitatively, in the transition to more realistic data models. Beam-hardening and scatter effects manifest themselves as artifacts, i.e., systematic shifts in the mean image intensities. While such streaking and nonuniformity artifacts caused by these data mismatches play a large role in subjective image quality and quantitative CT, we would not expect these nonlinear processes to substantially affect the spatial resolution-noise tradeoff characteristic of the device. The logical next step in translating AM benefits to quantitative CT imaging to the clinic is to repeat systematic studies of resolution-noise tradeoff using more realistic data models and experimentally acquired data sets derived from scanning phantoms of known geometry and composition. Another issue is the incorporation of 3D system geometry (spiral multirow detector geometry) into the forward SIR projector. 3D SIR algorithms have been shown to alleviate CBCT artifacts, e.g., incomplete data artifacts in off-axis planes) characteristic of conventional FBP reconstruction.[17] However, the Shi and Fessler[36] design of three-dimensional penalty functions pose challenges, providing another important area of future investigation.

Long SIR computing times constitute another barrier to widespread clinical acceptance. Recent literature describing GE's adaptive statistical iterative reconstruction (ASIR) algorithm shows that simplified statistical algorithms can still provide diagnostically viable images with 50% or 65% smaller doses than needed for conventional FBP.[37–39] While the ASIR algorithm does not include modeling of the system matrix, which can play a large role in reducing artifacts and noise,[16,17] trained observers have rated the ASIR images acquired at 50% of the FBP dose to have similar, if not better, image quality for almost all metrics studied. The literature has shown that the simplified ASIR algorithm has the capability to reconstruct image volumes acceptable to current trained observers in a clinically relevant timeframe of 65 s compared to 50 s for FBP.[39] For the AM algorithm, Keesing *et al.*[40,41] has demonstrated the feasibility of speeding up the computation time by parallelizing the projection operations for a fully 3D helical geometry.

Comparing the AM-100 and AM-700 results reveals the importance of optimizing the nonquadratic penalty function parameter δ. AM-700, with a penalty that transitions to linear growth for smaller pixel differences, shows greatly improved noise performance over AM-100 and the FBP algorithm when comparing high-contrast resolution. However, when comparing images with nearly matched high-contrast resolution metric values, AM-700 was seen to have worse resolution for the low-contrast inserts. The log-cosh penalty function with δ=700 could be beneficial where high-contrast

resolution is important and reduced low-contrast resolution is acceptable, e.g., for dose reduction in image registration applications using bony landmarks. For clinical situations in which low-contrast resolution is important, for example, intensity-driven soft-tissue deformable image registration or soft-tissue delineation for contouring, log-cosh penalized AM with $\delta=100$ could provide comparable image quality with 70% of the FBP dose. The results presented here show the need for future work in penalty function parameter optimization and those choices will certainly be task-specific.[42]

V. CONCLUSIONS

This work assessed the noise-resolution tradeoff of the penalized alternating minimization algorithm in comparison with FBP for a set of structures with a range of contrast magnitudes (±7% to +238%) and varying distance from the FOV center (2–6.5 cm). An idealized simulation environment was used to isolate the effects of each algorithm's smoothing technique. A spatial resolution metric $A_{0.5}$, derived from ESFs in the reconstructed image, was developed in response to the observation that the AM-700 MTF shape for high-contrast edges deviates significantly from that of FBP images. The parameter value used to specify AM's local log-cosh penalty function has been shown to drastically modulate noise-resolution tradeoff curves and subsequent dose-reduction potentials reported for SIR algorithms. The noise-resolution tradeoff was also found to be greatly affected by the contrast of the structure used for evaluating spatial resolution. The range of projection noise levels investigated here and the variation in structure distance from FOV center only minimally affected the noise-resolution tradeoff. The ratio of AM-to-FBP image variance ratio for matched resolution surrogate implies a dose-reduction potential; the AM algorithm has the potential to reconstruct images with comparable noise and MTF area using only 10%–70% of the FBP dose. These values are in line with other published literature. The result that log-cosh penalized AM noise-resolution tradeoff is dependent on the contrast magnitude implies that nonquadratic penalty function parameters can be optimized to maximize the dose-reduction potential for specific imaging tasks.

ACKNOWLEDGMENTS

This work was supported in part from Grant Nos. R01 CA 75371, P01 CA 116602, and 5P30 CA 016059 awarded by the National Institutes of Health.

[a]Authors to whom correspondence should be addressed.
[b]Electronic mail: evansjd4@mymail.vcu.edu
[c]Electronic mail: jwilliamson@mcvh-vcu.edu; Telephone: 804-828-8451; Fax: 804-827-1670.

[1]A. C. Kak and M. Slaney, *Principles of Computerized Tomographic Imaging* (IEEE, New York, 1988).
[2]J. Hsieh, "Adaptive streak artifact reduction in computed tomography resulting from excessive x-ray photon noise," Med. Phys. **25**(11), 2139–2147 (1998).
[3]M. Endo, T. Tsunoo, N. Nakamori, and K. Yoshida, "Effect of scattered radiation on image noise in cone beam CT," Med. Phys. **28**(4), 469–474 (2001).
[4]P. M. Joseph and R. D. Spital, "The effects of scatter in x-ray computed tomography," Med. Phys. **9**(4), 464–472 (1982).
[5]P. M. Joseph and R. D. Spital, "A method for correcting bone induced artifacts in computed tomography scanners," J. Comput. Assist. Tomogr. **2**(1), 100–108 (1978).
[6]P. M. Joseph and R. D. Spital, "The exponential edge-gradient effect in x-ray computed tomography," Phys. Med. Biol. **26**(3), 473–487 (1981).
[7]K. Lange and R. Carson, "EM reconstruction algorithms for emission and transmission tomography," J. Comput. Assist. Tomogr. **8**(2), 306–316 (1984).
[8]J. A. Fessler, "Statistical image reconstruction methods for transmission tomography," in *Medical Image Processing and Analysis*, Handbook of Medical Imaging, Vol. 2, edited by M. Sonka and J. M. Fitzpatrick (SPIE, Bellingham, 2000), pp. 1–70.
[9]D. L. Snyder, M. I. Miller, L. J. Thomas, and D. G. Politte, "Noise and edge artifacts in maximum-likelihood reconstructions for emission tomography," IEEE Trans. Med. Imaging **6**(3), 228–238 (1987).
[10]C. L. Byrne, "Iterative image reconstruction algorithms based on cross-entropy minimization," IEEE Trans. Image Process. **2**(1), 96–103 (1993).
[11]D. J. Brenner and E. J. Hall, "Computed tomography—An increasing source of radiation exposure," N. Engl. J. Med. **357**(22), 2277–2284 (2007).
[12]J. F. Williamson, S. Li, S. Devic, B. R. Whiting, and F. A. Lerma, "On two-parameter models of photon cross sections: Application to dual-energy CT imaging," Med. Phys. **33**(11), 4115–4129 (2006).
[13]J. A. O'Sullivan and J. Benac, "Alternating minimization algorithms for transmission tomography," IEEE Trans. Med. Imaging **26**(3), 283–297 (2007).
[14]P. J. La Rivière, "Penalized-likelihood sinogram smoothing for low-dose CT," Med. Phys. **32**(6), 1676–1683 (2005).
[15]A. Ziegler, T. Kohler, and R. Proksa, "Noise and resolution in images reconstructed with FBP and OSC algorithms for CT," Med. Phys. **34**(2), 585–598 (2007).
[16]J. Sunnegårdh and P. E. Danielsson, "Regularized iterative weighted filtered backprojection for helical cone-beam CT," Med. Phys. **35**(9), 4173–4185 (2008).
[17]J. B. Thibault, K. D. Sauer, C. A. Bouman, and J. Hsieh, "A three-dimensional statistical approach to improved image quality for multislice helical CT," Med. Phys. **34**(11), 4526–4444 (2007).
[18]I. Csiszar, "Why least squares and maximum entropy? An axiomatic approach to inference for linear inverse problems," Ann. Stat. **19**, 2032–2066 (1991).
[19]P. J. Green, "Bayesian reconstructions from emission tomography data using a modified EM algorithm," IEEE Trans. Med. Imaging **9**(1), 84–93 (1990).
[20]D. F. Yu and J. A. Fessler, "Edge-preserving tomographic reconstruction with nonlocal regularization," IEEE Trans. Med. Imaging **21**(2), 159–173 (2002).
[21]H. M. Hudson and R. S. Larkin, "Accelerated image reconstruction using ordered subsets of projection data," IEEE Trans. Med. Imaging **13**(4), 601–609 (1994).
[22]B. R. Whiting, P. Massoumzadeh, O. A. Earl, J. A. O'Sullivan, D. L. Snyder, and J. F. Williamson, "Properties of preprocessed sinogram data in x-ray computed tomography," Med. Phys. **33**(9), 3290–3303 (2006).
[23]G. M. Lasio, B. R. Whiting, and J. F. Williamson, "Statistical reconstruction for x-ray computed tomography using energy-integrating detectors," Phys. Med. Biol. **52**(8), 2247–2266 (2007).
[24]D. Chesler, S. Riederer, and N. Pelc, "Noise due to photon counting statistics in computed x-ray tomography," J. Comput. Assist. Tomogr. **1**(1), 64–74 (1977).
[25]M. M. Thornton and M. J. Flynn, "Measurement of the spatial resolution of a clinical volumetric computed tomography scanner using a sphere phantom," Proc. SPIE **6142**, 707–716 (2006).
[26]J. M. Boone and J. A. Seibert, "An analytical edge spread function model for computer fitting and subsequent calculation of the LSF and MTF," Med. Phys. **21**(10), 1541–1545 (1994).
[27]P. F. Judy, "The line spread function and modulation transfer function of a computed tomographic scanner," Med. Phys. **3**(4), 233–236 (1976).
[28]W. Zbijewski and F. J. Beekman, "Characterization and suppression of edge and aliasing artefacts in iterative x-ray CT reconstruction," Phys. Med. Biol. **49**(1), 145–157 (2004).
[29]J. A. Fessler and W. L. Rogers, "Spatial resolution properties of penalized-likelihood image reconstruction: Space-invariant tomographs," IEEE Trans. Image Process. **5**(9), 1346–1358 (1996).

[30]J. W. Stayman and J. A. Fessler, "Compensation for nonuniform resolution using penalized-likelihood reconstruction in space-variant imaging systems," IEEE Trans. Med. Imaging **23**(3), 269–284 (2004).
[31]H. R. Shi and J. A. Fessler, "Quadratic regularization design for 2-D CT," IEEE Trans. Med. Imaging **28**(5), 645–656 (2009).
[32]J. W. Stayman and J. A. Fessler, "Regularization for uniform spatial resolution properties in penalized-likelihood image reconstruction," IEEE Trans. Med. Imaging **19**(6), 601–615 (2000).
[33]S. Ahn and R. M. Leahy, "Analysis of resolution and noise properties of nonquadratically regularized image reconstruction methods for PET," IEEE Trans. Med. Imaging **27**(3), 413–424 (2008).
[34]K. Lange and J. A. Fessler, "Globally convergent algorithms for maximum a posteriori transmission tomography," IEEE Trans. Image Process. **4**(10), 1430–1438 (1995).
[35]C. H. Yan, R. T. Whalen, G. S. Beaupre, S. Y. Yen, and S. Napel, "Reconstruction algorithm for polychromatic CT imaging: Application to beam hardening correction," IEEE Trans. Med. Imaging **19**(1), 1–11 (2000).
[36]H. R. Shi and J. A. Fessler, "Quadratic regularization design for iterative reconstruction in 3D multi-slice axial CT," in Proceedings of the IEEE Nuclear Science Symposium, 2006 (unpublished).
[37]A. K. Hara, R. G. Paden, A. C. Silva, J. L. Kujak, H. J. Lawder, and W. Pavlicek, "Iterative reconstruction technique for reducing body radiation dose at CT: Feasibility study," AJR, Am. J. Roentgenol. **193**(3), 764–771 (2009).
[38]P. Prakash, M. K. Kalra, A. K. Kambadakone, H. Pien, J. Hsieh, M. A. Blake, and D. V. Sahani, "Reducing abdominal CT radiation dose with adaptive statistical iterative reconstruction technique," Invest. Radiol. **45**(4), 202–210 (2010).
[39]A. C. Silva, H. J. Lawder, A. Hara, J. Kujak, and W. Pavlicek, "Innovations in CT dose reduction strategy: Application of the adaptive statistical iterative reconstruction algorithm," AJR, Am. J. Roentgenol. **194**(1), 191–199 (2010).
[40]D. B. Keesing, J. A. O'Sullivan, D. G. Politte, and B. R. Whiting, "Parallelization of a fully 3D CT iterative reconstruction algorithm," in Proceedings of the IEEE International Symposium on Biomedical Imaging, pp. 1240–1243, 2006 (unpublished).
[41]D. B. Keesing, J. A. O'Sullivan, D. G. Politte, B. R. Whiting, and D. L. Snyder, "Missing data estimation for fully 3D spiral CT image reconstruction," in Proceedings of SPIE: Medical Imaging 2007: Physics of Medical Imaging, San Diego, CA, 2007 (unpublished).
[42]P. Sprawls, "AAPM tutorial. CT image detail and noise," Radiographics **12**(5), 1041–1046 (1992).

Appendix 3

Effect of contrast magnitude and resolution metric on noise-resolution tradeoffs in x-ray CT imaging: a comparison of non-quadratic penalized alternating minimization and filtered backprojection algorithms

Effect of contrast magnitude and resolution metric on noise-resolution tradeoffs in x-ray CT imaging: a comparison of non-quadratic penalized alternating minimization and filtered backprojection algorithms

Joshua D. Evans*[a], David G. Politte[b], Bruce R. Whiting[b], Joseph A. O'Sullivan[c], Jeffrey F. Williamson*[a]

[a]Department of Radiation Oncology, Virginia Commonwealth University, Richmond, VA 23298

[b]Mallinckrodt Institute of Radiology and [c]Department of Electrical and Systems Engineering, Washington University, St. Louis, MO 63130

*jwilliamson@mcvh-vcu.edu; phone: 1-804-828-8451

ABSTRACT

Purpose: To assess the impact of contrast magnitude and spatial resolution metric choices on the noise-resolution tradeoff of a non-quadratic penalized statistical iterative algorithm, Alternating Minimization (AM), in x-ray transmission CT.

Methods: Monoenergetic Poisson-counting CT data were simulated for a water phantom containing circular inserts of varying contrast (7% to 238%). The data was reconstructed with conventional filtered backprojection (FBP) and two non-quadratic penalty parameterizations of AM. A range of smoothing strengths is reconstructed for each algorithm to quantify the noise-resolution tradeoff curve. Modulation transfer functions (MTFs) were estimated from the circular contrast-insert edges and then integrated up to a cutoff frequency as a single-parameter measure of local spatial resolution. Two cutoff frequencies and two resolution comparison values are investigated for their effect on reported tradeoff advantage.

Results: The noise-resolution tradeoff curve was always more favorable for AM than FBP. For strongly edge-preserving penalty functions, this advantage was found to be dependent upon the contrast for which resolution is quantified for comparison. The magnitude of the reported dose reduction potential of the AM algorithm was shown to be dependent on the resolution metric choices, though the general contrast-dependence was always evident.

Conclusions: The penalized AM algorithm shows the potential to reconstruct images of comparable quality using a fraction of the dose required by FBP. The contrast-dependence on the tradeoff advantage implies that statistical algorithms using non-quadratic penalty functions should be assessed using contrasts relevant to the intended clinical task.

Keywords: computed tomography, alternating minimization, non-quadratic regularization, noise, resolution

1. INTRODUCTION

Conventional filtered backprojection (FBP) algorithms[1] provide an exact solution to the inverse problem of x-ray transmission computed tomography (CT) under the assumption that a complete set of noiseless attenuation line integral measurements are available. However, real CT data suffers from non-linearities and noise, which cause systematic and random fluctuations from the true intensity. Excessive image noise is undesirable as it limits the clinical utility of the reconstructed images. Attempts to reduce image noise via filter modification or post-reconstruction image smoothing come at the cost of increased edge blurring. The relationship between reducing spatial resolution associated with noise reduction techniques constitutes what we will refer to as the *noise-resolution tradeoff*.

Medical Imaging 2011: Physics of Medical Imaging, edited by Norbert J. Pelc, Ehsan Samei, Robert M. Nishikawa,
Proc. of SPIE Vol. 7961, 79612C · © 2011 SPIE · CCC code: 1605-7422/11/$18 · doi: 10.1117/12.876701

The Expectation-Maximization algorithm of Lange and Carson[2] was formed around the statistical nature of x-ray CT data and can directly incorporate many nonlinear signal-formation processes into their data models. While it is intuitive that algorithms that explicitly model CT-signal statistics should be able to reconstruct images with less noise than conventional FBP from the same noisy projection dataset, the image most likely to match the measured data still suffers from excessive image noise[3, 4]. A widely used approach to suppress image noise in statistically based reconstruction algorithms is to modify the objective function to incorporate some *a priori* assumptions about the scan subject, e.g., a local neighborhood penalty function that enforces the assumption of image smoothness.

An algorithm with an improved noise-resolution tradeoff means that it can reconstruct images from the same data with either less image noise for similar resolution or better resolution for similar image noise. By extension, an algorithm that provides a noise-resolution tradeoff advantage could provide images of comparable noise and resolution from data acquired with lower imaging dose, an important topic that has recently gained public attention due to the rapidly increasing use of x-ray CT procedures[5]. Reconstruction algorithms that exhibit noise-resolution tradeoff advantages are also attractive for quantitative CT applications. The specific problem of estimating photon cross-section information from dual-energy measurements has been shown to be extremely sensitive to uncertainty in the measured CT values[6] and could reasonably be expected to benefit from statistical reconstruction.

In this work, the noise-resolution tradeoff is assessed, in comparison to FBP, for the Alternating Minimization (AM) algorithm[7] that includes a non-quadratic penalty function, which is designed to preserve high contrast edge boundaries. Previous investigators have assessed the noise-resolution tradeoff to evaluate statistical algorithms using parabolic surrogates to model the Poisson log-likelihood[8, 9], adaptive statistical sinogram smoothing techniques[8], and iterative reconstruction algorithms for cone-beam CT imaging geometries[10, 11]. In contrast to these previous studies that have quantified resolution only for high-contrast structures such as steel bb's or bone, our study investigates the effect that structure contrast has on the noise-resolution tradeoff for the non-quadratic penalized AM algorithm. With the goal of isolating the smoothing effects of the two algorithms, an ideal monoenergetic simulation environment is used to avoid mean-value artifacts arising from data nonlinearities such as scattered radiation and beam hardening. This forms a baseline of noise-resolution tradeoff performance for the penalized Alternating Minimization algorithms, for ideal Poisson-counting projection data. We further investigate how the choice of metric for quantifying spatial resolution and choice of resolution level at which noise reduction advantage is estimated impact the reported noise-resolution advantage. Future work will extend the methods for the quantification of noise and resolution in this paper to images reconstructed from real CT data.

The methodology of study is described in detail in a previously published paper[12] and are only briefly described here. Our earlier work established, for a particular choice of spatial resolution metric and reference resolution level, that penalized AM image reconstruction had the potential to reduce image noise for a fixed dose (or reduce dose for a fixed noise level) compared to FBP, and that the apparent noise-resolution advantage exhibited contrast-dependence for the strongly edge-preserving penalty function. The effect of varying levels of projection noise and the spatial non-uniformity of the noise-resolution tradeoff was also investigated. The work herein specifically addresses the contrast-dependent variation of resolution within a single reconstructed image as well as the effects of the resolution comparison choices on the reported dose reduction potential.

2. MATERIALS AND METHODS

2.1 Penalized Alternating Minimization reconstruction

The penalized Alternating Minimization algorithm is used to reconstruct images from synthetic sinogram data sets derived from a monoenergetic forward projector. The AM algorithm reformulates the classic maximization of the Poisson log-likelihood as an alternating minimization of Csiszar's I-divergence[13], which quantifies the discrepancy between the measured data, d, and the expected data means, g. I-divergence is proportional to the negative of the log-likelihood, meaning that minimization of the I-divergence is equivalent to the maximization of the log-likelihood. For full details of the Alternating Minimization algorithm, the reader is referred to O'Sullivan's 2007 paper[7]. An edge-preserving log-cosh penalty term is included in the AM algorithm's objective function to enforce our *a priori* assumption of image smoothness:

$$\Phi(\mu') = I(d \,\|\, g) + \alpha \cdot R(\mu'), \qquad (1)$$

where α controls the relative weight of the penalty function in the optimization. The penalty chosen for this study is defined as

$$R(\mu') = \sum_{x} \sum_{x' \in N(x)} w(x') \cdot \left(\frac{1}{\delta}\right) \log\left[\cosh\left(\delta\left(\mu'(x) - \mu'(x')\right)\right)\right]. \quad (2)$$

The roughness penalty computes a penalty for a pixel *x* as a function of the pixel intensities in the local neighborhood *N(x)*. The neighboring pixels are weighted as 1.0 for the four directly adjacent pixels and 0 for all other pixels.

Quadratic penalty functions effectively suppress noise, but tend to blur high-contrast edges, as the penalty rapidly increases for large pixel intensity differences. The continuously defined log-cosh function[14] is similar to a Huber penalty[15] with quadratic growth for small pixel-to-pixel variations, so as to suppress noise, and linear growth for larger intensity variations, so as to preserve edge boundaries. The parameter δ controls the intensity difference at which the penalty transitions from quadratic to linear growth. Increasing the value of δ will make the transition to linear growth occur at smaller intensity differences. Two different values of δ are investigated as bounds of potential clinically relevant penalty parameter value choices. We let *AM-100* denote images reconstructed with the penalized AM algorithm with δ = 100, which transitions to linear penalty growth for pixel differences approximately 50% of the water background and is closer in shape to a quadratic penalty. *AM-700* denotes the AM algorithm using a log-cosh penalty with δ = 700, which has a growth transition for pixel differences around 10% of background and is closer in shape to a linear penalty function. Results for δ values between 100 and 700 would reasonably be expected to lie between the two presented parameter values. Figure 1 plots both of the log-cosh penalties investigated in this work and a quadratic penalty function for comparison.

To evaluate the tradeoff between image noise and resolution, a set of images was reconstructed with varying log-cosh penalty weights, α in eq. (1). Here we use the term *smoothing strength* to refer to both the penalty function weight, α, for the AM algorithm and the FWHM of the Gaussian-modified ramp filter in the FBP algorithm described in the following section. Both penalty function parameter values of the Alternating Minimization algorithm were run for 250 iterations with 22 ordered subsets to increase convergence rate[16]. The number of iterations was chosen from preliminary simulations that showed the images were well converged.

2.2 Filtered backprojection reconstruction

Weighted filtered backprojection as described in Kak and Slaney[1] is used to backproject the filtered fan beam projection data. The filter, *H(f)*, is a modified ramp filter defined in frequency space as

$$H(f) = s \cdot |f| \cdot W(f) \cdot G(f). \quad (3)$$

Here *s* is a constant scale factor that ensures the image intensities represent the correct units of linear attenuation, mm^{-1}, and $|f|$ is the ramp function. The window function $W(f)$ is rectangular up to frequencies of 90% of Nyquist and then rolls off to zero at Nyquist with a raised cosine function. The cosine roll off in the window function was incorporated to suppress high frequency ringing artifacts observed in prior simulations at Washington University when using a purely rectangular window function. The frequency at which the cosine roll-off kicks in (90% of Nyquist) was chosen as the highest frequency that suppressed the ringing artifacts, to retain as much high frequency content as possible. When compared side-by-side with reconstructions from the proprietary Siemens FBP, trained observers were unable to distinguish which FBP implementation was used for each image. *G(f)* is the Fourier transform of a Gaussian smoothing kernel that further reduces the amplitude of high spatial frequencies. A series of images with varying levels of noise and resolution is achieved by varying the full-width at half maximum (FWHM) of the Gaussian smoothing kernel. For consistency, the system matrix used for the filtered backprojection reconstruction is the same as that used for the penalized AM reconstruction.

2.3 Virtual CT system

The virtual 3rd generation CT system is composed of 1056 gantry positions equally spaced around a full 360º rotation. There are 384 detectors each subtending an arc angle of 4.0625 minutes. Source-to-isocenter distance is 570 mm and source-to-detector distance is 1005 mm. This gives a virtual detector width of 1.2 mm and projected width at isocenter of 0.67 mm. The image space, x, is composed of 512 x 512 square pixels with a length of 0.5 mm on a side, providing a field of view of 256 mm.

Scatter-free monoenergetic projection data is simulated to avoid systematic deviations, i.e., artifacts, in the image reconstruction. The truth phantom is defined as a superposition of analytically defined ellipses. Simulated projection data is computed by evaluating the monoenergetic line integral along each source-detector path using analytical intersections with the elliptical phantom regions. Simple Poisson noise is added to the analytically calculated transmission sinogram data, such that the standard deviation in unblocked detectors is ~ 0.3% of the mean intensity. This is on the order of experimentally observed projection noise levels on the Philips Brilliance Big Bore CT simulator using a scanning protocol of 120 kVp, 325 mAs and 0.75 mm slice thickness. The noiseless projection data is also reconstructed with all algorithms and smoothing strengths for use in quantifying noise and resolution.

2.4 Phantom

The *clock phantom* used in this work (figure 2) consists of a 20 cm diameter background water cylinder with 8 cylindrical inserts (2 cm diameter) of varying contrast ranging from ±7% to +238% (bone). The water background is set to $\mu = 0.0205$ mm^{-1}, corresponding to the 61 keV energy assumed by our monoenergetic synthetic dataset. Each insert center is located 5.5 cm from the image FOV center. The clock phantom allows us to investigate the effect of varying contrast magnitudes on the tradeoff of noise and resolution.

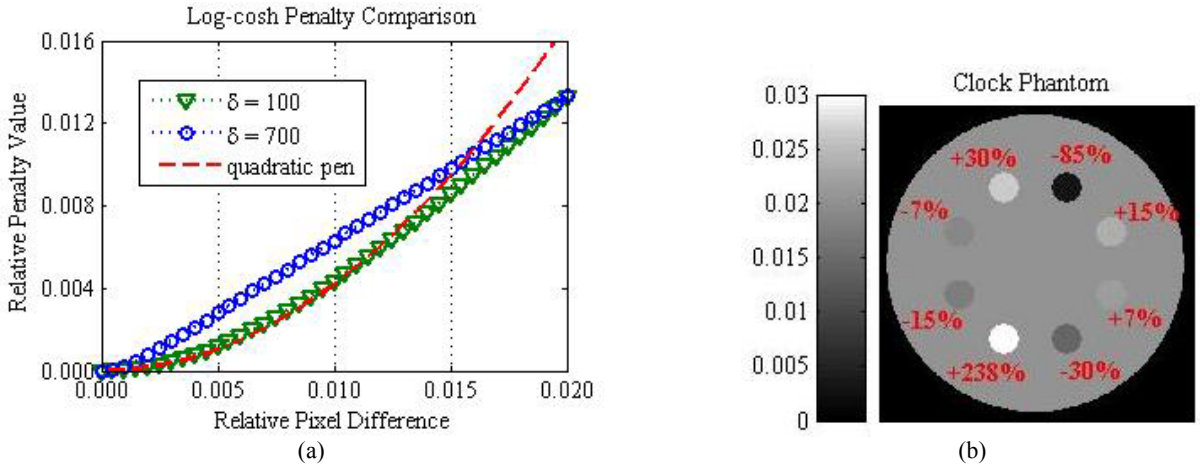

Figure 1. (a) Comparison of penalty function shape for the two log-cosh penalties investigated in this work and a quadratic penalty. Quadratic penalty functions grow too quickly for large pixel differences and consequently over-blur high-contrast edges. Note that the log-cosh penalties are scaled for plotting purposes and do not correspond to the values used in simulation. (b) Simulation clock phantom consists of a 20 cm water cylinder with 2 cm diameter inserts of varying contrast to investigate the contrast dependence of the noise-resolution tradeoff.

2.5 Noise measurement

Image noise is assessed in the water region surrounding each contrast insert. For an image reconstructed from a noisy projection dataset, the image noise is the standard deviation, as a percent of the background water intensity, for the pixels inside the noise region of interest (ROI), or

$$\%\ \text{Noise} = 100 \cdot \frac{\sigma_{ROI}}{\mu_{water}}. \qquad (4)$$

The noise ROI for each insert is an annulus that includes image pixels in the water background lying within 4-6 mm (inclusive) of the insert boundary, for a total of 756 pixels. A subtraction image between the noiseless and noisy data reconstructions is used for the variance measurement to remove systematic bias, such as sampling artifacts, from the calculation.

2.6 Calculation of dose reduction potential

An algorithm that can reconstruct an image of comparable resolution with less noise from the same projection data offers the clinical advantage of patient dose reduction. We assume that the image noise is proportional to projection noise[1, 17] and that projection variance is inversely proportional to the patient dose. From these assumptions, we can formulate an answer to the question, "What fraction of the FBP dose does the AM algorithm need to use to reconstruct an image with matched noise and resolution?" We calculate the dose fraction as the ratio of AM variance to FBP variance at a constant resolution metric value,

$$\text{dose fraction} = \frac{\sigma_{AM}^2}{\sigma_{FBP}^2}. \quad (5)$$

Intuitively, the ratio of variances, or dose fraction, represents the fraction of dose necessary for the AM algorithm to achieve the same image noise and resolution as the FBP algorithm for the chosen contrast insert. The dependence of reported dose reduction potential on the choice of reference resolution is investigated by calculating dose fractions at the highest and lowest resolution values along the noise-resolution tradeoff curves.

2.7 Resolution measurement

The resolution metric used in this work is based on the Modulation Transfer Function (MTF). While x-ray transmission CT is not a shift-invariant linear system, the MTF is considered to be a valid measure of local impulse response that can provide insight into the effect of reconstruction on edge blurring. As described in more detail elsewhere [12], the edge-spread function (ESF) is differentiated to obtain the line-spread function (LSF) and the Fourier transform of the LSF is calculated to obtain the MTF.

The circular symmetry of the contrast inserts is used to construct a super-sampled edge-spread function similar to Thornton's use of a sphere[18] to measure the in-plane MTF and slice-sensitivity profile for a multi-slice CT scanner. Since our simulation phantom is comprised of a set of circular structures, each reconstructed image pixel's intensity is plotted as a function of the distance between its center and the analytically defined insert edge. In this way, the transition between the water background and the contrast insert can be visualized. As multiple pixels have the same distance to the edge, the mean intensity at each unique distance is calculated and used for subsequent estimation of the MTF. Sampling pixels around a circularly symmetric insert to form a super-sampled edge-spread function reduces the apparent effect of resolution anisotropy, noise, and non-uniformity, and thus represents an average of the edge response function within the sampled region of interest. The edge-spread function is derived from images reconstructed from the noiseless projection dataset to avoid bias from the image noise and to improve the model fitting. As shown in section 3.1 the high contrast edges reconstructed with AM-700 were found to be poorly fit by a Gaussian edge model. To further smooth the ESF prior to differentiation and Fourier transformation, a 6-parameter Gaussian-exponential model[19] was fit to the super-sampled edge using the Matlab *fminsearch* function.

To analyze how the image noise and resolution vary as a function of smoothing strength for a particular algorithm, it is useful to extract a single parameter to characterize resolution. La Riviere[8], reports the FWHM of a Gaussian blurring model fit to line profiles of high-contrast bone inserts, which is an intuitive metric as a wider Gaussian represents a blurrier edge. However, our 6-parameter Gaussian-exponential model does not lead to such a straight-forward metric.

We chose to report the area under the MTF curve, called MTF area or A_x, where x is an arbitrary, spatial frequency limit.

$$A_x = \frac{1}{x}\int_0^x MTF(f)df. \quad (6)$$

Intuitively, the MTF area represents the fraction of ideal input signal that is recovered for spatial frequencies less than or equal to the cutoff frequency. The MTF area A_x is normalized to *x*, as this is the area under an ideal MTF curve that has amplitude 1.0 for all spatial frequencies. We chose x = 0.5 lp/mm to define a single-value surrogate, $A_{0.5}$, of edge resolution. The 0.5 lp/mm integration limit was chosen as it is near the frequency where the FBP and AM-700 MTF shapes differ the most (figure 2d). It is also close to the ACR's accreditation requirement of 0.6 lp/mm for high-contrast resolution. To investigate the variation in noise-resolution tradeoff and reported dose reduction factors, the MTF area integrated to the Nyquist frequency of 1.0 lp / mm, $A_{1.0}$, is also calculated.

3. RESULTS

3.1 Necessity of Gaussian-exponential edge-spread function model

Previous investigators have characterized CT image resolution under the assumption of Gaussian blurring, e.g., reporting the associated Gaussian FWHM of an error function fit to bone inserts as a surrogate of resolution[8]. Our preliminary work revealed that purely Gaussian blurring models did not adequately fit the AM-700 high-contrast edges. Figure 2 illustrates (a-c) the different shapes the high-contrast bone insert ESF as reconstructed with the FBP and AM algorithms and (d) the subsequently calculated MTFs. The smoothing strengths for comparison in figure 2 were chosen as they led to nearly the same image noise (~ 1.09% ± 0.01%) when reconstructing from the noisy dataset. The steep central transition and shoulder roll-off of the AM-700 high-contrast edges motivated us to model the edge-spread function as a linear combination of Gaussian and exponential components. Though the FBP and low-contrast AM ESFs were well fit by the purely Gaussian model, the Gaussian-exponential model was used to fit all reconstructed image edge-spread functions to provide a consistent methodology. No loss of ESF fitting quality with the Gaussian-exponential model was seen for the edges that were already well fit by the purely Gaussian model.

In contrast to the FBP and AM-100 bone MTF's, which exhibit a rapidly dropping frequency response, the AM-700 bone MTF shows an initial drop for low frequencies due to the rounded shoulder of the AM-700 ESF, and retention of higher spatial frequencies due to the sharp central transition of the ESF. The ESF and MTF shape of the high-contrast structures as reconstructed by the AM-700 algorithm were found to be markedly different than those seen in the literature[9, 10, 18, 20]. Conventional MTF descriptors, such as the spatial frequency corresponding to 10% MTF and 50% MTF, did not support robust comparison of AM-700 and FBP resolution, especially for high-contrast structures. For example, the 10% MTF for the displayed AM-700 bone insert occurs at a frequency of 2.79 lp / mm, where the FBP and AM-100 bone insert frequency responses are essentially zero.

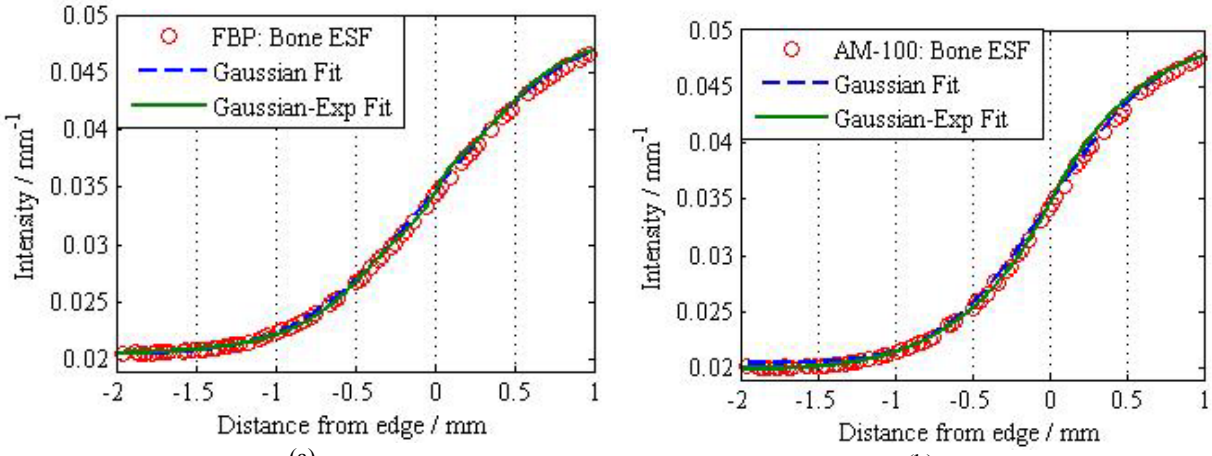

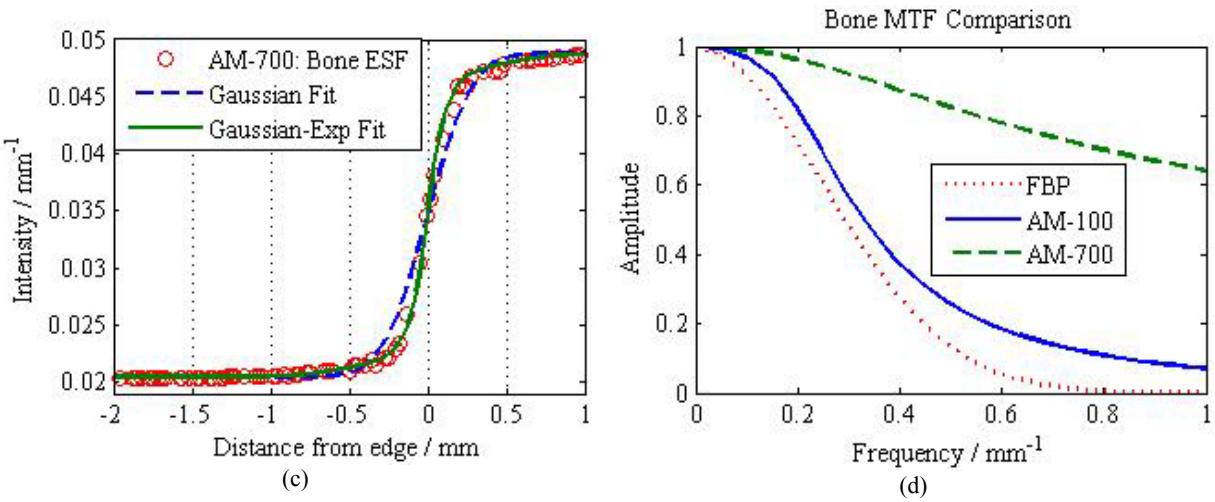

Figure 2. Noise-matched (1.09% ± 0.01%) comparison of bone edge sharpness. The bone ESFs are seen to be well fit by both Gaussian and Gaussian-exponential ESF models for the (a) FBP and (b) AM-100 algorithms. The bone ESF for (c) AM-700 is seen to be poorly fit by a purely Gaussian model due to the steep central transition and shoulder roll-off of the edge. (d) Comparison of the subsequent bone MTF for the three algorithms calculated from the Gaussian-exponential fit ESF.

3.2 Noise-resolution tradeoff curves

From each set of images reconstructed with varying smoothing strengths, the noise and resolution have been calculated around each of the 8 contrast inserts allowing a noise-resolution tradeoff curve to be plotted for each contrast magnitude. Figure 3 displays the noise-resolution (NR) tradeoff curves for the +7% (top row) and -85% (bottom row) inserts. The qualitative trends for the other contrast inserts follow those presented for these two inserts. The effect of choosing 0.5 lp / mm (left column) for the MTF area integration limit is compared to 1.0 lp / mm (right column).

The AM tradeoff curves in figure 3 always lie below the FBP tradeoff curve implying that AM-100 and AM-700 reconstruct images with either less image noise for the same resolution metric or sharper edges for matched image noise. By extension, a tradeoff advantage implies that AM can reconstruct images with similar resolution and image noise for less patient dose. Comparing the left and right columns, we see that the cutoff frequency changes the range of area fractions of the tradeoff curve, making head-to-head comparison of the resolution metric cutoff choice difficult. Qualitatively, it appears that the 1.0 lp / mm cutoff frequency pulls the low contrast curves closer together while pushing the high contrast curves further apart, which will affect the reported dose reduction potential as shown in the following section.

For both choices of MTF area cutoff frequency, the more strongly edge-preserving penalty parameterization, AM-700, provides increased noise-resolution tradeoff advantages for higher contrast inserts. Note that because all contrast inserts within a single reconstructed image exhibit essentially identical noise levels, the contrast-dependent nature of the AM tradeoff curves are due entirely to differences in the resolution. This is a direct result of the edge-preserving nature of the non-quadratic local neighborhood penalty function. Figure 4 clearly illustrates this by plotting (a) the MTF area integrated to 0.5 lp / mm for all contrast inserts within a single reconstructed image from the three algorithms. The MTF of selected inserts is also displayed for (b) AM-100 and (c) AM-700 images in figure 4. The FBP MTFs are omitted as they are not seen to vary with contrast and are similar in shaped to the AM-100 non-bone MTFs.

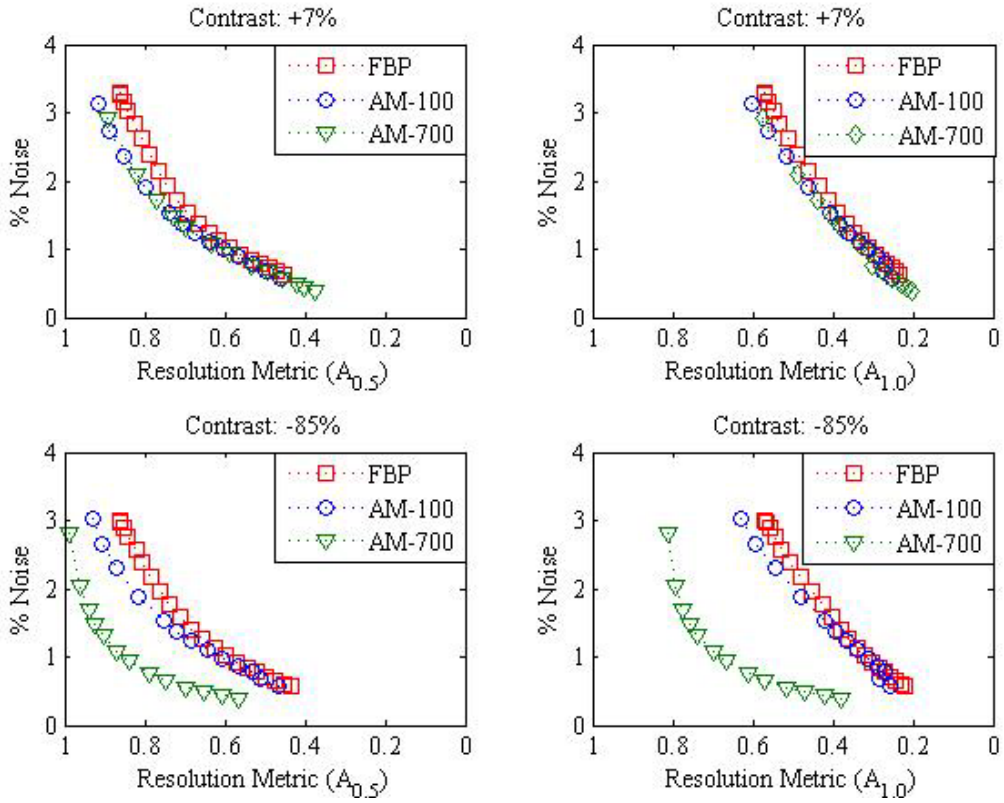

Figure 3. Noise-resolution tradeoff curves for two contrast inserts (TOP = +7%, BOTTOM = -85%) using two choices of MTF area integral cutoff (LEFT = A0.5, RIGHT = A1.0).

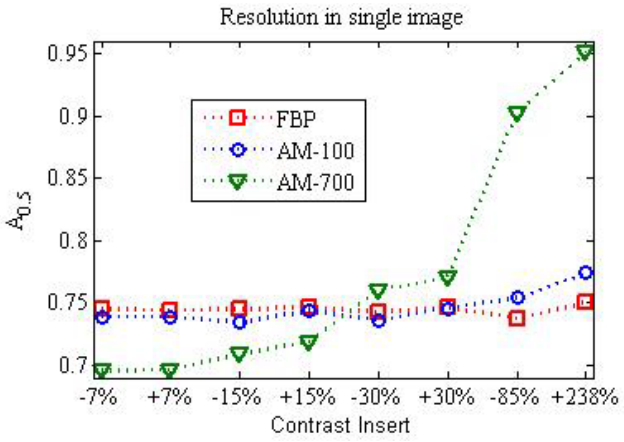

(a)

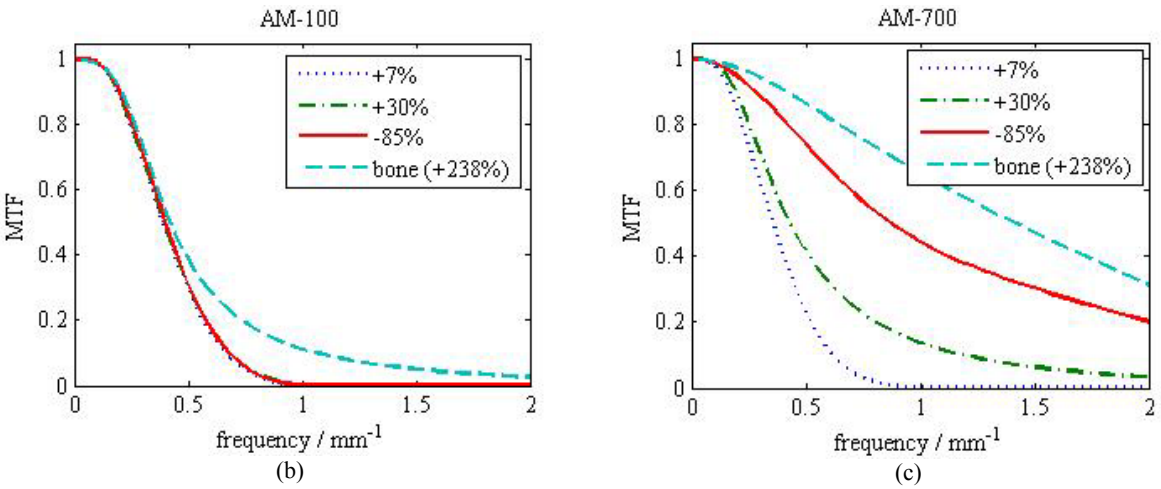

Figure 4. Illustration of the varying resolution within AM images. (a) Plot of the resolution metric value $A_{0.5}$ for all 8 contrast inserts within a single reconstructed image for the three algorithms. MTFs for selected contrast inserts within the (b) AM-100 and (c) AM-700 images are also displayed. FBP MTFs are omitted as they are not seen to be contrast-dependent. It is clear from these graphs that the shifts in the AM noise-resolution tradeoff curves are due to contrast-dependent resolution within the image.

3.3 Dose reduction potential

Resolution-matched noise comparisons can be performed only for resolution metric values that are existent on all tradeoff curves. We cannot compute the dose fraction for the bone insert since even the highest resolution FBP image (with no smoothing) is unable to achieve the $A_{1.0}$ value of the most strongly smoothed AM-700 image. The dose fraction results for the bone insert is thus omitted as the results follow the trend shown for the -85% high-contrast insert.

Figure 5 plots the dose fraction (ratio of AM to FBP variance at matched resolution metric value) for the AM-100 (TOP) and AM-700 (BOTTOM) algorithms. The effect of differing integration limits, 0.5 lp / mm (LEFT) and 1.0 lp / mm (RIGHT), are compared. Note that the maximum and minimum MTF areas available for comparison are different when integrating the MTF up to 0.5 and 1.0 lp / mm since the range of values differs for the two cutoff frequencies. Each plot contains two curves; based on the largest (red dashed) and smallest (blue dotted) common A_x values. Wider spread of the matched high and low resolution dose reduction values for the 0.5 lp / mm cutoff frequency seems to imply that it is more sensitive to the choice of resolution comparison point. However, this is not a straightforward comparison, considering the lowest and highest common resolution values are not the same between the two integration limits. The general trend of improved noise-resolution advantage as the structure contrast increases for the more strongly edge-preserving AM-700 algorithm is evident in both resolution metric cutoff frequencies.

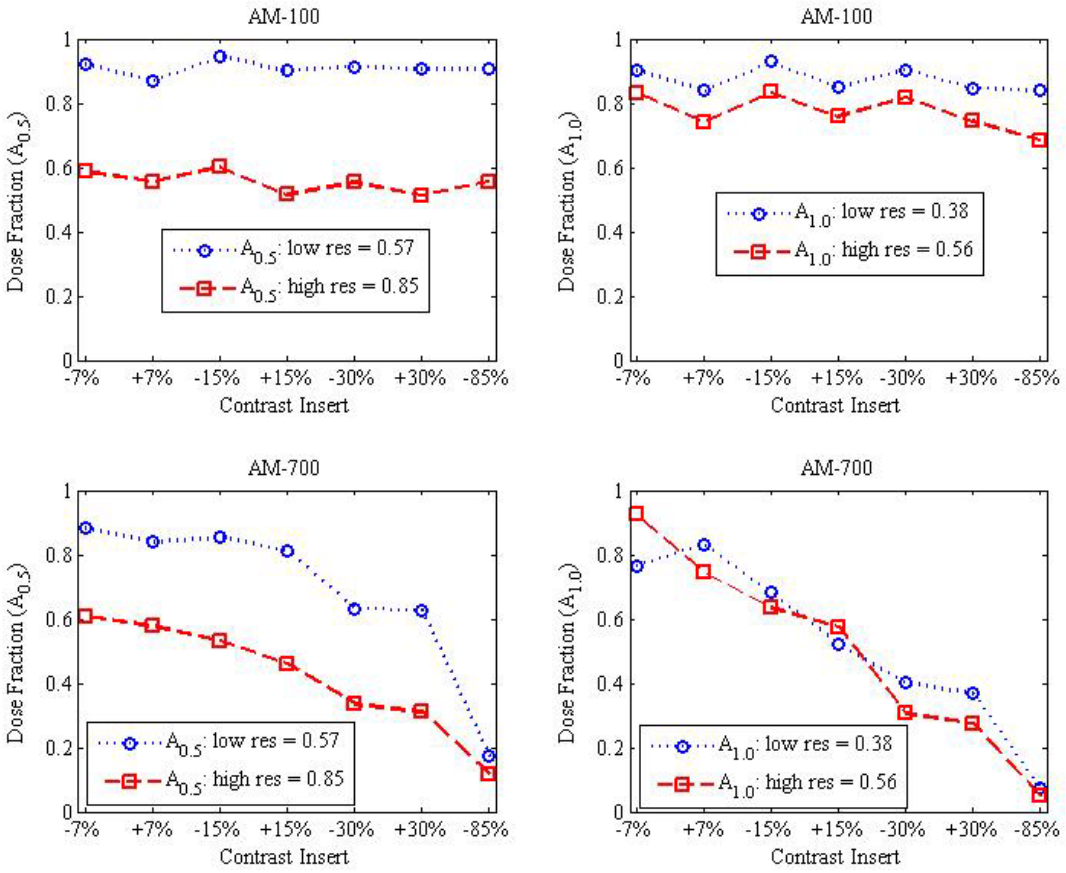

Figure 5. Dose fraction curves for (TOP) AM-100 and (BOTTOM) AM-700. LEFT displays dose fraction curves when integrating the MTF up to 0.5 lp / mm. RIGHT displays dose fractions when integrating the MTF up to 1.0 lp / mm. Each plot contains two curves for the highest and lowest resolution values available for noise comparison. The reported dose reduction potential of the AM-700 algorithm is seen to strongly depend on the magnitude of contrast for which resolution is quantified.

4. DISCUSSION AND CONCLUSIONS

In response to the unique shape of the AM-700 high-contrast edges, we selected the normalized MTF integral up to a cutoff frequency as a convenient, but somewhat arbitrary, single-parameter surrogate of edge resolution. The MTF area resolution surrogate has not been correlated with any observer performance metrics, making direct comparison of our results and existing literature difficult. To the author's knowledge, no gold standard metric for quantifying CT image resolution has been embraced by the community. It seems that future work that correlates an objective single-parameter metric of resolution to subjective parameters, such as low contrast detectability or perceived sharpness, would be especially useful for edge-preserving penalty functions that result in ESFs and MTFs with very different shapes than typically seen [9, 10, 18, 20].

As shown in [12], the log-cosh penalized Alternating Minimization algorithm is found to consistently reconstruct resolution-matched images with less noise than conventional FBP, and highlights the result that the noise-resolution tradeoff for local edge-preserving penalty functions depends strongly on the contrast magnitude for which resolution is chosen to be quantified. Specifically, this work shows that the magnitude of the advantage, reported as a potential for dose reduction, is subject to choices of resolution metric and reference resolution value that are used for comparison. The choice of reference resolution for the calculation of tradeoff advantage is relevant to all smoothing techniques, not just edge-preserving penalty functions. Advantage comparisons should be made at reference resolution values relevant to the clinical task at hand. The general result of the contrast-dependence for the edge-preserving penalty function is evident for all resolution metric choices investigated here. This implies that noise-resolution tradeoff

comparisons for edge-preserving penalty functions should utilize structures with contrasts relevant to the intended clinical task.

Acknowledgement: This work was supported in part by from grants R01 CA 75371, P01 CA 116602 and 5P30 CA 016059 awarded by the National Institutes of Health.

REFERENCES

[1] A. C. Kak, and M. Slaney, [Principles of Computerized Tomographic Imaging] IEEE Press, New York, (1988).
[2] K. Lange, and R. Carson, "EM reconstruction algorithms for emission and transmission tomography," Jour. Comput. Assist. Tomogr., 8(2), 306-316 (1984).
[3] D. L. Snyder, M. I. Miller, L. J. Thomas *et al.*, "Noise and edge artifacts in maximum-likelihood reconstructions for emission tomography," IEEE Trans Med Imaging, 6(3), 228-38 (1987).
[4] C. L. Byrne, "Iterative image reconstruction algorithms based on cross-entropy minimization," IEEE Trans Image Process, 2(1), 96-103 (1993).
[5] D. J. Brenner, and E. J. Hall, "Computed tomography--an increasing source of radiation exposure," N Engl J Med, 357(22), 2277-84 (2007).
[6] J. F. Williamson, S. Li, S. Devic *et al.*, "On two-parameter models of photon cross sections: application to dual-energy CT imaging," Med Phys, 33(11), 4115-29 (2006).
[7] J. A. O'Sullivan, and J. Benac, "Alternating minimization algorithms for transmission tomography," IEEE Trans Med Imaging, 26(3), 283-97 (2007).
[8] P. J. La Riviere, "Penalized-likelihood sinogram smoothing for low-dose CT," Med Phys, 32(6), 1676-83 (2005).
[9] A. Ziegler, T. Kohler, and R. Proksa, "Noise and resolution in images reconstructed with FBP and OSC algorithms for CT," Med Phys, 34(2), 585-98 (2007).
[10] J. Sunnegardh, and P. E. Danielsson, "Regularized iterative weighted filtered backprojection for helical cone-beam CT," Med Phys, 35(9), 4173-85 (2008).
[11] J. B. Thibault, K. D. Sauer, C. A. Bouman *et al.*, "A three-dimensional statistical approach to improved image quality for multislice helical CT," Med Phys, 34(11), 4526-44 (2007).
[12] J. D. Evans, D. G. Politte, B. R. Whiting *et al.*, "Noise-resolution tradeoffs in x-ray CT imaging: a comparison of Penalized Alternating Minimization and Filtered Backprojection algorithms," Med Phys, (In Press 2011).
[13] I. Csiszar, "Why least squares and maximum entropy? An axiomatic approach to inference for linear inverse problems," Annals of Statistics, 19, 2032-2066 (1991).
[14] P. J. Green, "Bayesian reconstructions from emission tomography data using a modified EM algorithm," IEEE Trans Med Imaging, 9(1), 84-93 (1990).
[15] D. F. Yu, and J. A. Fessler, "Edge-preserving tomographic reconstruction with nonlocal regularization," IEEE Trans Med Imaging, 21(2), 159-73 (2002).
[16] H. M. Hudson, and R. S. Larkin, "Accelerated image reconstruction using ordered subsets of projection data," IEEE Trans Med Imaging, 13(4), 601-9 (1994).
[17] D. Chesler, S. Riederer, and N. Pelc, "Noise Due to Photon Counting Statistics in Computed X-Ray Tomography," Journal of Computer Assisted Tomography, 1(1), 64-74 (1977).
[18] M. M. Thornton, and M. J. Flynn, "Measurement of the spatial resolution of a clinical volumetric computed tomography scanner using a sphere phantom," Proceedings of the SPIE: Physics of Medical Imaging, 6142, 707-716 (2006).
[19] J. M. Boone, and J. A. Seibert, "An analytical edge spread function model for computer fitting and subsequent calculation of the LSF and MTF," Med Phys, 21(10), 1541-5 (1994).
[20] P. F. Judy, "The line spread function and modulation transfer function of a computed tomographic scanner," Med Phys, 3(4), 233-6 (1976).

Appendix 4

Prospects for quantitative imaging on commercial fanbeam CT scanners: Experimental assessment of analytic and polyenergetic statistical reconstruction algorithms

Prospects for quantitative imaging on commercial fan-beam CT scanners: Experimental assessment of analytic and polyenergetic statistical reconstruction algorithms

Short Title: Validation of statistical image reconstruction on a commercial CT scanner

J D Evans[1], B R Whiting[2], D G Politte[2], J A O'Sullivan[3], P Klahr[4] and J F Williamson[1]

[1]Department of Radiation Oncology, Virginia Commonwealth University, Richmond, VA 23298

[2]Mallinckrodt Institute of Radiology, Washington University, St. Louis, Missouri 63110

[3]Department of Electrical and Systems Engineering, Washington University, St. Louis, Missouri 63130

[4] Philips Healthcare, 595 Miner Rd., Highland Hts., OH 44143

Corresponding Author:

Jeffrey F. Williamson, Ph.D.
Department of Radiation Oncology
Virginia Commonwealth University
401 College Street, B-129
PO Box 980058
Richmond, VA 23298
804-828-8451 (Phone)
804-827-1670 (Fax)
jwilliamson@mcvh-vcu.edu

Abstract

Quantitative CT applications require reconstructed image intensity for a given material to maintain a one-to-one correspondence to the underlying physical property of interest, regardless of location within a subject, subject size, or subject location in the field-of-view (FOV). This work utilizes data acquired on a commercial CT scanner of homogeneous cylinders of varying composition and diameter at three tube potentials to compare the performance of conventional filtered backprojection (FBP) reconstruction and a novel polyenergetic statistical reconstruction algorithm, Alternating Minimization (AM). Scatter-to-primary ratio (SPR) is estimated using a beam-stop technique. The x-ray spectrum for each tube potential is estimated by fitting a semi-empirical spectrum model to measured attenuation curves on central-axis. Off-axis spectral variations due to the bowtie filter are modeled using known geometry. Polyenergetic AM is seen to reconstruct images with better uniformity and less subject size dependence than FBP. Even in a low scatter environment, 3 mm beam collimation and a 1-D anti-scatter grid, a simple constant scatter estimate is found to be necessary to achieve AM accuracy of 0.5% for objects with SPR > 1%. Polyenergetic AM appears to be a good candidate for reducing systematic uncertainties for quantitative CT applications.

PACS: 87.57.-s (Medical Imaging)

Key Words: computed tomography, alternating minimization, filtered backprojection, polyenergetic statistical reconstruction

1. Introduction

Quantitative computed tomography (CT) applications such as bone mineral density measurement(Boden and Goodenough 1989; Cann 1988), measurement of blood perfusion(Konig 2003; Valdiviezo and Ambrose 2010), and dual-energy CT methods for material characterization(Bazalova and Carrier 2008) or direct estimation of radiological cross-section information(Williamson and Li 2006) all rely on accurate relationships between measured CT intensities and the underlying tissue property of interest(Wang and Yu 2008). For quantitative CT applications, the measured CT image intensity for a given material should be independent of subject size, location within the subject and location of the subject within the scanner's field-of-view (FOV). We refer to these requirements for quantitative CT as *image intensity consistency criteria*.

Conventional filtered backprojection (FBP) reconstruction algorithms for x-ray CT assume that acquired data are noiseless, linear functions of the attenuation line integral along each source-detector ray. However, inherent non-linearities in the CT data acquisition process lead to systematic deviations in reconstructed images that undermine the consistency criteria for quantitative CT if not properly corrected for. As the x-ray energy spectrum is polyenergetic, low energy photons are preferentially attenuated in the scan subject, an effect called beam-hardening (BH), causing the characteristic cupping artifact(Brooks and Di Chiro 1976; Joseph and Ruth 1997). It is also well known that scattered radiation causes similar systematic cupping artifacts in reconstructed images(Endo and Mori 2006; Glover 1982; Joseph and Spital 1982). Conventional FBP reconstructions often rely on empirical data correction schemes to linearize the data prior to backprojection, in an attempt to alleviate the effects of BH and scatter. However, residual cupping artifacts often remain for objects of larger size or composition that deviates considerably from water.

Statistical reconstruction algorithms seem well-suited to reducing these systematic errors, as they offer the flexibility of incorporating more realistic data acquisition physics in the forward model. Indeed, previous studies have shown that incorporating the polyenergetic nature of the x-ray spectrum directly into the reconstruction reduces the systematic bias of the cupping artifact from BH(Chueh and Tsai 2008; De Man and Nuyts 2001; Elbakri and Fessler 2002; Elbakri and Fessler 2003; O'Sullivan and Benac 2007;

Yan and Whalen 2000). For example, De Man et al.(De Man and Nuyts 2001) present a statistical iterative algorithm that includes a polyenergetic x-ray spectrum estimate in the data model. Noiseless, scatter-free simulations were used to quantitatively assess the accuracy of the polyenergetic algorithm, and real phantom data acquired on a commercial Siemens scanner qualitatively illustrated improved image quality relative to FBP. Elbakri et al.(Elbakri and Fessler 2003) also employed simulation studies to quantify the reduction of systematic error from BH for their polyenergetic statistical algorithm. In addition, they used real data of a 15 cm diameter water phantom acquired on a table-top x-ray CT system to validate the polyenergetic statistical algorithm's estimation of density to within 1.2% for potassium phosphate solutions of varying concentrations. While encouraging, the literature to date on polyenergetic statistical reconstruction seem to only assess the criterion that image intensities for a given material be consistent within an object and quantify absolute accuracy only in simulation studies or in limited experimental data cases.

In this work, we assess the potential of a novel polyenergetic statistical iterative reconstruction algorithm, Alternating Minimization (AM), to reduce systematic errors from BH and scatter on data acquired with a commercially available CT scanner. Polyenergetic AM reconstruction, using measured estimates of scattered radiation and the x-ray spectrum (including modeling of the bowtie filter), is compared to FBP reconstruction of data processed with the vendor-supplied BH-correction at three tube potentials. Homogeneous cylinders of water, PMMA and Teflon with varying diameters are used to assess the image consistency criteria. A single-basis object model matched to the cylinder material is used for polyenergetic AM reconstruction, allowing assessment of absolute accuracy in relation to an expected ground truth. To the best of the authors' knowledge, this is the first work to assess the absolute accuracy and a range of quantitative consistency criteria for polyenergetic statistical image reconstruction of data acquired on a commercial CT scanner.

2. Materials and methods

2.1. The polyenergetic Alternating Minimization reconstruction algorithm

CT image reconstruction was carried out for axial data acquired on the Philips Brilliance Big Bore scanner as described in section 2.3 below. The 2-D image space, x, is composed of 512 x 512 rectangular image pixels, each with a length of 1.0 mm on a side. The CT sinogram data space, $y=(\gamma,\beta)$, is defined by the angle of each source-detector ray, γ, and each gantry angle, β.

The polyenergetic Alternating Minimization (AM) algorithm is briefly presented here. For full details of the AM algorithm and its derivation, the reader is referred to O'Sullivan's 2007 paper(O'Sullivan and Benac 2007). An object is represented in image space as a map of linear attenuation coefficients, $\mu(x,E)$, that depend on spatial location, x, and energy, E. The material at location x is represented as a weighted sum of N basis materials:

$$\mu(\mathbf{x},E)=\sum_{i=1}^{N}\mu_i(E)c_i(\mathbf{x}) \qquad (1)$$

where $\mu_i(E)$ denotes the linear attenuation spectrum of the i-th basis material.

The polyenergetic forward model is used to calculate the expected data means from the current image estimate, $\mathbf{c}(x)=\left(c_1(x),\cdots,c_N(x)\right)$ according to

$$g(\mathbf{y}:\mathbf{c})=\sigma(\mathbf{y})+\sum_{E}I_0(\mathbf{y},E)\cdot\exp\left(-\sum_{x\in X}\sum_{i=1}^{N}h(\mathbf{y}\mid x)\cdot\mu_i(E)\cdot c_i(x)\right). \qquad (2)$$

Here $I_0(\mathbf{y},E)$ denotes the x-ray particle fluence spectrum incident on the scan subject. The dependence on y denotes the ability to model a spectrum that varies for each detector element γ, due to objects such as a bowtie filter, and each gantry angle β, for example when tube current modulation is employed. Incorporating the x-ray energy spectrum directly in the AM algorithm's forward model represents an implicit beam-hardening correction. Thus, the polyenergetic AM algorithm operates on energy-uncompensated data as discussed in section 2.3. Accounting for effects such as energy integrating detectors in the spectral model is discussed in section 2.5. An estimate of background events, i.e., scattered radiation, is represented by $\sigma(\mathbf{y})$, which can also vary for each source-detector ray and gantry angle. The system matrix, $h(\mathbf{y}\mid\mathbf{x})$, is the average distance traveled by photons crossing pixel x that are incident on the face of detector γ for gantry angle β and is pre-computed to increase the speed of the iterative algorithm.

The AM algorithm reformulates the classic maximization of the Poisson log-likelihood as an alternating minimization of Csiszar's I-divergence(Csiszar 1991), an information-theoretic measure of discrepancy between two functions, between the measured data *d* and the expected data means *g*:

$$I(\mathbf{d} \,\|\, \mathbf{g}) = \sum_{y \in Y} \left(d(y) \ln \frac{d(y)}{g(y : \mathbf{c}')} - d(y) + g(y : \mathbf{c}') \right), \qquad (3)$$

where $\mathbf{c}'$ is the current image estimate. The I-divergence is proportional to the negative of the Poisson log-likelihood, which means that minimization of the I-divergence is equivalent to maximization of the log-likelihood. The algorithm will reconstruct *N* images that represent the partial density of each basis material in each voxel, $c_i(x)$. In this work, images are reconstructed with a single basis substance (*N*=1) that was matched to the material of the scan subject. From equation (1), we expect the reconstructed image intensity to be *c(x)* = 1.0 for this case, providing an expected truth for which to assess the AM algorithm's absolute accuracy.

A log-cosh penalty term is included in the AM algorithm's objective function to enforce the *a priori* assumption of image smoothness:

$$\Phi(\mathbf{c}') = I(\mathbf{d} \,\|\, \mathbf{g}) + \alpha \cdot R(\mathbf{c}'), \qquad (4)$$

where the Lagrange multiplier, α, controls the relative weight of the penalty function. A value of $\alpha = 3^{-4}$ is used for all AM reconstructions. The roughness penalty computes the penalty for each pixel *x* as a function of its neighboring pixel intensities. The edge-preserving log-cosh penalty function(Elbakri and Fessler 2003; Green 1990) used in this work is defined as

$$R(\mathbf{c}') = \sum_{x} \sum_{x' \in N(x)} w(x') \cdot \left(\frac{1}{\delta} \right) \log\left[\cosh\left(\delta \left(c'(x) - c'(x') \right) \right) \right], \quad (5)$$

where *N(x)* is the set of pixels in the local neighborhood about *x*. Here the four directly adjacent pixels are weighted as $w(x') = 1$ and all other pixels as $w(x') = 0$. The parameter δ controls the pixel intensity difference for which the penalty transitions from quadratic to linear growth. The value of δ = 15 used in this study corresponds to a transition at intensity differences of 10% from background. As the purpose of this work is to assess systematic errors, noise was not matched between the AM and FBP images of the same data. For a more detailed discussion of the log-cosh penalty function in the AM

algorithm, the reader is referred to Evans(Evans and Politte 2011; Evans and Politte 2011). Ordered subsets were utilized to increase the convergence rate(Hudson and Larkin 1994). AM images were reconstructed using 512 to 1024 iterations and 33 ordered subsets, which was found to ensure that all image cases were well converged.

2.2 The filtered backprojection reconstruction algorithm

Weighted filtered back-projection(Kak and Slaney 1988) was used as a baseline for comparison to the penalized Alternating Minimization algorithm. The filter, *H(f)*, is a modified ramp filter defined in frequency space as

$$H(f) = s \cdot |f| \cdot W(f), \qquad (6)$$

where *s* is a constant scale factor that ensures the image intensities represent the correct units of linear attenuation, mm^{-1}, and $|f|$ is the ramp function. *W(f)* is a rectangular window function up to frequencies of 90% of Nyquist, which then rolls off with a raised cosine function to zero at Nyquist frequency. More information regarding the shape of this modified ramp filter can be found in Evans(Evans and Politte 2011). The FBP algorithm just described was compared to the Philips proprietary FBP reconstruction using the "axial pelvis protocol". The results reported in the following sections using our in-house algorithm were found to be indistinguishable from results when using the Philips FBP software. For consistency, our in-house FBP algorithm used the same system matrix as the polyenergetic AM algorithm forward model.

2.3. CT data acquisition and processing

All of the CT data in this work was acquired on a Philips Brilliance Big Bore 16-slice scanner. The Brilliance scanner is a 3rd generation, i.e., rotate-rotate, scanner used in VCU's radiation oncology clinic. All studies used an axial acquisition protocol, (identified as "axial pelvis protocol" by the vendor's software) with detector slice thickness of 0.75 mm and beam collimation of 3.0 mm, allowing 4 slices per rotation to be acquired. The raw data, corrected only for dark current, were then exported to a PC for processing and reconstruction.

Proprietary software provided by Philips enabled us to apply or omit any of the standard data preprocessing corrections. Standard system corrections such as detector

gain, reference detector normalization, slice normalization and crosstalk were applied to all data in this work. Two sets of processed data were generated from each raw dataset; one with the vendor's proprietary empirical beam hardening (BH) correction turned on for conventional FBP reconstruction, and one with the BH correction omitted for reconstruction with the polyenergetic AM algorithm. The BH correction is a water-equivalent polynomial fit. Also of note is that the Brilliance scanner utilizes a 1-D anti-scatter grid (ASG) for physical scatter rejection and does not apply any scatter correction to the data.

Four reconstructions of each CT dataset were performed: polyenergetic AM without a scatter estimate ($AM_{Sc\text{-}OFF}$), polyenergetic AM with a constant scatter estimate ($AM_{Sc\text{-}ON}$), FBP from BH-corrected data ($FBP_{BH\text{-}ON}$) and FBP of BH-uncorrected data ($FBP_{BH\text{-}OFF}$). FBP reconstruction with and without BH corrections applied to the data allow the effect of the vendor-supplied empirical BH correction to be studied. The most direct comparison between FBP and AM is for $FBP_{BH\text{-}ON}$ and $AM_{Sc\text{-}OFF}$ as both attempt to correct for beam-hardening, but not scatter. The reconstruction of $AM_{Sc\text{-}ON}$ images allows investigation into the effect of a constant scatter correction as described in section 2.6.

2.4 Physical phantoms and assessment of systematic bias

Homogeneous cylindrical phantoms of water, polymethyl methacrylate (PMMA) and Teflon were used to assess the systematic bias in AM and FBP images. The water cylinder (Victoreen CT performance phantom) consists of 20.3 cm diameter of water enclosed by a 6 mm thick acrylic shell. PMMA cylinders of four diameters (5.1 cm, 15.9 cm, 20.3 cm and 30.5 cm) and Teflon cylinders of three diameters (5.1 cm, 11.4 cm and 17.8 cm) were reconstructed to investigate the effect of subject size. The largest PMMA and Teflon diameters transmit roughly 10^{-3} of the primary beam to approximate typical clinical patient scans. All cylinders were scanned at tube potentials of 90, 120 and 140 kVp, and were immobilized to hang off the end of the CT table so that the table was not in the FOV. To investigate the dependence of location within the FOV, the cylinders were scanned both when centered and when shifted approximately 9 cm from the center of rotation.

With the goal of assessing systematic bias in the reconstructed images, spatial averaging was employed to remove the effect of random image noise. By exploiting the radial symmetry of the scan subjects, image pixels were binned according to their radial distance to the cylinder centroid D using bin widths of 0.5 cm for the smallest cylinders (5.1 cm diameter) and bin widths of 1.0 cm for all other cylinders. Only pixels with more than 4 mm of separation from the cylinder-air interface were included. The mean image intensity in each radial bin (henceforth referred to as the '*radial bin mean*') as a function of the radial bin's median distance to the cylinder centroid, $\overline{\mu}(D)$, represents the mean profile and was used in the subsequent assessments of systematic bias. Figure 1 shows an example of the radial averaging method for the 17.8 cm Teflon cylinder reconstructed with $FBP_{BH\text{-}ON}$ which shows visible cupping.

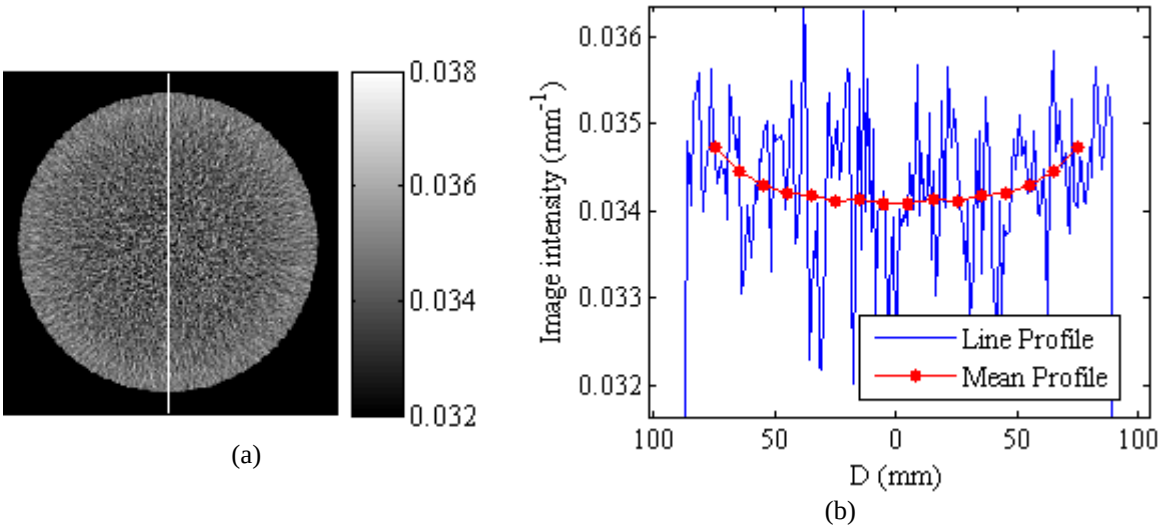

Figure 1. Illustration of the radial averaging method. **(a)** The cupping artifact can be visualized in $FBP_{BH\text{-}ON}$ reconstruction of the 17.8 cm Teflon cylinder scanned at 120 kVp with 220 mAs. **(b)** However, image noise makes it difficult to quantify the cupping artifact from a traditional line profile [location denoted by the vertical white line in (a)]. The mean profile, calculated by averaging pixels based on their radial distance to the cylinder centroid D, reveals the structure of the cupping artifact and allows assessment of the systematic bias.

As stated previously, the AM algorithm was employed with a single-basis image model using the material composition of the scan subject. AM accuracy was assessed by calculating the percent difference of all radial bin means from the expected $c(x) = 1.0$. Assessing AM accuracy in reference to an expected ground truth is performed to give confidence that the detector-dependent x-ray energy spectrum was properly modeled and

to investigate the effect of the measured scatter fractions as outlined in the following sections.

To assess the criterion that intensity be independent of location within the subject, the uniformity of image intensities within a homogeneous cylinder was calculated. The uniformity index (UI) metric is defined as

$$UI = \frac{100 \cdot \left(\overline{\mu}_{peripheral} - \overline{\mu}_{central} \right)}{\overline{\mu}_{central}}, \qquad (7)$$

where $\overline{\mu}_{central}$ and $\overline{\mu}_{peripheral}$ refer to the radial bin means for the pixels that are closest and furthest from the cylinder centroid respectively. A positive UI indicates image cupping (center < periphery) while a negative UI indicates image capping (center > periphery). The UI was calculated for each reconstructed cylinder to compare systematic intensity deviations within a cylinder for AM and FBP reconstructions.

2.5 Equivalent x-ray energy spectrum estimation

While measurement using an energy-selective detector is the most direct method to quantify the energy spectrum of a given x-ray beam, it is time consuming and costly as it requires specialized equipment. Monte Carlo methods can be used to estimate an x-ray spectra, but only if the beam transport and x-ray tube geometry can be fully and accurately characterized, along with the electrical potential waveform between the cathode and anode. As an alternative, we adopted Boone's equivalent spectrum method(Boone 1986; Boone 1988) in which a spectrum model is fit to measured attenuation data. The equivalent x-ray spectrum is thus an idealized x-ray energy distribution that matches the attenuation properties of the actual spectrum. This work utilized the well-established Birch-Marshall (BM) semi-empirical model for a tungsten-anode x-ray tube(Birch and Marshall 1979), which includes characteristic x-rays. The BM model, $\Phi_{BM}(E \mid kVp, mmAl)$, is a function of the known anode angle and two unknown free parameters, tube potential (*kVp*) and millimeters of inherent aluminum filtration (*mmAl*). It has been shown that the BM model using the known tube parameters overestimates the high-energy component of the spectrum, though Ay et al. found the differences between the BM modelled and measured spectra to be not statistically significant(Ay and Sarkar 2005). The equivalent spectrum method ensures the estimate

has a proper distribution of high and low energy photons since the BM model parameters are fit to the energy-dependence of measured attenuation data.

For each tube potential investigated in this work (90, 120 and 140 kVp), attenuation was measured on central-axis (CAX) through stacks of aluminum (Al) and copper (Cu) of varying total thickness. Fitting to attenuation curves of two materials with different energy dependence is shown to better condition the equivalent spectrum estimation, since there are two main interaction mechanisms in the diagnostic energy range(Sidky and Yu 2005). Fifteen Al thicknesses from 2.1 mm to 42.9 mm and fifteen Cu thicknesses from 1.0 mm to 15.4 mm were used, with the maximum thickness for each material chosen to attenuate the beam to roughly 10^{-3} of the primary intensity. A 2.1 mm thick Al filter was always placed immediately downstream of the Cu filter stack to avoid contaminating the detected signal with the 9 keV characteristic x-rays of Cu.

Narrow beam geometry was achieved by use of a collimator assembly as shown in figure 2. The phantom was immobilized such that the collimator opening was aligned to the central-axis (CAX) detector position ($\gamma = 0$), and was hung off the front of the CT table to avoid table attenuation and scatter. The collimator opening is ¼" wide allowing for roughly 5 to 6 central axis detectors to be irradiated. The scanner was operated in scout view mode, meaning the gantry was parked at the 6 o'clock position (β=180°) and the table was translated through the beam (z-direction) to collect multiple readings through each filter stack. At least 100 detector readings from the center of the collimator opening were averaged from the projection data to reduce statistical variation in each measurement. All data acquired for estimation of the x-ray spectrum were processed without the vendor-supplied BH correction. The ratio of detector signals *I* through the collimator assembly with and without a filter stack in place form the experimental measurement of attenuation, where *t* indexes the 30 measurements through both Al and Cu of varying total thickness:

$$T_{\exp}(t) = \frac{I(t)}{I(0)} \qquad (8).$$

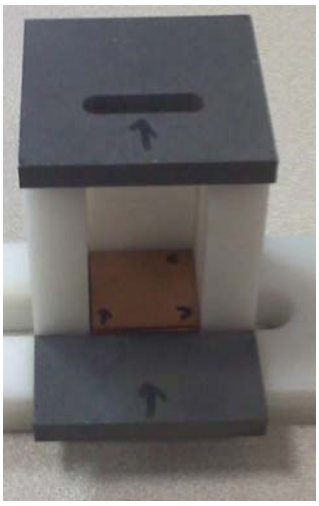

Figure 2: The attenuation measurement collimator assembly used for equivalent spectrum fitting. Stacks of high purity Al and Cu filters are placed in the phantom. The lead collimators are ¼" thick to block scattered radiation. The collimator opening is ¼" wide allowing approximately 5 to 6 detectors to be irradiated per view, and ¾" long in the z-direction allowing approximately 400 views to be acquired as the table translates in surview mode.

The expected transmission for a BM model spectrum $\Phi_{BM}(E \mid kVp, mmAl)$, through a stack of filters t with total thickness l_t is calculated by:

$$T_{\text{model}}(kVp, mmAl, t) = \frac{\sum_E E \cdot \Phi_{BM}(E \mid kVp, mmAl) \cdot BT(E) \cdot Detect(E) \cdot \exp\left(-\mu_t(E) \cdot l_t\right)}{\sum_E E \cdot \Phi_{BM}(E \mid kVp, mmAl) \cdot BT(E) \cdot Detect(E)}$$

$$BT(E) = \exp\left(-\mu_{BT}(E) \cdot l_{BT}(\gamma = 0)\right) \quad (9).$$

$$Detect(E) = \left(1 - \exp\left(-\mu_{\text{det}}(E) \cdot l_{\text{det}}\right)\right)$$

Attenuation coefficients $\mu_t(E)$ for the Al and Cu filters were calculated from NIST(Hubbell and Seltzer 1995) mass-attenuation coefficients, using certificates of analysis from the vendor to account for impurities in the metals, and measured the physical densities. The thickness of each individual filter l_t was also measured. The BM spectrum model and linear attenuation coefficients were all calculated on 1 keV energy steps. The BM model returns the particle-fluence spectrum of the x-ray beam, incident on the detector array. As the CT detectors are energy-integrating, multiplying by E converts to energy fluence. The term $Detect(E)$ represents a first-order correction for the quantum efficiency of the detector crystal of thickness l_{det}. $BT(E)$ represents the attenuation of the spectrum by the known central-axis bowtie filter (BT) thickness $l_{BT}(\gamma = 0)$. The equivalent spectrum thus represents the photon-counting spectrum just

upstream of the BT filter. The use of the CT detector array for transmission measurements, versus use of an independent ionization chamber, forms a closed measurement-model loop to account for errors in our simple detector-response model and the actual signal-formation process.

The equivalent spectrum is defined here as minimizing the sum of squared relative differences between the measured and modeled transmission values:

$$\Phi_0^{\mathrm{eq}}(\gamma=0,E)=\min_{\left(kVp_{\mathrm{eq}},mmAl_{\mathrm{eq}}\right)}\left[\sum_t\left(\frac{T_{\mathrm{model}}(kVp,mmAl,t)-T_{\exp}(t)}{T_{\exp}(t)}\right)^2\right] \quad (10).$$

The equivalent spectrum parameters kVp_{eq} and $mmAl_{eq}$ were found by performing a 2-D exhaustive search over a grid of BM parameter values; kVp and mmAl. Grid spacing was set such that ΔkVp = 1 keV and ΔmmAl = 0.1 mm.

For detectors away from central-axis, i.e. $\gamma \neq 0$, both the mean photon energy and the total incident energy fluence will be significantly modulated by the Brilliance's bowtie filter. Accounting for the detector-dependent energy distribution of the x-ray beam is essential for the polyenergetic AM algorithm to generate artifact-free image reconstructions. Inadequate modeling of the varying x-ray energy distribution across the detector array will cause systematic artifacts relative to the imaging axis for AM reconstruction. From an engineering diagram of the bowtie filter, the pathlength for each source-detector ray through the bowtie filter, $l_{BT}(\gamma)$, was calculated. The spectrum was further hardened by modeling the equivalent inherent filtration as an aluminum slab of thickness $mmAl_{\mathrm{eq}}$ and applying a $1/\cos\gamma$ correction for oblique filtration. In terms of the central-axis equivalent spectrum $\Phi_0^{eq}(\gamma=0,E)$, the equivalent detector-dependent spectrum $\Phi_0^{eq}(\gamma,E)$ is given by:

$$\Phi_0^{eq}(\gamma,E)=\Phi_0^{eq}(\gamma=0,E)\cdot\exp\left[-\mu_{BT}(E)\cdot l_{BT}(\gamma)-\mu_{Al}(E)\cdot mmAl_{\mathrm{eq}}\cdot\left(\frac{1}{\cos\gamma}-1\right)\right] \quad (11).$$

As the AM algorithm's forward model (2) does not explicitly incorporate detector modeling, the first-order detector model from (9) is applied to the equivalent detector-dependent spectrum before being provided to the AM algorithm as input data:

$$I_0(\mathbf{y},E)=E\cdot\Phi_0^{eq}(\gamma,E)\cdot Detect(E) \quad (12).$$

The off-axis hardening model (11) was validated by comparing the relative fluence profile $\sum_E I_0(\mathbf{y}, E)$ to the normalized measured in-air profiles $d(\bar{\beta}, \gamma : c = 0) / d(\bar{\beta}, \gamma = 0 : c = 0)$.

2.6. Scatter estimation using a beam-stop method

While the 1-D anti-scatter grid (ASG) on the Brilliance CT scanner can be expected to effectively reject large angle scatter, a non-trivial component of the scatter signal is due to small angle coherent scattering(Engel and Baumer 2008), which will bypass the ASG foils and contaminate the detected signal. The residual scatter signal was experimentally measured with a beam-stop technique in the spirit of Johns and Yaffe(Johns and Yaffe 1982). The scattered signal intensity was estimated from four measurements (M_1,…,M_4) for the CAX source-detector ray ($\gamma = 0$) for each cylindrical phantom at all three tube potentials. As a first-order correction, the signal intensity from scattered radiation was assumed to be constant for all detectors γ and all gantry angles β.

Borrowing from Endo's(Endo and Mori 2006) notation, the detected signal measured behind the scan subject M_1 is composed of three components:

$$M_1 = P + P' + S, \qquad (13)$$

where P is the signal from primary radiation originating from the focal spot, P' is the signal from off-focal radiation due to photon scattering upstream of the patient, e.g. in the BT filter, and S is the signal due to radiation scattered by the scan subject. A second measurement M_2 was taken with a ¼" thick lead block having finite width w inserted on CAX, which effectively blocks the signal from primary radiation ($P = 0$):

$$M_2(w) = \left[P' - P'_B(w)\right] + \left[S - S_B(w)\right]. \qquad (14)$$

As the off-focal signal P' does not originate from the focal spot, it passes around the beam-stopper and is still present in M_2. Here $P'_B(w)$ and $S_B(w)$ represent the reduction in off-focal and scatter components due to shadowing of the finite lead block of width w. To correct for block shadowing, $M_2(w)$ was measured for 3 block widths (w = 6, 10, and 15 mm) and the signal for a block of zero width, $M_2(w = 0) = P' + S$, was estimated as the intercept of a linear fit to the 3 blocker measurements. The effect of block shadowing

and this method of removal are well illustrated in Endo 2006(Endo and Mori 2006). The detected signal from primary radiation passing through the scan subject was then estimated as $P = M_1 - M_2(w=0)$.

The off-focal signal intensity is present in the absence of a scan subject, and is therefore considered as effective primary radiation. Neglecting to estimate and remove the off-focal component of signal intensity leads to an overestimation of the subject-scatter component. Estimation of the off-focal signal component was achieved by air measurements, i.e. with no scan subject present. Measurement of unblocked air signal will contain both primary and off-focal components:

$$M_3 = P_{air} + P'_{air} \quad (15)$$

The in-air off-focal signal component P'_{air} was estimated by in air measurement M_4 that uses the lead beam-stopper to block primary intensity ($P_{air} = 0$):

$$M_4(w) = \left[P'_{air} - P'_B(w)\right] \quad (16)$$

The block shadowing was again removed by repeating $M_4(w)$ for the three lead block widths and extrapolating to w=0 to give the in-air off-focal signal component $M_4(w=0) = P'_{air}$.

Since the radiation reaching the detector with the 1-D ASG in place is largely small angle scatter with little energy loss(Engel and Baumer 2008), the off-focal component is assumed to travel the same pathlength through the scan subject as the primary component. The ratio of the primary signal with and without the scan subject (P / P_{air}) was used to estimate the off-focal signal component attenuated by the scan subject:

$$P' = P'_{air} \cdot (P / P_{air}) \quad (17)$$

With the estimate of off-focal signal component passing through the scan subject *P'*, the component of detected intensity due to scatter from the scan subject, *S*, was calculated from (13). To perform the beam-stop scatter measurements just described, the scanner was operated in scout view mode, meaning the source was parked at a constant location as the table is translated in the z-direction. The lead beam-stoppers each have a length in

z of 21 mm, allowing at least 100 detector readings centered behind the beam-stopper to be averaged to reduce statistical variability.

3. Results

3.1. Equivalent x-ray spectrum estimation

The CAX equivalent spectra $\Phi_0^{eq}(\gamma = 0, E)$ derived from measured Al and Cu attenuation curves for the three investigated tube potentials are illustrated in figure 3. Table 1 summarizes equivalent BM spectrum model parameters which fit measured attenuation data to within 1.34% root mean square error. It is seen that the equivalent kVp of the BM model is within 1 keV of the nominal accelerating potential, and the equivalent millimeters of inherent aluminum filtration span a range of 0.3 mm across the three cases. In support of the off-axis spectral hardening model, the computed in-air energy fluence profiles of all three potentials match well with the measured air profiles as illustrated in figure 4 for the 120 kVp case.

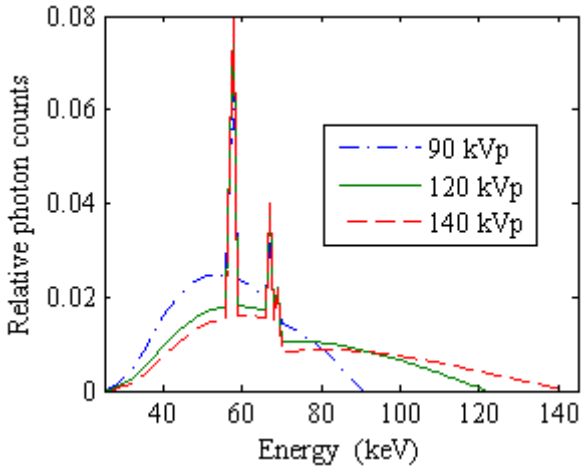

Figure 3. Equivalent Birch-Marshall x-ray spectra for three nominal tube potentials investigated in this work. All three spectra were normalized to have unit area for this plot.

Table 1. Equivalent Birch-Marshall spectrum parameters fit to attenuation measurements through Al and Cu filters on central axis (CAX). The root-mean-square and maximum errors between modeled and measured transmissions are reported as a percent of the measured values.

Nominal kVp (keV)	kVp_{eq} (keV)	$mmAl_{eq}$ (mm)	RMSE (%)	Max residual error (%)
90	90	12.5	1.34	3.81
120	121	12.3	1.07	1.54
140	141	12.6	1.20	2.03

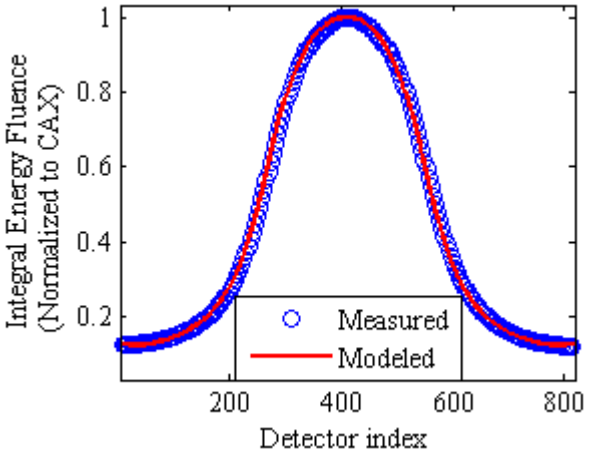

Figure 4. Example of excellent agreement between the measured and modeled in-air profiles for the 120 kVp nominal tube potential.

3.2. Measured scatter on central axis

Table 2 reports the measured scatter-to-primary ratios (SPR) reported as percentages for the cylindrical phantoms investigated in this work. Only the largest PMMA and Teflon cylinders, with diameters of 30.5 cm and 17.8 cm respectively, were estimated to have a SPR greater than 1%. From the beam-stop measurements made in air, the off-focal radiation, *P'*, was estimated to constitute 1.7% to 2.2% of the total signal for 90 kVp to 140 kVp respectively, which is in agreement with the literature(Johns and Yaffe 1982). If not accounted for in the beam-stopper measurements, the off-focal radiation leads to the SPR being overestimated by an additive 1.7% to 2.2% for all object sizes. For example, the smallest 5.1 cm PMMA disk at 120 kVp would have an estimated SPR of 2.25% if ignoring the off-focal radiation compared to 0.17% when accounting for the off-focal component.

Table 2. Measured scatter-to-primary ratios (%) for the 8 cylinders investigated in this work. With 3 mm beam collimation and the 1D-ASG, only the largest Teflon and PMMA cylinders have SPR > 1%.

Material	Water	PMMA				Teflon		
Diameter (cm)	20.3	5.1	15.9	20.3	30.5	5.1	11.4	17.8
90 kVp	0.20	0.13	0.44	0.68	2.91	0.09	0.49	1.36
120 kVp	0.59	0.17	0.34	1.00	3.00	0.21	0.80	1.93
140 kVp	0.39	0.18	0.48	0.63	3.63	0.27	0.59	2.72

3.3. Reconstructed image results – centered cylinders

Recall that radial averaging (section 2.4) was employed to assess the systematic intensity variations within reconstructed images of the homogeneous cylindrical phantoms. Figure 5 compares the mean profiles for the 8 cylindrical phantoms cylinders reconstructed with (from top to bottom) FBP of data without BH correction [$FBP_{BH\text{-}OFF}$], FBP of BH-corrected data [$FBP_{BH\text{-}ON}$], polyenergetic AM with no scatter estimate [$AM_{Sc\text{-}OFF}$], and polyenergetic AM including a constant scatter estimate [$AM_{Sc\text{-}ON}$]. The left column displays mean profiles for the four PMMA cylinders and the right column displays mean profiles for the water cylinder and the three Teflon cylinders. All data presented in this section are for the cylinders centered in the FOV; the off-centered reconstruction results are presented in the following section. All data in figure 5 were acquired at 120 kVp tube potential; the 90 kVp and 140 kVp results for the cylinders centered in the FOV show the same trends.

The polyenergetic AM mean profiles in figure 5 are absolute values of $c(x)$ using the single-basis object model (equation (1)) matched to the scan subject material. As the expected AM truth intensity is 1.0, absolute accuracy and relative % variations are easily visualized. The mean FBP profiles in figure 5 are normalized independently for each material. All PMMA bin means are normalized to the centermost bin mean of the 20.3 cm cylinder, all Teflon bin means to the centermost bin mean of the 11.4 cm cylinder, and all bin means for the 20.3 cm water cylinder are normalized to the centermost bin mean. Normalizing the mean FBP profiles for each material in figure 5 allows relative % variations of mean intensities for a given material to be more easily visualized.

The shape of the cupping artifact is easily discerned in the mean profiles of figure 5. The uniformity index (UI) was calculated to summarize the variation of image intensity within each homogeneous cylinder. Grouping all 24 image cases, i.e., all materials, all cylinder diameters and all tube potentials, figure 6 plots the cumulative distribution function of the UI values for each of the four reconstruction methods. Although the vendor's pre-reconstruction BH-correction improves FBP uniformity relative to uncorrected data, the polyenergetic AM algorithm performs better. The advantage of the polyenergetic AM algorithm is most substantial for the largest cylinders, since the x-ray spectrum has experienced more hardening. Taking the largest Teflon cylinder (17.8 cm) at 120 kVp for example, the UI for $AM_{Sc\text{-}OFF}$ is 0.5% compared to 1.9% for $FBP_{BH\text{-}ON}$. It should be noted that the largest UI values for the AM curves in figure 6 are due to error trends, which are discussed further below, while the largest FBP UI values are from cupping in the largest Teflon cylinders.

The mean profiles of $FBP_{BH\text{-}OFF}$ and $FBP_{BH\text{-}ON}$ in figure 5, not only show that the vendor-supplied BH correction reduces the systematic variations within a homogeneous object, but also reduces variations between objects of the same material and differing size. Comparing the overall mean intensity within each reconstructed cylinder (i.e., the average of all radial bin means), $FBP_{BH\text{-}ON}$ reconstructs all four PMMA cylinders to within 0.75% of each other. However, the mean intensity of the three Teflon cylinders using $FBP_{BH\text{-}ON}$ varies up to 2.5%. In comparison, polyenergetic $AM_{Sc\text{-}OFF}$ reconstructs both the PMMA and Teflon cylinders with overall mean intensities that vary less than 0.5% across all cylinder diameters.

The percent error of each polyenergetic AM radial bin mean is calculated in relation to the expected truth intensity of 1.0. The overall accuracy of the polyenergetic AM reconstructions is summarized in figure 7, which plots the cumulative distribution of radial bin mean errors for all centered cylinder experiments. The radial bins for all materials, object sizes, and tube potentials are grouped together. AM reconstruction using a constant scatter estimate from the beam-stop measurements is shown to bring most (90%) of the radial bins to within 0.45% of truth compared to $AM_{Sc\text{-}OFF}$ with 90% of radial bins within 0.84% of truth. The reduction in bias afforded by scatter correction is

greatest for larger disks where SPR was greater than 1%. This effect is easily visualized in the $AM_{Sc\text{-}OFF}$ and $AM_{Sc\text{-}ON}$ mean profiles of figure 5.

The largest errors seen in the CDF tails of figure 7 are a result of the same error trends mentioned previously that give the largest UI values for AM reconstruction. The first trend is an underestimation of intensity in the periphery of the 5.1 cm diameter Teflon and PMMA cylinders observed at all tube potentials. The mean profiles in figure 5 show that the magnitude of this "peripheral roll-off" for the 5.1 cm cylinders is approximately 1% and is present in both AM and FBP reconstructions. Figure 8 illustrates the peripheral roll-off in 120 kVp images of the 5.1 cm PMMA cylinder. The second error trend is an apparent underestimation for the centermost radial bins of the largest 30.5 cm diameter PMMA cylinder, again observed in images at all three tube potentials. The 120 kVp mean profiles of the 30.5 cm PMMA cylinder in figure 5 exhibit a relatively sharp drop in mean intensity of approximately 0.5% over the centermost two radial bins for both AM and FBP reconstructions.

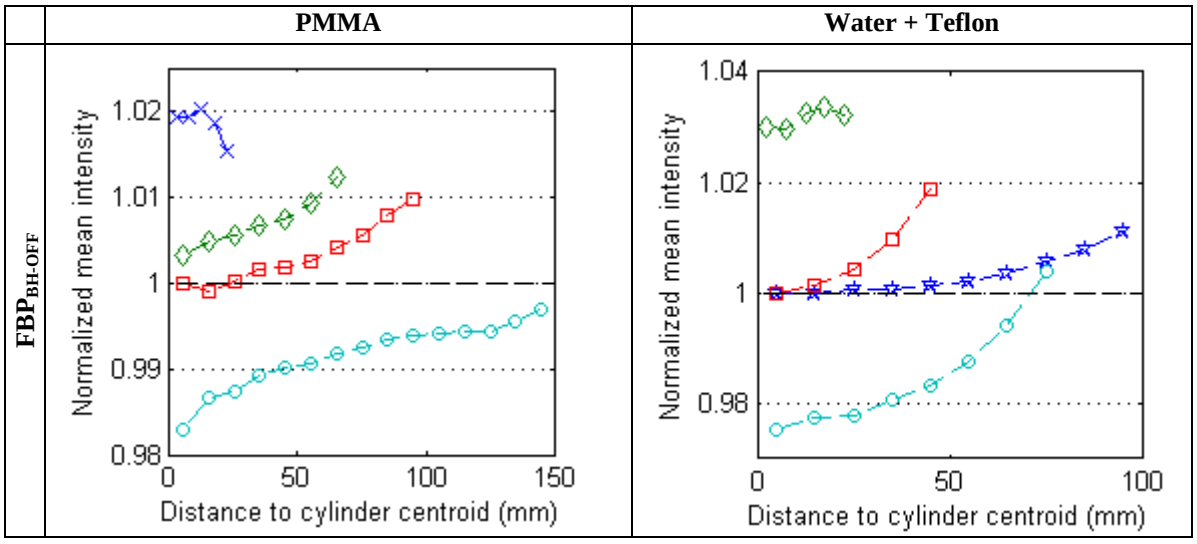

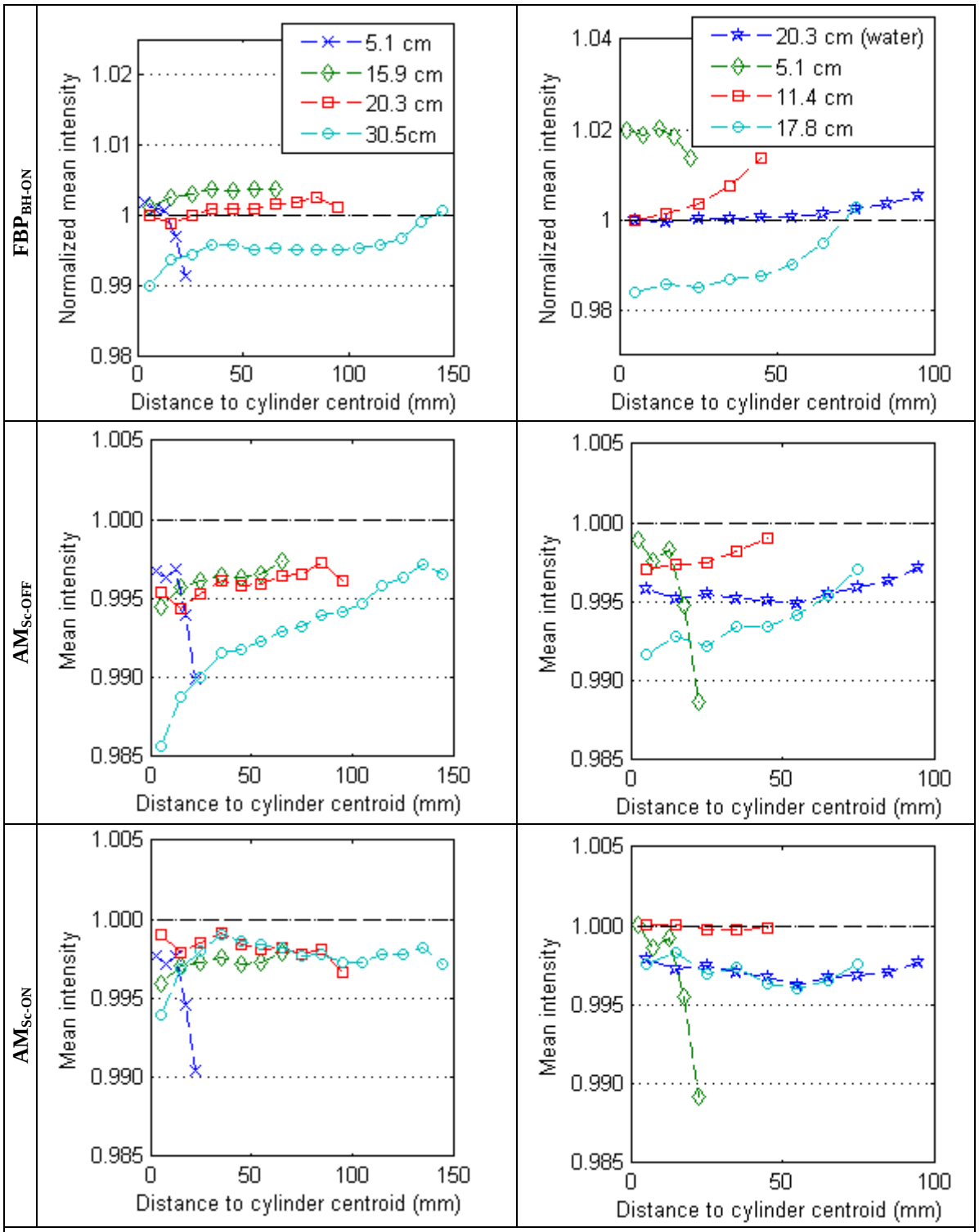

Figure. 5: Mean radial profiles for centered cylinders scanned at 120 kVp. Results for 90 kVp and 140 kVp are similar and are thus omitted. **LEFT** column displays the four PMMA cylinders and **RIGHT** column displays the water cylinder and three Teflon cylinders. The FBP profiles (**TOP** two rows) have been normalized to the centermost radial bin mean of the medium sized cylinders for all 3 materials, independently to display the relative variation of mean intensity for each material. The AM mean profiles (**BOTTOM** two rows) are absolute reconstructed intensities to display the error relative to expected ground truth intensity of 1.0. Note the varying y-axis scales.

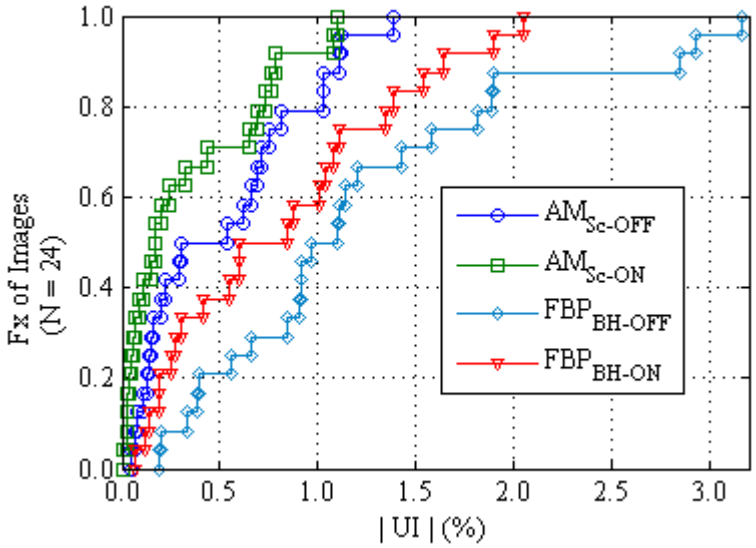

Figure 6. Cumulative distribution functions of the Uniformity Index for all reconstructed cylinders (8 cylinders at 3 tube potentials) sorted by reconstruction algorithm. Comparing the FBP reconstruction with and without BH corrections applied to the data (triangles and diamonds respectively) shows the improvement in image flatness by a current clinically used BH correction. It is seen that the implicit BH correction of the polyenergetic AM algorithm (circles) outperforms the FBP algorithm and that a scatter correction (squares) further enhances freedom from systematic cupping artifacts.

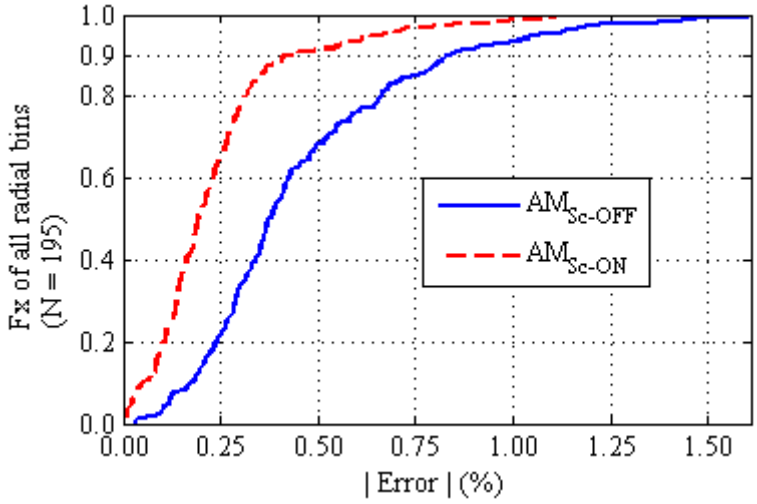

Figure 7. Cumulative distribution functions comparing the % error from expected truth of all polyenergetic AM radial bin means reconstructed with and without a constant scatter correction. Radial bin means from all cylinders and all tube potentials are grouped together into each CDF. It is seen that AM reconstruction with a constant scatter estimate from the central-axis beam-stopper measurements brings 90% of all radial bin means to within 0.45% of truth. Comparatively, AM without a constant scatter estimate reconstructs 90% of all radial bin means to within 0.84% of truth.

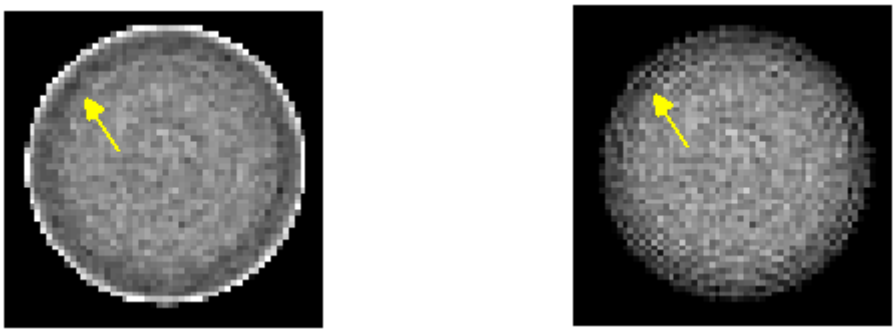

a) **b)**

Figure 8. 120 kVp images of the 5.1 cm PMMA disk scanned in air reconstructed with **(a)** $AM_{Sc\text{-}ON}$ and **(b)** $FBP_{BH\text{-}ON}$ illustrate the presence of the peripheral roll-off error trend seen in the mean profiles of the smallest 5.1 cm diameter PMMA and Teflon cylinders. A narrow window of ± 2% around the centermost radial bin mean is used for each image to display the 1% roll-off trend.

3.4. Off-centered cylinder results

Shifting the cylinders away from the imaging axis center allows assessment of the quantitative CT consistency criterion that image intensities for a given material be independent of subject location in the FOV. Figure 9 displays 140 kVp $AM_{Sc\text{-}ON}$ and $FBP_{BH\text{-}ON}$ reconstructions of the 15.9 cm PMMA cylinder shifted 9 cm away from the FOV center. It is seen that the intensities on the proximal edge, relative to the FOV

center, are systematically underestimated. This error trend was observed in the off-centered cylinders for all materials, object sizes, tube potentials, and reconstruction algorithms. The magnitude of the proximal edge depression varied between approximately 0.5% and 1.5% for the varying cylinder sizes. Excluding the peripheral radial bin, the off-centered results of image intensity consistency and AM absolute accuracy are nearly identical to the centered cylinder results presented above. Including a constant scatter estimate in the polyenergetic AM reconstruction of the off-centered cases decreased the systematic error in the same manner as seen for the centered cases. However, the magnitude of the proximal edge depression was unaffected by use of a constant scatter estimate.

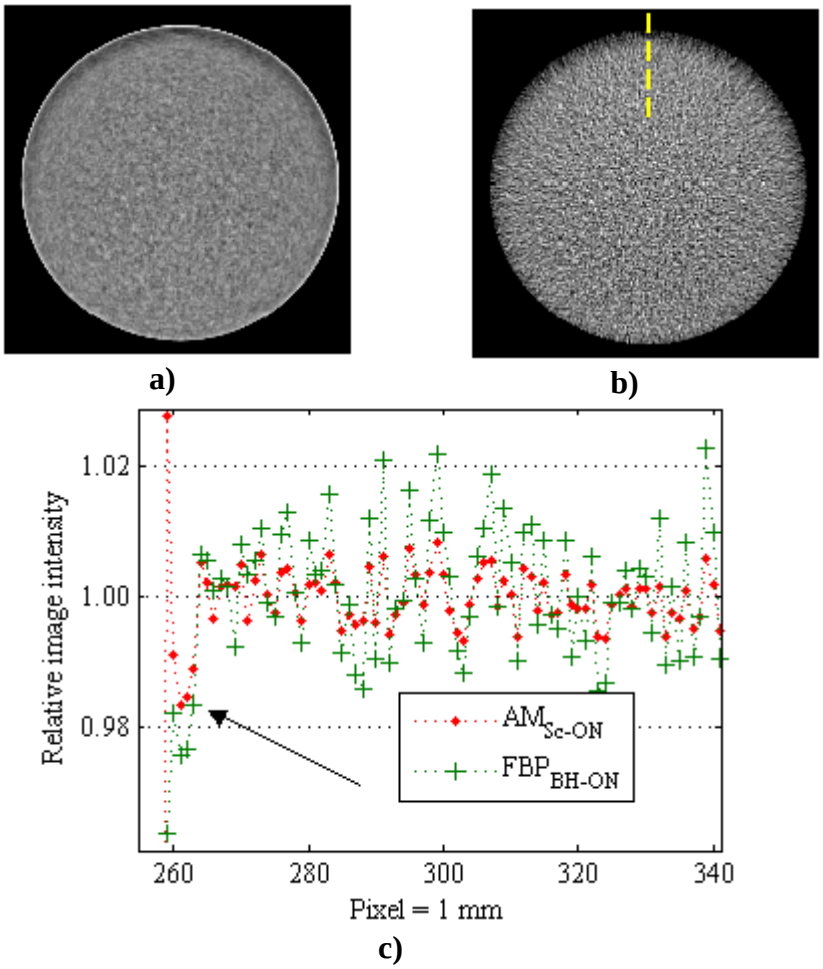

Figure 9. 140 kVp images of the 15.9 cm PMMA cylinder shifted ~ 9 cm down in the FOV reconstructed with $AM_{Sc\text{-}ON}$ and **(b)** $FBP_{BH\text{-}ON}$ illustrate the proximal edge depression. Images are displayed with a narrow window of ± 3% around the centermost radial bin mean. **(c)** Vertical line profiles through the images [location shown by dashed line in (b)] normalized to the centermost radial bin mean. The proximal edge depression is observed in all off-centered cylinder reconstructions, i.e. all algorithms, all materials, all object sizes, and all tube potentials.

4. Discussion

The results presented here show that the implicit beam-hardening correction of the polyenergetic AM algorithm reconstructs images that better meet a range of consistency criteria for quantitative CT applications than FBP reconstruction using a commercially available BH data correction. AM images show improved freedom from systematic cupping artifacts as evidenced by comparing uniformity within the

homogeneous cylinders. For the criterion of object-size independence, AM was found to reconstruct both PMMA and Teflon cylinders of various diameters to within 0.5% overall mean intensity, while FBP showed variation of up to 3% for the Teflon cylinders.

Including an estimate of scatter in the polyenergetic AM reconstruction was seen to further improve the relative uniformity of intensities within the cylinders and was found necessary to bring absolute AM accuracy to within 0.5%. Even for a 3rd generation geometry CT scanner with a highly collimated beam (3.0 mm width in the z-direction) and a 1-D ASG, scatter signal of greater than 1% were observed and were sufficiently large to sacrifice quantitative accuracy. For some quantitative applications, e.g., dual-energy estimation of photon cross sections, the loss of quantitative accuracy associated with neglecting scatter corrections would result in cross-section measurement errors exceeding 3%(Williamson and Li 2006). Increased slice thickness of multi-detector(Ohnesorge and Flohr 1999) and cone-beam geometries(Siewerdsen and Jaffray 2001) allow acceptance of greater amounts of scatter, making scatter correction for quantitative applications increasingly important in these scenarios.

Excluding the radial bin furthest from the cylinder centroid, the absolute AM accuracy and relative consistency results of the off-centered cases is nearly identical to those of the centered cases. However, all off-centered cylinder reconstructions were seen to suffer from a systematic underestimation on the proximal edge on the order of 0.5% to 1.5%. When shifting the cylinder away from the FOV center, the scatter can no longer be assumed to be symmetric across the detector array or constant for each gantry angle. We hypothesize that this proximal edge depression can be alleviated by incorporating detector and gantry angle dependent scatter estimates in image reconstruction. Future work is planned to assess this hypothesis by estimating detector and gantry angle dependent scatter profiles using an in-house transmission CT Monte Carlo code(Lazos and Williamson 2010) modified for the geometry of our 3rd generation commercial scanner.

Despite overall improved performance of the polyenergetic AM algorithm over conventional FBP, both reconstruction algorithms were seen to suffer from two error trends. The largest 30.5 cm PMMA cylinder shows an apparent depression of central mean values of about 0.5%. Both of the smallest 5.1 cm PMMA and Teflon cylinders

show a roll-off of peripheral mean intensities. Figure 10 displays AM and FBP reconstructed images of the 20.3 cm water cylinder with varying plastic inserts of 2.5 cm diameter. The 2.5 cm plastic cylinders in the water bath do not exhibit the peripheral roll-off of intensity seen for the 5.1 cm cylinders scanned in air. As both reconstruction algorithms exhibit the same error trends, it is not thought to be an inherent limitation of the AM algorithm. The causes of these error trends are currently unexplained and warrant future investigation.

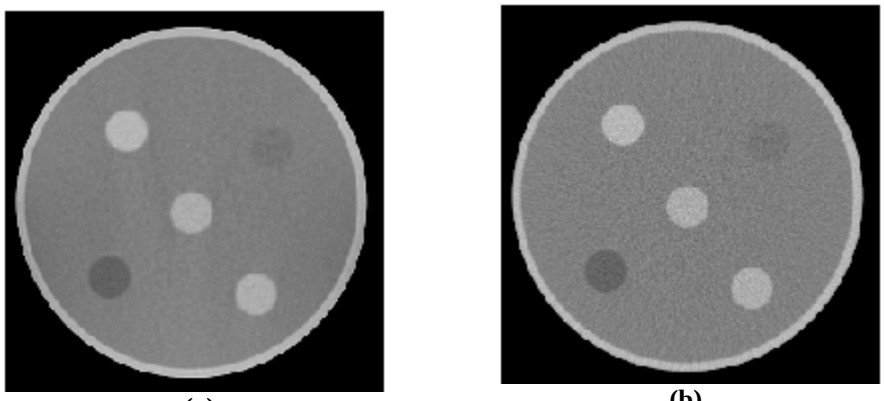

(a) **(b)**

Figure 10. 120 kVp images of the 20.3 cm water cylinder with 2.5 cm plastic inserts of various compositions including PMMA, acrylic and polystyrene. None of the 2.5 cm plastic inserts in the water bath reconstructed with either **(a)** $AM_{Sc\text{-}ON}$ or **(b)** $FBP_{BH\text{-}ON}$ exhibit the peripheral roll-off error trend observed for the 5.1 cm cylinders scanned in air. Images are displayed with a window of ± 30% of the mean water intensity.

Also of note is the presence of an edge-overshoot artifact at the air-phantom interface in the AM images, visible in figures 8a and 9a. The literature(Snyder and Miller 1987; Zbijewski and Beekman 2004) has shown these artifacts are in fact inherent to likelihood estimation methods and arise from sampling mismatches between the forward projection of a discrete object model and the measured projection data of a continuous physical object. Zbijewski(Zbijewski and Beekman 2004) shows that statistical reconstruction on a finer voxel grid effectively alleviates the edge-overshoot artifact as the inconsistency between discrete forward projections and measured data is reduced, but at the expense of longer computing times. For the fully statistical AM algorithm, Keesing et al.(Keesing and O'Sullivan 2006; Keesing and O'Sullivan 2007) have demonstrated the feasibility of speeding up the computation time by parallelizing the projection operations for a fully 3D helical geometry. Advances in computer

hardware and parallelization schemes are certainly an important area of research for bringing physically motivated statistical reconstruction algorithms into clinical use.

The use of a single-basis object model matched to the cylinder material was utilized in this work to provide a ground truth for which to quantitatively assess the accuracy of the AM intensities reconstructed from experimentally acquired data. However, it should be noted that reconstructed AM intensities will have a different interpretation when using a single-basis object model, equation (1), that is not matched to the scan subject material. When object model and subject material differ we expect from the polyenergetic forward model of equation (2) that the AM algorithm will reconstruct an image intensity that represents the spectrum-weighted ratio of subject and object-model linear attenuation coefficients. This is similar to the interpretation of FBP intensities as attenuation coefficients at the spectrally-averaged effective energy. Preliminary investigations have found support for this interpretation of mis-matched single-basis AM intensities, and future work intends to investigate the effect of this on polyenergetic AM image quality.

Assessing the reconstructed intensities relative to a ground truth allowed us to ensure that the x-ray spectrum distributions and scatter estimations were measured as accurately as possible. As shown in the results of Elbakri et al's(Elbakri and Fessler 2003) simulation study on polyenergetic statistical reconstruction, spectral mismatch directly leads to errors in the quantitative accuracy of reconstructed intensities. The presented accuracy of reconstructed AM intensities for a range of materials, cylinder diameters and locations within the FOV gives us confidence in the scatter and spectral estimates, especially in the model employed for off-axis spectral hardening due to the bowtie filter, supporting future work with data acquired on our Brilliance CT scanner.

5. Conclusions

The implicit beam-hardening correction of the polyenergetic AM algorithm is shown to reconstruct images that better meet consistency criteria for quantitative CT, i.e., that image intensities for a given material should be independent of subject size, location within a subject, and subject location within the FOV for data acquired on a commercial CT scanner at three tube potentials. Experimental methods to estimate scatter, the

equivalent x-ray spectrum, and to model off-axis spectral hardening from the bowtie filter are presented and are seen to be capable of supporting reconstructed AM image intensities to within 0.5% of expected. Two error trends were found to sacrifice AM accuracy in a limited number of cases. They were observed in both AM and FBP images and warrant further investigation. It is demonstrated that even in low scatter environments, i.e., narrow beam collimation and a 1-D ASG, a simple constant scatter correction is necessary to reconstruct mean image intensities with an accuracy of 0.5% in support of quantitative CT applications.

Acknowledgements

This work was supported in part from a grant (R01 CA 75371, J. Williamson, Principal Investigator) awarded by the National Institutes of Health and a grant funded by Varian Medical Systems.

References

Ay M R, Sarkar S, Shahriari M, Sardari D, Zaidi H 2005 Assessment of different computational models for generation of x-ray spectra in diagnostic radiology and mammography *Med Phys* **32** pp 1660-75

Bazalova M, Carrier J F, Beaulieu L, Verhaegen F 2008 Dual-energy CT-based material extraction for tissue segmentation in Monte Carlo dose calculations *Phys Med Biol* **53** pp 2439-56

Birch R, Marshall M 1979 Computation of bremsstrahlung X-ray spectra and comparison with spectra measured with a Ge(Li) detector *Phys Med Biol* **24** pp 505-17

Boden S D, Goodenough D J, Stockham C D, Jacobs E, Dina T, Allman R M 1989 Precise measurement of vertebral bone density using computed tomography without the use of an external reference phantom *J Digit Imaging* **2** pp 31-8

Boone J M 1986 Equivalent spectra as a measure of beam quality *Med Phys* **13** pp 861-8

Boone J M 1988 The three parameter equivalent spectra as an index of beam quality *Med Phys* **15** pp 304-10

Brooks R A, Di Chiro G 1976 Beam hardening in x-ray reconstructive tomography *Phys Med Biol* **21** pp 390-8

Cann C E 1988 Quantitative CT for Determination of Bone Mineral Density: A Review *Radiology* **166** pp 509-522

Chueh H S, Tsai W K, Chang C C, Chang S M, Su K H, Chen J C 2008 Development of novel statistical reconstruction algorithms for poly-energetic X-ray computed tomography *Comput Methods Programs Biomed* **92** pp 289-93

Csiszar I 1991 Why least squares and maximum entropy? An axiomatic approach to inference for linear inverse problems *Annals of Statistics* **19** pp 2032-2066

De Man B, Nuyts J, Dupont P, Marchal G, Suetens P 2001 An iterative maximum-likelihood polychromatic algorithm for CT *IEEE Trans Med Imaging* **20** pp 999-1008

Elbakri I A, Fessler J A 2002 Statistical image reconstruction for polyenergetic X-ray computed tomography *IEEE Trans Med Imaging* **21** pp 89-99

Elbakri I A, Fessler J A 2003 Segmentation-free statistical image reconstruction for polyenergetic x-ray computed tomography with experimental validation *Phys. Med. Bio.* **48** pp 2453-2477

Endo M, Mori S, Tsunoo T, Miyazaki H 2006 Magnitude and effects of x-ray scatter in a 256-slice CT scanner *Med Phys* **33** pp 3359-68

Engel K, Baumer C, Weigert J, Zeitler G 2008 Spectral analysis of scattered radiation in CT *Proceedings of SPIE - Physics of Medical Imaging* **6913** pp

675 Evans J D, Politte D G, Whiting B R, O'Sullivan J A, Williamson J F 2011 Effect of contrast magnitude and resolution metric on noise-resolution tradeoffs in x-ray CT imaging: a comparison of non-quadratic penalized alternating minimization and filtered backprojection algorithms *Proc. of SPIE - Physics of Medical Imaging* **7961** pp 79612C

Evans J D, Politte D G, Whiting B R, O'Sullivan J A, Williamson J F 2011 Noise-resolution
680 tradeoffs in x-ray CT imaging: a comparison of Penalized Alternating Minimization and Filtered Backprojection algorithms *Med Phys* **38** pp 1444-1458

Glover G H 1982 Compton scatter effects in CT reconstructions *Med Phys* **9** pp 860-7

Green P J 1990 Bayesian reconstructions from emission tomography data using a modified EM algorithm *IEEE Trans Med Imaging* **9** pp 84-93

685 Hubbell J H, Seltzer S M 1995 *Tables of X-Ray Mass Attenuation Coefficients and Mass Energy-Absorption Coefficients 1 keV to 20 MeV for Elements Z=1 to 92 and 48 Additional Substances of Dosimetric Interest*. Report No. NISTIR 5632, National Institutes of Standards and Technology, May 1995.

Hudson H M, Larkin R S 1994 Accelerated image reconstruction using ordered subsets of
690 projection data *IEEE Trans Med Imaging* **13** pp 601-9

Johns P C, Yaffe M 1982 Scattered radiation in fan beam imaging systems *Med Phys* **9** pp 231-9

Joseph P M, Ruth C 1997 A method for simultaneous correction of spectrum hardening artifacts in CT images containing both bone and iodine *Med Phys* **24** pp 1629-34

Joseph P M, Spital R D 1982 The effects of scatter in x-ray computed tomography *Med Phys* **9** pp
695 464-72

Kak A C, Slaney M 1988 Principles of Computerized Tomographic Imaging (New York: IEEE Press)

Keesing D B, O'Sullivan J A, Politte D G, Whiting B R 2006 Parallelization of a fully 3D CT iterative reconstruction algorithm," in, 2006, pp. *Proc. IEEE International Symposium on*
700 *Biomedical Imaging* pp 1240 – 1243

Keesing D B, O'Sullivan J A, Politte D G, Whiting B R, Snyder D L 2007 Missing data estimation for fully 3D spiral CT image reconstruction, J Hsieh & MJ Flynn (ed.) in Proceedings of SPIE: Medical Imaging 2007: Physics of Medical Imaging. San Diego, CA, USA, SPIE 65105V (12 pages)

705 Konig M 2003 Brain perfusion CT in acute stroke: current status *Eur J Radiol* **45 Suppl 1** pp S11-22

Lazos D, Williamson J F 2010 Monte Carlo evaluation of scatter mitigation strategies in cone-beam CT *Medical Physics* **37** pp 5456-5470

O'Sullivan J A, Benac J 2007 Alternating minimization algorithms for transmission tomography
710 *IEEE Trans Med Imaging* **26** pp 283-97

Ohnesorge B, Flohr T, Klingenbeck-Regn K 1999 Efficient object scatter correction algorithm for third and fourth generation CT scanners *Eur Radiol* **9** pp 563-9

Sidky E, Yu L, Pan X, Zou Y, Vannier M 2005 A robust method of x-ray source spectrum estimation from transmission measurements: Demonstrated on computer simulated, scatter-free transmission data *Journal of Applied Physics* **97** pp 124701

Siewerdsen J H, Jaffray D A 2001 Cone-beam computed tomography with a flat-panel imager: magnitude and effects of x-ray scatter *Med Phys* **28** pp 220-31

Snyder D L, Miller M I, Thomas L J, Politte D G 1987 Noise and edge artifacts in maximum-likelihood reconstructions for emission tomography *IEEE Trans Med Imaging* **6** pp 228-38

Valdiviezo C, Ambrose M, Mehra V, Lardo A C, Lima J A, George R T 2010 Quantitative and qualitative analysis and interpretation of CT perfusion imaging *J Nucl Cardiol* **17** pp 1091-100

Wang G, Yu H, De Man B 2008 An outlook on x-ray CT research and development *Med Phys* **35** pp 1051-64

Williamson J F, Li S, Devic S, Whiting B R, Lerma F A 2006 On two-parameter models of photon cross sections: application to dual-energy CT imaging *Med Phys* **33** pp 4115-29

Yan C H, Whalen R T, Beaupre G S, Yen S Y, Napel S 2000 Reconstruction algorithm for polychromatic CT imaging: application to beam hardening correction *IEEE Trans Med Imaging* **19** pp 1-11

Zbijewski W, Beekman F J 2004 Characterization and suppression of edge and aliasing artefacts in iterative x-ray CT reconstruction *Phys Med Biol* **49** pp 145-57

Appendix 5

Prospects for in vivo estimation of photon cross-sections using post-processing dual-energy CT imaging on a commercial scanner: comparison of analytic and polyenergetic statistical reconstruction algorithms

Prospects for in vivo estimation of photon cross-sections using post-processing dual-energy CT imaging on a commercial scanner: comparison of analytic and polyenergetic statistical reconstruction algorithms

Short Title: Experimental accuracy of post-processing DECT photon cross-section estimation.

J D Evans[1], B R Whiting[2], J A O'Sullivan[3], P Klahr[4] and J F Williamson[1]

[1]Department of Radiation Oncology, Virginia Commonwealth University, Richmond, VA 23298

[2]Mallinckrodt Institute of Radiology, Washington University, St. Louis, Missouri 63110

[3]Department of Electrical and Systems Engineering, Washington University, St. Louis, Missouri 63130

[4]Philips Healthcare, 595 Miner Rd., Highland Hts., OH 44143

Corresponding Author:

Jeffrey F. Williamson, Ph.D.

Department of Radiation Oncology

Virginia Commonwealth University

401 College Street, B-129

PO Box 980058

Richmond, VA 23298

804-828-8451 (Phone)

804-827-1670 (Fax)

jwilliamson@mcvh-vcu.edu

Abstract

Accurate patient-specific photon cross-section information is needed to support dose calculation for low energy photon modalities in medicine such as brachytherapy and kilovoltage x-ray imaging procedures. A post-processing dual-energy CT (pDECT) imaging technique for non-invasive *in vivo* photon cross-section estimation has been experimentally implemented on a commercial CT scanner. Materials of known composition and density were used to compare pDECT attenuation coefficient measurements to reference values over the 10 keV to 1 MeV energy range. Because statistical image reconstruction (SIR) has been shown to reconstruct images with less random and systematic error than conventional filtered backprojection (FBP), the pDECT technique was implemented with both an in-house polyenergetic SIR algorithm as well as a FBP reconstruction algorithm. Improvement from increased spectral separation was also investigated by additional filtration of the high-energy beam. When averaging a large number of pixels in-plane to reduce statistical uncertainty (reconstructed voxel size = 1x1x3 mm^3), the linear attenuation coefficient is estimated to within 1% of reference for energies of 30 keV to 1 MeV, with errors rising to 3% to 6% at 10 keV. The SIR algorithm is shown to estimate photon cross-sections with less random uncertainty than FBP owing to improved noise performance. However, the post-processing DECT method is shown to be highly sensitive to uncertainty in reconstructed images.

Key Words: computed tomography, dual-energy, alternating minimization, filtered backprojection, cross-section estimation

1. Introduction

Accurate in vivo mapping of photon cross-section information is needed to improve the dose-calculation accuracy of low energy photon-emitting radiation modalities such as brachytherapy, mammography, and x-ray computed tomography (CT). Large dose calculation errors can occur in these modalities if tissue composition and heterogeneities are ignored. For photon energies below 50 keV, estimated doses are exquisitely sensitive to tissue composition, as energy deposition is dominated by photoelectric absorption, which is strongly dependent on the material's atomic number. For example, neglecting tissue composition heterogeneities in low energy Pd-103 and I-125 permanent seed implants of the breast and prostate leads to errors in dose-volume histogram (DVH) metrics used for prescription and plan assessment ranging from 8% to 40% (Afsharpour and Pignol 2010; Carrier and D'Amours 2007; Chibani and Williamson 2005; Landry and Reniers 2010). Even higher energy brachytherapy sources, such as Ir-192 and Yb-169, have been shown to suffer dose calculation errors on the order of 5% to 30% when neglecting tissue composition and geometry (Lymperopoulou and Papagiannis 2006; Pantelis and Papagiannis 2005).

Single-energy CT (SECT) methods have been shown to support sufficiently accurate tissue heterogeneity corrections for megavoltage (MV) beam dose calculations (du Plessis and Willemse 1998; Schneider and Bortfeld 2000). However, for low kilovoltage (kV) modalities SECT methods have been found to introduce cross-section measurement errors in excess of 20%(Watanabe 1999), due to cross-section dependence on two independent parameters. Using recommended bulk tissue compositions(ICRP 2003) is not a satisfactory substitute for in vivo measurement as these recommendations are derived from a handful of measurements that exhibit large sample-to-sample variability(White and Widdowson 1991; Woodard and White 1986). In addition, large patient-to-patient variations in bulk tissue composition have been observed in some sites, for example the relative amount of glandular tissues in the breast has been shown to vary from 16% to 68% (Geise and Palchevsky 1996; Yaffe and Boone 2009). A method to non-invasively measure patient-specific, low-energy photon cross-section information would thus be of great value for improving dose-calculation accuracy for low energy

brachytherapy radiation therapy modalities and kV imaging procedures as well as improving the accuracy of quantitative CT applications.

CT scans at multiple energies can be used to de-couple the dependence of photon attenuation on two or more independent material parameters. Much effort has been focused on the use of dual-energy CT (DECT) information for material characterization, often in terms of electron density and effective atomic number(Heismann and Leppert 2003; Rutherford and Pullan 1976; Torikoshi and Tsunoo 2003). Electron density (ρ_e) and effective atomic number (Z_{eff}) have been shown to be estimated with errors ranging up to approximately 5% and 12%, respectively, from experimentally acquired DECT data of known test materials(Bazalova and Carrier 2008; Goodsitt and Christodoulou 2011). Bazalova et al. further reported dose calculated using the DECT estimated Z_{eff} and ρ_e values to be within 1% of dose calculated with exactly assigned material parameters for 18 MV, 6MV and 250 kVp photon beams(Bazalova and Carrier 2008). However, the effect of the Z_{eff} and ρ_e errors on dose for the low energy regime of brachytherapy seeds (10 – 30 keV) where the PE mechanism dominates is unclear.

The accuracy with which multi-energy CT can be used to directly estimate radiological cross-section values as input to more accurate model-based dose calculation algorithms has not been extensively studied. Midgley developed a non-separable four-parameter model capable of fitting low energy cross-sections to within 1.5% for energies greater than 30 keV in an idealized simulation(Midgley 2004). He further demonstrated cross-section estimation accuracy on the order of 1.5% (for energies between 32 keV and 66 keV) in an experimental study using near-monochromatic characteristic x-ray beam scanning(Midgley 2005). However, clinical implementation of this approach may not be feasible, as it requires scans at four energies using an x-ray source that cannot be easily extrapolated to clinical practice. In a simulation study, Williamson et al. demonstrated that a simple two-parameter basis-vector model could fit low energy cross-sections from ideal DECT images with 1% accuracy(Williamson and Li 2006). Though, their error analysis illustrated that the cross-section estimates are extremely sensitive to uncertainties in reconstructed CT image intensities. Similarly, Goodsitt et al. recently reported on difficulties obtaining accurate low energy cross-section estimates (in the form of synthesized monochromatic images) for known tissue-equivalent phantom materials from

data acquired on a commercially available DECT scanner(Goodsitt and Christodoulou 2011).

Statistical iterative reconstruction (SIR) algorithms, as they are founded on the inherently statistical nature of the data, have been shown to reconstruct images with less noise, for matched resolution, than conventional FBP reconstruction (Evans and Politte 2011; Ziegler and Kohler 2007). SIR algorithms can also incorporate more accurate models of the CT signal formation process, which has been shown to mitigate systematic artifacts such as cupping(De Man and Nuyts 2001; Elbakri and Fessler 2003; O'Sullivan and Benac 2007) and streaking(Williamson and Whiting 2002). By reducing random and systematic uncertainties of CT image intensity relative to FBP, we hypothesize that SIR can further improve the accuracy of pDECT photon cross-section measurements.

In this work, we evaluate the accuracy of linear attenuation coefficient estimates in the 10 keV to 1 MeV energy range derived from experimentally acquired DECT data reconstructed with conventional FBP and a polyenergetic SIR algorithm, Alternating Minimization (AM)(O'Sullivan and Benac 2007). Aqueous solutions and industrial plastics of known composition simulating a range of biological tissues are used to compare DE-estimated linear attenuation coefficients to NIST reference coefficients in idealized phantom geometries scanned on a Philips Brilliance Big Bore CT scanner. Increased DE spectral separation is also investigated for potential performance improvement via additional filtration of the high kVp beam. To the best of the authors' knowledge, this is the first work to systematically assess the cross-section accuracy achievable by a post-processing DECT method using data acquired on a commercially available CT scanner.

2. Materials and methods

2.1. Test substances and phantom geometries

The three basis materials and eight test substances used in Williamson et al.'s theoretical study of post-processing DECT photon cross-section measurement were physically realized in this work as reported in Table 1. The solutions of precise percent-by-mass composition were fabricated by mixing high purity dehydrated salts, or ethanol

(ETOH), with high purity water, using a calibrated analytical balance with estimated uncertainty of 0.1 mg. An elemental analysis (Elemental Analysis Inc., Lexington, KY) was performed on the solid plastic rods to account for high and medium Z impurities, which if neglected, were found to induce mass-attenuation coefficient differences of up to 1.5% in the low energy range. The mass density of each material was estimated to within 0.5% uncertainty by measuring the mass of a known volume, determined by machining samples of known dimensions for the solid samples and measured using a Fisherbrand Finnipette II in the case of the solutions. The compositions, measured impurities and mass densities are used to derive the total linear attenuation coefficient benchmark, $\mu_{NIST}(E)$, as a function of photon energy for each material in table 1, using the NIST XCOM program (NIST Standard Reference Database 8)(Hubbell and Seltzer 1995). In this work, the word cross-section is also used to describe the attenuation coefficient of a material as the two quantities are related by the material-specific density constant. The meaning of the basis pair reported in table 1 is described later in section 2.3.

Table 1. Basis materials and test substances investigated in this work. Note the composition percentages denote fraction by mass. "Basis pair" refers to the two materials used to represent a test substance, as described in sections 2.2 and 2.3

Substance	Composition	State	ρ (g/cm^3)	Basis pair (α,β)
	Basis Materials			
Water	H_2O	Liquid	1.000	-
Polystyrene	$[C_8H_8]_n$	Solid	1.044	-
23% $CaCl_2$	23% $CaCl_2$, 77% H_2O	Liquid	1.214	-
	Test Substances			
18% $CaCl_2$	18% $CaCl_2$, 82% H_2O	Liquid	1.166	(Water, 23% $CaCl_2$)
7% $CaCl_2$	7% $CaCl_2$, 93% H_2O	Liquid	1.066	(Water, 23% $CaCl_2$)
29% $NaClO_3$	29% $NaClO_3$, 71% H_2O	Liquid	1.237	(Water, 23% $CaCl_2$)
Teflon	$[C_2F_4]_n$	Solid	2.155	(Water, 23% $CaCl_2$)
ETOH	100% C_2H_5OH	Liquid	0.787	(Water, Polystyrene)
50% ETOH	50% C_2H_5OH, 50% H_2O	Liquid	0.909	(Water, Polystyrene)
Methyl-ethyl ketone (MEK)	$CH_3CH_2COCH_3$	Liquid	0.804	(Water, Polystyrene)
PMMA (Lucite)	$[C_5H_8O_2]_n$	Solid	1.186	(Water, Polystyrene)

All solutions were contained in 30 mL polyethylene Nalgene bottles with outer diameters of 34 mm with the exception of Methyl-ethyl ketone (MEK), which due to its corrosiveness, was stored in a 31 mm diameter, 30 mL vial with 1 mm thick Teflon walls. The solid rods had a diameter of 26 mm. The solutions and solid rods were immobilized in the center of a cylindrical water phantom using an out-of-field acrylic plate. The water cylinder (Victoreen CT performance phantom) consists of a 20.3 cm diameter water cylinder enclosed by a 6 mm thick acrylic shell for a total diameter of 21.5 cm (figure 1). The 21.5 cm water cylinder is referred to as the *head phantom* geometry. To test accuracy within a phantom more representative of a pelvic patient, a 26 cm x 35 cm elliptical acrylic shell was placed around the water cylinder. This setup is referred to as the *body phantom* geometry. Images of the head and body phantoms with a pure ethanol (ETOH) sample positioned at their centers are displayed in figure 1.

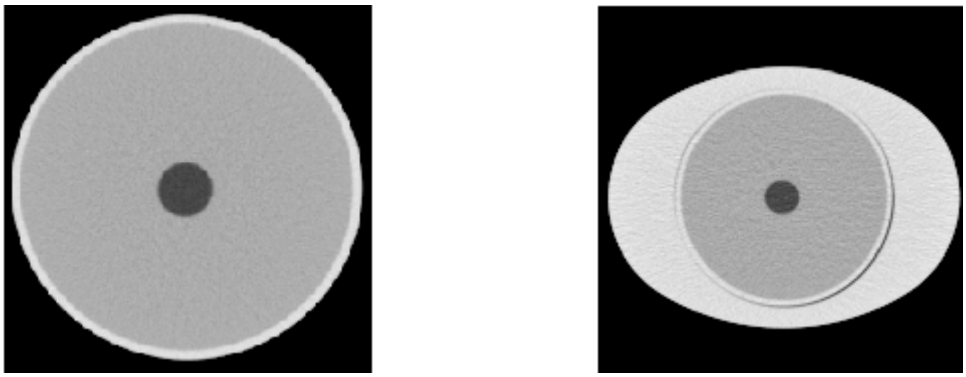

(a) (b)

Figure 1. FBP images of the **(a)** *head phantom* and **(b)** the *body phantom*, with ETOH samples at their centers Scan parameters are 90 kVp and 220 mAs, with 3 mm beam collimation. Images are windowed to [-40% : +20%] of the mean water intensity.

2.2. The two-parameter basis vector model and dual-energy CT

Two-parameter models are the core of DECT methods, as they relate CT image intensity to the underlying material properties to be estimated. Williamson et al.(Williamson and Li 2006) found that the two parameter basis-vector model, in which photon cross sections of an arbitrary material are approximated as a weighted mixture of two dissimilar reference materials (basis substances), more accurately represents low-energy cross sections than the more widely used parametric fit model, which represents cross-sections as simple functions of effective atomic number (Z_{eff}), energy, and electron density (ρ_e) (Rutherford and Pullan 1976).

The basis vector model (BVM)(Lehmann and Alvarez 1981) utilized here assumes that the linear attenuation coefficient of an unknown material in voxel *x* can be accurately represented as a linear combination of two basis substances α and β:

$$\mu(x,E) = w_\alpha(x)\cdot\mu_\alpha(E) + w_\beta(x)\cdot\mu_\beta(E), \qquad (1)$$

where $w_\alpha(x)$ and $w_\beta(x)$ are the weighting coefficients for each basis substance. Assuming that reconstructed CT image intensities are proportional to the linear attenuation coefficient of the substance occupying the location *x*, at the effective scanning energies E_1 and E_2, the BVM results in a pair of linear equations with two unknowns, $w_\alpha(x), w_\beta(x)$:

$$\begin{aligned}\mu(x,E_1) &= w_\alpha(x)\mu_\alpha(E_1) + w_\beta(x)\mu_\beta(E_1)\\ \mu(x,E_2) &= w_\alpha(x)\mu_\alpha(E_2) + w_\beta(x)\mu_\beta(E_2)\end{aligned}, \qquad (2)$$

which can be solved on a voxel-by-voxel basis, yielding a basis-vector image $\left(w_\alpha(\mathbf{x}), w_\beta(\mathbf{x})\right)$.

This post-processing dual-energy CT (pDECT) technique does not require explicit knowledge of E_1 and E_2 as the basis material expansion vectors $\left(\mu_\alpha(E_1), \mu_\alpha(E_2), \mu_\beta(E_1), \mu_\beta(E_2)\right)$ are obtained from calibration images acquired using the same scanning technique as the test substances. Given that the composition and density of the basis materials are known, the basis coefficient images $w_\alpha(\mathbf{x})$ and $w_\beta(\mathbf{x})$ derived from the DECT image pair can be used to estimate the entire photon cross-section curve as a function of energy for the substance at location *x* from equation (1). Williamson et al. show that the basis weights can be further used to calculate other radiological quantities, such as partial cross-sections, mass-energy absorption coefficients, and differential cross-sections(Williamson and Li 2006) required by radiation transport codes. In this work, the focus is on the accuracy with which the BVM model can estimate the total linear attenuation coefficient of the test substances.

2.3. Dual-energy data acquisition

All dual-energy CT data were acquired on the Philips Brilliance 16 detector-row Big Bore CT scanner (Philips Medical Systems, Cleveland, OH) used in VCU's radiation oncology clinic, utilizing clinically available protocols and tube potentials. Axial scan protocols were used (denoted in the vendor's software as *Axial Pelvis*) for scanning both head and body phantom geometries. The data from the central 4 rows of detectors, each 0.75 mm wide in the z-direction, were averaged together to give an axial slice thickness of 3 mm. This is the narrowest beam collimation available and was chosen to minimize the amount of scattered radiation. Maximum allowable tube currents for the chosen scan protocols of 220 mAs and 175 mAs were used to acquire dual-energy data at tube potentials of 90 kVp and 140 kVp, respectively. These acquisition parameters lead to $CTDI_{vol}$ dose values in a pelvis phantom (as reported on the scanner) of 8.7 mGy (90 kVp) and 22.7 mGy (140 kVp). For calibrating the basis substances in the body phantom geometry, repeat scans were acquired and the data averaged to simulate higher dose

scans. This was to avoid systematic streaking artifacts that are known to arise from photon starvation (Hsieh 1998) in the larger body phantom. However, all of the test substances in the body phantom, unless otherwise noted in the results section, were acquired with the standard protocol described above.

The raw data, corrected only for dark current, were exported from the scanner for processing and reconstruction. Proprietary software provided by Philips enabled any of the standard data preprocessing corrections to be applied or omitted. System corrections such as detector gain, reference detector normalization, slice normalization and crosstalk were applied to all data in this work. The Brilliance scanner uses a 1-D anti-scatter grid (ASG) for physical scatter rejection, and does not apply any additional scatter correction to the data. Two sets of processed data were generated from each raw dataset; one with the vendor's proprietary water-equivalent beam hardening (BH) correction turned on for conventional FBP reconstruction, and one with the BH correction omitted for reconstruction with the polyenergetic AM algorithm.

Previous literature has shown that additional filtration of the high kVp beam improved the dual-energy material discrimination problem (separating iodine and bone)(Primak and Ramirez Giraldo 2009) by increasing the separation of the high and low energy scanning spectra. To test the potential of this strategy to improve pDECT cross-section imaging, a high purity tin filter of 0.5 mm thickness was machined to be retrofitted to the Brilliance CT's collimator system. Figure 2 shows how the additional tin filtration increases the spectral separation between the low and high energy scans. The accuracy of cross-section estimation is compared using DE image pairs acquired with the standard 90 kVp and 140 kVp beams (*90+140 Std*) and DE image pairs acquired with the standard 90 kVp beam and the tin filtered 140 kVp beam (*90+140 Tin*). However, it should be noted that the 0.5 mm tin filter reduces the 140 kVp beam particle fluence incident on the scan subject to approximately 25% of its standard intensity, meaning the tin filtered 140 kVp data is acquired with less dose and will have more quantum noise.

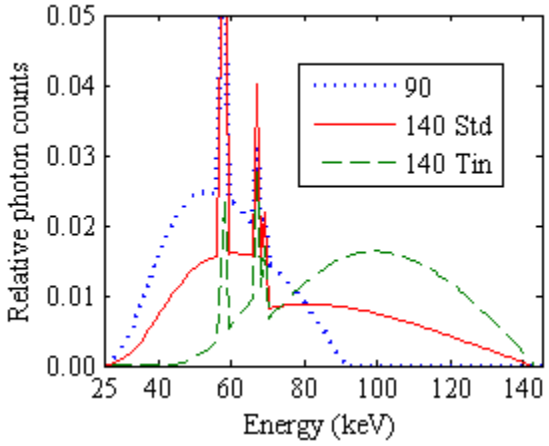

Figure 2. X-ray spectra (normalized to unit area) for DE imaging. It is seen that additional tin filtration of the 140 kVp beam increases the spectral separation with the standard 90 kVp beam. Spectra were estimated by fitting a Birch-Marshall model to measured attenuation data as described in section 2.4.

The calibration basis material image intensities $\left(\mu_\alpha(E_1), \mu_\alpha(E_2), \mu_\beta(E_1), \mu_\beta(E_2)\right)$ required for pDECT analysis were averaged within 7 mm or 9 mm diameter circular regions-of-interest (ROIs) centered on each plastic rod or solution respectively. Basis material calibration measurements were obtained within both the head and body phantom geometries, using the data processing and reconstruction as for the test substance scans. Hence, basis and test material intensities were measured under identical conditions except for differences between sample composition and density. In this near ideal situation, the impact of residual artifacts arising from non-linearities such as beam-hardening and scatter within the test substance datasets will be minimized.

Regarding choice of basis materials, previous work (Williamson and Li) found that BVM modeling accuracy was improved by using two pairs of bases. Materials with Z_{eff} lower than water were modeled by a basis pair of water and polystyrene while higher Z materials (Z_{eff} > water) were represented as linear combinations of water and a 23% $CaCl_2$ aqueous solution. Each image pixel x is classified as low-Z or high-Z, and assigned the corresponding basis pair, by comparing the relative CT image intensities at low and high-energy:

$$\begin{cases} \left(\frac{\mu_x}{\mu_{water}}\right)(E_1) \le \left(\frac{\mu_x}{\mu_{water}}\right)(E_2); \ (\alpha,\beta) = (\text{Water, polystyrene}) \\ \left(\frac{\mu_x}{\mu_{water}}\right)(E_1) > \left(\frac{\mu_x}{\mu_{water}}\right)(E_2); \ (\alpha,\beta) = (\text{Water, 23\% } CaCl_2) \end{cases} . \quad (3)$$

In practice, image noise can lead to pixel misclassification, i.e., assignment of a pixel to the sub-optimal basis pair. To avoid potential bias in comparing one reconstruction algorithm to another due to varying magnitudes of image noise, the pixels that are known to lie within the test substance are assigned the ideal basis pair as denoted in Table 1.

2.4 Dual-energy attenuation coefficient accuracy endpoints

Once the basis pair is assigned for each pixel, the basis material weighting coefficients, $\left(w_\alpha(\mathbf{x}), w_\beta(\mathbf{x})\right)$, are then calculated for each pixel *x*, using the reconstructed DE image intensities, $\left(\mu(\mathbf{x}, E_1), \mu(\mathbf{x}, E_2)\right)$, and the averaged basis material intensities calibrated in the appropriate phantom geometry and at the appropriate scan energies, $\left(\overline{\mu_\alpha}(E_1), \overline{\mu_\alpha}(E_2), \overline{\mu_\beta}(E_1), \overline{\mu_\beta}(E_2)\right)$.

From the basis coefficient images, the linear attenuation coefficient can be estimated at any energy *E* from equation (1) for every pixel location *x*. For pixels within the test sample footprint, pDECT accuracy was quantified by the ratio of the measured to NIST reference attenuation coefficient as a function of energy in the 10 – 1000 keV range. The distribution of pixel-specific cross-section ratios within each ROI was used to quantify statistical uncertainty of pDECT measurements. The mean pDECT bias was quantified as the attenuation coefficient ratio averaged over the sample ROI pixels, $\left(\overline{\mu_{DE}}(E)_{\mathbf{x}\in ROI} \Big/ \mu_{NIST}(E)\right)$.

The sensitivity of the estimated linear attenuation coefficients to input image uncertainty was investigated using the law of propagation of uncertainty(Taylor and Kuyatt 1994). As described in more detail in Williamson et al.'s 2006 paper(Williamson and Li 2006), the estimated uncertainty in the six reconstructed image intensities (four calibration values and two values at each voxel *x*) required by equations (1) and (2) are used to compute the uncertainty of the DE estimated attenuation coefficient, $\mu_{DE}(x, E)$.

2.5. Polyenergetic Alternating Minimization image reconstruction

The sinogram data exported from the scanner is denoted by $d(\mathbf{y})$ where the data space, $\mathbf{y}=(\gamma,\phi)$, is defined by the angle of each source-detector pair ray, γ, and each gantry angle, ϕ. The 2-D image space is composed of a 512 x 512 rectangular array of 1 mm square pixels with 1.0 mm length on a side where **x** denotes the indices of each pixel. For the Alternating Minimization (AM) algorithm, an object is represented in image space as a map of linear attenuation coefficients that depend on spatial location x and energy E. The object is represented as a weighted sum of N basis materials:

$$\mu(\mathbf{x},E)=\sum_{i=1}^{N}\mu_i(E)c_i(\mathbf{x}), \qquad (4)$$

where $\mu_i(E)$ denotes the linear attenuation spectrum of the ith basis material. The AM algorithm will estimate N images that represent the partial density of each basis material in each voxel; $c_i(\mathbf{x})$. In this work, we reconstruct images with a single basis substance (N=1) of water. Given this restriction, AM models the sinogram data, by computing the expected data means g from an image estimate **c'** according to the forward model

$$g(\mathbf{y}:c')=\sigma(\mathbf{y})+\sum_{E}I_0(\mathbf{y},E)\cdot\exp\left(-\sum_{x\in X}h(\mathbf{y}\mid\mathbf{x})\cdot\mu_{water}(E)\cdot c'(\mathbf{x})\right). \qquad (5)$$

The system matrix, $h(\mathbf{y}\mid\mathbf{x})$, is the average distance traveled by photons crossing pixel x that are incident on the face of detector γ for gantry angle ϕ and is pre-computed to increase the speed of the iterative algorithm. An estimate of scattered radiation, $\sigma(\mathbf{y})$, can be included in the forward model, though none is included in the main data cases presented here since using the same phantom geometry for test substances and basis material calibrations is expected mitigate the effect of scatter. $I_0(\mathbf{y},E)$ denotes the x-ray particle fluence spectrum incident on the scan subject. Incorporating the x-ray spectrum directly in the AM algorithm's forward model represents an implicit beam-hardening correction. The polyenergetic AM algorithm thus operates on energy-uncompensated data; that is data with all system pre-processing corrections performed excluding the vendor's BH correction.

The AM algorithm's objective function is based on Csisazar's I-divergence(Csiszar 1991), $I(d\,\|\,g)$, a scalar-valued information-theoretic measure of the

discrepancy between two functions, in this case the noisy measured data $d(\mathbf{y})$ and the expected noiseless data means $g(\mathbf{y})$, equation (5). The I-divergence is proportional to the negative of the Poisson log-likelihood, which means that the image which minimizes the I-divergence also maximizes the log-likelihood of observing the data $d(\mathbf{y})$. The reformulation of the optimization problem in terms of the I-divergence and a novel application of the convex decomposition lemma allow for a closed form image update step. The reader is referred to O'Sullivan et al. 2007(O'Sullivan and Benac 2007) for a more complete treatment of the AM algorithm.

The penalized objective function includes a penalty term to enforce the *a priori* assumption of image smoothness:

$$\Phi(\mathbf{c}') = I(d \,||\, g) + \lambda \cdot R(\mathbf{c}'), \qquad (6)$$

where **c'** is the current image estimate and λ controls the relative weighting of the penalty function. A value of λ=5.0x10^{-4} is used for all AM reconstructions in this work and was chosen from preliminary reconstructions that were found to well balance noise and resolution. The roughness penalty $R(\mathbf{c}')$ computes a penalty for all pixels **x** as a function of the neighboring pixel intensities **x**'. The edge-preserving log-cosh penalty function(Elbakri and Fessler 2003; Green 1990) used in this work is defined as

$$R(\mathbf{c}') = \sum_{\mathbf{x}} \sum_{\mathbf{x}' \in N(\mathbf{x})} w(\mathbf{x}') \cdot \left(\frac{1}{\delta}\right) \log\left[\cosh\left(\delta\left(c'(\mathbf{x}) - c'(\mathbf{x}')\right)\right)\right], \qquad (7)$$

where $N(\mathbf{x})$ is the set of neighboring pixels weighted as $w(\mathbf{x}') = 1$ for the four directly adjacent pixels and as $w(\mathbf{x}') = 0$ for all other pixels. The parameter δ controls the penalty transition from quadratic to linear growth. Here δ = 15 is used, which corresponds to a transition at intensity differences of 10% from background. For a more detailed treatment of the parameters λ and δ in the log-cosh penalized AM algorithm, the reader is referred to Evans 2011 (Evans and Politte 2011). Ordered subsets are utilized to increase the convergence rate (Hudson and Larkin 1994). All AM images are reconstructed using 1024 iterations and 33 ordered subsets, which was found to ensure the images were well converged.

The x-ray spectrum, $I_0(\mathbf{y}, E)$, required by the AM forward projection model was obtained by fitting the semi-empirical Birch-Marshall spectrum model, including

tungsten characteristic x-rays, to narrow-beam attenuation curves through high purity aluminum and copper filters of varying thickness for the central-axis ($\gamma = 0$) source-detector ray. The resultant equivalent spectrum model (shown in figure 2) fit the measured attenuation data to within 1.5% RMS error for all tube potentials investigated in this work, including the tin filtered 140 kVp beam. The off-axis hardening of the spectrum due to the bowtie filter was modeled by computationally hardening the central axis equivalent spectrum with the known thickness and material of the filter. More details are given elsewhere (Evans and Whiting 2011), including a demonstration that AM was able to reconstruct homogeneous phantom image intensities with 0.5% accuracy.

2.6. Filtered backprojection image reconstruction

An in-house weighted filtered back-projection algorithm (Kak and Slaney 1988) was used for two reasons: to ensure that FBP and AM used the same system matrix $h(\mathbf{y}\,|\,\mathbf{x})$ for, and to allow management of the FBP reconstruction kernel. Preliminary studies comparing in-house FBP reconstructions with the Philips clinical software and our in-house algorithm have revealed no discernible differences. The sinogram data were pre-processed with all Philips corrections, including the beam-hardening (BH) correction. Since no vendor-supported BH correction was available for the 140 kVp beam with the additional 0.5 mm of tin filtration, pDECT was not performed using FBP reconstruction of *90+140 Tin* sinogram pairs. The in-house FBP filter, *H(f)*, is a modified ramp filter defined in frequency space as

$$H(f) = s \cdot |f| \cdot W(f) \cdot G(f), \qquad (8)$$

where *s* is a constant scale factor that ensures the image intensities represent units of linear attenuation, mm^{-1}, and $|f|$ is the ramp function. *W(f)* is a rectangular window function up to frequencies of 90% of Nyquist which then rolls off with a raised cosine function to zero at Nyquist frequency. More detailed information regarding this modified ramp filter can be found in Evans (Evans and Politte 2011). *G(f)* is the Fourier transform of a Gaussian smoothing kernel, which allows control of reconstructed image noise and resolution by further reducing the amplitude of high spatial frequencies. As a first-order

attempt to match the resolution of AM and FBP images, the FWHM of the Gaussian smoothing kernels, 1.0 mm and 2.0 mm for head and body phantoms respectively, were selected so that FBP and AM images exhibited similar edge-response functions at the PMMA rod boundary (Evans and Politte 2011).

390

3. Results

Post-processing DECT is illustrated in figure 3 for the 50% ETOH solution in the head phantom scanned with the *90+140 Std* energy pair. For the 50% ETOH solution, the ideal pair of basis materials is (α,β) = (water, polystyrene). From the basis
395 coefficient images, it can be seen that the 50% ETOH is modeled as being predominantly composed of polystyrene. In the water background the α basis coefficient (always water) dominates as expected. The total linear attenuation coefficient at any energy can be estimated using the basis coefficient images and equation (1). Here, simulated mono-energetic images calculated at 28 keV and 100 keV are presented. It is seen that the
400 contrast between the polystyrene test substance and the water background is increased in the 28 keV image, however the image noise is greater due to larger attenuation coefficient estimation uncertainty at lower energies as shown later.

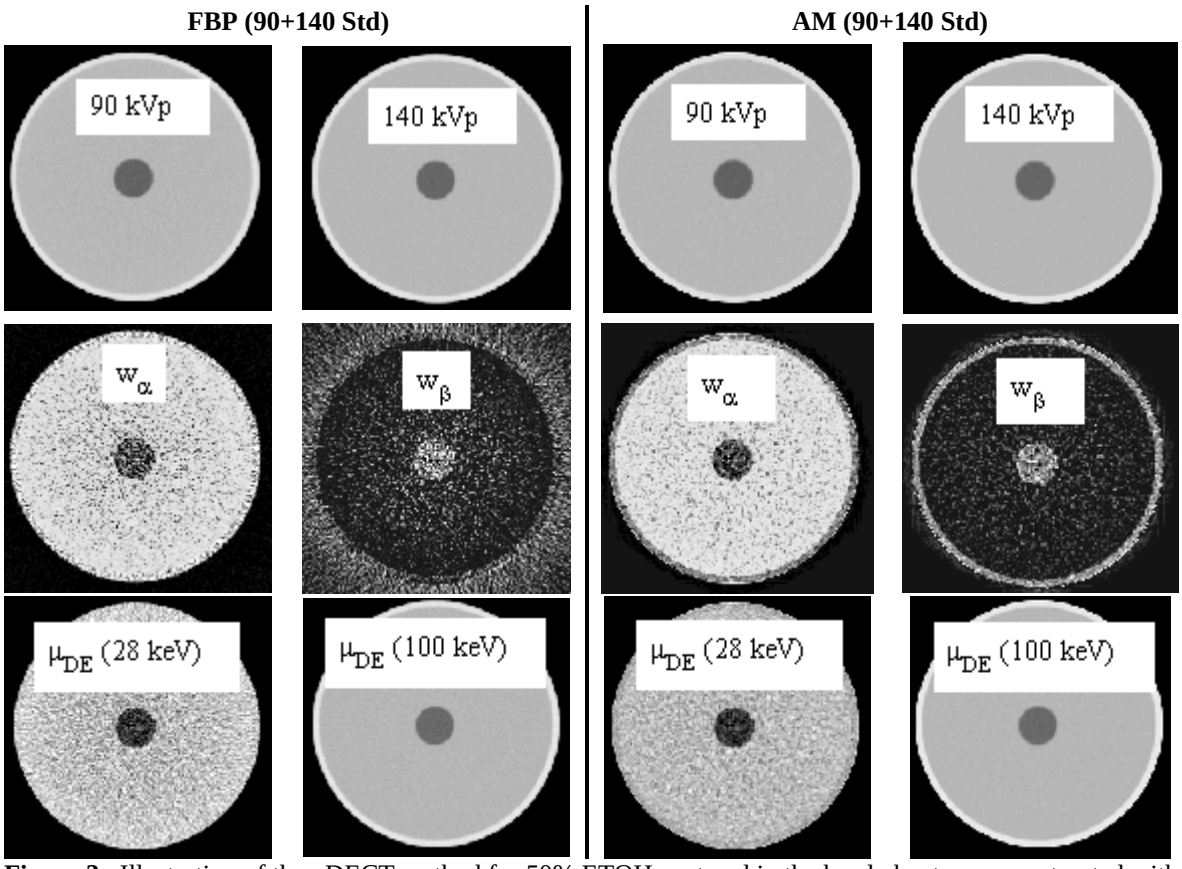

Figure 3. Illustration of the pDECT method for 50% ETOH centered in the head phantom reconstructed with FBP (**Left**) and AM (**Right**). **Top Row**: Reconstructed images of 90 kVp and 140 kVp sinogram data. In conjunction with the corresponding basis material calibration images, the DE images are used to calculate the basis material weighting coefficient images (**Middle row**). From the basis coefficient images, monoenergetic images can be calculated at any energy. **Bottom row**: Displayed here are mono-energetic linear attenuation images computed at 28 keV and 100 keV. Note that all images are windowed to [-50% : +20%] of the mean water intensity, except the w_α, w_β images, which are windowed to weights of [-0.1 : +1.1].

405

The ratio of total linear attenuation coefficients estimated by pDECT to NIST reference values is used to assess pDECT accuracy. The mean ratio of the pixels within each test substance ROI, $\left(\overline{\mu_{DE}}(E)_{\mathbf{x}\in ROI} \Big/ \mu_{NIST}(E) \right)$, is plotted as a function of energy in figure 4. In both the head and body phantom geometries, FBP and polyenergetic AM 410 estimate total linear attenuation with a mean error (or bias) of 0.5% to 1.0% for energies above 30 keV to 40 keV. However, for lower energies, mean error exceeds 1% rising to 2% to 3% at 10 keV for most materials and 3% - 6% for Teflon.

For the MEK in the body phantom a higher effective scanning dose was required to achieve the displayed level of mean accuracy for the MEK in the body phantom. The higher effective scanning dose was achieved by averaging seven repeat acquisitions for a slice of data 12 mm wide in *z*. All other test substances were acquired with the standard dose and 3 mm slices as described in section 2.3. Data with inadequate signal statistics, i.e., acquired without enough dose, can suffer from systematic streaking artifacts due to photon starvation(Hsieh 1998). Using the standard scanning protocol, mean MEK linear attenuation coefficient estimates deviated by as much as 60% from NIST reference at 10 keV.

At first glance, increasing the spectral separation by using the *90+140 Tin* spectral pair does not appear to improve the pDECT-AM accuracy, and is in fact slightly worse for certain materials. However, it is tough to draw conclusions at this point as the scanning dose is not matched between the *140 Std* and *140 Tin* protocols. As noted in section 2.3, the 0.5 mm tin filter reduces the total photon fluence incident on the scan subject to about 25% of its unfiltered intensity. Mean bias for the *90+140 Tin* protocol may also be expected to decrease as effective scanning dose increases, as was the case for the MEK in the body phantom.

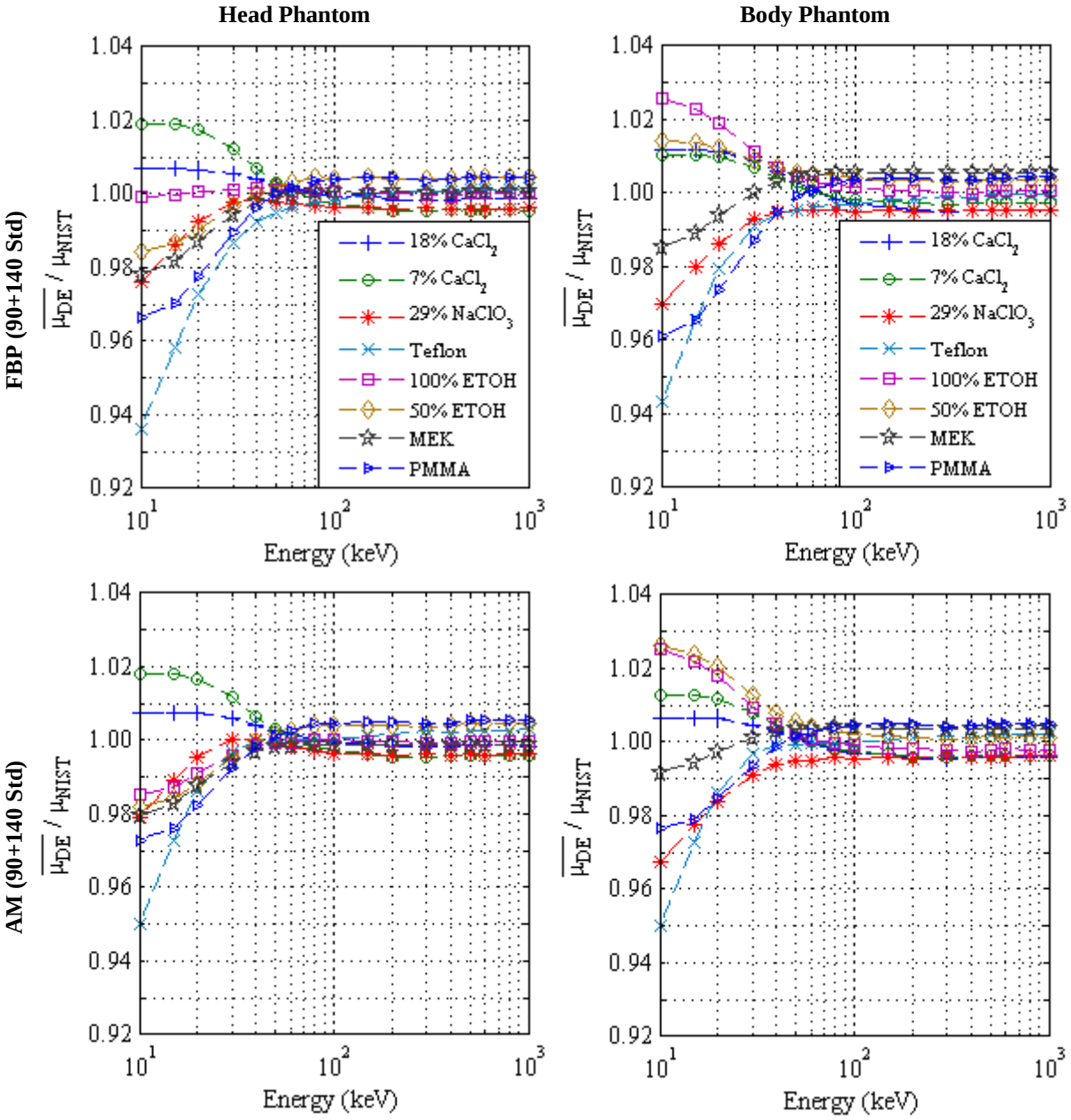
Head Phantom
Body Phantom
FBP (90+140 Std)
AM (90+140 Std)
$\overline{\mu_{DE}} / \mu_{NIST}$
Energy (keV)
18% $CaCl_2$
7% $CaCl_2$
29% $NaClO_3$
Teflon
100% ETOH
50% ETOH
MEK
PMMA

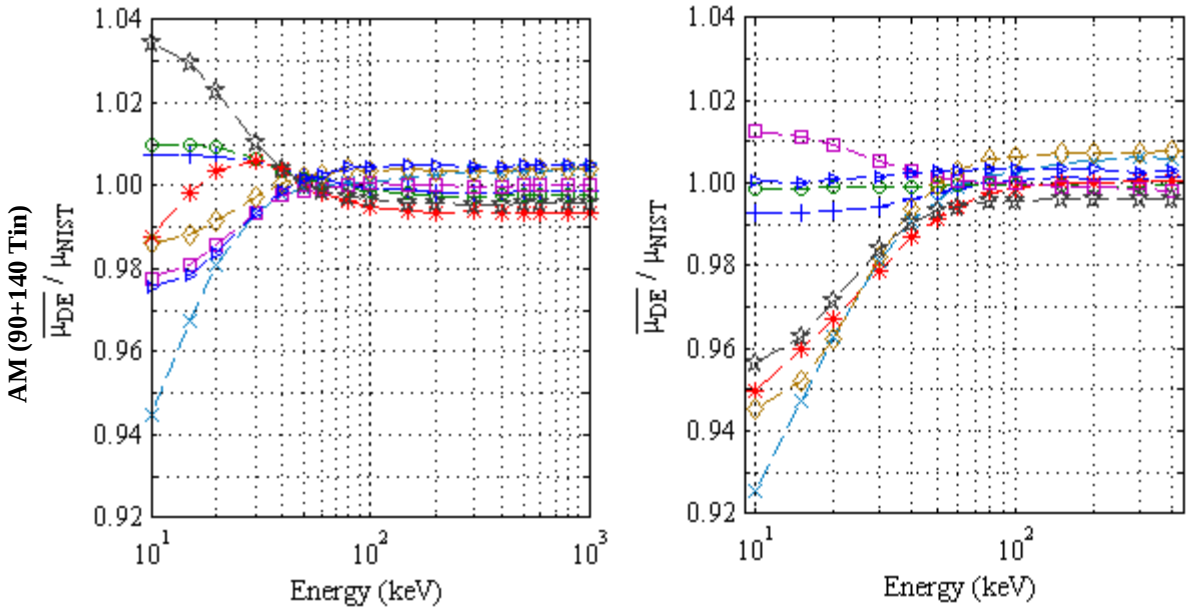

Figure 4. Ratio of mean pDECT estimated cross-sections (averaged over all pixels within the material ROI) to NIST reference values for all test substances. Columns denote test substances centered in the (**Left**) head phantom and (**Right**) body phantom geometries. Rows compare accuracy *90+140 Std* DE images using (**Top**) FBP and (**Middle**) AM reconstruction and (**Bottom**) AM reconstruction using the *90+140 Tin* image pair with increased spectral separation. All data was acquired with the standard scanning doses and 3 mm slice thicknesses, except for the three basis materials and the MEK test substance in the body phantom (**Right**). For these materials in the body phantom a higher effective dose was achieved by averaging seven repeat acquisition for a 12 mm slice thickness.

While the mean pDECT attenuation coefficient estimation accuracy for each material is important, the accuracy will vary from pixel-to-pixel due to image noise. Figure 5 displays the distribution of $\mu_{DE}(\mathbf{x},E)/\mu_{NIST}(E)$ ratios for pixels within the PMMA rod ROI at 28 keV for the various pDECT scenarios. The mean of the distribution corresponds to the mean bias at 28 keV, as displayed in figure 4. The standard deviation of the distribution provides a measure of how widely the pDECT attenuation coefficient estimate varies for pixels within the test substance ROI. Figure 5 shows that while both AM and FBP images give a mean bias of less than 1.4% for PMMA at 28 keV in the head phantom, the pDECT estimates have a wider spread using FBP reconstruction (σ = 12.2%) than when using AM reconstruction (σ=7.5%). The situation is seen to be similar in the body phantom case.

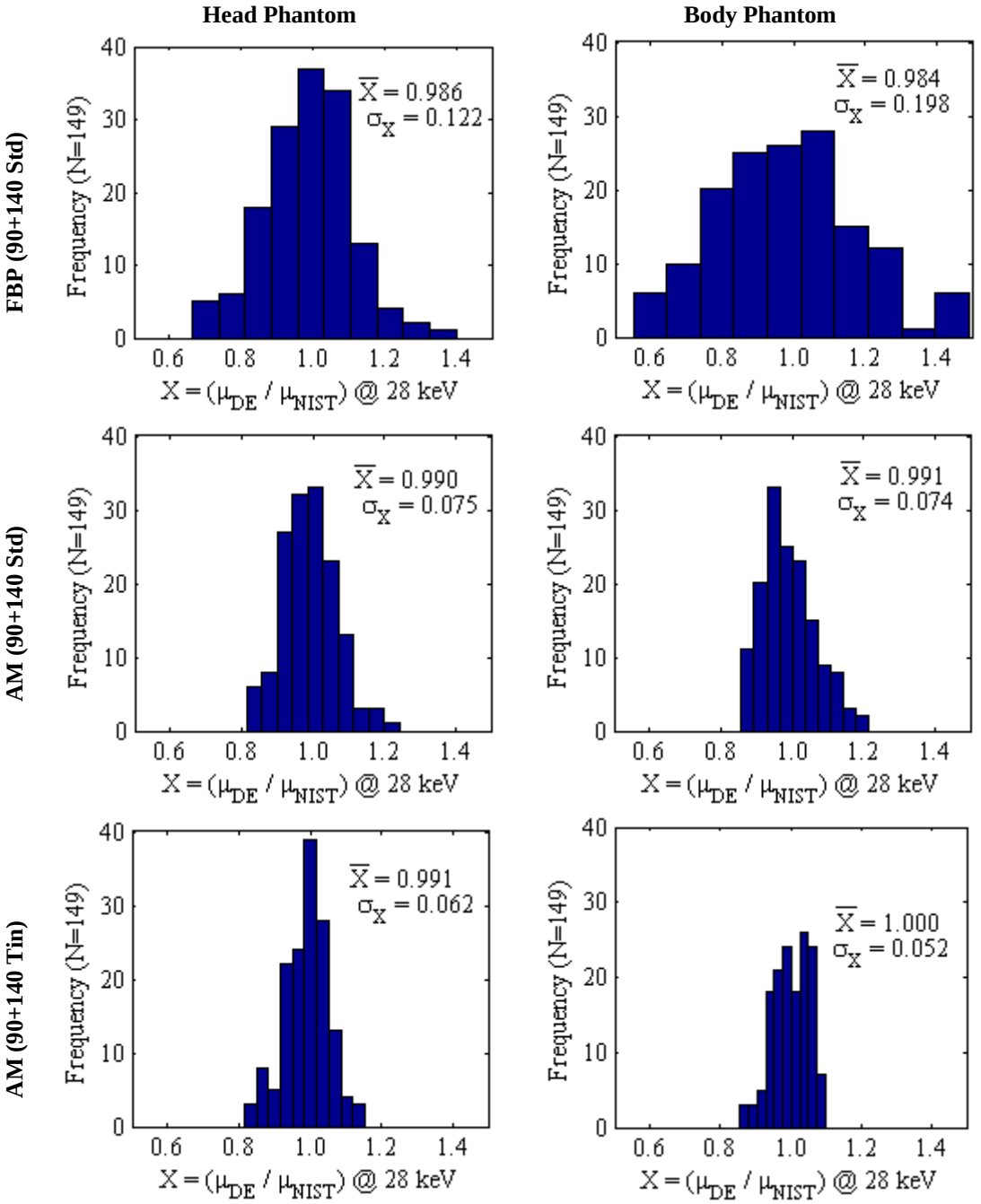

Figure 5. Distribution of bias for pixels within the PMMA ROI at 28 keV. Images were all acquired with the standard scanning protocol and reconstructed with 1x1x3 mm^3 voxel dimensions. **Left** column is for the head phantom and **right** column is for the body phantom. Rows compare the cross-section bias distribution for *90+140 Std* DE images using (**Top**) FBP and (**Middle**) AM reconstruction and (**Bottom**) AM reconstruction using the *90+140 Tin* image pair with increased spectral separation. For each distribution of ratios, the mean and standard deviation is reported.

The width of the bias distribution for each test substance illustrates the impact of image noise on pDECT performance. To summarize the results, table 2 reports the mean and standard deviation of the attenuation coefficient errors for all pixels within each test substance for all pDECT scenarios. 200 keV is taken as representative of energies between 100 keV and 1 MeV, where mean bias of less than 1% is consistently achieved and 28 keV is representative of low-energy applications, where mean attenuation coefficient estimation errors often exceed 1%. Comparing values at 28 keV and 200 keV shows us that both the mean bias (systematic uncertainty) and the standard deviation of the bias (random uncertainty) of estimated attenuation coefficients are larger at low energies.

460

Table 2. Mean percent error of pDECT attenuation coefficients relative to NIST reference values within the test substance ROIs at 28 keV and 200 keV. Values in parentheses denote the corresponding standard deviation of the pDECT error over all pixels within the test substance ROIs. Scanning doses and reconstructed pixel dimensions are the same as described in figure 4.

Test Substance	Energy (keV)	Phantom	FBP (90+140)	AM (90+140)	AM (90+140 Tin)
18% $CaCl_2$	28	Head	0.5% (4.7%)	0.6% (2.6%)	0.6% (2.3%)
		Body	0.9% (8.5%)	0.5% (3.9%)	-0.6% (2.6%)
	200	Head	-0.2% (1.5%)	-0.2% (0.8%)	-0.2% (1.0%)
		Body	-0.5% (2.4%)	-0.4% (1.2%)	0.1% (1.0%)
7% $CaCl_2$	28	Head	1.2% (7.4%)	1.1% (4.2%)	0.6% (4.2%)
		Body	0.6% (9.7%)	0.7% (3.7%)	-0.3% (4.3%)
	200	Head	-0.5% (1.6%)	-0.4% (0.9%)	-0.3% (1.1%)
		Body	-0.3% (1.6%)	-0.4% (0.6%)	-0.1% (1.1%)
29% NaClO3	28	Head	-0.5% (6.0%)	-0.2% (3.1%)	0.4% (3.8%)
		Body	-1.0% (10.2%)	-1.1% (4.0%)	-2.4% (4.3%)
	200	Head	-0.4% (1.4%)	-0.4% (0.7%)	-0.7% (1.4%)
		Body	-0.5% (2.0%)	-0.4% (0.8%)	0.0% (1.3%)
Teflon	28	Head	-1.7% (6.3%)	-0.6% (2.8%)	-1.0% (2.7%)
		Body	-1.2% (8.8%)	-0.6% (2.4%)	-2.3% (3.2%)
	200	Head	0.0% (1.1%)	0.2% (0.5%)	0.3% (0.7%)
		Body	-0.2% (1.2%)	0.1% (0.4%)	0.5% (0.7%)
ETOH	28	Head	0.0% (17.3%)	-0.6% (10.8%)	-0.9% (10.7%)
		Body	1.1% (25.3%)	1.0% (12.4%)	0.5% (8.8%)
	200	Head	0.0% (1.8%)	0.0% (1.1%)	0.0% (1.5%)
		Body	0.1% (2.2%)	-0.2% (1.2%)	-0.1% (1.3%)
50% ETOH	28	Head	-0.5% (13.1%)	-0.7% (8.0%)	-0.5% (8.8%)
		Body	0.9% (22.7%)	1.3% (9.6%)	-2.2% (5.9%)
	200	Head	0.4% (1.5%)	0.4% (0.9%)	0.4% (1.5%)
		Body	0.3% (2.6%)	0.1% (1.1%)	0.7% (0.9%)
MEK	28	Head	-0.8% (20.1%)	-0.8% (12.7%)	1.1% (9.4%)
		Body	-0.8% (12.7%)	0.6% (16.6%)	-1.9% (8.3%)
	200	Head	0.1% (2.0%)	-0.1% (1.3%)	-0.4% (1.3%)
		Body	1.5% (2.9%)	1.6% (3.1%)	-0.4% (1.0%)
PMMA	28	Head	-1.4% (12.2%)	-1.0% (7.5%)	-0.9% (6.2%)
		Body	-1.6% (19.8%)	-0.9% (7.4%)	0.0% (5.2%)
	200	Head	0.4% (1.2%)	0.5% (0.7%)	0.5% (0.8%)
		Body	0.4% (1.9%)	0.5% (0.8%)	0.3% (0.7%)

The law of propagation of uncertainty was employed to further investigate the sensitivity of the estimated linear attenuation coefficient to errors in the reconstructed CT images. Figure 6 plots the percent unexpanded uncertainty (coverage factor of $k = 1$) of the linear attenuation coefficient estimate of the test material as a function of energy. Note that the term 'uncertainty' refers to the total uncertainty arising from both systematic and random components. For this propagated uncertainty analysis, we chose the total input image uncertainty for all eight test materials to have the same input image intensity uncertainty of 0.50% and 0.25% at 90 kVp and 140 kVp, respectively. Basis material image uncertainty was chosen to be 0.07% (90 kVp) and 0.03% (140 kVp). These levels of input image-intensity uncertainty were chosen as they are similar to the image noises reconstructed using the standard scanning protocol. It is seen that this level of reconstructed image uncertainty leads to pDECT attenuation coefficient uncertainty of around 1% for energies greater than 50 keV. The uncertainty increases as energy decreases, ranging from 4% to 20% at 10 keV. This is similar to the trend of the mean bias increasing for low energies as shown in figure 4 and table 2. Figure 6 also illustrates that for the same input reconstructed image uncertainty, the pDECT attenuation coefficient estimate is more sensitive for some materials than others. Broadly speaking, the test substances that use the (water, polystyrene) basis pair are more sensitive to input image error than the test substances that use the (water, 23% $CaCl_2$) basis pair.

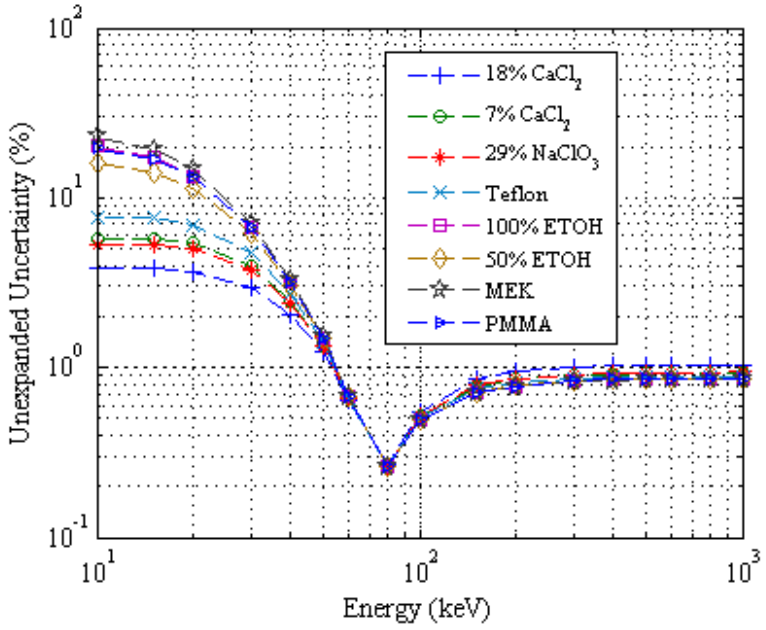

Figure 6. Percent unexpanded (k=1) uncertainty of the DE estimated linear attenuation coefficient as a function of energy. All eight test materials are shown here and were assumed to have the same input image uncertainty of 0.50%, 0.25% (90, 140 kVp) and basis uncertainty of 0.07%, 0.03%. This level of input image uncertainty was chosen as it was similar to the reconstructed image noises using the standard scanning protocol employed here for 1x1x3 mm^3 voxel dimensions.

Using the law of propagated uncertainty, we can also answer the question, "what reconstructed image uncertainty is required to achieve a target attenuation coefficient uncertainty at a given energy?" Table 3 reports the image uncertainty needed to achieve DE estimated attenuation coefficient uncertainty of 3% at 20 keV. It is seen that for the high-Z materials modeled by the (water, 23% $CaCl_2$) basis pair, image uncertainty of less than [0.20% : 0.40%] and [0.10% : 0.20%], for 90 kVp and 140 kVp respectively, is required. For the low-Z materials modeled by the (water, polystyrene) basis pair, image uncertainty of less than [0.06% : 0.12%] and [0.03% : 0.06%], for 90 kVp and 140 kVp respectively, is required.

Given a target reconstructed image uncertainty, we can further estimate the pixel size necessary to achieve the target uncertainty for the same scanning dose. This analysis assumes that the image uncertainty (σ_X) is dominated by random image noise which can be reduced by averaging pixels according to the familiar $1/\sqrt{N}$ relationship. The AM and FBP noise values used here were measured within each test substance from images acquired with the standard scanning dose and reconstructed with 1x1x3 mm^3 voxel dimensions. Table 3 reports the estimated in-plane pixel size necessary to achieve the

target image uncertainty, for the same cross-plane pixel dimension of 3 mm. It is seen that the AM algorithm has the potential to achieve the target image uncertainty with in-plane pixel dimensions around 40% smaller than FBP. It is also clear that the greater sensitivity of the low-Z cross sections to input image uncertainty requires in-plane pixel dimensions on the order of 10 mm in order to achieve 3% measurement uncertainty at 20 keV at clinically-acceptable doses.

Table 3. Percent reconstructed image uncertainty required to achieve a target linear attenuation coefficient uncertainty of 3% at 20 keV. Basis material intensities are assumed to have an uncertainty of 0.07% and 0.03% for 90 kVp and 140 kVp, respectively. From the image noise reconstructed using 1.0x1.0x3.0 mm^3 voxels, the in-plane pixel size (for the same slice thickness of 3.0 mm) necessary to achieve the target image uncertainty can be estimated for each algorithm.

Basis pair (α,β)	Test Substance (X)	σ_X @ 90 kVp (%)	σ_X @ 140 kVp (%)	AM pixel size (mm x mm)	FBP pixel size (mm x mm)
(Water, 23% $CaCl_2$)	18% $CaCl_2$	0.40	0.20	1.2 x 1.2	2.1 x 2.1
	7% $CaCl_2$	0.28	0.14	2.1 x 2.1	3.4 x 3.4
	29% $NaClO_3$	0.30	0.15	1.6 x 1.6	3.0 x 3.0
	Teflon	0.20	0.10	1.9 x 1.9	3.5 x 3.5
(Water, Polystyrene)	ETOH	0.08	0.04	9.5 x 9.5	15.1 x 15.1
	50% ETOH	0.12	0.06	5.4 x 5.4	8.8 x 8.8
	MEK	0.06	0.03	14.7 x 14.7	22.4 x 22.4
	PMMA	0.09	0.05	6.0 x 6.0	9.6 x 9.6

4. Discussion

The two-parameter models used to represent photon cross-sections often have model-fitting accuracy around the 1% level(Midgley 2004; Williamson and Li 2006). The mean accuracy of pDECT total linear attenuation coefficient estimation from real data demonstrated here, which includes both modeling and measurement error, is thus encouraging. In the case where a large number of voxels can be averaged to reduce statistical uncertainty, mean linear attenuation coefficient errors are less than 1% for energies between 30 keV and 1 MeV with errors rising to between 3% and 6% at 10 keV. Both FBP and polyenergetic AM image reconstruction are shown to confer similar pDECT mean attenuation coefficient estimation accuracy, likely due to the idealized calibration procedure used here in which basis materials and test substances were scanned in identical phantom geometries.

Very few experiences of directly estimating attenuation coefficients from experimentally acquired dual-energy data are reported in the literature. Goodsitt et al.

recently published on their experience using the GE dual-energy system to estimate the effective atomic number and synthesized monochromatic images for a range of phantom materials(Goodsitt and Christodoulou 2011). The GE system utilizes fast-kVp switching for data acquisition and a proprietary pre-reconstruction method for decomposing the data into the basis components. In the range of 40 keV to 120 keV, they observed synthesized monochromatic CT # errors on the order of 1% up to 20%. It is difficult to compare Goodsitt et al.'s results to those reported here for a number of reasons. The test materials used are different and both reports show a dependence on test material. In addition, no information regarding GE's proprietary basis materials or calibration procedure is available. However, Goodsitt et al. provide a good discussion regarding the sensitivity of their results to phantom size and assumed test material density that are similar to the results of the work presented here and will help focus future research in the area.

In this work, the increased spectral separation of the *90+140 Tin* scanning energies is found to have similar mean attenuation coefficient estimation accuracy as the *90+140 Std* scanning energies, despite delivering 25% of the patient dose. The data acquisition protocols used in this work utilized the maximum tube current available. Work is ongoing to quantify the scanning dose of the tin filtered 140 kVp beam and to explore other data acquisition protocols with which we can increase the mAs per rotation. Future studies are intended to compare pDECT performance between the *Std* and *Tin* x-ray spectrum with matched scanning dose.

The statistically motivated AM algorithm does show the ability to reconstruct cross-section estimates with less pixel-to-pixel variation around the mean value, as shown in figure 5 and table 2. The noise advantage of the AM algorithm implies that to achieve a target level of cross-section uncertainty either fewer pixels will need to be averaged, less smoothing applied to the images, or DECT data can be acquired at lower imaging dose than for conventional FBP reconstruction. From the uncertainty analysis, the pixel size required to meet a target pDECT uncertainty was estimated. The noise advantage of the AM algorithm shows the potential to achieve a target level of pDECT uncertainty for reconstructed pixels with in-plane dimensions approximately 40% smaller than FBP.

The analysis of propagated attenuation coefficient uncertainty also highlights the exquisite sensitivity of the post-processing DECT method to errors, both random and systematic, in the reconstructed images. Low atomic-number materials are shown to be particularly sensitive to image-intensity errors. For DECT cross-section estimation and quantitative CT applications at large, the reconstructed image intensities for a given material need to be consistent. i.e., independent of location within the scan subject, overall size of the scan subject, and location of the subject within the FOV (Evans and Whiting 2011). SIR algorithms have been shown to reconstruct images that better satisfy these criteria of image consistency than FBP (De Man and Nuyts 2001; Elbakri and Fessler 2003; Evans and Whiting 2011; O'Sullivan and Benac 2007) and thus may provide an advantage over FBP in more complex geometries. Future work is planned to assess the effect of multiple test substances within the phantom and varying locations within the phantom on pDECT cross-section estimation accuracy.

The results from the experimentally acquired data in this work support the pDECT sensitivity shown in the propagated uncertainty analysis. Systematic streaking artifacts known to arise from excessively noisy data(Hsieh 1998) were found to compromise mean pDECT accuracy in the larger body phantom. Averaging repeat data acquisitions to increase the effective scanning dose was needed to achieve acceptable accuracy in the body phantom geometry for the basis materials and the MEK test substance. For calibration of the basis substances there is no need to limit scanning dose. However, the sensitivity of the low-Z materials, such as MEK, raises concern about the accuracy achievable in patients for which limiting the scanning dose is important. Target reconstructed image uncertainty on the order of a fraction of a percent as shown in table 3 is unlikely to be practically achievable on existing CT hardware. Further investigation is warranted to assess the level of cross-section uncertainty required to achieve acceptable levels of dose calculation uncertainty. The sensitivity of the post-processing DECT method to image-intensity uncertainties motivates interest in more sophisticated reconstruction approaches. For example, using the AM algorithm to simultaneously operate on the DE sinograms to estimate the basis component fractions (O'Sullivan and Benac 2004) may be a promising approach.

A practical limitation of the simple pDECT cross-section estimation method presented here is the selection of the optimal basis pair. Basis pair selection by equation (3) can lead to the assignment of non-ideal basis pairs since image noise can often exceed the difference between average high and low energy image intensities. As noted in the methods, potential bias from varying amounts of basis pair misclassification in AM and FBP images was avoided by assigning pixels known to be within each test substance to the ideal basis pair. Utilizing a highly smoothed pair of DECT images for basis pair selection could be employed to reduce the fraction of misclassified pixels, however the effect of increased edge blurring from the aggressive image smoothing would need to be assessed for this method.

5. Conclusions

In this work we have experimentally assessed the accuracy of post-processing DECT imaging for estimating the total attenuation coefficients in the 10 keV to 1 MeV energy range. Phantom materials with composition and density spanning the range of biological tissues were investigated in idealized geometries from datasets acquired on a commercially available CT scanner. Estimated photon attenuation coefficients were found to have clinically acceptable mean bias on the order of 1%-3%, for both small head-like phantoms and larger body-like phantoms for energies greater than 30 keV. For lower energies down to 10 keV, mean bias was found to increase to around 5%-6%. The larger body phantom necessitated scanning the basis materials and one test substance at a higher dose to achieve adequate signal-to-noise ratio. Additional tin filtering of the high kVp beam to increase the spectral separation of the DE scans was found to confer similar accuracy to the standard x-ray spectra even though the effective scanning dose of the tin filtered beam was less than 25% of the standard beam.

For the post-processing DECT method with matched basis material calibration and test substance geometries, the main advantage of polyenergetic statistical reconstruction is the improved noise performance with a corresponding decrease in cross-section measurement uncertainty for a given patient dose. Directly incorporating the statistical nature of the CT data is seen to reduce the pixel-to-pixel variability of the estimated cross-section, implying SIR can support pDECT cross-section estimation to a specified uncertainty with less pixel averaging, less smoothing or less imaging dose than conventional FBP reconstruction. Incorporating a more accurate forward model in SIR reconstruction is expected to demonstrate an advantage for future work which plans to utilize more complex phantom geometries. That a simple post-processing DECT method can estimate photon cross-sections from experimental data acquired on a commercially available scanner on the order of 1% accuracy is encouraging for kV dose calculation applications, which are sensitive to material composition. However, the highly sensitive nature of the post-processing DECT method may limit the clinical utility in more complex patient geometries where image uncertainty can easily exceed 0.5%.

Acknowledgements

This work was supported in part from grants (R01 CA 75371 and R01 CA149305, J. Williamson, Principal Investigator) awarded by the National Institutes of Health and a grant funded by Varian Medical Systems.

References

Afsharpour H, Pignol J P, Keller B, Carrier J F, Reniers B, Verhaegen F, Beaulieu L 2010 Influence of breast composition and interseed attenuation in dose calculations for post-implant assessment of permanent breast 103Pd seed implant *Phys Med Biol* 55 pp 4547-61

Bazalova M, Carrier J F, Beaulieu L, Verhaegen F 2008 Dual-energy CT-based material extraction for tissue segmentation in Monte Carlo dose calculations *Phys Med Biol* 53 pp 2439-56

Carrier J F, D'Amours M, Verhaegen F, Reniers B, Martin A G, Vigneault E, Beaulieu L 2007 Postimplant dosimetry using a Monte Carlo dose calculation engine: a new clinical standard *Int J Radiat Oncol Biol Phys* 68 pp 1190-8

Chibani O, Williamson J F 2005 MCPI©: A sub-minute Monte Carlo dose calculation engine for prostate implants *Med. Phys.* 32 pp 3688-3698

Csiszar I 1991 Why least squares and maximum entropy? An axiomatic approach to inference for linear inverse problems *Annals of Statistics* 19 pp 2032-2066

De Man B, Nuyts J, Dupont P, Marchal G, Suetens P 2001 An iterative maximum-likelihood polychromatic algorithm for CT *IEEE Trans Med Imaging* 20 pp 999-1008

du Plessis F C P, Willemse C A, Lotter M G 1998 The indirect use of CT numbers to establish material properties needed for Monte Carlo calculation of dose distributions in patients *Medical Physics* 25 pp 1195-1201

Elbakri I A, Fessler J A 2003 Segmentation-free statistical image reconstruction for polyenergetic x-ray computed tomography with experimental validation *Phys. Med. Bio.* 48 pp 2453-2477

Evans J D, Politte D G, Whiting B R, O'Sullivan J A, Williamson J F 2011 Effect of contrast magnitude and resolution metric on noise-resolution tradeoffs in x-ray CT imaging: a comparison of non-quadratic penalized alternating minimization and filtered backprojection algorithms *Proc. of SPIE - Physics of Medical Imaging* 7961 pp 79612C

Evans J D, Politte D G, Whiting B R, O'Sullivan J A, Williamson J F 2011 Noise-resolution tradeoffs in x-ray CT imaging: a comparison of Penalized Alternating Minimization and Filtered Backprojection algorithms *Med Phys* 38 pp 1444-1458

Evans J D, Whiting B R, Politte D G, O'Sullivan J A, Klahr P, Williamson J F 2011 Prospects for quantitative imaging on commercial fan-beam CT scanners: Experimental assessment of analytic and polyenergetic statistical reconstruction algorithms *Under Review at Phys. Med. Biol.* pp

Geise R A, Palchevsky A 1996 Composition of mammographic phantom materials *Radiology* 198 pp 347-50

Goodsitt M M, Christodoulou E G, Larson S C 2011 Accuracies of the synthesized monochromatic CT numbers and effective atomic numbers obtained with a rapid kVp switching dual energy CT scanner *Med Phys* 38 pp 2222-32

Green P J 1990 Bayesian reconstructions from emission tomography data using a modified EM algorithm *IEEE Trans Med Imaging* 9 pp 84-93

Heismann B J, Leppert J, Stierstorfer K 2003 Density and atomic number measurements with spectral x-ray attenuation method *J. Appl. Phys.* 94 pp 2073-2079

Hsieh J 1998 Adaptive streak artifact reduction in computed tomography resulting from excessive x-ray photon noise *Med Phys* 25 pp 2139-47

Hubbell J H, Seltzer S M 1995 *Tables of X-Ray Mass Attenuation Coefficients and Mass Energy-Absorption Coefficients 1 keV to 20 MeV for Elements Z=1 to 92 and 48 Additional Substances of Dosimetric Interest.* Report No. NISTIR 5632, National Institutes of Standards and Technology, May 1995.

Hudson H M, Larkin R S 1994 Accelerated image reconstruction using ordered subsets of projection data *IEEE Trans Med Imaging* 13 pp 601-9

ICRP 2003 *ICRP Publication 89: Basic Anatomical and Physiological Data for Use in Radiological Protection: Reference Values.* Report No. International Commission on Radiological Protection, Pergamon Press,

Kak A C, Slaney M 1988 Principles of Computerized Tomographic Imaging (New York: IEEE Press)

Landry G, Reniers B, Murrer L, Lutgens L, Gurp E B, Pignol J P, Keller B, Beaulieu L, Verhaegen F 2010 Sensitivity of low energy brachytherapy Monte Carlo dose calculations to uncertainties in human tissue composition *Med Phys* 37 pp 5188-98

Lehmann L A, Alvarez R E, Macovski A, Brody W R, Pelc N J, Riederer S J, Hall A L 1981 Generalized image combinations in dual KVP digital radiography *Med Phys* 8 pp 659-67

Lymperopoulou G, Papagiannis P, Angelopoulos A, Karaiskos P, Georgiou E, Baltas D 2006 A dosimetric comparison of 169Yb and 192Ir for HDR brachytherapy of the breast, accounting for the effect of finite patient dimensions and tissue inhomogeneities *Med Phys* 33 pp 4583-9

Midgley S M 2004 A parameterization scheme for the x-ray linear attenuation coefficient and energy absorption coefficient *Phys Med Biol* 49 pp 307-25

Midgley S M 2005 Materials analysis using x-ray linear attenuation coefficient measurements at four photon energies *Phys Med Biol* 50 pp 4139-57

O'Sullivan J A, Benac J 2007 Alternating minimization algorithms for transmission tomography *IEEE Trans Med Imaging* 26 pp 283-97

O'Sullivan J A, Benac J, Williamson J F 2004 Alternating Minimization Algorithm for Dual Energy X-ray CT *Proc. IEEE International Symposium on Biomedical Imaging* pp 579 - 582

Pantelis E, Papagiannis P, Karaiskos P, Angelopoulos A, Anagnostopoulos G, Baltas D, Zamboglou N, Sakelliou L 2005 The effect of finite patient dimensions and tissue inhomogeneities on dosimetry planning of 192Ir HDR breast brachytherapy: a Monte Carlo dose verification study *Int J Radiat Oncol Biol Phys* 61 pp 1596-602

Primak A N, Ramirez Giraldo J C, Liu X, Yu L, McCollough C H 2009 Improved dual-energy material discrimination for dual-source CT by means of additional spectral filtration *Med Phys* 36 pp 1359-69

Rutherford R A, Pullan B R, Isherwood I 1976 Measurement of effective atomic number and electron density using an EMI scanner *Neuroradiology* 11 pp 15-21

Schneider W, Bortfeld T, Schlegel W 2000 Correlation between CT numbers and tissue parameters needed for Monte Carlo simulations of clinical dose distributions *Phys Med Biol* 45 pp 459-78

Taylor B N, Kuyatt C E 1994 *Guidelines for evaluating and expressing the uncertainty of NIST measurement results*. Report No. NIST Technical Note 1297, National Institute of Standards and Technology, 1994.

Torikoshi M, Tsunoo T, Sasaki M, Endo M, Noda Y, Ohno Y, Kohno T, Hyodo K, Uesugi K, Yagi N 2003 Electron density measurement with dual-energy x-ray CT using synchrotron radiation *Phys Med Biol* 48 pp 673-85

Watanabe Y 1999 Derivation of linear attenuation coefficients from CT numbers for low-energy photons *Phys Med Biol* 44 pp 2201-11

White D R, Widdowson E M, Woodard H Q, Dickerson J W 1991 The composition of body tissues (II). Fetus to young adult *Br J Radiol* 64 pp 149-59

Williamson J F, Li S, Devic S, Whiting B R, Lerma F A 2006 On two-parameter models of photon cross sections: application to dual-energy CT imaging *Med Phys* 33 pp 4115-29

Williamson J F, Whiting B R, Benac J, Murphy R J, Blaine G J, O'Sullivan J A, Politte D G, Snyder D L 2002 Prospects for quantitative computed tomography imaging in the presence of foreign metal bodies using statistical image reconstruction *Med Phys* 29 pp 2404-18

Woodard H Q, White D R 1986 The composition of body tissues *Br J Radiol* 59 pp 1209-18

Yaffe M J, Boone J M, Packard N, Alonzo-Proulx O, Huang S Y, Peressotti C L, Al-Mayah A, Brock K 2009 The myth of the 50-50 breast *Med Phys* 36 pp 5437-43

Ziegler A, Kohler T, Proksa R 2007 Noise and resolution in images reconstructed with FBP and OSC algorithms for CT *Med Phys* 34 pp 585-98